DMPCO 2025

3rd International Conference
DESIGN AND MANAGEMENT OF PORT, COASTAL AND OFFSHORE WORKS

Organized by:

Laboratory of Hydraulic Engineering

Laboratory of Maritime Engineering and Maritime Works

Laboratory of Harbor Works

Laboratory for Floating Structures and Mooring Systems

7-9 MAY 2025

CONFERENCE & CULTURAL CENTER OF THE UNIVERSITY OF PATRAS | PATRAS, GREECE

PROCEEDINGS

3rd International Conference
DESIGN AND MANAGEMENT OF PORT, COASTAL AND OFFSHORE WORKS

DMPCO 2025

MAY 7-9, 2025

Conference & Cultural Center of the University of Patras

Patras, Greece

Proceedings of the 3rd International Conference
Design and Management of Port, Coastal and Offshore Works

Published by: Laboratory of Hydraulic Engineering, Department of Civil Engineering, University of Patras

Edited by: A. Dimas, A. Dimakopoulos, G. Leftheriotis

Year of Publication: 2025

COMMITTEES

ORGANIZING COMMITTEE

CHAIR

Athanassios Dimas, Professor, Director of the Laboratory of Hydraulic Engineering, University of Patras

CO-CHAIRS

Theofanis Karambas, Professor, Director of the Laboratory of Maritime Engineering and Maritime Works, Aristotle University of Thessaloniki

Vasiliki Tsoukala, Professor, Director of the Laboratory of Harbor Works, National Technical University of Athens

LOCAL COMMITTEE

Aggelos Dimakopoulos, Assistant Professor, University of Patras

Nikolaos Fourniotis, Associate Professor, University of the Peloponnese

Gerasimos Kolokythas, Dr. Coastal Engineer, ACTAEA

Georgios Leftheriotis, Dr. Research Associate, University of Patras

Christoforos Pappas, Assistant Professor, University of Patras

SCIENTIFIC COMMITTEE

Androulidakis Y., Assoc. Professor, University of the Aegean

Athanasoulis G., Professor Em., NTUA

Belibassakis K., Professor, NTUA

Chalmoukis I., Postdoctoral Assoc., University of Patras

Chatzigeorgiou I., Professor, NTUA

Chatzimpiros K., Professor Em., AUTH

Chlomoudis K., Professor, University of Piraeus

Chondros M., Assist. Professor, NTUA

Christopoulos S., Dr. Coastal Engineer, HYDROMARE, Greece

Depountis N., Assoc. Professor, University of Patras

Dimakopoulos A., Assist. Professor, University of Patras

Dimas A., Professor, University of Patras

Fourniotis N., Assoc. Professor, University of the Peloponnese

Galani K., Dr. Coastal Engineer, Patras Port Authority

Grigoriadis D., Assoc. Professor, University of Cyprus

Grigoropoulos G., Professor, NTUA

Karampas Th., Professor, AUTH

Karmpadakis I., Assoc. Professor, Imperial College

Katsardi V., Assist. Professor, UTH

Kolokythas G., Dr. Coastal Engineer, ACTAEA, Greece

Konispoliatis D., Assist. Professor, NTUA

Koutitas Ch., Professor Em., AUTH

Koutrouveli Th., Dr. Coastal Engineer, IMDC, Belgium

Krestenitis Y., Professor Em., AUTH

Kupraios N., Dr. Civil Engineer, ΜΟΔ Α.Ε.

Langousis A., Professor, University of Patras

Leftheriotis G., Postdoctoral Assoc., University of Patras

Loizidou M., Professor, NTUA

Loizidou X., Dr. Coastal Engineer, ISOTECH, Cyprus

Loukogeorgaki E., Professor, AUTH

Makris C., Assist. Professor, DUTH

Mavrakos S., Professor Em., NTUA

Melissas D., Professor, NTUA

Memos K., Professor Em., NTUA

Metallinos A., Dr. Civil Engineer, Research Assoc., NTUA

Michailidis C., Assistant Professor, IHU

Mpardakis B., Dr. Civil Engineer, President of HCCE

Nikolakopoulos C., Professor, University of Patras

Pallis A., Professor, University of the Aegean

DMPCO 2025

CONTENTS 7

PREFACE 13

EXTENDED ABSTRACTS OF DMPCO 2025 PROCEEDINGS

COASTAL MODELLING

HYDRODYNAMICS

WAVE MODELLING

WAVE STRUCTURE INTERACTION

SEDIMARE: ADVANCED HYDRO-MORPHODYNAMICS

FLOATING WIND ENERGY

OFFSHORE, COASTAL AND PORT MANAGEMENT I

OFFSHORE, COASTAL AND PORT MANAGEMENT II

SEDIMARE: WAVE ENERGY

ENGINEERING DESIGN AND CONSTRUCTION

REMOTE SENSING

COASTAL HAZARDS

DMPCO 2025

PREFACE

The 3rd International Conference "Design and Management of Port, Coastal and Offshore Works", DMPCO 2025, was held in Patras, Greece, at the Conference & Cultural Center of the University of Patras, from 7 to 9 May 2025. DMPCO 2025 was organized by the Laboratory of Hydraulic Engineering, Department of Civil Engineering, University of Patras, with the collaboration of the Laboratory of Maritime Engineering and Maritime Works, Department of Civil Engineering, Aristotle University of Thessaloniki, the Laboratory of Harbor Works, School of Civil Engineering, National Technical University of Athens, and the Laboratory for Floating Structures and Mooring Systems, School of Naval Architecture and Marine Engineering, National Technical University of Athens.

The conference aimed to the presentation of results and the stimulation of comprehensive discussions on the contemporary and state-of-the-art research (pure and applied) and engineering (technology and practice) advances associated with the conference topics which include (but are not limited to): extreme environmental conditions in the offshore and coastal zones, offshore and nearshore hydro-morphodynamic processes, nature-based coastal protection solutions, design-construction-installation-management of offshore structures (fixed and floating) for underwater mining and exploitation of hydrocarbons, renewable energy (wind and wave) in the offshore-coastal-harbor environment, coastal protection against erosion and inundation, design-construction-management of harbor, coastal and offshore structures, climate change effects on physical processes in the offshore and the coastal environment as well on harbor, coastal and offshore structures, vulnerability and risk assessment associated with the offshore and coastal environment and infrastructures, protection of coastal heritage monuments, digital and AI technology in coastal applications.

DMPCO 2025 has successfully attracted the interest of about 250 authors from Greece, Austria, Belgium, China, Cyprus, France, Georgia, Italy, the Netherlands, New Zealand, Poland, Portugal, Saudi Arabia, Spain, Turkey, UAE, the United Kingdom and the USA. The final technical program included 79 presentations distributed into 12 sessions, as well as 3 keynote presentations, where worldwide recognized speakers presented cutting-edge topics. The DMPCO 2025 Proceedings include 79 extended abstracts, which are grouped in eleven main thematic areas of the Conference corresponding to: Coastal Modelling; Hydrodynamics; Wave Modelling; Wave Structure Interaction; Advanced Hydro-Morphodynamics; Floating Wind Energy; Offshore, Coastal and Port Management; Wave Energy; Engineering Design and Construction; Remote Sensing and Coastal Hazards.

We would like to thank all authors and keynote speakers for their contributions, the non-authors for the active participation, as well as all the members of the Organizing and the Scientific Committees for their valuable help and support. DMPCO 2025 received enthusiastic comments by all participants (authors and non-authors) in terms of the organization and conference venue, the scientific quality of the presentations, the stimulating technical discussions as well as the organization of social events.

We are looking forward to DMCPO 2027 in Athens, Greece.

Dr. Athanassios Dimas, Professor
Dr. Aggelos Dimakopoulos, Assistant Professor
Dr. Georgios Leftheriotis, Postdoctoral Research Associate

3rd International Conference
DESIGN AND MANAGEMENT OF PORT, COASTAL AND OFFSHORE WORKS
DMPCO 2025

Long-term Coastline Evolution: A Hybrid One-Line Model Approach for Urban Shorelines

Demetriade S.[1,*] and Stagonas D.[1]

[1] University of Cyprus, Kallipoleos 75, Nicosia, 1678, Cyprus

*corresponding author:
e-mail: sdemet04@ucy.ac.cy

Coastal areas are highly dynamic environments, susceptible to both anthropogenic influences and natural changes. Urbanization, combined with natural phenomena, has significantly altered coastal dynamics. Rising sea levels, coupled with the increasing frequency and intensity of storm surges, pose significant threats to the stability of coastal ecosystems, further amplifying their vulnerability (Oppenheimer et al., 2019). To address coastal erosion and stabilize shorelines, hard engineering structures have been widely implemented. However, in many cases, these structures have exacerbated coastal erosion (Komar, 1983), often due to inadequate understanding of nearshore coastal dynamics.

Hard engineering structures can induce localized changes in hydro- and sediment-dynamics, which are highly site-specific and depend on factors such as sediment characteristics, climate conditions, structural design, and nearshore hydro-morphodynamics (Hashim et al., 2013; Fairley et al., 2009; Fan et al., 2006). Therefore, evaluating the effectiveness of these structures requires a comprehensive understanding of sediment dynamics, including the erosional and depositional patterns they influence, as well as the processes governing sediment transport rates.

Simplified-process-based models such as equilibrium shoreline models are often utilized in predicting chronic shoreline changes. Such models are simple and computationally efficient, however, they do not explicitly resolve specific processes and their accuracy is limited, in e.g., locations where the unresolved processes contribute to the coastal evolution and/ or coastal squeeze occurs, and by the quantity of site-specific data available to fit the model. Contradicting the above, physics-based numerical models can accurately resolve hydrodynamic, sediment transport and morphological processes and are capable of simulating the response of a shoreline to a range of severe and extreme events, they come however at a significant computational cost (Luijendijk et al., 2017). Conclusively, large- (in the context of shoreline length) and long- (in the context of time) scale simulations are computationally expensive, and the evolution of heavily defended shorelines, were up to now excluded from predictions and simulations (Vitousek et al., 2017).

The coastal area of Limassol, in Southern Cyprus, presents an example of a heavily protected and modified coastline, having 61 breakwaters and 28 groins in a coastal stretch of 9 km. Considering the modelling limitations outlined above, and in achieving a fine balance between them, the present study aims in expanding and adapting a 1-line model (Roelvink et al., 2020) along with its combination with a shoreface translation tool (McCarrol et al., 2021) in predicting long-term evolution of the coastline. Expanded and adapted 1-line model utilizes the flexible-grid and unstructured mesh in representing the coastline as freely moving string of points as described in Roelvink et al., (2020). In capturing longshore sediment movement, the CERC formula (Shore Protection Manual, US Army Corps of Engineers, 1984) and the analytical scheme of Leont'yev and Akivis (2023) were adapted, while consideration of cross-shore sediment re-distribution due to sea level rise was achieved using the method of McCarroll et al., (2021).

The given work presents an innovative approach for investigating coastal evolution in the vicinity of hard engineering structures, by merging, adapting and expanding a 1-line model with a shoreface translation tool. In doing so, the historical sediment transport and erosion-deposition patterns in the locality of detached low-crested breakwaters were investigated for the coastline of Limassol, Cyprus. The data used for this study were collected from field measurements and secondary sources from 1963 to 2019. Seasonal bathymetric and topographic surveys were initiated in January 2025, utilizing a sonar transducer and a specialized drone with a vertical accuracy of $\pm$ 0.1 m, in creating cross-shore beach profiles (Figure 1).

Beach profiles will be used to investigate sediment movements in the cross-shore direction. In addition, satellite derived shoreline positions from 1963 to 2019 were extracted from the Public Works Department of Cyprus and Luijendijk et al., (2018). The model has been shown capable of predicting volumetric changes as well as changes in the shoreline contour in the vicinity of the series of breakwaters, on time scales from hours to years.

REFERENCES

Fairley, I., Davidson, M., & Kingston, K. (2009). The Morpho-dynamics of a Beach Protected by Detached Breakwaters in a High Energy Tidal Environment. *J. Coast. Res.* 56, 607–611.

Fan, D., Guo, Y., Wang, P., & Shi, J.Z. (2006). Cross-Shore Variations in Morphodynamic Processes of an Open-Coast Mudflat in the Changjiang Delta, China: With an Emphasis on Storm Impacts. *Cont. Shelf Res.* 26(4), 517–538.

Hashim, R., Fitri, A., Motamedi, S, & Hashim, A.M. (2013). Modeling of Coastal Hydrodynamic Associated with Coastal Structures: A Review. *Malays. J. Sci.* 32, 149–154.

Komar, P.D. (1983). Coastal erosion in response to the construction of jetties and breakwaters. In Komar (1st ed) Handbook of Coastal Processes and Erosion. CRC Press.

Leont'yev, I.O. & Akivis, T.M. (2023). Morphological changes of a sandy beach under the influence of a breakwater. In Chaplina, T. (eds) Processes in GeoMedia – Volume VI. Springer Geology.

Luijendijk, A. et al. (2017). The initial morphological response of the Sand Engine: A process-based modelling study. *Coast. Eng.* 119, 1–14.

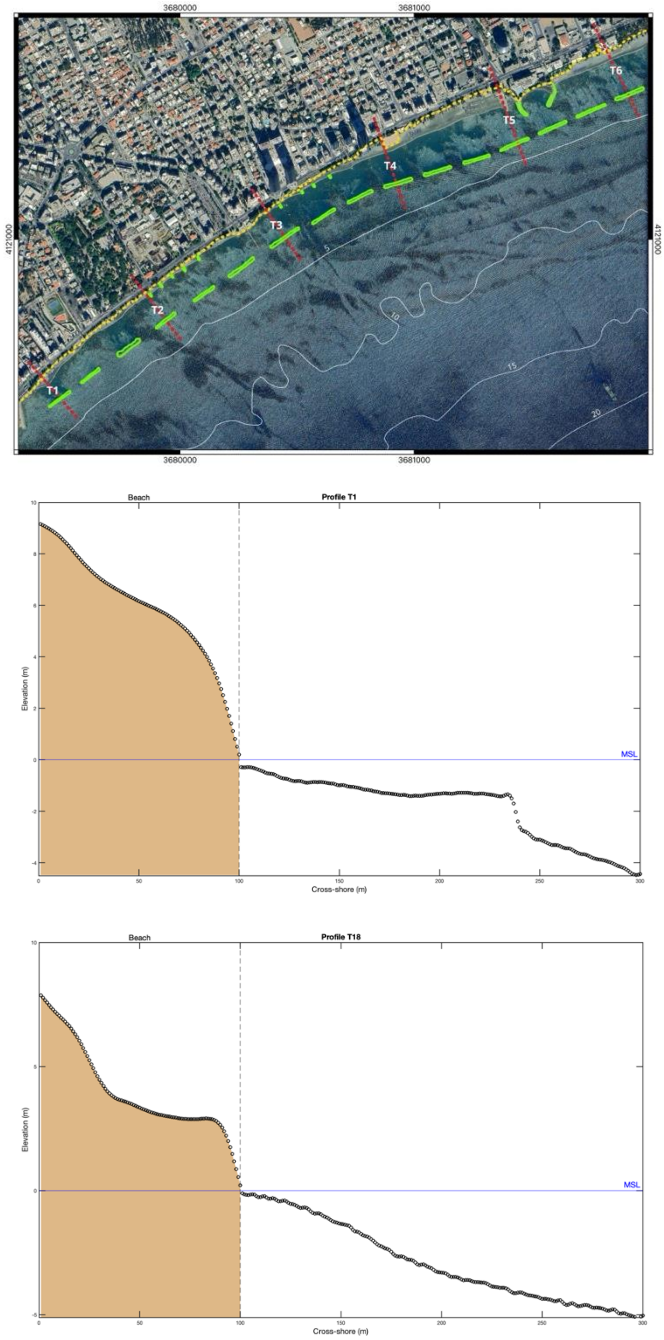

Figure 1. Site demonstration (top) indicating the build backbone of the area (yellow dashed line), cross-shore profile locations selected for model application (red dashed line T1-T18) and coastal structures (green line). Two profiles are presented for the Limassol area: the first profile (T1) and the last profile (T18), highlighting the beach zone and the underwater topography.

Luijendijk, A. et al. (2018). The State of the World's Beaches. *Sci. Rep.* 8, 6641.

McCarroll J.R. et al. (2021). A rules-based shoreface translation and sediment budgeting tool for estimating coastal change: ShoreTrans. *Mar. Geol*. 435(6), 106466.

Nam, P.T., Larson, M., & Hanson, H. (2011). Modeling Morphological Evolution in the Vicinity of Coastal Structures. *Coast. Eng. Proc.* 1(32), 68.

Oppenheimer et al. (2019). Sea level rise and implication for low lying islands, coasts and communities. Cambridge University Press, Cambridge UK, 321-445.

Roelvink, D, Huisman, B., Elghandour, A., Ghonim, M., & Reyns, J. (2020) Efficient Modeling of Complex Sandy Coastal Evolution at Monthly to Century Time Scales. *Front. Mar. Sci.* 7(535).

Shore Protection Manual. (1984). CERC, Waterways Experiment Station, Vicksburg, USA.

Vitousek, S, Barnard, P.L., Limber, P., Erikson, L., & Cole, B. (2017). A model integrating longshore and cross-shore processes for predicting long-term shoreline response to climate change. *J. Geoph. Res. Earth Surf.* 112, 782-806.

Assessing the Impact of Climate Change on Shoreline Evolution in Alykes Beach, Zakynthos, Greece

Metallinos A.[1,2*], Papadimitriou A.[1,2], Chondros M.[1,2], Reyns J.[3,4] and Roelvink, D.[3,4]

[1] Scientia Maris, Agias Paraskevis Str. 117, 15234, Chalandri, Greece
[2] Laboratory of Harbour Works, School of Civil Engineering, NTUA, 9 Iroon Polytechniou Str., 15780, Zografou, Greece
[3] IHE Institute for Water Education, Delft, Netherlands
[4] Deltares, Delft, Netherlands

*corresponding author:
e-mail: ametallinos@scientiamaris.com

INTRODUCTION

Coastal zones are vital areas that support diverse ecosystems, economies, and communities while remaining among the most dynamic and ever-changing environments. The continuous shift in shoreline position has significant implications for the environment, economic activities, and public safety. Climate change, through rising sea levels and alterations in wave climate, intensifies the risks of erosion, shoreline retreat, and coastal flooding, making these regions even more vulnerable. Consequently, the urgency for effective coastal management strategies and adaptation planning has never been greater. These strategies must be based on robust and as accurate as possible projections of coastal morphological evolution in the coming years and decades to ensure sustainable and resilient coastal development. This research aims to simulate the medium-term shoreline evolution on Alykes Beach, Zakynthos, Greece, a region with a history of erosion issues that pose a significant challenge to the local tourism-dependent economy. By comparing historical data with projected climate change scenarios (RCP4.5 and RCP8.5), the main objective of this research is to assess the potential impacts of climate change on shoreline evolution considering both alteration of the wave climate and mean sea level rise.

NUMERICAL MODEL & METHODOLOGY

The medium-term shoreline evolution is simulated using the ShorelineS cloud model, based on the source code developed by Roelvink et al. (2018, 2020) and the user interface developed by Scientia Maris (2025). The governing equation for updating of the coastline position is based on the conservation of sediment:

$$\frac{\partial n}{\partial t} = -\frac{1}{D_c}\frac{\partial Q_s}{\partial s} - \frac{RSLR}{\tan\beta} + \frac{1}{D_c}\sum q_i \qquad (1)$$

where n is the cross-shore coordinate, s the longshore coordinate, t is time, D_c is the active profile height, Q_s is the longshore transport rate (m^3/yr), tanβ is the average profile slope between the dune crest and the depth of closure, $RSLR$ is the relative sea-level rise (m/yr) and q_i is the source/sink term (m^3/m/yr) due to cross-shore transport, overwashing, nourishments and exchanges with rivers and tidal inlets.

The study area spans a 3.5 km stretch of coastline (Figure 1), bounded to the east by Alikarnas Marina. The sediment in the area is fine-grained, and there is significant longshore sediment transport along the coastline. Two groynes, each approximately 110 m in length, are located around the mid-point of the coast, influencing significantly the coastal processes. Aerial imagery from various satellite missions (Sentinel-2, Landsat-8, Landsat-9) were obtained and the ones with optimal resolution were used to digitize the coastline for the validation period. Offshore wave characteristics were derived from the Copernicus Climate Change Service Pan-European Wave model, covering two 20-year periods: 1986–2005 for historical data and 2041–2060 for climate change projections, at a point located about 12 km offshore the study area. Notably, the most frequent offshore mean wave direction is North-Northwest (310° using the nautical convention) across all datasets, with a mean annual occurrence of 9.21% for the historical period, 9.26% for RCP 4.5, and 9.35% for RCP 8.5. Sea Level Rise (SLR) projections for the study area are based on the IPCC's 6th Assessment Report (AR6), for both RCP4.5 and RCP8.5 scenarios, with median values of 6 mm/year and 8 mm/year respectively. To ensure a fair comparison, all simulations use the coastline position of May 29, 2024, as the baseline initial condition.

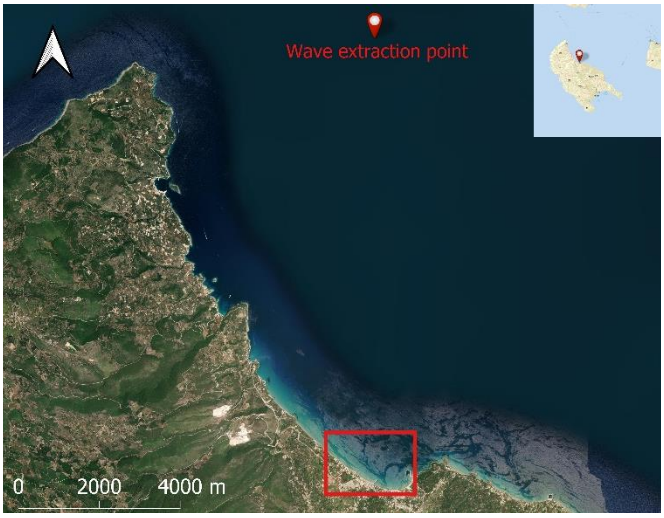

Figure 1. Study area (enclosed in red rectangle).

At first, model validation and calibration were performed to assess the model's capability to capture the dominant longshore coastal processes for a 14-month period, from April 2016 until June 2017. Offshore wave characteristics were obtained from the Climate Change Service dataset, with the full timeseries used to drive the model, propagated at the depth of closure with the Maris PMS model (Scientia Maris, 2022). As shown in Figure 2, the ShorelineS, with a grid resolution of 50 m, reproduces the annual shoreline evolution with satisfactory accuracy. In particular the model accurately captures the erosion east of the south groyne, although it slightly overestimates the accretion near the structure.
Consequently, in order to simulate the shoreline evolution for each 20-year period, offshore wave characteristics were divided into 36 sectors and representative waves were selected based on the method of Chondros et al. (2022). Similarly, these waves were then propagated in the nearshore

area using Maris PMS. For future projections, changes in wave climate were considered both independently and along with SLR projections to assess the contribution of each forcing factor.

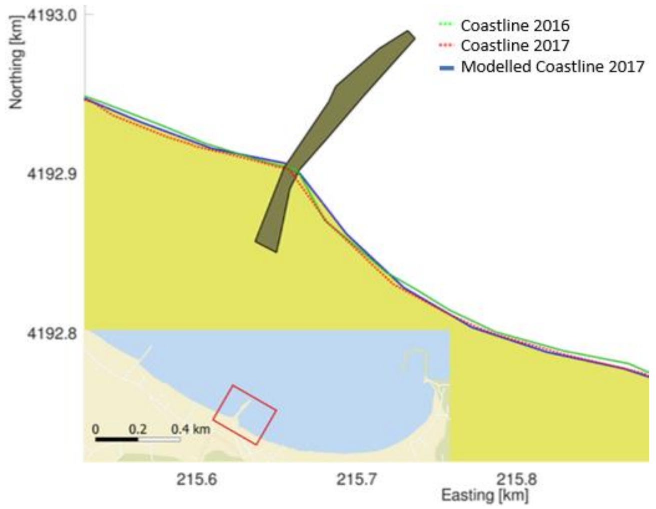

Figure 2. Model calibration for a 14-month period.

RESULTS & DISCUSSION

The obtained results reveal significant variations in shoreline evolution under different climate scenarios compared to the historical period. The projected shoreline changes for RCP 4.5 at the end of the 20-year period, specifically at the area between the two groynes, are presented in Figure 3, while the corresponding results for RCP 8.5 are shown in Figure 4 (in comparison to the historical shoreline evolution).

For RCP 4.5, when considering only alterations in wave climate, the shoreline evolution exhibits less erosion compared to the historical dataset. This is primarily attributed to the presence of less energetic waves in RCP 4.5. However, when factoring in the effects of SLR, cross-shore variations lead to a more pronounced shoreline retreat in the study area. For RCP 8.5, the projected wave climate leads to almost identical results compared to the historical dataset. SLR has a much more pronounced impact, leading to a more significant shoreline retreat compared to RCP 4.5. It is noteworthy that the shoreline shift, due to SLR, is not a simple parallel offset of the initial shoreline, highlighting the importance of including the interaction between the projected wave climate and mean SLR when simulating the future shoreline evolution incorporating the effect of climate change.

CONCLUSIONS

This research highlights the significant impacts of climate change on shoreline evolution at Alykes Beach, Zakynthos, Greece. By analyzing both historical data and projected climate scenarios, this study identifies key drivers of coastal change, particularly the influence of wave climate alterations and SLR. The ShorelineS cloud model provides valuable insights into the long-term effects of these drivers, demonstrating an intensification of erosion, especially when SLR is included in the model forcing. The findings indicate that the latter is the dominant factor influencing future shoreline evolution, not only because of the direct rise in sea level but also due to its interaction with changes in wave conditions in the nearshore. For instance, the shift of the shoreline position due to SLR affects wave refraction angles, thereby indirectly altering the longshore sediment transport rates. The results emphasize the urgent need for adaptive coastal management strategies to mitigate the impacts of climate change. Ongoing research will focus on evaluating the effectiveness of "soft" (e.g. beach nourishment) and "hard" protection measures (e.g. detached breakwaters), with both easily simulated with the ShorelineS cloud model.

Figure 3. Shoreline evolution for a 20-year period for the historical wave dataset and RCP 4.5 with and without SLR.

Figure 4. Shoreline evolution for a 20-year period for the historical wave dataset and RCP 8.5 with and without SLR.

REFERENCES

Chondros, M., Papadimitriou, A., Metallinos, A., Tsoukala, V. (2022). Sediment Transport Equivalent Waves for Estimating Annually Averaged Sedimentation and Erosion Trends in Sandy Coastal Areas. *J. Mar. Sci. Eng.* 10(11), 1726.

Roelvink, D. Huisman, B., Elghandour, A. 2018. Efficient modelling complex coastal evolution at monthly to century timescales. 6th Internation Conference on Estuaries and Coasts (ICEC 2018), August 20-23, Caen, France.

Roelvink, D. Huisman, B., Elghandour, A., Ghonim, M. Reyns, J. (2020). Efficient modelling complex coastal evolution at monthly to century timescales. *Front. Mar. Sci.* 7, 535.

Scientia Maris (2022) Maris PMS User Guide. Athens, Greece

Scientia Maris (2025) ShorelineS cloud, Shoreline evolution model, User Guide v01.2025.

The Compound Hazard of Coastal Flooding and Beach Erosion at the Beaches of Platania and Agia Marina in Crete, Greece

Malliouri D.[1,*], Kyriakidou C., Petrakis S.[1], Vandarakis D.[1], Moraitis V.[1], Gad F.-K. [2], Drakopoulou P.[1], and Kapsimalis V.[1]

[1] Hellenic Centre for Marine Research, Greece
[2] Region of South Aegean, Greece

*corresponding author:
e-mail: d.malliouri@hcmr.gr

ABSTRACT

Coastal areas, and especially the low-lying beaches, are usually prone to seawater flooding, which can negatively affect human life, property, and activities. Furthermore, a relevant hazard to coastal flooding is the shoreline recession due to wave storms induced-beach erosion and extreme storm surges. Although flooding and erosion are physically linked, they are typically modeled separately due to complex relationships between driving processes. The present approach seeks to address this gap in current practice. This is accomplished through the derivation of several storm scenarios from a long-term wave dataset, the consideration of sea level rise and storm surge, the implementation of an open-source numerical model to quantitatively estimate wave runup, coastal flooding, and short-term coastal morphology change, and through the quantification of the storm induced-erosion and flooding extents via proper indices. These indices are derived from state-of-the-art tools and existing knowledge. The proposed methodology is applied and validated for the case study of the Gulf of Chania, in Crete Island, Greece. In this manner, the necessary information for assessing the compound hazard of coastal flooding and erosion is obtained to assure coastal resilience.

INTRODUCTION

Coastal areas, recognized as regions particularly vulnerable to the imminent threats of climate change, have been the subject of extensive research focusing on understanding and implementing resilience strategies. A key element for effective and timely adaptation actions is the accurate assessment of coastal risks induced either by extreme weather conditions (e.g. storm waves, extreme sea levels, compound events) or gradual changes (e.g. eustatic sea level rise) (Malliouri et al., 2024). The two most dominant coastal risks are flooding and erosion, usually presenting an interactive relationship (Pollard et al., 2019); specifically, seawater flood is dependent on coastal morphology; future flood risk depends on moving shoreline position; and last but not least, erosion and flooding events often occur simultaneously. Therefore, it is evident that an accurate quantitative assessment of coastal flooding risk considering the concomitant effect of coastal erosion/accretion is imminent to advance current coastal engineering approaches and assist coastal communities increasing their resilience (Toimil et al., 2023).

METHODOLOGY

Two open-source models were implemented: the SWAN model (Holthuijsen et al., 1993), developed at Delft University of Technology, which is a third-generation wave model that computes random, short-crested wind-generated waves in offshore and coastal regions, and the hydro-morpho-dynamical model XBeach. It is a two-dimensional model capable of simulating wave propagation, sediment transport, and morphology changes on beaches (Roelvink et al., 2010). In the present analysis, wave storms corresponding to 50, 100, and 250 years return periods were selected to be simulated and combined with the mean sea level for the present and distant future, incorporating climate change effects and storm surge. Then, the erosion and flooding extents are measured from the 2d maps of the model's results and the beach profiles using a variety of measures, e.g. the inundation areas, the wave runup, and the shoreline retreat.

CASE STUDY

The beaches of Platania and Agia Marina in the Gulf of Chania in Crete consist mainly of fine sand, which can be easily used for morphological simulations. Furthermore, being a highly urbanized area, commercial, administrative, cultural and tourist activities are concentrated along the coast. Hence, it is of particular interest to engineers/scientists and the public.

RESULTS

The three selected wave scenarios (see Table 1), corresponding to 50, 100, and 250 years return periods were combined with the mean sea level rise due to climate change for the 2-future shared socioeconomic pathway (SSP) scenarios, namely a pessimistic one SSP8.5 and an optimistic one SSP4.5, and the 95% quantile of total water level (storm surge (SS) and tide (T)).

Table 1. Wave scenarios to be simulated

i/n	T_r (years)	H_s (m)	T_p (s)	MWD (deg. from North)
1	50	5.80	10.40	0
2	100	6.00	10.60	0
3	250	6.25	10.85	0

The obtained results of the combination of wave scenario 2 and optimistic scenario SSP4.5 through the use of SWAN model and Xbeach model are indicatively presented in Figures 1-3. It is derived that in this compound scenario, 83% of the shoreline is characterized by erosion measured with shoreline retreat, 7% by accretion, while the rest part presents insignificant evolution. It is noted that the shoreline retreat ranges between 2 m and 34 m in this combined scenario in the study area.

Furthermore, it is observed that the neglecting of the effect of the short-term erosion in assessing coastal flooding risk under extreme sea conditions can lead to spurious and often underestimated coastal flood risk projections (see Figure 2), and consequently maladaptation (Toimil et al., 2023).

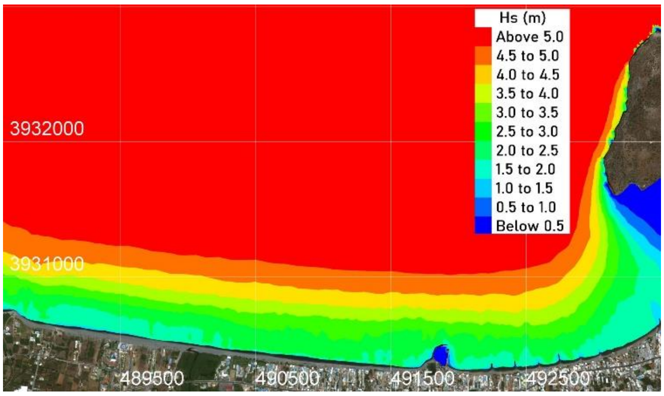

Figure 1. Propagation of wave scenario 2 with Swan.

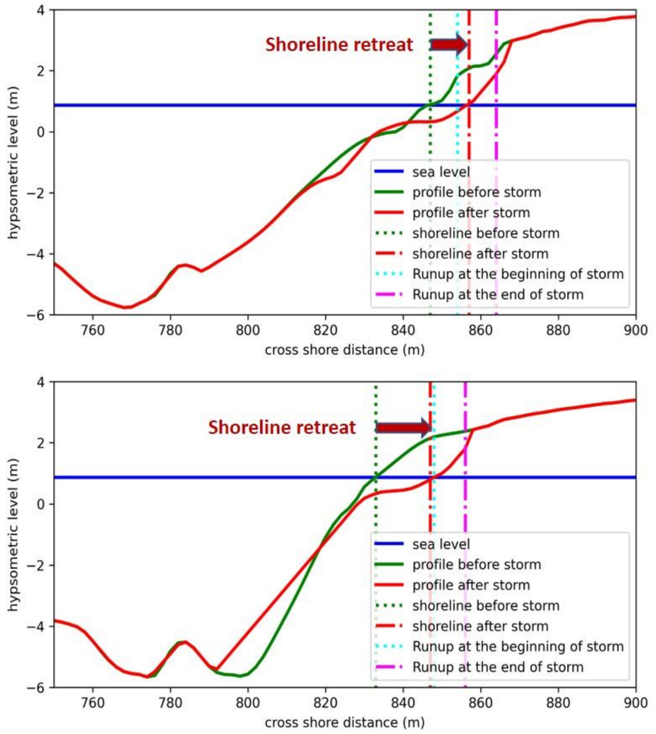

Figure 2. Beach profile, shoreline position, and runup position at the beginning of storm and at the end of storm at two indicative beach profiles in the study area, derived from Xbeach simulations, for wave scenario 2.

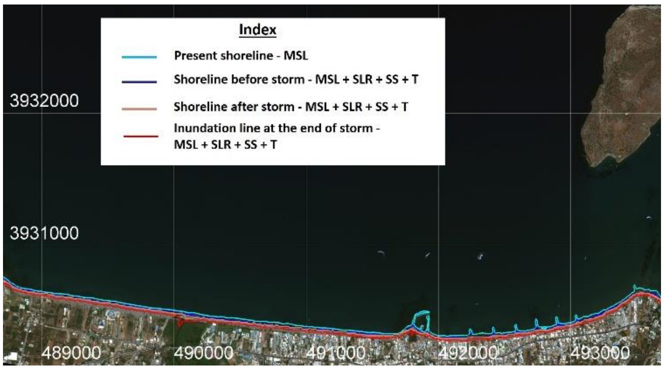

Figure 3. Present shoreline (cyan line), shoreline before storm combined with MSL, SLR, SS, and T (blue line), shoreline after storm combined with MSL, SLR, SS, and T (orange line), and inundation line at the end of storm, (red line) derived from Xbeach simulations, for wave scenario 2.

CONCLUSIONS

The paper deals with the related hazards of coastal flooding and erosion risk at the Platania and Agia Marina beaches in the Gulf of Chania in Crete. The results revealed that the coast of interest is highly vulnerable to coastal hazards exacerbated by climate change, so mitigation measures should be implemented in the future.

Moreover, the proposed methodology gives insight into compound numerical modeling of coastal hazards and highlights the proper tools that quantify and characterize coastal flooding and erosion. Hence, some essential tools are derived from the present approach contributing thus to coastal protection and resilience.

ACKNOWLEDGEMENTS

D. Malliouri acknowledges support of this work by the Research Project “ESSENCE”: Risk Assessment in Coastal Areas, at Hellenic Centre for Marine Research (HCMR), funded by a private international fund.

REFERENCES

Holthuijsen, L.H., Booij, N., & Ris, R.C. (1994). A Spectral Wave Model for the Coastal Zone, Ocean Wave Measurement and Analysis, 630–641.

Malliouri, D.I., Kyriakidou, C., Moraitis, V., Vandarakis, D., Martzikos, N., Gad, F.-K., Hatiris, G.-A., & Kapsimalis, V. (2024). A new approach for the assessment of coastal flooding risk. Application in Rhodes island, Greece. *Appl. Ocean Res.* 148, 104006.

Pollard, J., Spencer, T., & Brooks, S. (2019). The interactive relationship between coastal erosion and flood risk. *Prog. Phys. Geogr.* 43, 574–585.

Roelvink, D., Reniers, A., Van Dongeren, A., Van Thiel De Vries, J., Lescinski, J., & Report, R.M. (2010). XBeach Model Description and Manual.

Toimil, A., Álvarez-Cuesta, M., & Losada, I.J. (2023). Neglecting the effect of long- and short-term erosion can lead to spurious coastal flood risk projections and maladaptation. *Coastal Eng.* 179, 104248.

Developments in Wave-Induced Cross-Shore Sediment Transport Modelling Using the TELEMAC Suite

Kolokythas G.[1,3*], Breugem W.A.[2], Wang L.[2,3] and De Maerschalck B.[3]

[1] ACTAEA Consulting Engineers, Patras, Greece
[2] International Marine and Dredging Consultants, Antwerp, Belgium
[3] Flanders Hydraulics Research, Antwerp, Belgium

*corresponding author
e-mail: gkolokithas@gmail.com

INTRODUCTION

During the last years, the TELEMAC open-source platform (www.opentelemac.org) has presented significant advances in the wave-induced sediment transport modelling at the nearshore areas. As there is still space for further development, the work presented here aims to make the TELEMAC suite capable of simulating cross-shore sediment transport through the implementation of different cross-shore processes in the wave and sediment transport modules, namely,: (a) The surface roller energy generated in the breaking wave front, (b) the return current that counterbalances the so-called Stokes drift, (c) the wave non-linearities that become important in shallow water, i.e. wave skewness and wave asymmetry and (d) the wave breaking turbulence produced in the collapsing wave front.

In this article, the evaluation of a 2D-morphodynamic model for the central part of the Belgian coast, the so-called Ostend model, is presented. The Ostend model was constructed so that the new developments on the cross-shore transport modelling can be validated against field measurements under realistic forcing conditions. The modelling strategy involves the online coupling of the hydrodynamic, wave and sediment transport modules, i.e. TELEMAC-2D, TOMAWAC and GAIA, respectively. The morphological validation of the model is performed by means of a hindcasting exercise, where bottom changes at the nearshore area of interest are predicted at the time-scale of one year.

FORMULATION & CODE DEVELOPMENT

The simulation of the cross-shore sediment transport is performed by combining the advection-diffusion equation for the tempo-spatial variation of sediment concentration, and the erosion-deposition terms for the calculation of the bed level changes:

$$\frac{\partial hC}{\partial t} + \frac{\partial h\, U_{tot} C}{\partial x} + \frac{\partial h V_{tot} C}{\partial y} = \frac{\partial}{\partial x}\left(h\varepsilon_s \frac{\partial C}{\partial x}\right) + \frac{\partial}{\partial y}\left(h\varepsilon_s \frac{\partial C}{\partial y}\right) + E - D \tag{1}$$

where C is the depth-averaged concentration, U_{tot} and V_{tot} are the velocities at which the sediment is transported, t is time, x and y are the two horizontal dimensions, h is the water depth, ε_s is the eddy viscosity, and E and D are the non-cohesive erosion and deposition, respectively. This approach has two advantages: (a) it is easier to modify the advection velocity to take cross-shore transport into account and (b) it leads to less instabilities than the numerical methods available in GAIA for calculation of bed level changes by the Exner equation. For non-cohesive sediments, the net sediment flux $E - D$ is determined based on the concept of equilibrium concentration C_{eq} as:

$$E - D = w_s R_{cs}\left(C_{eq} - C\right) \tag{2}$$

where w_s is the settling velocity and R_{cs} is the ratio between the near-bed concentration and the mean concentration (C_{Zref}/C), which actually represents the entrainment response of sediment (adaptation time). R_{cs} can be calculated as described in Kolokythas et al. (2024).

The main cross-shore transport mechanisms are introduced in (1) as additional velocity components, based on the formulation implemented in XBeach (Roelvink et al., 2009). The depth-averaged flow velocities accounting for cross-shore sediment transport are expressed as:

$$\begin{aligned} U^{tot} &= U^L + \cos\theta\,(U_{NL} - U_{ST} - U_{SR}) \\ V^{tot} &= V^L + \sin\theta\,(U_{NL} - U_{ST} - U_{SR}) \end{aligned} \tag{3}$$

where U^L, V^L are the Lagrangian velocities calculated by TELEMAC-2D and θ is the wave direction. The rest terms in the right-hand side of (4) are the velocity components due to Stokes drift (U_{ST}), wave non-linearity (U_{NL}) and surface rollers (U_{SR}). The expressions for the addidional velocities can be found in Kolokythas et al. (2024).

The breaking turbulence effect on sediment transport is introduced through the equilibrium concentration formula ($C_{eq,}$), as proposed by Van Thiel de Vries (2009), considering an enhanced wave orbital velocity. Finally, the effect of the bed slope is taken into account by properly modifying the depth-averaged velocity shown in (3), as described in Kolokythas et al. (2024).

MODEL SETUP

The study area and the outlines of the computational domains of the TELEMAC and the TOMAWAC models are shown in Figure 1. The extent of the TELEMAC domain was selected such that morphological changes due to cross-shore and longshore sediment transport can be investigated at the coast located west of the port of Ostend. The port structures were included in the domain, taking into account their effect on the flow and the morphodynamics in the area of interest. The TELEMAC (and GAIA) computational grid consists of 33,535 nodes. Generally, the minimum element size of 25 m is found nearshore along the coastline and especially at the location of the beach groins, the size becomes less than 20 m. The TOMAWAC computational grid consists of 22,535 nodes. The minimum element size of ≈20 m at the area of the groins is also chosen for the wave calculations, while the general element size at the nearshore is now relatively larger, equal to 40 m. The resolution along the offshore (open) boundaries for both TELEMAC and TOMAWAC grids is equal to 250 m. The bathymetry and topography of the model domain results from the compilation of data from different campaigns, all conducted within the years 2015 and 2016.

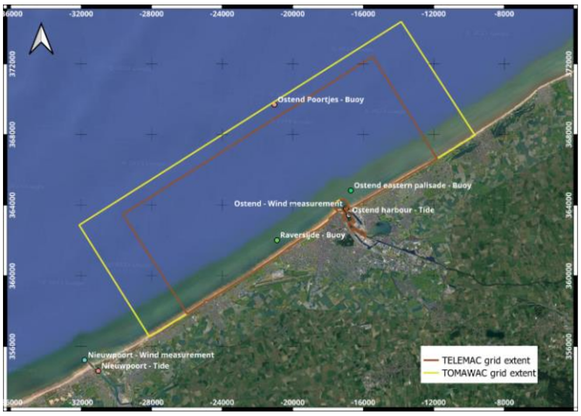

Figure 1. Outlines of the TELEMAC and the TOMAWAC computational domains and measurement stations at the area of interest (Horizontal coordinate system: RD Paris).

For the hydrodynamic forcing of the model, tidal signals from the gauges installed at Ostend and Nieuwpoort, are used. At the lateral boundaries of the TELEMAC module, Neumann conditions are imposed (Breugem et al., 2018). As for the wave forcing of the model, time-series from the wave buoy at Ostend Poortjes, located at the offshore boundary of the TOMAWAC domain, are used. Wind time series from Ostend and Nieuwpoort are imposed uniformly on the computational domain. The locations of the measurement stations are depicted in Figure 1.

MORPOLOGICAL VALIDATION

Before undergoing morphological validation, the model was successfully validated for its hydrodynamic and wave transformation predictions. The results are presented in Kolokythas et al. (2024). For the morphological validation, a hindcast with a simulation period of 243 days in the years 2016-2017 was considered. The selection of the specific period is mainly based on the availability of topographic/bathymetric measurements and the fact that this period is free from beach/foreshore nourishments.

Comparing the numerically predicted beach-foreshore sedimentation-erosion (sed/ero) patterns to the measured ones (Figure 2), focusing at the west of Ostend harbour, some main observations could be made:

- The order of magnitude of the numerically predicted bed level changes are similar to the measured ones.
- The measured sedimentation between the beach groins is more or less predicted by the model especially at the western part of the area of interest.
- The model predicts relatively more erosion between the groins at the middle part of the area of interest.
- The model seems to predict the sed/ero patterns at the eastern part of the coast (close to Ostend harbour) reasonably well. Measured accretion around $X_{RD} = 18$ km is possibly a human intervention (not recorded).
- Strong sedimentation in the navigation channel is predicted, due to missing dredging activity in the model.

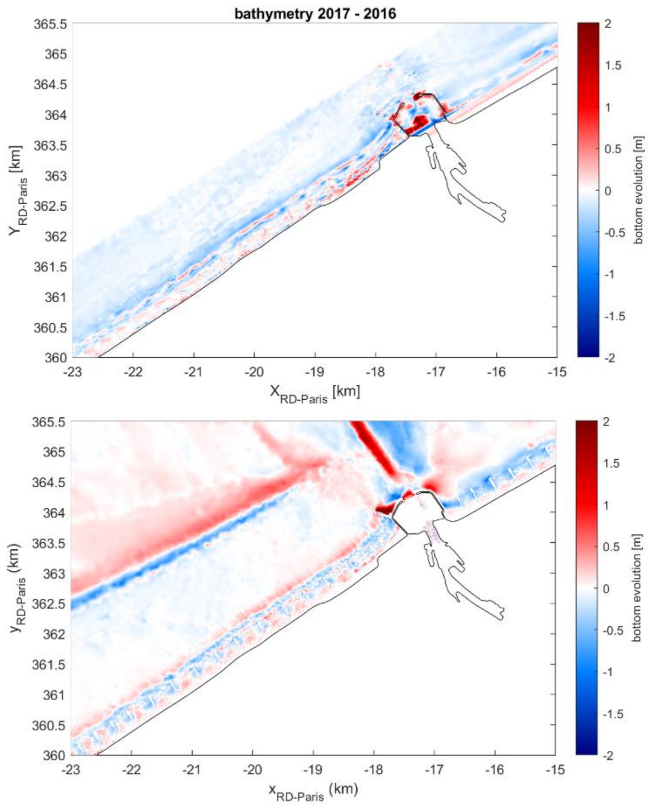

Figure 2. Measured bed level change [m] between years 2016 and 2017 (top figure) and modelled bed level change [m] at the end of the simulation period (bottom figure).

CONCLUSIONS

The main goal of the presented work was the evaluation of a 2D-morphodynamic model for the central part of the Belgian coast, the so-called Ostend model, which was constructed so that the new developments on the cross-shore transport modelling can be validated against larger scale (field) measurements under realistic (measured) forcing conditions. The major cross-shore processes incorporated in the model are the Stokes drift (return flow), the surface rollers, the wave non-linearity and the wave breaking induced turbulence. The model was validated by means of a morphological hindcasting exercise. In general the results of Ostend model with cross-shore current included, are in reasonable agreement to the measured bed evolution.

REFERENCES.

Breugem, W.A., Fonias, E., Wang, L., Bolle, A., Kolokythas, G., & De Maerschalck, B. (2018). Neumann boundaries in TELEMAC 2D and their application to wave current interaction. Proc. XXVth TELEMAC-MASCARET User Conference, Norwich, UK.

Kolokythas, G., Breugem, W.A., Wang, L., & De Maerschalck, B. (2024). Advances in cross-shore transport modelling with GAIA. Proc XXXth TELEMAC-MASCARET User Conference, Chambery, France.

Roelvink, J.A., Reniers, A., Van Dongeren, A., Van Thiel de Vries, J., McCall, R., & Lescinski, J. (2009) Modelling storm impacts on beaches, dunes and barrier islands. *Coastal Eng*. 56, 1133–1152.

Van Thiel de Vries, J. (2009). Dune erosion during storm surges, PhD Thesis, Delft Hydraulics Laboratory, NL.

Numerıcal Modelıng of Seagrass Effects on Cross-Shore Morphology

Karambas Th.[1], Samaras A.G.[2]

[1] Department of Civil Engineering, Aristotle University of Thessaloniki, University Campus, 54124 Thessaloniki, Greece
[2] Department of Civil Engineering, Democritus University of Thrace, University Campus - Kimmeria, 67100 Xanthi, Greece

*corresponding author:
e-mail: karambas@civil.auth.gr

INTRODUCTION

Nature-based Solutions (NbS) can play a significant role in reducing the vulnerability of coastal communities to coastal hazards such as flooding and erosion, driven by climate change and increasing urban pressure. The planting of seagrass (such as Posidonia Oceanica meadows) in the nearshore region is a Nature-based Solution that can result to coastal protection against erosion and coastal flooding mitigation, as the presence of the seagrass leads to wave attenuation. Wave energy dissipation is a function of the plant characteristics (stem width, height, density, etc.) obstructing the water column, and the water depth. The reduction of the wave energy results in the mitigation of wave setup/runup and coastal inundation, as well as to the reduction of sediment transport and to cross-shore coastal erosion.

In this work a cross-shore hydro-morphodynamic model is developed and applied to simulate nonlinear wave energy dissipation over seagrass, wave setup/runup, sediment transport and morphology evolution.

WAVE AND SEDIMENT MODEL

A nonlinear Boussinesq-type model with improved linear dispersion characteristics is used to describe wave motion and wave induced current field. The existing model is described in Tsiaras et al. (2020) and it is applied to simulate the flow in areas without seagrass and the free-surface above the seagrass.

In the seagrass areas, the only change in the existing Boussinesq-type model is the inclusion of two extra terms in the continuity equation. The terms account for the interaction between the waves over the seagrass and the flow within the porous medium, where the canopy flow equation is solved according to Karambas et al. (2015).

The continuity equation of free-surface flow is written:

$$\frac{\partial \zeta}{\partial t}+\frac{\partial\left[(d+\zeta)U\right]}{\partial x}+\frac{\partial\left[(d+\zeta)V\right]}{\partial y}+ n\frac{\partial(h_c U_s)}{\partial x}+n\frac{\partial(h_c V_s)}{\partial y}=0 \tag{1}$$

where U, V = depth averaged horizontal velocities, ζ = surface elevation, d = water depth, U_s = seepage (fluid) velocity inside the porous medium, h_c = porous medium thickness and n = porosity.

The seepage velocities are calculated by a canopy flow model which is solved simultaneously with the free surface flow model (Karambas et al., 2015). The existing 1DH model is extended here in two horizontal dimensions (2DH). The governing momentum equations are written:

$$\frac{\partial U_s}{\partial t}+U_s\frac{\partial U_s}{\partial x}+V_s\frac{\partial U_s}{\partial y}+\frac{1}{\rho}\frac{\partial P}{\partial x}+ \frac{C_d\,\lambda_f}{2h_c(1-\lambda_p)}U_s\sqrt{U_s^2+V_s^2}+\frac{C_m\,\lambda_p}{(1-\lambda_p)}\frac{\partial U_s}{\partial t}=0 \tag{2}$$

$$\frac{\partial V_s}{\partial t}+U_s\frac{\partial V_s}{\partial x}+V_s\frac{\partial V_s}{\partial y}+\frac{1}{\rho}\frac{\partial P}{\partial y}+ \frac{C_d\,\lambda_f}{2h_c(1-\lambda_p)}V_s\sqrt{U_s^2+V_s^2}+\frac{C_m\,\lambda_p}{(1-\lambda_p)}\frac{\partial V_s}{\partial t}=0 \tag{3}$$

where P is the pressure above the canopy (which is calculated by adopting the parabolic pressure distribution of the Boussinesq equations), C_d and C_m are the drag and inertia coefficients respectively. The value of C_m =1 is adopted for the inertia coefficient while the drag coefficient C_d is related to the Reynolds number (Karambas et al., 2015). The canopy geometry is represented by the height h_c and two other parameters: (1) λ_f, defined as the ratio of the total frontal area of the canopy elements to the total plan area occupied by the canopy, and (2) λ_p, defined as the ratio of the plan area occupied by the canopy elements to the total plan bed area. Coefficient λ_p, is directly related to the porosity n (λ_p=1- n).

The governing equations are discretized using the finite difference method utilizing a composite 4th-order Adams-Bashforth-Moulton scheme (utilizing a 3d-order Adams-Bashforth predictor step and a 4th-order Adams-Moulton corrector step). Terms involving first order spatial derivatives are discretized utilizing a five-point formula. Regarding the sediment transport module, this work builds on the improvements introduced by Karambas and Samaras (2014) and adopts the latest update of the transport formula, bed load and sheet flow transport, proposed by (Zhang and Larson, 2020). Suspended load and bed morphology evolution are simulated as in Samaras and Karambas (2024).

MODEL VALIDATION

The valicity of the model is confirmed by comparing the numerical results with the experimental data of Astudillo et al. (2022). The wave-sediment-plant interaction experiments were carried out at the CIEM wave flume of LIM/UPC in Barcelona (100 m length, 3 m wide, 4.5 m deep). The initial beach profile were consisted by a flat concrete section and a 1:15 sandy slope with mean grain size d_{50}=0.25 mm.. Here the cases BR60 (without seagrass) and R60 (with seagrass) are reproduced. The seagrass mimic was deployed in the flat section at a length of 10 m. The significant wave heights was H_s = 0.60 m, and the peak period T_p= of 3.71 s.
Figure 1 presents the cross-shore morphology evolution with and without seagrass. Due to the reduction of eave energy the

resulting bar crest is positioned closer to the shoreline when seagrass was present, thus reducing the value of the freeboard. However, the meadow has a relatively small protective effect against the recession of the coastline.

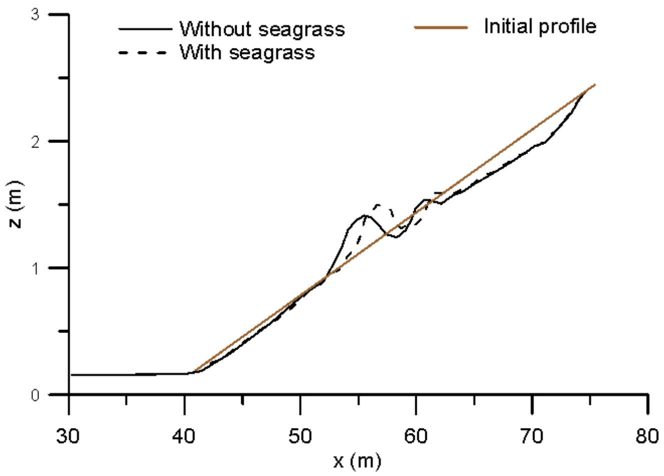

Figure 1. Cross-shore morphology evolution with and without seagrass.

Figures 2 and 3 present model results together with the experimental data. The numerical results agree quite well with the data indicating the ability of the model to simulate wave propagation and dissipation as well as cross-shore bed morphology evolution. In order to indicate more clearly the effects of seagrass on the coastal erosion the model is also applied by increasing the length of seagrass into 20 m (instead of 10 m). As a result, there was a reduction of both the incident wave energy and also coastal erosion (Figure 4).

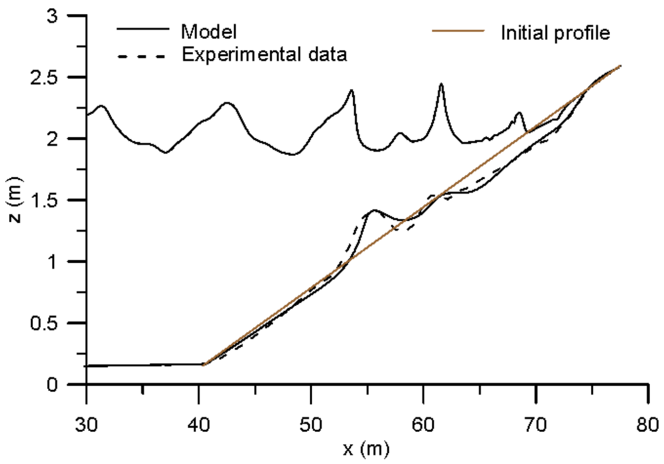

Figure 2. Wave surface elevation and beach profile without seagrass: comparison between model results and experimental data.

CONCLUSIONS

The presence of seagrass reduces incident wave energy resulting in the protection of a beach against the erosion due to wave action. The presented numerical model simulated well the seagrass effects on cross-shore coastal morphology.

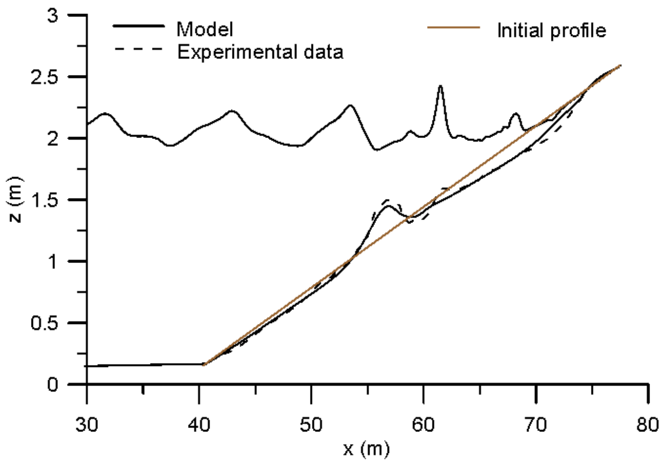

Figure 3. Wave surface elevation and beach profile with seagrass: comparison between model results and experimental data.

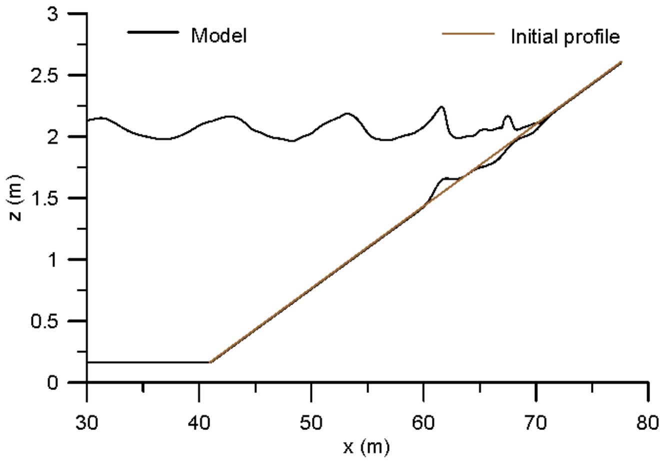

Figure 4. Wave surface elevation and beach profile with seagrass deployed at a length of 20 m (numerical model results).

REFERENCES

Astudillo C., Gracia V., Cáceres I., Sierra J.P. & Sánchez-Arcilla A. (2022). Beach profile changes induced by surrogate Posidonia Oceanica: Laboratory experiments. *Coastal Eng.* 175, 104144.

Karambas, T., Koftis, T. & Prinos, P. (2015). Modeling of Nonlinear Wave Attenuation Due to Vegetation. *J. Coastal Res*. 32 (1), 142–152.

Karambas, T.V. & Samaras, A.G. (2014). Soft shore protection methods: The use of advanced numerical models in the evaluation of beach nourishment. *Ocean Eng.* 92, 129–136.

Samaras, A.G. & Karambas, T.V. (2024). Simulating Erosive and Accretive Conditions in the Swash: Applications of a Nonlinear Wave and Morphology Evolution Model. *J. Mar. Sci. Eng.* 12, 140.

Tsiaras, A.C., Karambas, T.V. & Koutsouvela, D. (2020). Design of Detached Emerged and Submerged Breakwaters for Coastal Protection: Development and Application of an Advanced Numerical Model. *J. Waterw. Port Coast. Ocean Eng.* 146 (4), 04020012.

Zhang, J. & Larson, M. (2020) A Numerical Model for Offshore Mound Evolution. *J. Mar. Sci. Eng*. 8, 160.

Composite Modeling for the Simulation of Coastal Processes in the Fishing Shelter of Kato Pyrgos, Cyprus

Chondros M.[1,2,*], Metallinos A.[1,2], Papadimitriou A.[1,2] and Tsoukala V.[1]

[1] Laboratory of Harbour Works, School of Civil Engineering, NTUA, 9 Iroon Polytechniou Str., 15780, Zografou, Greece
[2] Scientia Maris PC, 117 Agias Paraskevis Str., 15234, Chalandri, Greece

*corresponding author:
e-mail: michondros@mail.ntua.gr

INTRODUCTION

Fishing shelters and marinas are typically constructed in shallow waters, as the vessels they accommodate have a relatively small draft. As a result, many of these structures are located within the littoral drift zone and often face sedimentation issues at their entrance and within the basin. A characteristic example of such a case is the fishing shelter of Kato Pyrgos in Cyprus, where coastal processes lead to significant sediment deposition inside the basin. Such challenges are generally addressed through the appropriate design of external harbour structures, including the geometry of the windward and leeward breakwaters, as well as the positioning and orientation of the port entrance in relation to sediment transport pathways. To assess the effectiveness of a particular harbour layout in mitigating these issues, engineers typically employ either mathematical or physical modeling. The former is more commonly used due to its cost-effectiveness, whereas the latter, despite being more expensive and time-consuming, provides higher accuracy. The optimal approach involves a combination of both methodologies, referred to as composite modeling. The composite modeling methodology consists of three main steps: (1) mathematical modeling is first employed to assess the performance of various alternative port layouts, leading to the selection of the most efficient design; (2) the chosen layout is then tested through physical modeling, which may also enable optimization; (3) finally, experimental measurements from the physical model are used to calibrate numerical models. Once calibrated, these models are applied to simulate multiple scenarios, allowing for further refinement of the layout. In this context, the present study utilizes experimental data from tests conducted by the Laboratory of Harbour Works (LHW) of the the National Technical University of Athens. These data are used for the calibration and validation of a wave and a hydrodynamic model to explore multiple simulation scenarios with high accuracy and reliability, ensuring an optimized and effective design.

PHYSICAL MODELING

The experiments were conducted in the largest wave basin of LHW. The physical model was constructed at a 1:80 scale and was rotated 30° counterclockwise relative to true North (Figure 1). The water depth in the tank was approximately 39 cm in deep-water region. Irregular long-crested waves following a JONSWAP spectrum were generated. Four dominant mean wave directions were examined, corresponding to the primary wave exposure of the fishing shelter: NNE (with simulated offshore wave characteristics: Hs=2.18 cm, Tp=0.62 s), NNW (Hs=2.61 cm, Tp=0.64 s), N (Hs=2.79 cm, Tp=0.65 s), and ENE (Hs=1.96 cm, Tp=0.6 s). Seven resistance-type wave gauges were positioned in deep and intermediate waters, while seven acoustic wave gauges were placed in shallower waters and within the shelter basin. Additionally, current velocity measurements were obtained using an acoustic velocimeter. Further details on the experimental setup and methodology can be found in Tsoukala et al. (2025).

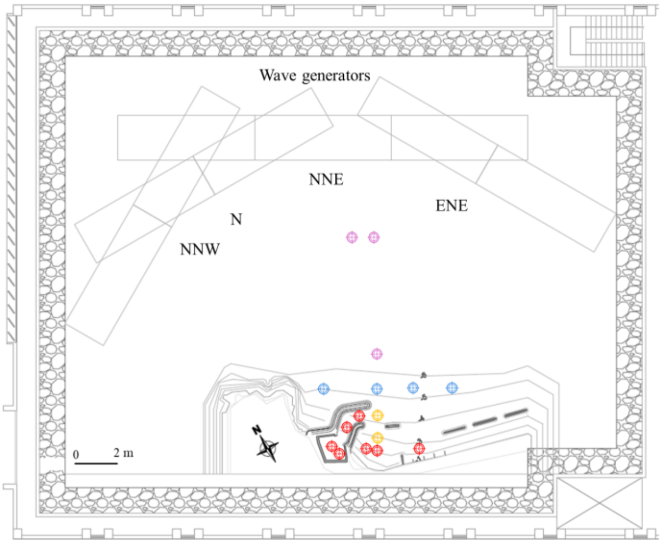

Figure 1. Experimental layout showing the placement of measurement instruments within the wave basin. Pink and light blue markers indicate the position of resistance-type wave gauges, red markers of acoustic wave gauges, and orange markers of the acoustic velocimeter.

NUMERICAL MODELING

In the present study, the wave propagation model Maris HMS (Scientia Maris, 2022) and the hydrodynamic model Maris HYD (Scientia Maris, 2022) were utilized. Maris HMS is based on the following continuity and momentum equations (Chondros et al., 2024):

$$\frac{\partial \zeta}{\partial t} + \nabla \cdot (\boldsymbol{U_w} h) = -w_b \frac{\partial \zeta}{\partial t} \tag{1}$$

$$\frac{\partial (\boldsymbol{U}h)}{\partial t} + \frac{c^2}{n} \nabla (n\zeta) = v_{wh} \nabla^2 \cdot \boldsymbol{U_w} - w_{bf} \boldsymbol{U_w} \tag{2}$$

where ζ represents the elevation of the sea surface, h denotes the water depth, $\boldsymbol{U_w}$ represents the vector of mean water particle velocity, c is the phase celerity, $n = (1/2 + kh/\sinh kh)$, k is the wave number, v_{wh} is the horizontal eddy viscosity coefficient responsible for replicating partial wave reflection, w_{bf} denotes energy dissipation due to bottom friction, and w_b denotes energy dissipation due to depth-induced breaking.

Maris HYD is based on the depth-integrated incompressible Reynolds-averaged Navier–Stokes equations, composed of the following continuity and momentum equations (Papadimitriou et al., 2022):

$$\frac{\partial \bar{\eta}}{\partial t} + \frac{\partial (Uh)}{\partial x} + \frac{\partial (Vh)}{\partial y} = P \tag{3}$$

$$\frac{\partial U}{\partial t} + U\frac{\partial U}{\partial x} V\frac{\partial U}{\partial y} + g\frac{\partial \bar{\eta}}{\partial x} = -\frac{1}{\rho h}\left(\frac{\partial S_{xx}}{\partial x} + \frac{\partial S_{xy}}{\partial y}\right) + \frac{1}{h}\frac{\partial}{\partial x}\left(v_{ch} h \frac{\partial U}{\partial x}\right) + \frac{1}{h}\frac{\partial}{\partial y}\left(v_{ch} h \frac{\partial U}{\partial y}\right) + fV + \frac{\tau_{sx}}{\rho h} - \frac{\tau_{bx}}{\rho h} + P_x \tag{4}$$

$$\frac{\partial V}{\partial t} + U\frac{\partial V}{\partial x} V\frac{\partial V}{\partial y} + g\frac{\partial \bar{\eta}}{\partial y} = -\frac{1}{\rho h}\left(\frac{\partial S_{yy}}{\partial y} + \frac{\partial S_{xy}}{\partial x}\right) + \frac{1}{h}\frac{\partial}{\partial x}\left(v_{ch} h \frac{\partial V}{\partial x}\right) + \frac{1}{h}\frac{\partial}{\partial y}\left(v_{ch} h \frac{\partial V}{\partial y}\right) - fU + \frac{\tau_{sy}}{\rho h} - \frac{\tau_{by}}{\rho h} + P_y \tag{5}$$

where $\bar{\eta}$ denotes the mean sea surface elevation, U and V denote the depth-averaged current velocities in the two horizontal directions (x and y), respectively, ρ is the seawater density, h is the total water depth, f is the Coriolis coefficient, g is the gravitational acceleration, v_{ch} is the horizontal turbulent eddy viscosity coefficient, τ_{sx} and τ_{sy} are the x- and y-components of the wind shear stress at the air–sea interface, τ_{bx} and τ_{by}, are x- and y-components of the bottom friction shear stresses, and P, P_x, P_y are external discharges either added or subtracted for an external point source or sink, respectively. The simulation of wave-generated currents involves the incorporation of the radiation stress components S_{xx}, S_{xy}, and S_{yy}.

COMPOSITE MODELING

The methodology followed in this study is based on the calibration and validation of the two aforementioned models, followed by the execution of multiple simulation scenarios. Specifically, the first wave incidence scenario was used for model calibration, while the remaining three scenarios were used for validation. For the calibration process, the selected tuning parameters were the horizontal eddy viscosity coefficient, v_{wh}, and the bottom friction coefficient in w_{bf} (Eq. 1). Through a sensitivity analysis, the eddy viscosity coefficient was found to be significantly more critical than the friction coefficient and was ultimately chosen as the primary calibration parameter. For Maris HYD, both the eddy viscosity coefficient, v_{ch}, and the friction coefficient in τ_{bx} and τ_{by} (Eqs. 4 & 5) were used for calibration. Once the models were calibrated, validation was carried out using the three remaining wave incidence scenarios. The results demonstrated a highly satisfactory model performance, with simulation outputs closely matching the experimental data across all measurement gauges. This agreement confirms the accuracy and reliability of the models in simulating the coastal processes.

RESULTS

The calibrated and validated models were then employed to simulate multiple wave incidence scenarios. The spatial resolution was set to dx = dy = 0.025 m, while the temporal step was defined as dt = 0.0025 s. The simulation time for both models was set to 100 seconds. Two representative results are presented in Figures 2 and 3 for the NNE incident wave (Hs=2.18 cm, Tp=0.62 s), illustrating the model's performance in capturing wave transformation and hydrodynamic processes.

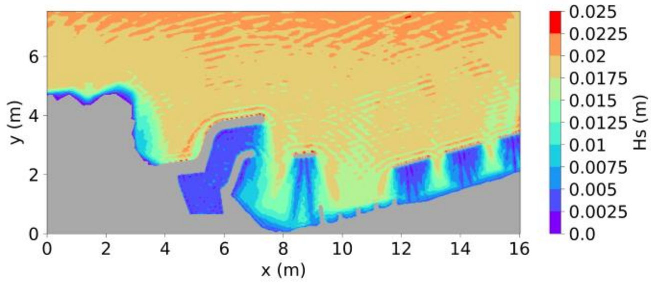

Figure 2. Nearshore wave field simulated by Maris HMS for the NNE incident wave.

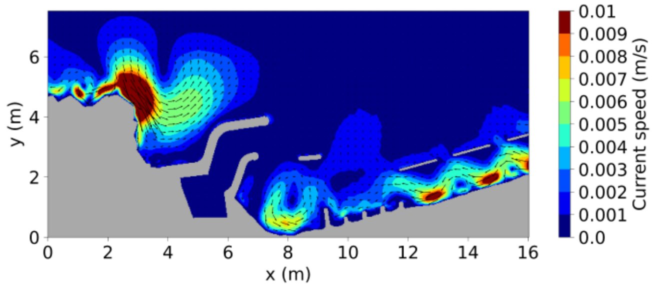

Figure 3. Nearshore wave-generated current field simulated by Maris HYD for the NNE incident wave.

CONCLUSIONS

The appropriate design of efficient, climate-resilient, and environmentally friendly port and coastal structures requires an understanding of the complex phenomena occurring in the coastal zone. This study highlights the combination of physical and mathematical modeling for understanding these phenomena and ultimately optimizing the structures. Through the development of mathematical models that have been calibrated and validated with experimental measurements from the physical model, it is possible to simulate numerous scenarios with high reliability.

REFERENCES

Chondros M., Metallinos A. & Papadimitriou, A. (2024). Integrated Modelling of Coastal Processes Driven by an Advanced Mild Slope Wave Model. *Modelling* 5, 458–482.

Papadimitriou A., Chondros M., Metallinos A. & Tsoukala, V. (2022). Accelerating Predictions of Morphological Bed Evolution by Combining Numerical Modelling and Artificial Neural Networks. *J. Mar. Sci. Eng.* 10(11), 1621.

Scientia Maris (2022), Maris HMS & Maris HYD User Guides.

Tsoukala V., Chondros M., Ziros A., Mplounas G., Eleftheriadou E., Sartampakos P., Kalpias A., Toumazis A., Solomonidis C. & Zervos S. (2025). Experimental Measurements on a Physical Model for the Optimization of the Kato Pygros Fishing Shelter Layout in Cyprus. 3rd International Conference on Design and Management of Port, Coastal and Offshore Works (DMPCO 2025), Patras, Greece, May 7-9.

Numerical Modeling and Machine Learning Techniques for Predicting Wave Disturbance: A Case Study at the Marina of Kalamata, Greece

Angelopoulou O.[1,*] and Chondros M.[1]

[1] Laboratory of Harbour Works, National Technical University of Athens, 9 Iroon Polytechniou Str., 15780, Zografou, Greece

*corresponding author:
e-mail: olga.angelopoulou6@gmail.com

INTRODUCTION

Accurate estimation of wave disturbance within port basins is essential for ensuring safe and efficient port operations. Several wave models have been developed to estimate wave disturbance, including both physical and numerical approaches. While physical models offer high realism, they are often time-consuming and costly. In contrast, numerical models can effectively simulate wave phenomena but typically require significant computational resources and calibration.

Recent research has explored the integration of Machine Learning (ML) techniques with modelling to improve predictive accuracy and efficiency. For instance, Kankal and Yüksek (2012) evaluated port calmness by estimating wave height in Trabzon Port using both an experimental model and an Artificial Neural Network (ANN). Likewise, Zheng et al. (2022) combined the spectral model WAVEWATCH III with an ANN for rapid and accurate predictions in Hambantota Port. López and Iglesias (2013) utilized ML to estimate the significant height of infragravity waves in Ferrol Port, while López et al. (2015) applied an ANN model to assess port functionality by analyzing wave height based on deep-water observations and operational constraints.

This study combines numerical modeling with ML techniques, utilizing offshore wave characteristics from open-access databases, to develop a fast and accurate model for predicting wave disturbance in port basins. The model is implemented at the Marina of Kalamata, Greece.

METHODOLOGY, NUMERICAL MODEL AND MACHINE LEARGING TECHNIQUES

The proposed methodology aims to develop an efficient model to: 1) be integrated into a forecasting platform (e.g. Makris et al., 2021) for wave disturbance in port basins, ensuring high accuracy with minimal computational demand, and 2) serve as a valuable tool for assessing the impact of climate change on wave disturbance in ports, offering long-term operational insights without requiring extensive simulations. The methodology is structured in two phases as follows.

Phase A: Wave climate data for the study area is sourced from the Copernicus Marine Service and processed by categorizing significant wave height (Hs) and peak period (Tp) pairs based on their mean wave direction (MWD). Representative Hs-Tp pairs are selected for ML training, while additional random pairs with intermediate values are chosen for validation. A bathymetric file for the area is created, and the Maris HMS model is used to simulate both training and validation scenarios using wave height, period, and direction data.

Phase B: Wave height results from the mathematical model are extracted specifically for the port basin and stored in a dataset containing the Hs-Tp and MWD values that were used as inputs in the numerical model. Additionally, wave heights for a single direction are extracted into another dataset to evaluate the performance of the model. The performance of ML techniques is assessed using statistical metrics, and the best-performing models undergo further testing to determine the optimal architecture.

The Maris HMS model (developed by Scientia Maris, 2022), employed in this study to simulate wave disturbance within the port basin, is an advanced nonlinear wave model based on hyperbolic mild-slope equations (Chondros et al., 2024):

$$\frac{\partial \zeta}{\partial t} + \nabla \cdot (\boldsymbol{U_w} h) = -w_b \frac{\partial \zeta}{\partial t} \tag{1}$$

$$\frac{\partial (\boldsymbol{U}h)}{\partial t} + \frac{c^2}{n} \nabla (n\zeta) = v_{wh} \nabla^2 \cdot \boldsymbol{U_w} - w_{bf} \boldsymbol{U_w} \tag{2}$$

where ζ represents the elevation of the sea surface, h denotes the water depth, $\boldsymbol{U_w}$ represents the vector of mean water particle velocity, c is the phase celerity, $n = (1/2 + kh/\sinh kh)$, k is the wave number, v_{wh} is the horizontal eddy viscosity coefficient responsible for replicating partial wave reflection, w_{bf} denotes energy dissipation due to bottom friction, and w_b denotes energy dissipation due to depth-induced breaking.

In this study, Artificial Neural Networks (ANN) and k-Nearest Neighbors (k-NN) are presented. It is noteworthy that two additional machine learning techniques, namely Decision Trees and Random Forests, were also used; however, ANN and k-NN were found to be more accurate.

CASE STUDY – MARINA OF KALAMATA

The methodology proposed herein is applied to the Marina of Kalamata, located in the southwestern region of the Peloponnese in Greece. Due to its geographical location and the orientation of its port entrance, the study area is exposed to waves generated by SSE, S, SSW, and WNW winds. To ensure an accurate simulation of the wave climate, 156 representative pairs of significant wave height (Hs) and peak wave period (Tp) were selected. Hs values ranged from 0.5 to 4.5 m, with a 0.5-meter increment, and Tp values ranged from 5 to 14 s, with a 1-second increment. Additionally, 60 extra pairs were included for intermediate wind directions of 165°, 195°, and 225°. In total, 216 scenarios were utilized as the training dataset for the ML algorithms. Furthermore, 12 randomly selected Hs–Tp pairs with intermediate values were used as the validation dataset, ensuring the model's ability to generalize to previously unseen wave conditions. Only the wave height values from the port's basin (Figure 1) were extracted from the results of the numerical model to serve as the target values for the ML algorithms.

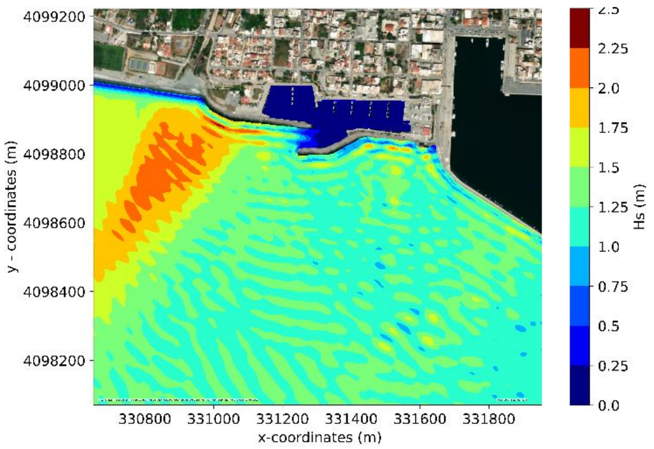

Figure 1. Maris HMS simulation results for offshore wave conditions: Hs = 2m, Tp = 9s, coming from 230° N.

To evaluate the performance of the ML algorithms, the following metrics were used: Correlation Coefficient, Maximum Absolute Error, Mean Absolute Error, Mean Squared Error, and BIAS.

RESULTS

A thorough investigation was carried out on various hyperparameters of the ML algorithms to determine the optimal architecture. For ANN, hyperparameters such as the number of neurons, number of hidden layers, learning rate, epochs, and batch size were considered, while for k-NN, parameters including the number of neighbors, weights function, distance metrics, and p parameter were evaluated. The optimal architectures for both algorithms, along with their respective metric values, are presented in the following tables and figures.

Table 1. Optimal ANN Architecture

Number of layers	Hidden neurons	Learning rate	Epochs	Batch Size
4	32	0.01	800	32

Table 2. Optimal k-NN Architecture

Neighbors	Weights	p parameter	Metric
1	‘uniform’	1	minkowski

CONSLUSIONS

The conclusions drawn from this study indicate that the ANN and k-NN models outperform Decision Trees and Random Forests for predicting wave disturbance. Additionally, the step size of 0.5 meters for wave height and 1 second for wave period is essential for the performance of the algorithms, as larger step sizes result in lower performance. Both models (ANN and k-NN) provide satisfactory results, suggesting that the proposed methodology and the developed models could be integrated into a forecasting platform or serve as a tool for assessing the impact of climate change. Further research includes the exploration of other ML methods, such as SVM and XGBoost, as well as incorporating sea level change as an input parameter.

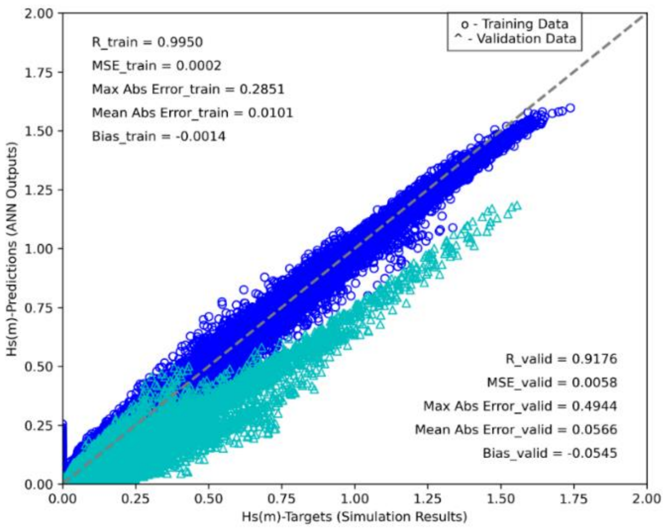

Figure 2. ANN’s performance in training and validation.

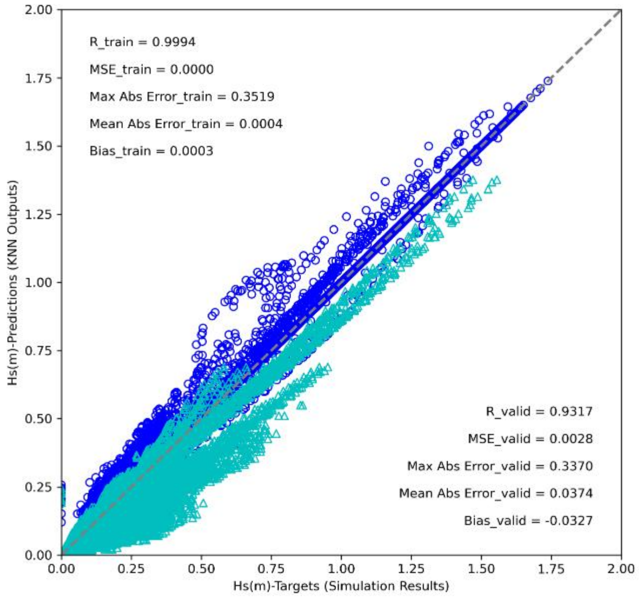

Figure 3. k-NN’s performance in training and validation.

REFERENCES

Chondros M., Metallinos A. & Papadimitriou, A. (2024). Integrated Modelling of Coastal Processes Driven by an Advanced Mild Slope Wave Model. *Modelling* 5, 458–482.

López, M. & Iglesias, G. (2013). Artificial intelligence for estimating infragravity energy in a harbour. *Ocean Eng.* 57, 56–63.

López, I., López, M. and G. Iglesias (2015). Artificial neural networks applied to port operability assessment. *Ocean Eng.* 109, 298–308.

Makris et al. (2021). Integrated modelling of sea-state forecasts for safe navigation and operational management in ports: Application in the Mediterranean Sea. *Appl. Math. Model.* 89(2), 1206–1234.

Scientia Maris (2022), Maris HMS User Guide.

Zheng, Z., Ma, X., Huang, X., Ma, Y. & Dong, G. (2022). Wave forecasting within a port using WAVEWATCH III and artificial neural networks. *Ocean Eng.* 255, 111475.

Calibration Approach for Mediterranean Wave, Current, and Tide Models

Scala A.[1,*], De Cristofano V.[1], Tomassetti E.[1], Ligorio F.[1], and Cuomo G.[1]

[1] SPERI Società di Ingegneria e di Architettura SpA , Via Lungotevere delle Navi, 19, Rome, Italy

*corresponding author:
e-mail: ascala@sperispa.com

Abstract

This paper presents an improved methodology for metocean modeling at regional scale and its application to the Mediterranean Sea, based on coupling of independently calibrated wave and hydrodynamic models. Each model—wave and current/tide—undergoes a similar sensitivity analysis and calibration process to ensure individual accuracy before the models are coupled. The resulting coupled system provides a more comprehensive and accurate representation of real-world oceanographic phenomena by accounting for the interactions between waves, currents, and tides. Model calibration is carried out using wave buoy data for the wave model and tide gauges for the current and tide model. Performance evaluation of the coupled system is based on various standard metrics to ensure robustness across different environmental conditions, including calms, frequent and extreme storm events. The integration of these models enhances the reliability of metocean forecasts, supporting applications in coastal zone management, maritime operations, and the Blue Economy.

INTRODUCTION

The Blue Economy is driven by sustainable development, which fosters opportunities and attracts investments to promote social, financial, and productive growth on a global scale. Ensuring a balance between economic activities and marine ecosystem preservation is crucial for long-term sustainability. Key oceanographic parameters such as wave height, tides, and currents play a fundamental role in maritime operations, coastal resilience, and resource management. However, in situ observations—such as wave buoys, tide gauges, and current meters—are necessarily spatially limited, making it challenging to obtain a comprehensive view of marine conditions. Advanced digital tools and numerical models can bridge this gap, providing high-resolution data where direct measurements are unavailable, thereby informing decision-making for Blue Economy stakeholders.

The SeaSmartEye project, funded by Regione Puglia, addresses this need by offering access to highly informative content powered by cutting-edge technologies. Designed to meet the demands of Blue Economy stakeholders, the project promotes a responsible and sustainable approach to marine resource management. Its tools form an integrated technological framework that supports key sectors of the Blue Economy, including marine environment protection and development; maritime, coastal, and offshore engineering; risk assessment and mitigation; renewable marine energies and site prospections; logistics and transportation; as well as fisheries and recreational activities. By facilitating data-driven planning and management, SeaSmartEye contributes to the sustainable growth of marine industries while ensuring the protection and resilience of marine ecosystems.

MODEL CALIBRATION

An efficient model sensitivity and auto-calibration procedure has been applied to our in-house metocean regional models of the Mediterranean Sea (Figure 1), covering both wave and current/tide dynamics. The models use state of the art, multipurpose hydrodynamic modelling suite TELEMAC (Galland et al., 1991; Hervouet & Ata, 2017), which is capable of resolving various metocean processes at different scales (Bourban et al., 2017).

First, a sensitivity analysis was performed independently for each model to determine optimal time step, mesh resolution, and key physical parameters (Figure 2).

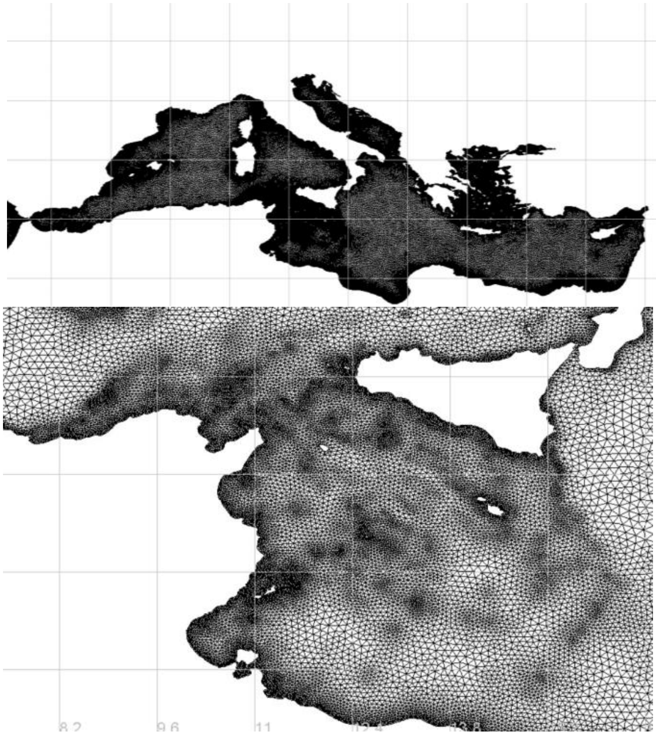

Figure 1. Meshing of the regional model of the Mediterranean Sea.

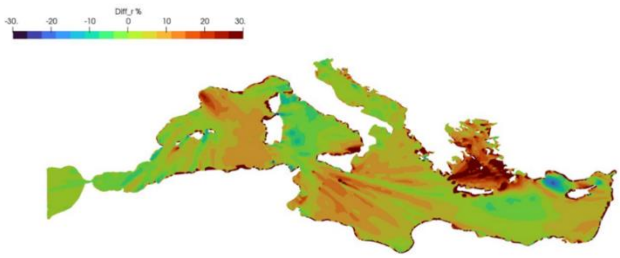

Figure 2. Contour plot showing the relative differences across the computational domain between investigated meshes.

Secondly to optimize the calibration process, a genetic algorithm was considered. This algorithm is a popular heuristic that simulates natural selection among a population of parameters. Starting with an initial generation of individuals (representing the input variables for each module), the algorithm evaluates each individual by assigning a score. It then selects the best-performing parameters to generate the next generation by applying crossover between them and introducing occasional random mutations. This method is well-suited to high-dimensional problems and efficiently explores the parameter space. The regions covered by a genetic algorithm can be visualized in a 2D space, as illustrated in Figure 3.

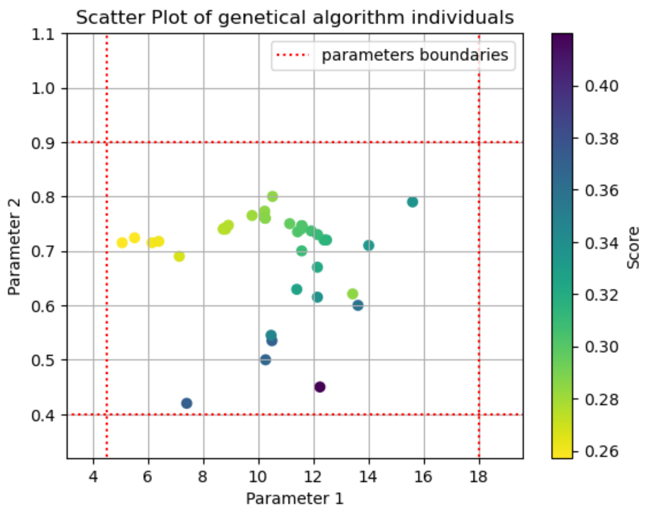

Figure 3. Example of a 2D scatter plot of the parameters explored by the algorithm.

Then, an auto-calibration procedure was implemented accounting optimization algorithm and observational data—wave buoy networks for the wave model and tide gauges for the current and tide model—through the TELEMAC API (Figure 4 and Figure 5).

After individual calibration, the two models were coupled to provide a more complete and accurate representation of real-world metocean processes, enhancing the overall reliability of the forecasts.

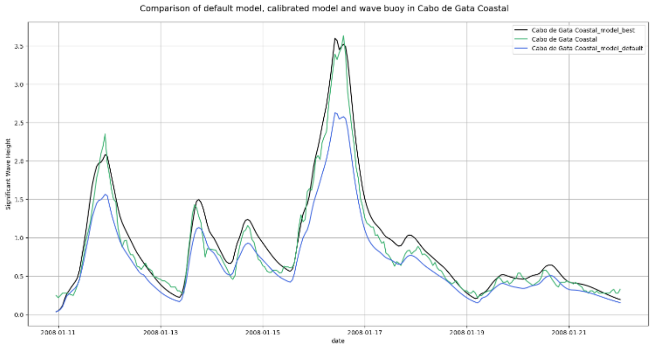

Figure 4. Comparison of wave height from wave buoy and model output with default and calibrated parameters in Capo de Gata.

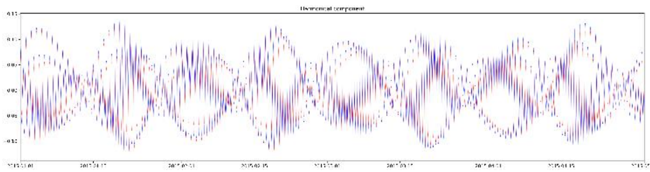

Figure 5. Comparison of astronomical tide component from tide gauge and model output in Catania.

CONCLUSIONS

This study presents a refined approach to metocean modeling in the Mediterranean Sea, demonstrating significant advancements in accuracy and reliability through the integration of independently calibrated wave and hydrodynamic models. By first calibrating the models separately and then coupling them, the methodology ensures a detailed representation of the complex interactions between waves, currents, and tides. This comprehensive framework enhances the predictive capability of metocean systems across varying environmental conditions. The research leverages the TELEMAC modeling suite, a state-of-the-art tool capable of resolving a wide range of metocean processes. Through sensitivity analyses, key model parameters such as mesh resolution and time steps were optimized, ensuring robust performance. In addition, the innovative use of a genetic algorithm facilitated the efficient exploration of the high-dimensional parameter space, allowing for effective optimization and auto-calibration. This heuristic, inspired by natural selection, proved particularly effective in refining the model parameters.

The calibration process was grounded in observational data, utilizing wave buoy measurements for the wave model and tide gauge records for the current and tide models. This data-driven approach yielded significant improvements in the accuracy of wave height predictions and the representation of tidal components. Ultimately, this work showcases the capability of modern metocean modeling to improve forecast accuracy while promoting sustainability in marine resource management. The findings contribute to a deeper understanding of Mediterranean oceanographic dynamics and provide a strong foundation for future developments in this field.

ACKNOWLEDGEMENTS

This research is being carried out as part of the SeaSmartEye Project, funded by Regione Puglia within the Aiuti ai programmi Integrati promossi da PICCOLE IMPRESE" - PIA (ART.27) framework. The authors wish to thank Jean Le Goff, Clément Ingelaere, and the many other colleagues and friends at SPERI SpA who have contributed to this work.

REFERENCES

Galland J.C., Goutal N., & Hervouet J.M. (1991). TELEMAC: A new numerical model for solving shallow water equations, *Adv. Water Resour*. 14(3), 138–148.

Hervouet, J.M., & Ata, R. (2017). User manual of open software TELEMAC-2D, Report, EDF-R&D, http://www.opentelemac.org/, ISBN:9780470035580.

Bourban, S.E., Turnbull, M.S., & Cooper, A.J. (2017). The Earth by TELEMAC. Proc. XXIVth TELEMAC-MASCARET User Conference, Graz, Austria.

The-Oceans: A Cutting-Edge Solution for Global Metocean Insights

Tomassetti E.[1], Scala A.[1,*], De Cristofano V.[1], and Cuomo G.[1]

[1] SPERI Società di Ingegneria e di Architettura SpA , Via Lungotevere delle Navi, 19, Rome, Italy

*corresponding author:
e-mail: ascala@sperispa.com

INTRODUCTION

The-oceans web-gis platform aims to support a broad range of activities within the Blue Economy. The platform enables access to the most up-to-date metocean databases and assimilates them within state-of-the-art evolution models (Scala et al.. 2024). Advanced analysis techniques are used to provide a new class of services to the actors of the world oceans. The metocean data on the-oceans platform will be made available using different thematic layers. The-oceans' technology is based on a comprehensive modelling suite, coupled with 'on-the-fly' analysis tools capable of extracting and visualize metocean information anywhere around the world. The quality of data is ensured by that of the databases, the modeling and analysis tools. Input data are combined and integrated by SeaSmartEye models, allowing a timely and constant update of forecasts and hindcasts in every corner of the blue planet.

Sustainable development is central to the Blue Economy: it drives opportunities and fosters investments in social, financial, and productive growth on a global scale. The SeaSmartEye project, funded by Regione Puglia, aims to grant access to highly informative content powered by cutting-edge tools, addressing the needs of Blue Economy stakeholders. Focused on promoting sustainable "blue" development, it encourages the conscious use of marine resources and prioritizes the sustainability and protection of the marine environment. In line with these objectives, the-oceans.org is a powerful web GIS application developed to support the Blue Economy by providing advanced solutions for forecasting, hindcasting, statistical analysis, and risk assessment and management. Designed to aid in the planning and management of critical sectors, the-oceans.org offers comprehensive tools for:

- Marine environment management, protection, and development
- Maritime, coastal, and offshore engineering products and services
- Risk assessment, management, and mitigation
- Renewable marine energies and site prospection
- Logistics and transportation
- Fisheries and recreational activities

Through its advanced features, the-oceans.org enables stakeholders to make data-driven decisions, ensuring efficient resource use while safeguarding marine ecosystems. By integrating real-time forecasts with historical analyses, it empowers users to anticipate changes, assess potential risks, and promote sustainable growth across various marine sectors.

WebGIS APPLICATIONS

WebGIS applications are designed to distribute geospatial data over the Internet or intranet networks. They leverage GIS software for analysis and use web-based functionalities to publish geographic information online. A WebGIS system operates on a typical client-server architecture, where the client is any web browser (e.g., Mozilla Firefox), while the server side consists of custom-developed applications specifically designed to manage and serve standardized geospatial data through web services.

The-oceans.org

The presentation will illustrate the generality of the methodology and the technologies adopted within the architecture. The-oceans.org platform provides a robust and useful yet intuitive and user-friendly visualization and interrogation tool for data at regional and global scales.

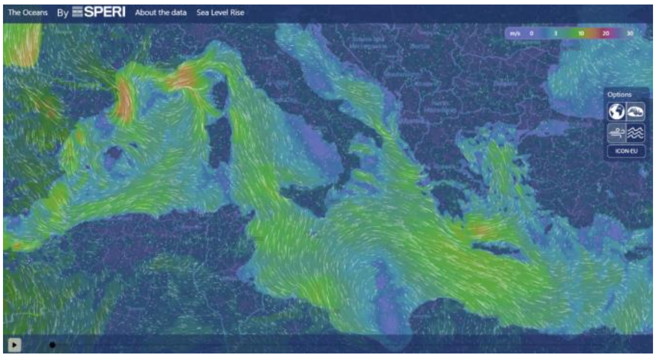

Figure 1. Visualisation of wind field over the Mediterranean

Figure 2. Visualisation of wave field over the Mediterranean

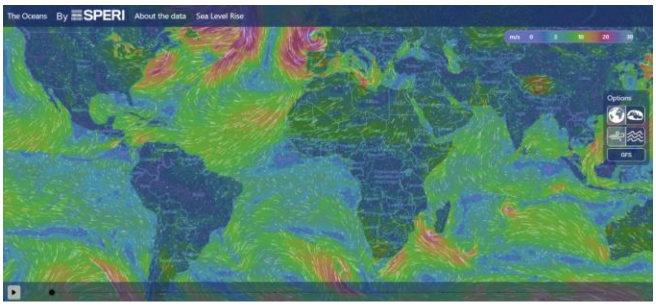

Figure 3. Visualisation of wind field at global scale

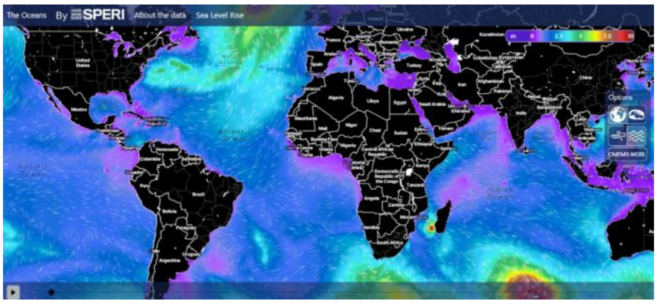

Figure 4. Visualisation of wave field at global scale

The platform enables visualization of data over the map using a dynamic color scale that adapts based on zoom levels (Figure 5) along with mean wave or wind direction (Figure 6), ensuring a clearer and more intuitive representation of the data at different resolutions.

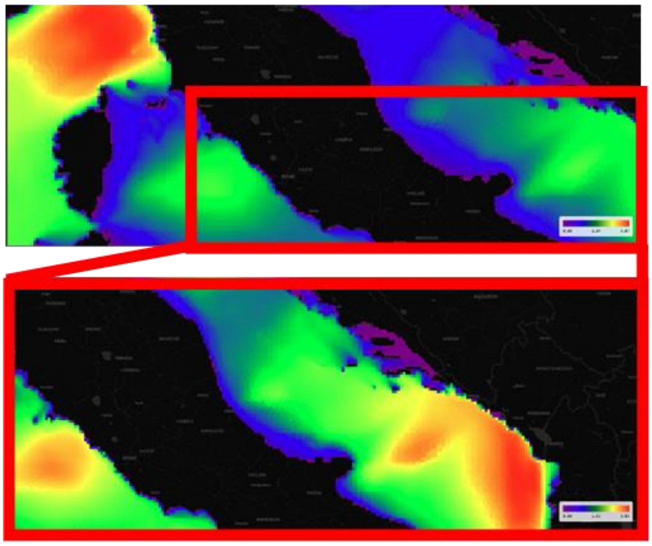

Figure 5. Example of dynamic color scale based on zoom levels

Finally, some practical usage examples of the web-GIS app will be demonstrated. Figure 7 illustrates the "The-Oceans" function for forecast analysis, which highlights key parameters related to sea conditions in the Mediterranean. This view focuses on a specific location, providing a detailed forecast through predicted time series for significant wave height and peak period. Additionally, it offers an intuitive representation of wind and wave data using synthetic pointers, enhancing the clarity and usability of the visualization for maritime analysis and decision-making.

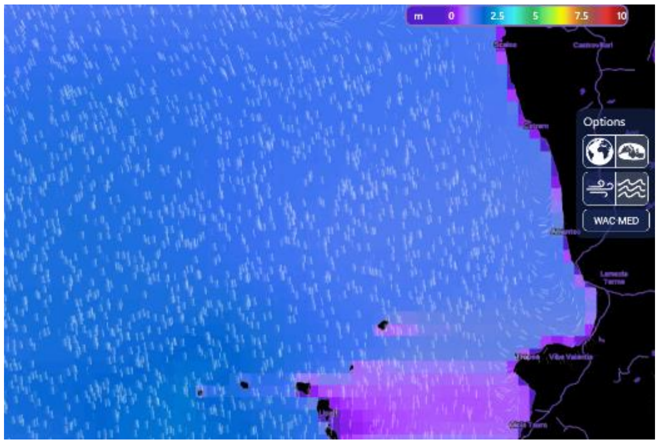

Figure 6. Visualisation of wave direcion. https://the-oceans.org/.

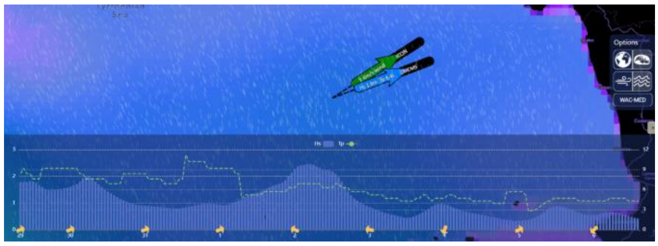

Figure 7. Interrogation of wave field in forecasting mode. https://the-oceans.org/.

CONCLUSIONS

The development of the-oceans.org platform represents a significant step forward in supporting sustainable growth within the Blue Economy. By offering comprehensive tools for real-time forecasting, hindcasting, risk assessment, and site prospection, the platform ensures that key stakeholders—ranging from policymakers to private enterprises—can make informed, data-driven decisions. The integration of advanced analysis tools with high-quality metocean databases enhances the precision of predictions and assessments, which is crucial for planning in dynamic marine environments.

ACKNOWLEDGEMENTS

This research is being carried out as part of the SeaSmartEye Project, funded by Regione Puglia within the Aiuti ai programmi Integrati promossi da PICCOLE IMPRESE" - PIA (ART.27) framework. The authors wish to thank Ready2Use S.r.l.,Thomas Sailour, Jean Le Goff, and the many other colleagues and friends at SPERI SpA who have contributed to this work.

REFERENCES

Scala, A., Le Goff, J., Ingelaere, C., De Cristofano, V., Lupoi, G., & Cuomo, G. (2024). Auto-calibration method for a Mediterranean regional wind wave model. Proc. XXXth Telemac User Conference, Chambéry, France.

The Fate of Floating Particles Released in the Gulfs of Patras and Corinth System (Greece): A Numerical Study

Aspioti A.G.[1] and Fourniotis N.Th.[1,*]

[1] Department of Civil Engineering, University of the Peloponnese, 26334 Patras, Greece

*corresponding author:
e-mail: nfou@uop.gr

ABSTRACT

The distribution and fate of floating particles released offshore as well as nearshore, close to ports and marinas areas in the Gulfs of Patras and Corinth system is numerically studied. It is shown that the particles, under the tidal forcing and in barotropic conditions, move westward of the Gulfs system towards the Ionian Sea. Strong tidal currents in the area of Rio-Antirio strait and the western part of the Gulf of Corinth gradually lead the particles towards the Gulf of Patras while the particles in the central and eastern area of the Gulf of Corinth remain nearly stagnant.

INTRODUCTION

The Gulfs of Patras and Corinth system, in central Greece, includes many ports and marinas with great commercial, touristic and environmental importance. As a result of human activities possible marine litters initially released nearshore from the ports and marinas spread throughout the whole system. Knowledge of the fate and distribution of floating particles in the Gulfs system remains a crucial factor for its management and restoration.

Simulations and numerical models have been proven to be a useful tool in the description of the transport of the floating particles as they fil the gaps between observations and test hypotheses about how floating particles behave in the marine environment (Sebille et al., 2020).

In this work a two dimensional (2D) hydrodynamic and particle tracking model has been applied for the numerical study of the distribution of floating particles released offshore and nearshore in the Gulfs of Patras and Corinth system. The ultimate goal is to track the fate and distribution of possible floating particles coming from ports and marinas as well as terms of their residence time in the system.

METHODOLOGY

The numerical simulations presented herein were performed utilizing the CFD code MIKE 21 FM (HD, PT) (DHI, 2024). For the tidal flow, at the open boundaries, time series of tidal elevations constructed by astronomical constituents of the tide (Achilleopoulos, 1990; HNHS, 1992) were used and barotropic flow was considered as an initial approach. Initially, floating particles' sources were spread throughout the whole Gulfs system covering the offshore and nearshore region (see Figure 1) and the simulation performed for 1 year. After the initial 1-year simulation, another case was examined focusing exclusively on the nearshore region of the Gulfs system. Simulations were conducted for 6-months, 1 and 5 years, examining the fate of possible released particles from ports and marinas. More specifically, the particles' sources were placed on known locations close to the ports and marinas in the system's area. In Figure 3 we can see the initial location of the particles as well as the most significant ports of the system. In each case the particles were released once and simultaneously at the beginning (t = 0) of the simulations.

RESULTS AND DISCUSSION

The features of the floating particles' distribution that emerged from the numerical simulations, in the absence of wind, i.e., pure tidal circulation, are as follows:

The particles follow the tidal flow moving westward of the system through the gulf of Patras, before their outflow in the Ionian Sea. In the eastern and central part of the Gulf of Corinth the weak tidal currents leave the particles nearly unaffected throughout the simulation. On the northern part of the Gulf of Corinth the complex topography traps the particles while on the south only a few particles escape towards the westerly of the gulf. Based on the numerical simulations the western part of the Gulf of Corinth seems to be more active as tidal currents there, are slightly stronger.

In the Rio-Antirio strait all particles, initially released there, are removed from this area after 6 months because of strong tidal currents. Moving on, the Gulf of Patras receives floating particles from the eastern part of the system, whereas the particles initially released in the gulf move towards the Ionian Sea. In the center and southerly of the Gulf of Patras the accumulation of particles is high whereas in the northern part, due to strong currents, the particles leave earlier the area (Figure 2).

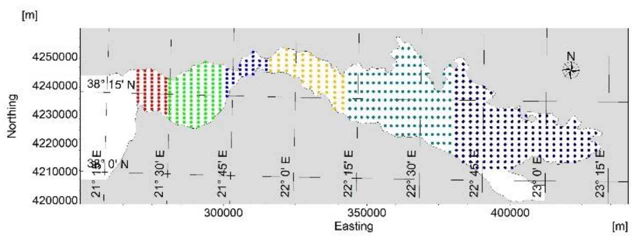

Figure 1. Initial (t = 0) distribution of the floating particles released in the Gulfs system.

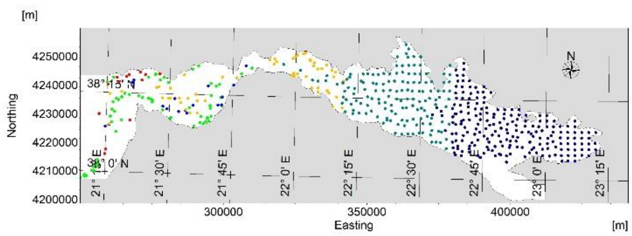

Figure 2. Numerical distribution of the floating particles in the Gulfs system after 1 year simulation.

The distribution of the particles released from the ports and marinas of the system is also defined by tidal flow. Tracking the particles numerically released in areas close to the significant ports of the system, such as the port of Patras (marked with A in Figure 3), Rio and Antirio ports (marked with B and C, respectively, in Figure 3) as well as the port of Corinth (marked with D in Figure 3), it is clear that they move westward of the system. On the other hand, based on the numerical simulation it is shown that particles released from ports in the eastern and central part of the Gulf of Corinth remain nearly unaffected, even after 5 years.

It is worth noting that the particle released from the port of Corinth (marked with D) seems to respond immediately moving towards the center of the gulf but does not escape the area throughout the simulation period (Figures 4,5,6). Particles in the western part of the Gulf of Corinth respond to the tidal movement and gradually move towards the Rio-Antirio strait.

Due to strong tidal currents in the wider area of the Rio-Antirio strait (> 0.5 m/s) the particles move in the northern part of the Gulf of Patras, towards the west exit of the system. Regarding the floating particles released close to the Rio-Antirio ports (marked with B, C), they were calculated to leave the straits area within the first 6 months (Figure 4). As we can see in Figure 5 it takes less than one year for the particles of the Rio and Antirio ports to be completely removed from the system.

The particle released from the port of Patras (marked with A) moves towards the center of the Gulf of Patras and remains there at least one year moving slowly towards the west exit of the system before the outflow in the open Ionian Sea. (Figure 4).

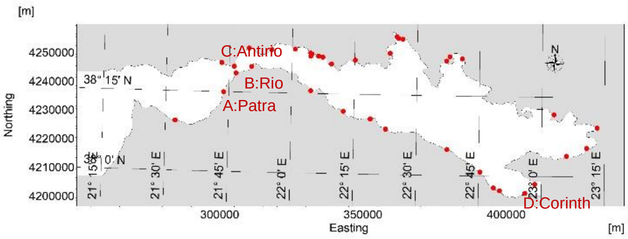

Figure 3. Initial (t = 0) distribution of the floating particles released in areas close to ports and marinas of the Gulfs system**.**

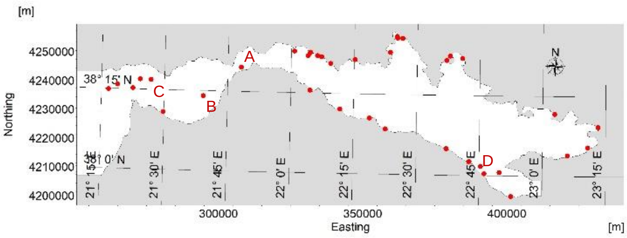

Figure 4. Numerical distribution of the floating particles released in areas close to ports and marinas in the Gulfs system after 6-month simulation.

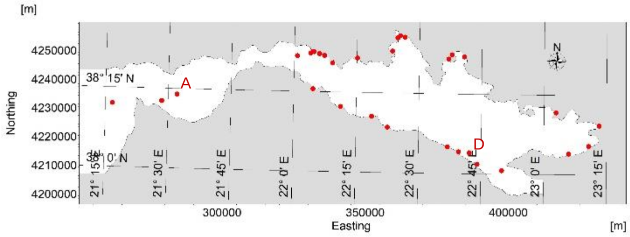

Figure 5. Numerical distribution of the floating particles released in areas close to ports and marinas in the Gulfs system after 1 year simulation.

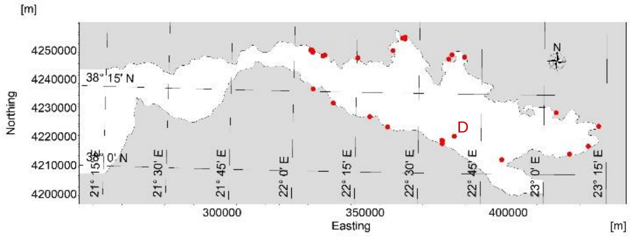

Figure 6. Numerical distribution of the floating particles released in areas close ports and marinas in the Gulfs system after 5-year simulation.

CONCLUSIONS

Based on the numerical simulations the following conclusions are drawn:

- The replenishment of the system is achieved via the Gulf of Patras towards the open Ionian Sea.
- Floating particles released close to ports and marinas in the wider area of the Rio-Antirio strait are easily removed from this area.
- The hydrodynamic circulation in the central and eastern part of the Gulf of Corinth seems to have a minor effect on distribution and fate of initially released floating particles in these areas.

ACKNOWLEDGEMENTS

We would like to express our gratitude to the Danish Hydraulic Institute (DHI) for making available to Alexandra G. Aspioti, the 2024 version of MIKE 21 Flow Model FM (HD) (DHI Water and Environment, 2024).

REFERENCES

Achilleopoullos, P. (1990). Tides in gulfs and straits of western Greece. Patras, Greece: University of Patras, Ph.D. dissertation, 265p. (in Greek).

DHI Water and Environment (2023). MIKE 21 Flow Model FM, Hydrodynamic Module, User Guide, Horsholm, Denmark: DHI: 2023, 171p.

DHI Water and Environment (2024). MIKE 21 Flow Model FM, Particle tracking Module, User Guide, Horsholm, Denmark: DHI: 2024, 62p.

Hellenic Navy Hydrographic Service (1992) Harmonic analysis of tides in Greek harbors, No 17, 50p.

Van Sebille, E., Aliani, S., Law, K.L., et al. (2020). The physical oceanography of the transport of floating marine debris. *Environ. Res. Lett.* 15 (2), 023003.

Numerical Modelling of Marine Macroplastic Transport: Application to the Saronikos Gulf, Greece

Pospotikis A.[1,*] and Chondros M.[1]

[1] Laboratory of Harbour Works, National Technical University of Athens, 9 Iroon Polytechniou Str., 15780, Zografou, Greece

*corresponding author:
e-mail: thanpospo@gmail.com

INTRODUCTION

Plastic pollution has become one of the most persistent environmental challenges, driven by the continuous increase in global plastic production, which reached approximately 367 million tons in 2020 (Stachurska & Sulisz, 2024). The transport mechanisms of plastic debris, combined with their complex and dynamic interactions within marine environments, contribute to the widespread and long-lasting nature of plastic pollution (Sebille et al., 2020). Marine macroplastics ultimately accumulate in sensitive ecosystems, posing severe ecological risks (Christensen et al., 2023), further emphasizing the urgency for a more comprehensive understanding of the advection and dispersion processes governing plastic transport.

Numerical modeling has been widely employed to quantify and predict the transport dynamics of marine plastics. Existing modeling approaches are primarily categorized into Eulerian and Lagrangian frameworks. Eulerian models describe the transport of plastics as a continuous concentration field, making them suitable for analyzing large-scale dispersal patterns. In contrast, Lagrangian models track individual particles, enabling a more detailed representation of transport mechanisms such as advection, diffusion, and stochastic effects (Saidi et al., 2014). Most studies investigating the motion of marine plastics have adopted Lagrangian approaches (Sebille et al., 2020). For instance, Christensen et al. (2023) implemented a Lagrangian super-individual model, in which each virtual particle represents a cluster of plastic debris. Their study, conducted in the Baltic Sea, incorporated advection due to wind, waves, and ocean currents, along with stochastic eddy diffusion effects. An alternative, simplified approach was introduced by Ng et al. (2023), who employed a Cellular Automata model based on probabilistic advection and diffusion rules. Their model was applied to various locations worldwide to assess different plastic source scenarios.

The present study aims to develop a numerical model capable of accurately simulating the transport of floating or near-surface marine macroplastics (i.e., plastic particles larger than 5 mm). The model incorporates the effects of wind, waves, and ocean currents to provide a more detailed and realistic representation of macroplastic transport dynamics. The model is applied to a real study area to improve our understanding of macroplastic transport mechanisms in real-life challenges, contributing to the development of more effective marine plastic mitigation strategies.

NUMERICAL MODEL AND VALIDATION

The developed numerical model consists of two main components. The first component involves initializing the wind, wave, and current fields within the study area. By the end of this initialization phase, each point on the sea surface is assigned a corresponding velocity and direction for wind, wave-induced drift, and ocean currents at each time step. The second component focuses on tracking the motion of a virtual particle released within the computed flow field. Throughout the simulation, the particle's position is continuously updated, and its trajectory is ultimately mapped to visualize its transport pathways.

A Lagrangian-type model is employed to simulate the movement of macroplastics. Initially, the Stokes drift is computed based on the relative water depth and the prevailing wave conditions. The influence of wind on the plastic particle (windage effect) is then determined as a fraction of the 10-meter wind velocity, following the approach of Christensen et al. (2023). The position of the virtual particle at time step t is computed using the following equation:

$$\vec{\mathrm{x}}_{\mathrm{t}} = \vec{\mathrm{x}}_{\mathrm{t-1}} + (\chi \cdot \vec{\mathrm{u}}_{\mathrm{s}} + \vec{\mathrm{u}}_{\mathrm{c}} + k \cdot \vec{\mathrm{u}}_{\mathrm{w}})\mathrm{dt} \tag{1}$$

where:
$\vec{\mathrm{x}}_{\mathrm{t}}$: the position of particle at time step t
$\vec{\mathrm{x}}_{\mathrm{t-1}}$: the position of particle at the previous time step t-1
$\vec{\mathrm{u}}_{\mathrm{s}}$: the Stokes drift velocity vector
$\vec{\mathrm{u}}_{\mathrm{c}}$: the current velocity vector
$\vec{\mathrm{u}}_{\mathrm{w}}$: the 10m wind velocity vector
dt : the time step
χ: the Stokes drift enhancement factor depending on the shape, density and size of the plastic object as calculated by Calvert et al.2024
k: windage coefficient as given by the formula below

$$k = k_0\sqrt{\frac{A_a}{A_w}} \text{ (Christensen et al.,2023)} \tag{2}$$

where $k_0 = 0.03$, wind pressure coefficient and A_α, A_w are the cross-sectional areas above and below water respectively.

Since the hydrodynamic forcing fields (wind, waves, and currents) are provided on a discrete grid, but particle positions are continuous, the required velocity values at arbitrary locations must be interpolated from the available grid data. This interpolation ensures that the particle receives realistic forcing inputs throughout its motion.

The model has been validated against experimental datasets and benchmarked against well-established numerical models like the experimental datasets by Calvert et al.,2024 and Forsberg et al.,2020 as well as the numerical model by Christensen et al.,2023. The validation process ensures the reliability of the simulated macroplastic transport pathways and enhances confidence in the model's applicability to real-world scenarios.

STUDY AREA AND APPLICATION

The developed numerical model is applied to the Saronikos Gulf, Greece, a region of significant environmental and economic importance. Since the Gulf is home to the main navigational channel serving the Port of Piraeus, the largest and busiest port in Greece it is particularly vulnerable to plastic pollution, emphasizing the need for a detailed study of macroplastic transport in the area.

Meteorological, wave, and ocean current data were obtained from open-access databases for the location with coordinates LAT: 37.856694, LON: 23.630219, situated within the Saronikos Gulf. Wave and ocean current data were retrieved from the European Copernicus Marine Service database, which provides high-resolution oceanographic information for European waters. Wind data were sourced from the European Centre for Medium-Range Weather Forecasts (ECMWF), ensuring reliable atmospheric forcing inputs. All datasets have an hourly temporal resolution and cover multiple past decades, allowing for a robust statistical representation of the hydrodynamic conditions in the region.
Additionally, bathymetric data were collected to determine the relative water depth at the particle's location (i.e., deep, intermediate, or shallow waters). This classification is crucial, as different wave-induced mass transport equations apply depending on the water depth regime. In particular, the Longuet-Higgins (1953) theory distinguishes between wave-driven transport in deep waters and that in intermediate to shallow depths.

Figure 1 presents a characteristic example of an individual floating macroplastic trajectory simulated within the Saronikos Gulf. The macroplastic has a diameter of 0.02 m and a density of 1024 kg/m³. The simulation covers a period from 04/05/2005 00:00 to 07/05/2005 00:00, with the initial release point at LAT: 467312, LON: 4192558 (GGRS87-EPSG2100 Greek Grid). During this period, wind velocities ranged from 0.04 m/s to 8.61 m/s, predominantly from the Northwest. The significant wave height varied between 0.15 m and 1.12 m, with a mean direction from the Northwest. The sea currents exhibited velocities between 0 m/s and 0.15 m/s, with an alternating flow direction, but in total dominating toward the Northwest. Simulation results indicate that current is the main driver of microplastic transport, exerting a significantly greater influence compared to wave-induced Stokes drift and windage effects. After 72 hours, the macroplastic's final position was determined at LAT: 465947, LON: 4198542, near the entrance of the Port of Piraeus.

CONCLUSIONS

This study aimed to simulate the transport pathways of a floating macroplastic particle in the Saronikos Gulf to identify the dominant mechanisms governing its dispersion.

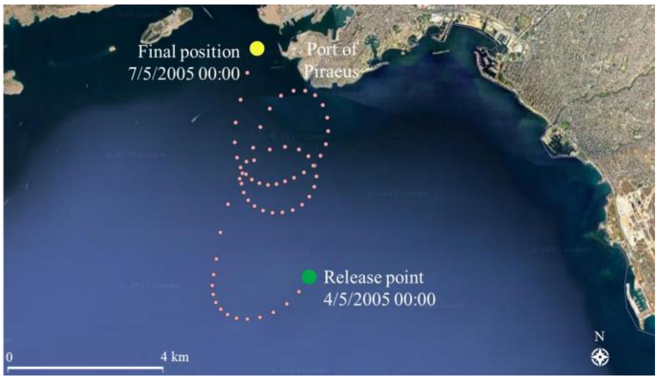

Figure 1. Characteristic example of an individual floating macroplastic trajectory simulated within the Saronikos Gulf.

Understanding these transport dynamics is crucial for assessing pollution hotspots and informing mitigation strategies. The accumulation of plastic debris in marine environments has long been recognized as a pressing environmental issue. However, only in recent years has the scientific community begun to systematically investigate the transport processes governing plastic motion. The present numerical model provides a first attempt to analyze macroplastic transport. However, the model remains in its early stages of development, and comprehensive validation against experimental measurements and, most crucially, real field observations is still required. Future work should focus on incorporating more refined physical processes and improving the model's predictive capabilities to ensure greater reliability in real-world applications.

REFERENCES

Calvert, R., Peytavin, A., Pham, Y., Duhamel, A., van der Zanden, J., van Essen S.M., Sainte-Rose, B., & van den Bremer, T.S. (2024). A Laboratory Study of the Effects of Size, Density, and Shape on the Wave-Induced Transport of Floating Marine Litter. *J. Geophys. Res. Oceans* 129 (7), e2023JC020661.

Christensen, A., Murawski, J., She J., & St. John, M. (2023). Simulating transport and distribution of marine macro-plastic in the Baltic Sea. PLoS ONE 18(1): e0280644.

Longuet-Higgins, M.S. (1953). Mass Transport in Water Waves. *Philos. Transact. A Math. Phys. Eng. Sci.* 245 (903), 535–581.

Ng, P.S., Maqueda, M.M., & Goh, K.L. (2023). Modelling the Transportation of Marine Plastics over the Ocean Surface by Cellular Automata. *Mar. Pollut. Bull.* 191, 114950.

Saidi, M.S., Rismanian, M., Monjezi, M., Zendehbad, M. & Fatehiboroujeni S. (2014). Comparison between Lagrangian and Eulerian Approaches in Predicting Motion of Micron-Sized Particles in Laminar Flows. *Atmos. Environ.* 89, 199–206.

van Sebille, E., Aliani S., Law K.L., Maximenko N., Alsina, J.M, Bagaev, A. & Bergmann M. (2020). The Physical Oceanography of the Transport of Floating Marine Debris. *Environ. Res. Lett.* 15 (2), 023003.

Stachurska, B. & Sulisz, W. (2024). Laboratory Investigations of Wave-Induced Transport of Plastic Debris over a Rippled Bottom. *Sci. Total Environ*. 946, 174380.

Quasi-3D Modelling of Micro Plastics Advection and Dispersion in the Marine Environment

Karambas Th.[1,*], Zafeirakou A.[1], Katsoulea A.[1] and Palantzas G.[1]

[1] Department of Civil Engineering, Aristotle University of Thessaloniki, University Campus, 54124 Thessaloniki, Greece

*corresponding author:
e-mail: karambas@civil.auth.gr

INTRODUCTION

Plastic debris has accumulated in marine environments due to the improper disposal of plastic materials. Plastic particles smaller than 5 mm in size, with various shapes (spheres, films, fibers), are characterized as microplastics (MP). These particles are difficult to biodegrade and are found in almost all marine systems, both in surface waters and at the sea bottom.

MP pollution is a significant environmental issue and has motivated numerous studies (Jalón-Rojas et al., 2019; Cai et al., 2023). However, a better understanding of MP behavior, transport, and deposition on the sea bottom is still required (Cai et al., 2023).

The aim of this work is to develop and present a model for the 3D transport of marine MP particles that incorporates their main physical processes. A quasi-3D numerical model is developed to simulate 3D wind-induced current velocities, and a 3D Lagrangian particle-tracking model is used to simulate the advection and dispersion of MP particles.

QUASI 3D HYDRODYNAMIC MODEL

A quasi-3D hydrodynamic model is used to predict wind induced current velocities. The model equations are derived from Navier-Stokes equations, after the assumption of hydrostatic pressure distribution and parabolic distribution over the depth of the vertical eddy viscosity coefficient. The assumption leads to a double-logarithmic velocity profile including both the surface and bottom sublayer (Tsanis, 1989, Wu and Tsanis, 1995). A typical distribution of the horizontal velocity is shown in Figure 1. By substituting the adopted profile in the convection terms of the Navier-Stokes equations and average over the depth we obtain a two-dimensional wind-induced circulation model:

$$\frac{\partial \zeta}{\partial t}+\frac{\partial\left(U_c\left(d+\zeta\right)\right)}{\partial x}+\frac{\partial\left(V_c\left(d+\zeta\right)\right)}{\partial y}=0$$

$$\begin{aligned}&\frac{\partial U_c}{\partial t}+T_1U_c\frac{\partial U_c}{\partial x}+T_2V_c\frac{\partial U_c}{\partial y}=-\frac{1}{\rho}\frac{\partial p_a}{\partial x}-g\frac{\partial \zeta}{\partial x}+\\&\quad\frac{1}{h}\frac{\partial}{\partial x}\left(\nu_h h\frac{\partial U_c}{\partial x}\right)+\frac{1}{h}\frac{\partial}{\partial y}\left(\nu_h h\frac{\partial U_c}{\partial y}\right)+\frac{\tau_{sx}}{\rho h}-\frac{\tau_{bx}}{\rho h}\\[1em]&\frac{\partial V_c}{\partial t}+T_1U_c\frac{\partial V_c}{\partial x}+T_2V_c\frac{\partial V_c}{\partial y}=-\frac{1}{\rho}\frac{\partial p_a}{\partial y}-g\frac{\partial \zeta}{\partial y}+\\&\quad\frac{1}{h}\frac{\partial}{\partial x}\left(\nu_h h\frac{\partial V_c}{\partial x}\right)+\frac{1}{h}\frac{\partial}{\partial y}\left(\nu_h h\frac{\partial V_c}{\partial y}\right)+\frac{\tau_{sy}}{\rho h}-\frac{\tau_{by}}{\rho h}\end{aligned}\tag{1}$$

where U_c and V_c are the mean over the depth current velocities, ζ is the free surface elevation, h is the total depth, p_a the pressure at the surface of the sea, τ_{sx} and τ_{sy} are the surface shear stresses, τ_{bx} and τ_{by} are the bottom shear stresses, ν_h is the horizontal eddy viscosity which given through the Smagorinsky eddy parameterization and T1 and T2 are correction terms accounting for momentum dispersion due the non-uniform velocity distribution of the horizontal velocities, according to Wu and Tsanis (1995).

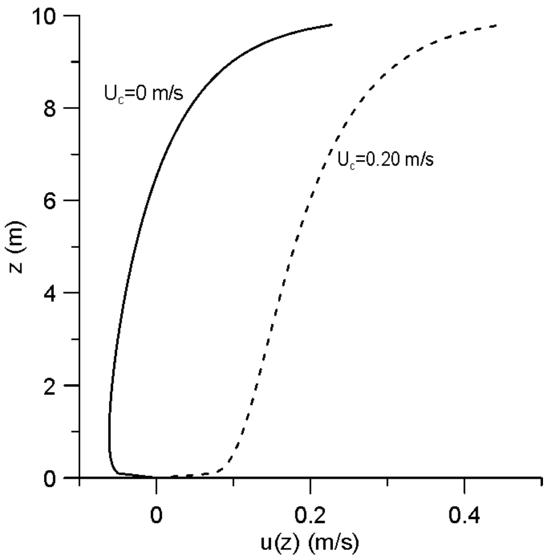

Figure 1. Vertical profile of the horizontal velocity in the direction of the wind (total depth h=10 m, wind speed 20 m/s) Solid line: mean of the depth velocity U_c=0, dashed line U_c=0.2 m/s.

Wave-induced currents are also described by incorporating radiation stress terms derived from a wave propagation model (Samaras and Karambas, 2021).

LAGRANGIAN PARTICLE-TRACKING MODEL

Lagrangian particle-tracking models describe the transport and dispersion of individual particles under the assumption that interactions between particles are ignored and that particle velocity is equal to water velocity.

The particles are tracked in a Lagrangian frame of reference, and their coordinates (*x*, *y*, and *z*) are governed by the following kinematic conditions (Zafirakou et al., 2023):

$$\begin{aligned}&x(t+dt)=x(t)+u(x,y,z,t)\,dt+u_r(x,y,z,t)(2Rnd-1)\,dt\\&y(t+dt)=y(t)+v(x,y,z,t)\,dt+v_r(x,y,z,t)(2Rnd-1)\,dt\\&z(t+dt)=z(t)-w_f\,dt+w_r(x,y,z,t)(2Rnd-1)\,dt\\&u_r=\sqrt{6\nu_h/dt}\quad v_r=\sqrt{6\nu_h/dt}\quad w_r=\sqrt{6\nu_z/dt}\end{aligned}\tag{2}$$

where dt is the time step, $u(z,y,x,t)$ and $v(z,y,x,t)$ represent the horizontal velocity provided by the circulation model and the double-logarithmic velocity profile, w_f is the settling velocity Rnd represents random numbers and ν_z is the vertical turbulent diffusion coefficient.

Particle's positions are defined by its Cartesian coordinates (x, y, z) updated every time-step. The last terms of the first two equations of (2) represent the horizontal stochastic displacements due to horizontal turbulent dispersion and diffusion. The last term of the third equation of (2) represents the vertical stochastic displacement which depends on the vertical turbulent diffusion. The value of the random numbers *Rnd* have a uniform statistical distribution and range from 0 to +1.

The model describes not only the advection and dispersion of MP particles but also their deposition on the seabed and their resuspension. Resuspension is considered by comparing the critical shear near-bottom velocity with the shear velocity induced by wind-driven currents.

FALL VELOCITY AND BIOFOULING

The fall velocity of MP particles depends on their properties (e.g., density, size, and shape) and their interaction with other suspended particulate matter. In this study, MP is treated as a sphere, following Equation (12) of Jalón-Rojas et al. (2019).

The behavior of MP can be altered by the fouling of organisms (biofouling), which increases their size and density, consequently affecting their trajectories. The increase in MP density due to the biofilm layer and its temporal variation is simulated here based on Jalón-Rojas et al. (2019) and Cai et al. (2023). The density ρ_b of a fouled particle due the attachment of a biofilm with density ρ_D and thickness BT can be approximated by:

$$\rho_b = \rho_o \frac{R_o^3}{\left(R_o + BT\right)^3} + \rho_D \left[1 - \frac{R_o^3}{\left(R_o + BT\right)^3}\right] \tag{3}$$

where ρ_o is the initial density of the polymer particle (g/cm^3), R_o is the radius of a sphere (m), BT is the biofilm thickness. It is assumed that biofilm thickness (BT) is increased over time at a constant rate according to Jalón-Rojas et al. (2019).

MODEL APPLICATION

The present model is applied in Thermaikos Gulf assuming a continuous release of 1000 MP particles per m^3 in the coastal area near the wastewater disposal site of Thessaloniki Wastewater Treatment Plant.

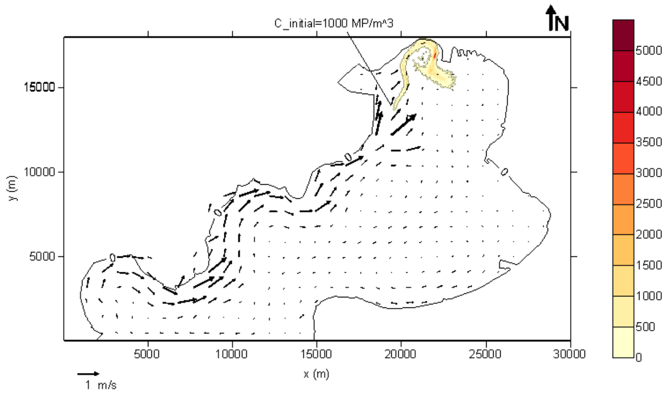

Figure 2. Velocity field and MP concentrations Thermaikos Gulf.

Figure 2 shows the wind-induced currents and the concentration of MP under the action of Eastern winds with a speed of 20 m/s. Figure 3 illustrates the bottom concentration after MP particles deposition.

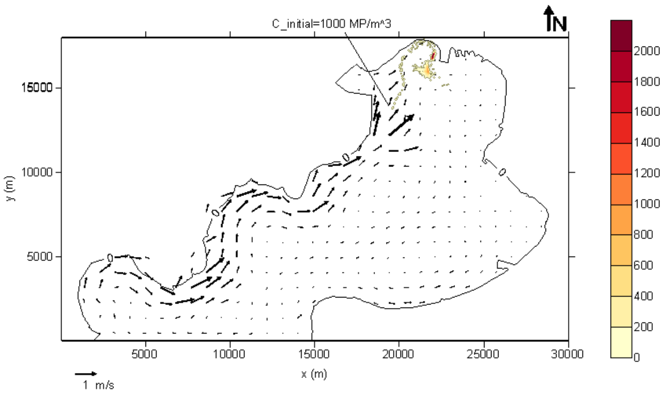

Figure 3. Velocity field and bottom MP concentrations Thermaikos Gulf.

The advection of MP particles follows the velocity pattern, along with their dispersion. The deposition and accumulation of MP particles in sediment layers, due to their density increase from the biofouling process, are quite significant.

CONCLUSIONS

The proposed quasi-3D hydrodynamic and advection-diffusion-dispersion-deposition numerical model serves as a useful tool for modeling marine plastic transport in coastal and marine environments.

ACKNOWLEDGEMENTS

The present work was undertaken under the CARE SEA Interreg VI-B NEXT Black Sea Basin Programme

REFERENCES

Cai C., Zhu L., Hong B. (2023). A review of methods for modeling microplastic transport in the marine environments, *Mar. Pollut. Bull.* 193, 1–19.

Jalón-Rojas I., Wang X. H., Fredj E. (2019). A 3D numerical model to Track Marine Plastic Debris (TrackMPD): Sensitivity of microplastic trajectories and fates to particle dynamical properties and physical processes, *Mar. Pollut. Bull.* 141, 256–272.

Samaras, A.G., & Karambas, T.V. (2021). Modelling the Impact of Climate Change on Coastal Flooding: Implications for Coastal Structures Design. *J. Mar. Sci. Eng.* 9(9), 1008.

Tsanis I. (1989). Simulation of wind-induced water currents. *J. Hydraul. Eng.* 115 (8),1113–1134.

Wu J., Tsanis I. (1995). Numerical study of wind-induced water currents. *J. Hydraul. Eng.* 121(5), 388–395.

Zafeirakou, A., Pechlivanidis, G. & Koutitas, C. (2023). Theoretical analysis and experimental investigation of air-bubble-stream-induced water circulation. *Euro-Mediterr J Environ Integr.* 8, 275–286.

Numerical Simulations of Oil Spill Incidents in the Framework of a Digital Twin

Keramea P.[1], Kokkos N.[1] and Sylaios G.[1,*]

[1] Department of Environmental Engineering, Democritus University of Thrace, 67100 Xanthi, Greece

*corresponding author:
e-mail: gsylaios@env.duth.gr

INTRODUCTION

Recent studies on oil spill accidents, such as the Deepwater Horizon (DwH) oil spill, have highlighted their immense and devastating impacts on the environment, economy, and society, with long-term effects that disrupt entire ecosystems (Hook, 2020). In the North Aegean, the high traffic of oil tankers and cargo vessels through the Dardanelles Strait, along with the establishment of the LNG terminal in Alexandroupolis in the Thracian Sea and the overall increase in human activities, significantly raises the probability of an oil spill accident (Keramea et al., 2022). This renders the region a vulnerable and environmentally sensitive area.

The environmental oil spill impacts depend on multiple factors, including the type and quantity of oil released, the region's geomorphology, prevailing winds, ocean currents, waves, sea temperature, and salinity (Dong et al., 2022; Keramea et al., 2023). For this reason, a Digital Twin was developed to investigate the seasonal trends and effects on the fate and transport of spilled oil in the North Aegean, considering both surface and subsea release scenarios.

The Thracian Sea oil spill DT consists of: (a) the RT oil spill identification component, using ML algorithms for the identification of oil spills at the sea surface, (b) the RT citizen science component, scanning social media posts (mainly on Twitter), georeferenced in the area of accidental release, to collect information relevant to the event, (c) the RT oil spill trajectory forecasting modelling component, providing the accurate tracking of oil particles, coupled to meteorological, hydrodynamic, wave and biogeochemical models, (d) the citizen science response evaluation component, to assess public perceptions on the coordinated actions and timely authorities response to minimize the environmental impacts of the oil spill.

In this work, the oil spill model runs (OpenOil model) integrated met-ocean forecasts (hydrodynamics, waves, and winds) from the CMEMS and NOAA-GFS forecasting products.

MATERIALS AND METHODS

OpenOil is a recently integrated oil spill transport and fate model, based on the OpenDrift trajectory framework, which is python-based and open source (Dagestad et al., 2018). The model incorporates algorithms simulating a broad range of physical processes, such as oil emulsification, oil resurfacing due to buoyancy, vertical mixing caused by oceanic turbulence, and oil entrainment by waves (Röhrs et al., 2018). In OpenOil, the oil properties are obtained from the open-source ADIOS Oil Library (Lehr et al., 2002). Moreover, OpenOil has been applied in several cases worldwide, such as the Norwegian Sea, the Gulf of Mexico, and the Thracian Sea (Keramea et al., 2023).

In this study, two seasonal surface-subsea scenarios were investigated: the release of crude oil at the western Thracian Sea. Initially, approximately 3,500 oil particles were positioned at the surface and 40 meters depth in the two scenarios, respectively. The type of oil used was Generic Diesel with density of 841.2 kg m^{-3} and viscosity 5 cPoise. The period for the surface seasonal simulations was 3.5 days (from 4/8/2024 at 23:00 to 8/8/2024 at 11:00, summer case; from 4/3/2024 at 23:00 to 8/8/2024 at 11:00, winter case). In the Subsea release scenarios, the model simulated for approximately 12 hours. The OpenOil model was coupled with real-time winds from NCEP/NCAR (National Centers for Environmental Prediction / National Center for Atmospheric Research) Reanalysis from NOAA GFS (Global Forecasting System). In addition, OpenOil was coupled with hydrodynamic, wave, salinity, and temperature data from the Copernicus Marine Environment Monitoring Service database.

RESULTS

The results revealed that seasonal forcing changes influence the oil particles' probability distribution, the oil dispersion patterns, and the oil mass distribution within the water column. Specifically, in the winter case, the dispersion and spread of oil particles were significantly greater than in the summer test case, due to the stronger winds, currents, and waves prevailing in the region. In the winter oil release event, strong southwestward (SW) currents ranged from 0.15 m/s to 0.4 m/s, and winds from 2 m/s to 7 m/s prevailed in the region. The majority of the particles drifted towards the coasts of Halkidiki, with a significant portion accumulated in the Bay of Athos (Figure 1a). Additionally, numerous oil particles adhered near the Ierissos Gulf at the end of 3.5 day simulation, while several particles were transported southward and remained offshore of Halkidiki, towards the beaches of Sarti, without making direct contact with the coastline.

Conversely, in the summer case, the biodegradation rates were higher, attributed to the increased sea temperature during the summer months. Particle dispersion was considerably lower, exhibiting a northwestward drift by the weaker surface currents (0.08 m/s to 0.16 m/s) and winds (1 m/s to 3 m/s). In this case, most particles accumulated along the southern coasts of Mount Pangaion and were subsequently transported westward, offshore from the beaches of Ofrinio (Figure 1b).

Concerning mass distribution within the water column, it was observed that due to the stronger currents in winter, a significant percentage of oil particles remained submerged (~20%) and dispersed (~20%), in contrast to the near-zero values recorded in the summer (Figure 2). On the other hand, biodegradation rates were notably higher in summer (~22%) compared to winter (~5%), with a seasonal difference of approximately 20%. This variation is attributed to the higher summer temperature (28°C) compared to winter (14°C) (Figure 2).

Regarding the subsea seasonal scenario at a depth of 40 meters, a high percentage of dispersed oil (~20%) was observed in the winter due to the stronger currents compared to the summer (Figure 3). In contrast, during the summer, the dispersed oil fraction was zero. Biodegradation rates were significantly higher in summer (~10%), while in winter, they reached only 1%, resulting in a seasonal difference of approximately 10% (Figure 3).

ACKNOWLEDGEMENTS
This research was funded by EU Horizon 2020 European Green Deal Research and Innovation Program (H2020-LC-GD-2020-4), Grant No. 101037643 – ILIAD (Integrated Digital Framework for Comprehensive Maritime Data and Information Services).

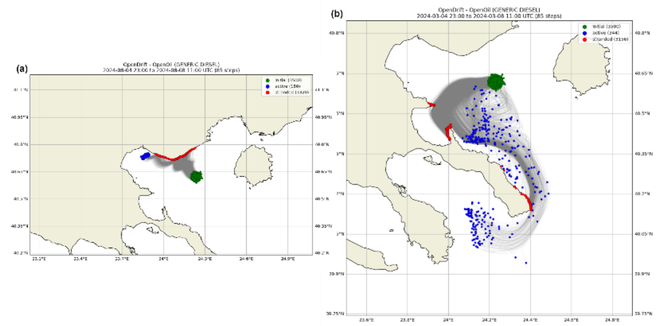

Figure 1. **(a)** Oil spill simulation in the Thracian Sea at the end of the 3.5-day surface simulation at **Summer Case (August 2024)**; (b) Oil spill simulation near to in the Thracian Sea at the end of the 3.5-day surface simulation at **Winter Case (March 2024)** via OpenOil submodule. Green dots represent the initial positions of the oil elements, grey lines are their trajectories over time, and blue dots are the positions of oil droplets at the end of the simulation. Red dots represent elements that have been stranded and beached.

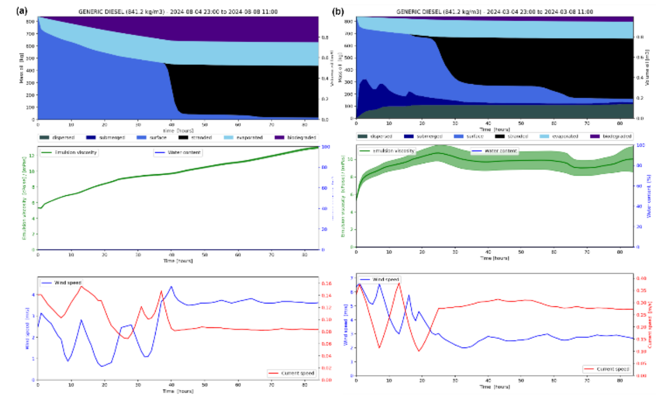

Figure 2. Time evolution of OpenOil model for **(a) surface results** for the 3.5-day **summer** simulation **period** and **(b)** for **winter** simulation **period**, for a) the oil budget and the relative impact of each physical and biochemical process; b) the oil properties; c) the prevailing wind and surface current speed.

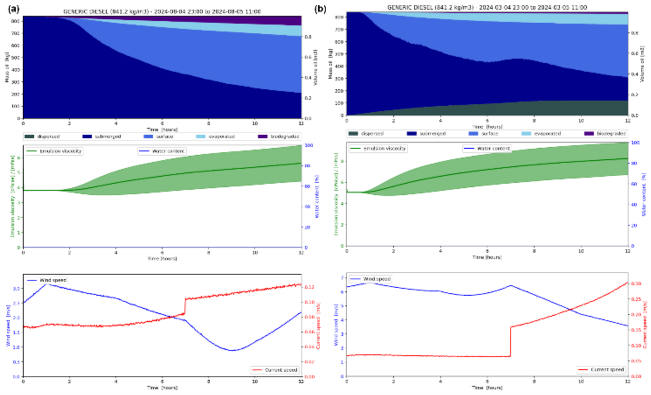

Figure 3. Time evolution of OpenOil model **subsea results**, during the 12-hours **(a) summer simulation period** (August 2024) and **(b) winter simulation period** (March 2024) at depth 40m for a) the oil budget and the relative impact of each physical and biochemical process; b) the oil properties; c) the prevailing wind and surface current speed.

REFERENCES

Dagestad, K. F., Röhrs, J., Breivik, Ø., & Ådlandsvik, B. (2018). OpenDrift v1. 0: a generic framework for trajectory modelling. *Geosci. Model Dev.* 11(4), 1405–1420.

Dong, J., Asif, Z., Shi, Y., Zhu, Y., & Chen, Z. (2022). Climate change impacts on coastal and offshore petroleum infrastructure and the associated oil spill risk: A review. *J. Mar. Sci. Eng.* 10(7), 849.

Hook, S.E. (2020). Beyond thresholds: A holistic approach to impact assessment is needed to enable accurate predictions of environmental risk from oil spills. *Integr. Environ. Assess. Manag.* 16(6), 813–830.

Keramea, P., Spanoudaki, K., Zodiatis, G., Gikas, G., & Sylaios, G. (2021). Oil spill modeling: A critical review on current trends, perspectives, and challenges. *J. Mar. Sci. Eng.* 9(2), 181.

Keramea, P., Kokkos, N., Gikas, G. D., & Sylaios, G. (2022). Operational modeling of North Aegean oil spills forced by real-time met-ocean forecasts. *J. Mar. Sci. Eng.* 10(3), 411.

Keramea, P., Kokkos, N., Zodiatis, G., & Sylaios, G. (2023). Modes of operation and forcing in oil spill modeling: state-of-art, deficiencies and challenges. *J. Mar. Sci. Eng.* 11(6), 1165.

Lehr, W., Jones, R., Evans, M., Simecek-Beatty, D., & Overstreet, R. (2002). Revisions of the ADIOS oil spill model. *Environ. Model. Softw.* 17(2), 189–197.

Röhrs, J., Dagestad, K. F., Asbjørnsen, H., Nordam, T., Skancke, J., Jones, C. E., & Brekke, C. (2018). The effect of vertical mixing on the horizontal drift of oil spills. *Ocean Sci.* 14(6), 1581–1601.

3rd International Conference on
Design and Management of Port, Coastal and Offshore Works

Patras, Greece, May 7-9 2025

Hydrodynamic Study of Upwelling Events in the Coastal Zone of Mussel Cultures of Chalastra (NW Thermaikos Gulf)

Savvidis Y.[1,*]

[1] Department of Environmental Engineering, International Hellenic University, Thessaloniki 57400, Greece

*corresponding author:
e-mail: savvidis@ihu.gr

INTRODUCTION

The dynamics of the water masses of a coastal basin hosting aquaculture units is of particular importance for the sustainable development of this type of cultivated marine organisms. The interaction of hydrodynamics and mussel farms in the Chalastra basin (Figure 1) with average depths of 8 m and maximum 25 m (NW Thermaikos gulf), has been the subject of research for several decades (Galinou-Mitsoudi et al. 2006, Moriki 2007, Savvidis et al. 2019).

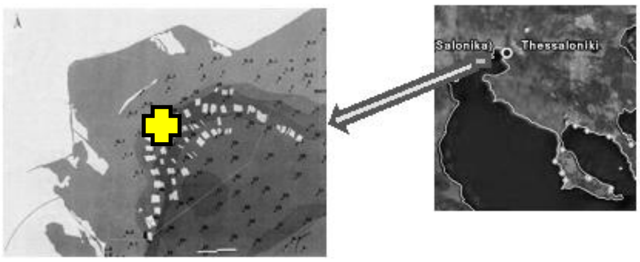

Figure 1. Map of the mussel units of the Chalastra basin from Hellenic Center of Marine Research -HCMR (left) and Thermaikos Gulf (right) from Google Earth. The cross shows the area of field measurements.

The hydrodynamic circulation in the coastal area of Chalastra, as well as in the wider area of Thermaikos gulf, is predominantly wind-driven. The influence of tides in the Thermaikos Gulf is of low importance (Hyder et al., 2002a). Regarding the influence of the neighboring estuary systems of the rivers' south and southwest of the Chalastra area, their effect on the generation of density currents is seasonal and has minor importance during the recent years due to the limited rivers' runoff (Moriki, 2007). Previous study revealed downwelling events in the area under the influence of south winds (Savvidis et al. 2019). The aim of this work is to study the phenomena of upwelling processes developing in this basin. Studies on upwelling events have been conducted for large or small sea basins (Dodou et al. 2002, Savvidis et al. 2004, Androulidakis, 2017). The present research examines the case of upwelling in the coastal basin of Chalastra, via numerical experiments. The study area is characterized by shallow depths and small density differences between the surface and deeper waters, which were found during field measurements.

METHODOLOGY

Field Measurements. Measurements of sea currents as well as water temperature and salinity were conducted during the period August 2014 to August 2015. The velocity measurements were realized around a mussel farm in the center of the basin marked with a cross in Figure 2b and was based on the use of two drifters. These drifters, carried in their upper part, a well-fixed box with a mobile phone device with an activated GPS system in order to record the course of the drifters' transported by the currents. The thermohaline parameters of the water were realized by a CTD devise.

Mathematical model. A two-layer mathematical model was used in this study. The mathematical description of the model is given in detail by Koutitas and Scarlatos (2015). The model was based on the application of the well-known mass and momentum conservation equations for two layers (an upper and a lower) given an initial stratification of the water column. An initial thickness of 2 m of the upper layer is taken into account for the model. The present application concerns the hydrodynamics developed by north winds.

RESULTS

Field measurements of sea currents and water density. Temperature and salinity data led to the calculation of seawater density. It was found that the density differences between the surficial and deeper waters were 1 ‰. Concerning velocity measurements, a NW current at the area marked with the cross in Figure 1, was recorded by one of the drifters under north wind prevailing on November 22, 2014. The other drifter was stuck inside the mussel culture unit.

Model runs. The model for north wind generated currents, resulted in the velocity fields of Figure 2.

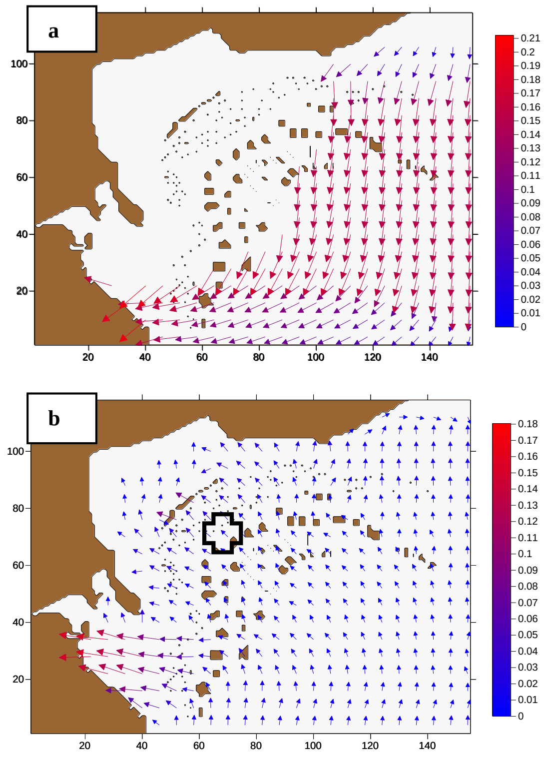

Figure 2. Current velocities of the (a) upper and (b) lower layer (six hours after the wind begun to blow over the area). The colored bar at right is in m/s. The cross in Figure 2b refers to the area of field recorded data (control point).

The velocity vectors of Figures 2a and 2b correspond to the sea currents of the upper and lower layer respectively, after six hours of north wind blowing over the area (reaching steady state flow conditions). The areas with no vectors in Figure 2a (no water circulation) shows that the waters of the upper layer were substituted by waters from the lower layer. In this way, upwelling events are documented. The computed model current velocity (area in the cross) seems to be in good agreement with the field measurement. The evolution of the thickness of the two layers at the control position marked with the cross in Figure 2b, for a 6 hours' time period of constant north wind is given in Figure 3.

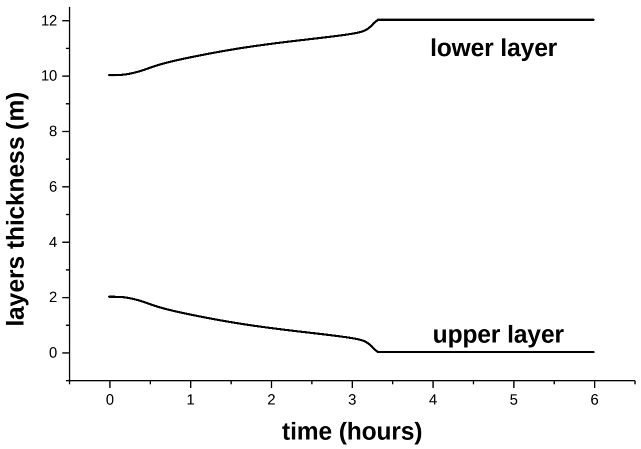

Figure 3. Time evolution of upper and lower layers for 6 hours of north wind of 5 m/sec (it refers to the point marked with the cross in Figure 2b).

Figure 3, shows that, in less than 3.5hours of constant north wind, waters from the lower layer, replaced totally the waters of the upper layer (upwelling event). More analytically, the upper layer (with an initial thickness of 2 m) decreases gradually in time, while the lower layer (with an initial thickness of 10 m) increases until the full substitution of the upper layer by the lower, which indicates upwelling phenomena.

DISCUSSION AND CONCLUSIONS

It is well-known that upwelling processes may contribute positively to the enrichment of surficial waters with nutrients from deeper layers of water. The present research is focused on the study of an upwelling event on a small coastal area on NW Thermaikos Gulf. More specifically, measurements of seawater density data in the coastal basin of Chalastra from August 2014 to August 2015 showed that usually small density differences were recorded throughout the study period. Regarding the hydrodynamic characteristics, the water circulation due to north winds was presented here. The study was realized by the use of the mathematical simulations. The model was initially confirmed by Savvidis et al (2019), where downwelling events were revealed under the influence of south winds. Here, the above mentioned study was completed with the analysis of upwelling processes. In more detail, the present study revealed that northern winds generate upwelling events. It should be noted that the general rule of developing upwelling phenomena under the influence of winds blowing parallel to a coastline with particular direction, does not apply here where the coastal topography is quite complex and the bathymetry is characterized by shallow depths. It is also important to point out that a detailed analysis of wind data often reveals some periodicity in the occurrence of specific winds blowing over an area. Such a periodicity was discussed in Hyder et al. (2002b) and Savvidis et al. (2019). This knowledge can be successfully used in a comprehensive study of the hydrodynamics that characterize Chalastra basin. The information of the evolution of the thickness of the two layers during the development of upwelling or downwelling phenomena can be used to the appropriate spatial design of mussel's socks in the farming units. Thus, the mathematical model presented here, can contribute significantly to a deeper investigation of the upwelling and downwelling phenomena in combination with optimal coastal management practices.

REFERENCES

Androulidakis, Y.S., Krestenitis Y.N., & Psarra, S. (2017), Coastal upwelling over the North Aegean Sea: Observations and simulations. *Cont. Shelf Res.* 149, 32–51.

Dodou M.G., Savvidis, Y.G., Krestenitis, Y.N., & Koutitas, C.G. (2002). Development of a two-layer mathematical model for the study of hydrodynamic circulation in the sea. Application to the Thermaikos Gulf. *Mediterr. Mar. Sci.* 3, 5–25.

Galinou-Mitsoudi, S., Savvidis, Y. & Dimitriadis, X. (2006). Interaction between Mussel Culture and Hydrodynamic; a Preliminary Study in the Gulfs of Thesaloniki and Thermaikos, Greece. *J. Biol. Res.* 5, 1–7.

Hyder, P., J., Simpson, H. & Christopoulos, S. (2002a). Sea-breeze forced diurnal surface currents in the Thermaikos Gulf, North-west Aegean. *Cont. Shelf Res.* 22, 585–601.

Koutitas, C., & Scarlatos, P. (2015) Computational Modelling in Hydraulic and Coastal Engineering; CRC Press: Boca Raton, FL, USA, 2015; p. 313

Moriki, A. (scientific coordinator). 2007. Water circulation in organized areas of aquaculture development and landplanning and environmental management interventions final technical report (in Greek). Archimed II, Alexander Technological Educational Institute of Thessaloniki, Moudania, Greece.

Savvidis, Y., Antoniou, A., Moriki, A., & Stoilas, V.O. (2019). Downwelling events in a Coastal Mussel Farming Area, NW Thessaloniki's Gulf (NW Aegean Sea). *Ocean Sci. J.* 54(4), 543–558

Savvidis Y., Dodou, M., Krestenitis, Y., & Koutitas, C. (2004). Modelling of the upwelling hydrodynamics in the Aegean Sea. *Mediterr. Mar. Sci.* 5(1), 5–18.

A Methodology for Systematic Analysis and Processing of Critical Wave Events for Floating Structures, Towards the Definition of Design Wave Events

Paradeisiotis A.[1,*], Stagonas D.[1]

[1] Department of Civil and Environmental Engineering, University of Cyprus, Nicosia, Cyprus

*corresponding author:
e-mail: aparad01@ucy.ac.cy

ABSTRACT

A novel methodology is presented, for accurately recreating and validating the effects of extreme loading events on offshore floating wind turbines, with a focus on enhancing the design process. The methodology leverages Gaussian Elementary Envelopes to isolate and reconstruct wave events, enabling the probabilistic definition of "Design Wave Groups" (DWGs). These DWGs provide a broadly applicable, time- and cost-efficient alternative to traditional methods that rely on computationally expensive simulations.

Fully non-linear propagation of sea-state realizations is performed using potential flow solvers, while computational simulations of wave-structure interactions are conducted using wind turbine simulation software. Correlated wave events responsible for extreme structural responses are characterized using Gaussian wave groups, parametrically stored in a data library. This enables stochastic processing of the resulting datasets, allowing the formulation of a design wave event and a systematic reconstruction process.

The methodology was tested through an experimental campaign using a scaled model of an offshore floating wind turbine in an ocean towing tank. Random sea-states, isolated wave events, and their reconstructions were tested, with free surface elevations and structural responses such as platform motions and mooring loads carefully monitored. It was confirmed that critical wave events could be accurately isolated and reconstructed using Gaussian Elementary Wave Groups. These reconstructed events adequately replicated the extreme structural responses observed during original wave events, providing strong experimental evidence for the methodology's accuracy.

INTRODUCTION

The interaction between sub-harmonic wave components and structural modes of floating offshore wind turbines (FOWTs) poses significant challenges for their design and safety. Sub-harmonic components, arising from non-linear interactions in irregular wave fields, exhibit low frequencies that often overlap with the natural modes of FOWTs, such as surge, pitch, and heave. This overlap can lead to resonance, amplifying motions and forces, particularly in mooring systems, and resulting in extreme loads (Robertson, 2017; Borg et al., 2024). Severe sea states with high energy and pronounced wave grouping exacerbate these interactions (Pegalajar-Jurado and Bredmose, 2019), making the identification of critical wave events essential for effective design strategies.

Traditional extreme value analysis relies on statistical models of random sea states (Palfy, 2016), but these methods are computationally expensive and fail to identify specific wave events driving extreme responses. Advanced approaches such as the NewWave method of Tromans et al. (1991), model extreme wave events through linear superposition of focused waves. However, these methods neglect the effects of the preceding wave-train. Enhanced methodologies like the constrained NewWave (Hann et al., 2018; Cassidy et al., 2001) which significantly improve the reliability of wave-structure interaction predictions, yet their complexity and computational cost limit their practicality for parametric studies.

This study introduces a novel methodology combining harmonic separation and Gaussian regression techniques to systematically isolate and reconstruct critical wave events. Experimental validation assesses whether this approach effectively captures the critical features of extreme wave-structure interactions, offering a robust, practical solution for improving FOWT design under extreme loading conditions.

THEORY

By leveraging only the linear components of wave events to approximate their envelopes, the method provides an efficient, data-driven framework for defining design wave events. A regression approach based on Farazmand and Sapsis (2017) is followed, but applied on the temporal wave propagation at a given point instead for spatial wave evolution, i.e. the space variable is replaced with time in the elementary Gaussian envelope:

$$g_n(t) = a_n\, exp\left[-\left(\frac{t-t_n^c}{T_n}\right)^2\right] \tag{1}$$

The original envelope $u(t)$ of a wave event is approximated through a sum of Gaussian envelopes:

$$u(t) \approx G(t) = \sum_{n=1}^{N} g_n\,(t) \tag{2}$$

The corresponding variance spectrum of each Gaussian WG:

$$P_n(f) = \frac{1}{2}\frac{\left|\mathcal{F}\{g_n e^{-i\widetilde{\omega} t}\}\right|^2}{\Delta f} \tag{3}$$

where $\widetilde{\omega}$ is calculated characteristic frequency of the wave event. This spectrum is used to generate a focused wave group as

$$\eta_n(t) = \frac{a_n}{\sum P_n \Delta f}\sum_{i=1}^{N_f} P_n(f_i)\Delta f\, cos[-\omega_i(t-t_n^c)+\beta_n] \tag{4}$$

Thus the reconstructed surface elevation of the wave event is obtained as:

$$\eta_G(t) = \sum_{n=1}^{N} \eta_n\,(t) \tag{5}$$

where N is the number of Gaussian focused wave groups.

RESULTS

Following the harmonic separation process, the 1st order component of wave events is isolated (Buldakov et al., 2017), facilitating the regression and reconstruction of the wave event via the proposed methodology. Figure 1 presents an example of regression of the envelope of a wave event with elementary Gaussian envelopes. The yellow line is the sum of these elementary envelopes, each corresponding to a peak of the envelope.

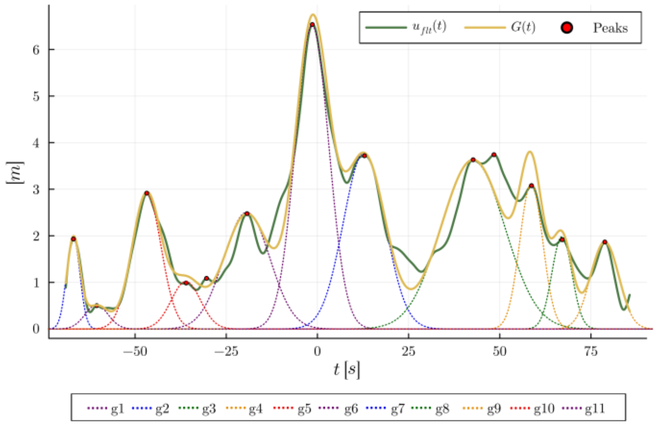

Figure 1. Gaussian regression of wave event envelope.

Figure 2 presents the experimental surface elevation of a reconstructed wave event and the resulting mooring line anchor tension of the FOWT experimental model. The results are compared to the surface elevation of the full sea-state and the induced anchor tension, along with the results for the original isolated wave event.

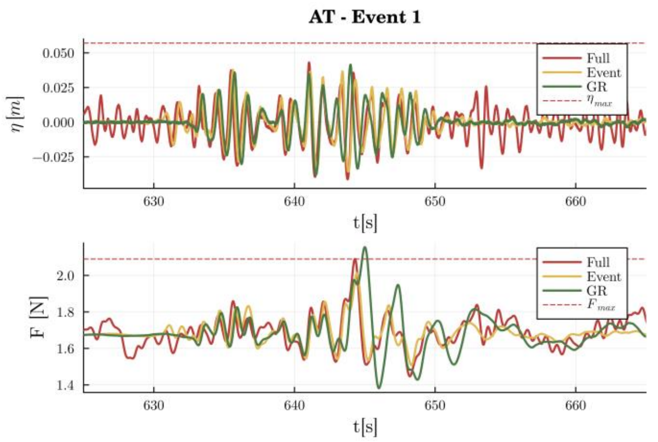

Figure 2. Anchor tension (AT) extreme response event. (a) Surface elevation. (b) Anchor tension response.

Table 1. Peak anchor tension statistics for Event 1.

	Full	Event	GR
F_{max} [N]	2.090	2.013	2.155
ε [%]	-	-3.68	3.11

CONCLUSIONS

The proposed methodology offers a systematic and effective approach for identifying, reconstructing, and evaluating wave events responsible for extreme responses in floating offshore wind turbines. By employing harmonic separation and Gaussian regression, the method isolates critical wave events within random sea-states, capturing the interplay between wave group characteristics and the low-frequency structural modes. This approach emphasizes that extreme structural responses, such as fairlead tensions, are influenced not solely by wave amplitude but by wave grouping and phase relationships, offering a nuanced perspective on the factors driving extreme events. Simulation and experimental results validate the accuracy of this methodology in reproducing critical response events. The reconstructed events successfully predicted extreme mooring line tensions with minimal deviation from full sea-state tests. Findings demonstrate that successive wave groups, rather than isolated high-amplitude waves, often induce the most severe responses. The focus on low-frequency components and discontinuities in instantaneous frequency ensures that the reconstructed events retain the defining features necessary for practical design.

ACKNOWLEDGEMENTS

Andreas Paradeisiotis has received funding from the European Union's Horizon 2020 research and innovation programme under the Marie Sklodowska-Curie Grant Agreement No 101034403. Thanks to UCL's CEGE and Mechanical Engineering departments for allowing use of their experimental facilities.

REFERENCES

Borg, M., et al. (2024). Dynamic response analysis of the TetraSpar floater in waves: Experiment and numerical reproduction. *Mar. Struct.* 94, 103546.

Buldakov, E., Stagonas, D., & Simons, R. (2017). Extreme wave groups in a wave flume: Controlled generation and breaking onset. *Coast. Eng.* 128, 75–83.

Cassidy, M.J., Taylor, R.E., & Houlsby, G.T. (2001). Analysis of jack-up units using a Constrained NewWave methodology. *Appl. Ocean Res.* 23(4), 221–234.

Farazmand, M. & Sapsis, T.P. (2017). Reduced-order prediction of rogue waves in two-dimensional deep-water waves. *J. Comput. Phys.* 340, 418–434.

Hann, M., Greaves, D., Raby, A., & Howey, B. (2018). Use of constrained focused waves to measure extreme loading of a taut moored floating wave energy converter. *Ocean Eng.* 148, 33–42.

Palfy, J. (2016). Guidance Notes on Selecting Design Wave by Long Term Stochastic Method, American Bureau of Shipping (ABS).

Pegalajar-Jurado, A. & Bredmose, H. (2019). Reproduction of slow-drift motions of a floating wind turbine using second-order hydrodynamics and Operational Modal Analysis. *Mar. Struct.* 66, 178–196.

Robertson, A.N., et al. (2017). OC5 Project Phase II: Validation of Global Loads of the DeepCwind Floating Semisubmersible Wind Turbine. *Energy Procedia* 137, 38–57.

Tromans, P.S., Anatruk, A.H., & Hagemeijer, P. (1991). A new model for the kinematics of large ocean waves - Application as a design wave. Proc. 1st International Offshore and Polar Engineering Conference (ISOPE 1991), Edinburgh, The United Kingdom.

3rd International Conference on
Design and Management of Port, Coastal and Offshore Works

Patras, Greece, May 7-9 2025

The Evolution of Regular Wave Surface Elevations and Kinematics in the Coastal Zone

Millar O.[1,*], Ma L.[1] and Karmpadakis I.[1]

[1] Imperial College London, Department of Civil & Environmental Engineering, SW7 2AZ, UK

*corresponding author:
e-mail: oliver.millar18@imperial.ac.uk

INTRODUCTION

The design of coastal and offshore infrastructure requires an accurate understanding of wave kinematics. These are the primary inputs to traditional loading formulae, and drive mass transport processes. Regular waves are often used as design conditions in engineering practice. Accordingly, regular wave kinematics have been the subject of a number of prior investigations. These have generally indicated that higher-order Stokes models produce satisfactory estimates when water depth is constant, for example in Swan (1990). In nearshore regions, variable bathymetry causes waves to shoal and eventually break. This results in significant changes in wave height and steepness, which are well documented. In contrast, there have been few studies relating to the evolution of wave kinematics, such as horizontal and vertical wave velocities.

This paper presents the results of an experimental investigation into the evolution of regular waves over a uniform slope. A broad range of regular waves are generated with varying degrees of nonlinearity. The spatial evolution of wave height, celerity and kinematics is examined. Comparisons to theoretical models are produced, and errors are quantified and analyzed. Time-averaged properties are displayed and discussed.

METHODOLOGY

Seventeen unidirectional wave cases were generated in the Coastal Flume at Imperial College London. The test matrix is summarised in Table 1. It includes waves breaking within and after the experimental domain. Their propagation over a 1:30 bed was sampled using a dense array of resistance-type wave gauges, as discussed in Bellos et al. (2023). Acoustic Doppler Velocimeters measured kinematics at 36 locations along the flume, considering multiple depths. Results were ensemble-averaged across a regular wave train, to provide an assessment of experimental uncertainties.

Table 1. Test matrix.

Category	T [s]	H_0 [m]	$d_0/(gT^2)$	$H_0/(gT^2)*10^{-3}$
A	2	0.02 – 0.20	0.0127	0.5 – 5.1
B	1.25	0.04 – 0.20	0.0326	2.6 – 13.0
C	0.91	0.02 – 0.14	0.0615	2.5 – 17.2
D	0.67	0.02 – 0.08	0.1135	4.5 – 18.2
E	0.5	0.04	0.2039	16.3

RESULTS

The effects of shoaling on wave height, celerity and particle velocity are investigated and compared. This provides insight into the behaviour prior to and following wave breaking. For example, Figure 1 displays the evolution of wave heights in category B. These initially remain relatively constant, with some fluctuation due to reflection patterns, before increasing as the waves approach breaking. Breaking causes a steep immediate decline, which reduces in rate after a certain distance. The results predominantly agree with shoaling theory, though important constraints of the experimental setup are identified. In particular, as wave period reduces, the importance of frictional dissipation rises.

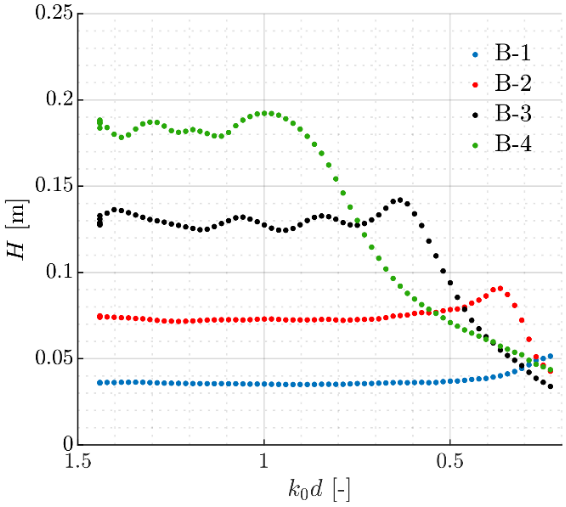

Figure 1. Spatial evolution of wave heights in category B.

Using the laboratory data, kinematics predictions are generated using Stokes and Cnoidal wave theory. Qualitative comparisons to the experimental results are created. Figure 2 contains the theoretical and measured velocity depth-profiles for a single wave case (H=0.4m, T=0.91s). Cnoidal theory is of variable accuracy, producing significant over- and underestimates, and reaching the limits of its theoretical validity where effective depth is large. In contrast, Stokes theory produces strong predictions in all non-breaking waves. Its accuracy falls only near to and after breaking.

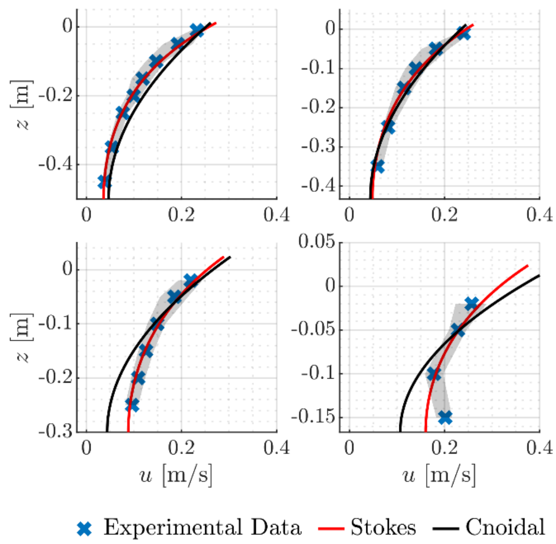

Figure 2. Experimental velocity depth profiles and 95% confidence intervals, alongside predictions of Stokes and Cnoidal theory. Wave Case C-3, at d=[0.5, 0.43, 0.3, 0.23]m.

In order to further assess the accuracy of Stokes theory, appropriate metrics are investigated. These include the Normalized Mean Average Percentage Error (nMAPE), as applied by Windt et al. (2021). The results are compared across all waves and locations to investigate the influence of water depth and wave properties. Figure 3 compares the nMAPE of the non-breaking wave cases, at all locations within the flume.

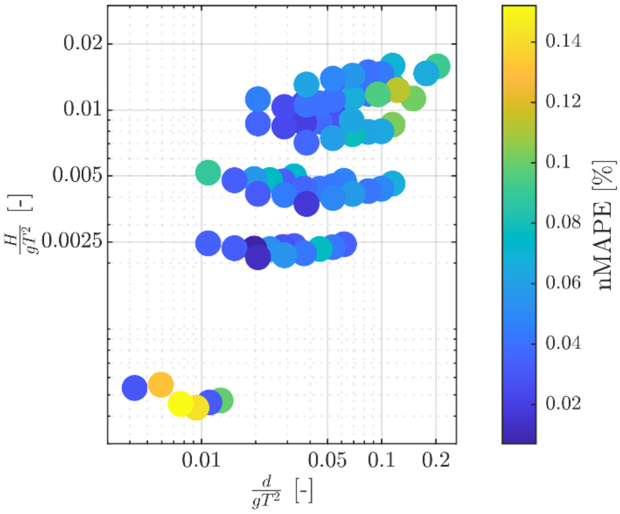

Figure 3. nMAPE of Stokes theory against wave effective depth and steepness, for all non-breaking waves.

Finally, the time-averaged behaviour of the surface elevation and particle kinematics are presented. These are discussed with reference to the theory of Stokes drift, and considering the results of previous studies.

REFERENCES

Bellos, V., Karmpadakis, I. & Swan, C. (2023). Spatial evolution of wave height and crest height distributions of waves propagating over sloping coastal bathymetry. Proc. 2nd International Conference on Design and Management of Port, Coastal and Offshore Work (DMPCO, 2023), Thessaloniki, Greece.

Swan, C. (1990). Wave kinematics within the crest to trough region. *Environmental Forces on Offshore Structures and their Prediction* 26, 45–60.

Windt, C., Untrau, A., Davidson, J., Ransley, E.J., Greaves, D.M., & Ringwood, J.V. (2021). Assessing the validity of regular wave theory in a short physical flume using particle image velocimetry. *Exp. Therm. Fluid Sci.* 121.

The Evolution of Steep Wavefields as they Propagate into Shallower Water

Spiliotopoulos G.[1] and Katsardi V.[1,*]

[1] Department of Civil Engineering, University of Thessaly, Volos Pedion Areos 38334, Greece

*corresponding author:
e-mail: vkatsardi@civ.uth.gr

INTRODUCTION

This paper describes field observations of limiting surface gravity waves recorded at the Natural Ocean Engineering Laboratory (NOEL) of the Mediterranea University of Reggio Calabria, Italy. The experiment focuses on the evolution of a sea state as it propagates from the deep to the shallowest boundary of intermediate waters. The purpose of this experiment is to measure a large number of sea states developing in a range of water depths. The goal of these measurements is to highlight the effects of peak period, wave steepness, and water depth on the wave profile and its statistical properties.

BACKGROUND

Previous laboratory studies (Katsardi et al., 2013) have shown that the characteristics and formation of limiting waves are critically dependent on the effective water depth, which reflects the peak period and local water depth. However, these were limited by the laboratory environment, whereas field conditions at the NOEL can address these weaknesses. The NOEL has been the site of a large number of field experiments, some of the results of which appear in the book by Boccotti (2014) and a variety of other publications. It is well known that the effects on the formation of large waves are reflected in the statistical properties of the wavefield, such as the wave crest and height distributions (Gibson and Swan, 2007) and the probability density functions (Fedele and Arena, 2010). While the nonlinearity is very significant, wave breaking mitigates its effects, resulting in a constraint on the wave height, which modifies the statistical properties of the wavefield (Karmpadakis and Swan, 2020).

EXPERIMENTAL SETUP

At NOEL, the governing wind field (both fetch and velocities), as well as the local bathymetric characteristics, allow field experiments to be conducted on a length scale of 1:30-1:50 compared to open-ocean experiments, and thus on a time scale of 1:5-1:7. The local bed slope is ≈1:10. Measurements were made using a set of 7 ultrasonic probes above the mean water level and 5 underwater pressure transducers, all supported by 4 separate steel columns. In this study, only the surface elevation data from the ultrasonic probes were used.

PROCESSING FIELD DATA

The time window chosen to be representative of a full-scale storm is 1h, corresponding to about 5-7h for scale factors of 1:30-50, while the underlying spectra were extracted using FFTs. The waves were analyzed using a zero up-crossing method to extract individual wave properties. The records selected here are the least noisy compared to those at the same depth to ensure reliable results. The measured surface height data are stored in individual 5-minute records. By extracting the H_s of each such record, we were able to assess and focus on periods of significant wavefield steepness on several occasions throughout the duration of the experiment. Herein we will examine a 1h record of significant wave activity and assess its characteristics. The record contains ≈1700 individual waves.

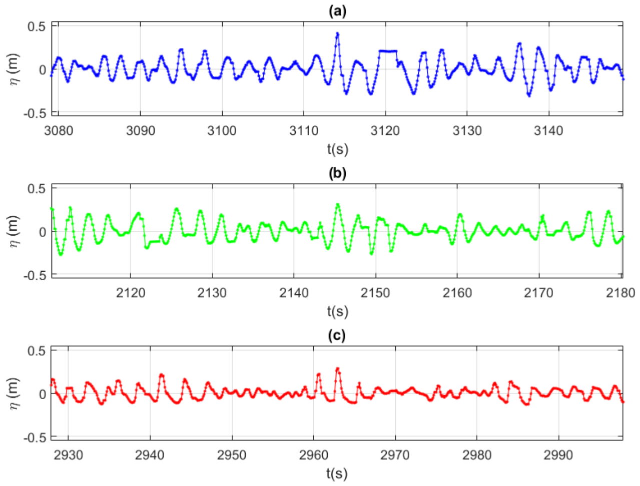

Figure 1. Wave profile close to H_{max}, a) d=3.80m - k_pd=2.16, b) d=1.76m - k_pd=1.18, c) d=0.45m - k_pd=0.57

WAVE PROFILE

Figure 1 shows the wave profile near the largest measured wave height, H_{max}, of each record. The wavefield is relatively steep (deep water steepness $H_{so}k_p/2$=0.106) propagating from effectively deep water to shallow water (2.16>k_pd>0.57). By analyzing the wave profile at different depths for this sea state, the different shapes of the largest waves are evident; at greater water depth the wavefield is relatively dispersed, while at the shallowest probe the wavefield is much less dispersed and the largest waves resemble a wave soliton.

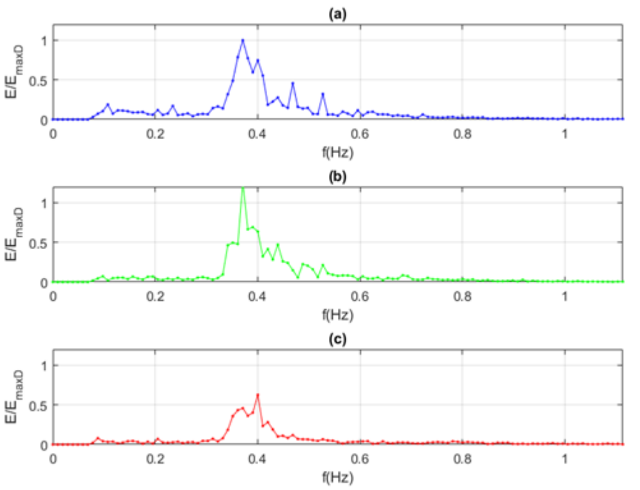

Figure 2. Energy density spectra (normalised with maximum of the deepest sensor) a) d=3.80m - k_pd=2.16, b) d=1.76m - k_pd=1.18, c) d=0.45m - k_pd=0.57

FREQUENCY SPECTRUM

The extracted power density spectra are shown in Figure 2. The spectrum is broad in deeper waters and becomes narrower in intermediate water depth. In shallower water the wave energy has dissipated due to wave breaking.

WAVE BREAKING

From Figure 3 we can see that in deeper water the wavefield does not contain many breaking waves, but in shallow water the wavefield is much closer to the breaking limit. In fact, some of the red dots representing the shallow record are above the limit of the Miche (1944) criterion. As the waves propagate into shallower water, they move even closer to the breaking limit, where the local parameters of each wave are compared to the established breaking limits. Sometimes a steeper sea state in deep water can cause more energy to be dissipated before the waves reach their more depth-limited state closer to the coast.

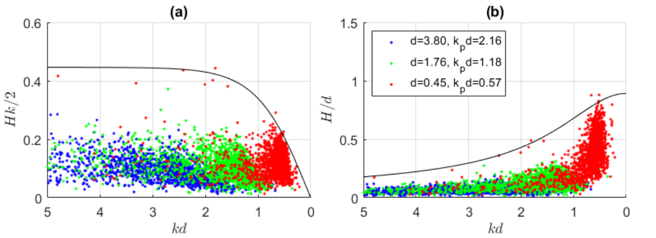

Figure 3. Variation of wave steepness ($Hk/2$) (a) and H/d per effective water depth (kd) (b) with Miche breaking criterion superimposed.

PROBABILITY OF EXCEEDENCE

In Figure 4, the wave steepness $Hk_p/2$, the H/d parameter, the H/H_s parameter, and the η_c/H_s parameter are plotted against their exceedance probability, Q, for the waves at each water depth level. In Figure 4a, there is an apparent increase in wave steepness with decreasing water depth, especially in the shallowest record. Also, the shallow water waves appear to have reached a height threshold due to wave breaking. This can be seen in Figure 4b where the H/d parameter reaches 0.85 in shallow water. In deeper water, H/d is small, reflecting a wave field that is not depth limited. In Figure 4c, the deep and intermediate water distributions are similar, with a slight increase in the H/H_s ratio for the intermediate depth, reflecting the small increase in wavefield steepness (Figure 4a). However, the shallower distribution has a different shape, with the H/H_s ratio being higher than deep for $Q > 1.5 * 10^{(-2)}$ and lower for $Q < 1.5 * 10^{(-2)}$ compared to the deep water distributions. This is due to the competing influence of the increase in both wave field steepness and wave breaking. Finally, Figure 4d (η_c/H_s) shows the gradual increase of the crest-trough asymmetry as we move from deep to shallow water, which is directly related to the increase of nonlinearity or wave steepness.

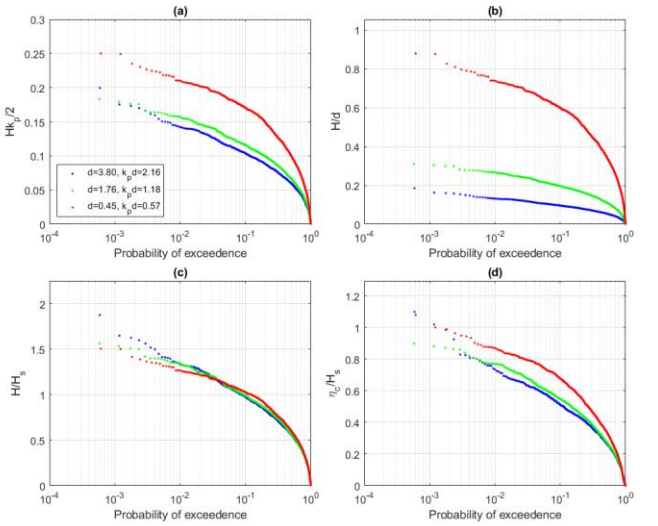

Figure 4. a) $Hk_p/2$, b) H/d, c) H/H_s and d) η_c/H_c plotted against their probability of exceedance.

CONCLUDING REMARKS

The results show the distinct change in the wave profile as steep waves propagate in shallower water while approaching their breaking limit, with a soliton-like behavior being characteristic of steep waves in shallower water. The reason for this transition is the change in the dispersive properties of the wavefield. Both wave steepness and breaking dominate the formation of the wave profile and the evolution of the wavefield, albeit in a competing manner.

ACKNOWLEDGEMENTS

Many thanks go to the staff of NOEL at the Mediterranea University of Reggio Calabria; Profs. Fiamma, Romolo, Malara and Arena, Dr Ruzzo and fellow PhD student Antonino Spano.

REFERENCES

Boccotti, P. (2014). Wave Mechanics and Wave Loads on Marine Structures. Elsevier.

Fedele, F., & Arena, F. (2010). Long-Term Statistics and Extreme Waves of Sea Storms. *J. Phys. Oceanogr.* 40(5), 1106–1117.

Gibson, R., & Swan, C. (2007). The evolution of large ocean waves: The role of local and rapid spectral changes. *Proc. R. Soc. Lond. A.* 463(2077), 21–48.

Karmpadakis, I. & Swan, C. (2020). On the Average Shape of the Largest Waves in Finite Water Depths. *J. Phys. Oceanogr.* 50(4), 1023–1043.

Katsardi, V., De Lutio, L., & Swan, C. (2013). An experimental study of large waves in intermediate and shallow water depths. Part I: Wave height and crest height statistics. *Coastal Eng.* 73, 43–57.

Miche, M. (1944) Mouvements ondulatoires de la mer en profondeur constante ou décroissante. *Ann. Ponts Chaussees.* 114(1), 131–164, 270–292, 369–406.

Spectral Wave Modelling Using Different Forms of 1st Order Quasi-Coherent Approximations of the General Transport Equation

Baltikas V.[1,*] and Krestenitis Y.[1]

[1] Laboratory of Maritime Engineering and Maritime Works, School of Civil Engineering, Aristotle University of Thessaloniki, GR-54124, Thessaloniki, Greece

*corresponding author:
e-mail: vmpaltik@civil.auth.gr

THEME OF RESEARCH

The present study is part of a wider research, that aims to implement and further develop the Quasi-Coherent (QC) spectral wave modelling approach (Smit et al., 2013). It directly follows the introduction of a Quasi-Coherent spectral wave model with the purpose of further validating the underlying theory and gaining more insight into the behavior of such a spectral wave model (Baltikas et al., 2023). Spectral wave models of this type can be developed using governing equations derived from different forms of the 1st order Quasi-Coherent approximation of a general transport equation. The present study demonstrates, that different variants of the 1st order Quasi-Coherent approximation should not be considered invariantly equivalent. Even though they can reproduce the theory's main findings, slight differences can be detected in the results they yield for the same test cases. Furthermore, under specific conditions found in the wave field and medium variations (bathymetry), some may satisfy the conditions of the 1st order Quasi-Coherent approximation more consistently, therefore, be in better agreement with the physics of the underlying theory.

METHODOLOGY (MODEL & DATA)

Two variants of the 1st order Quasi-Coherent approximation, were implemented in the numerical spectral wave model proposed by Baltikas & Krestenitis (2023). Subsequently, the model was used to perform numerical simulations of water waves propagating over a submerged elliptical shoal, following the experimental set-up of Vincent & Briggs (1989) and specifically the M2 Test Case of monochromatic, non-breaking waves. The first set of governing equations is based on the 1st order Quasi-Coherent approximation variant proposed and implemented in Smit et al. (2015b):

$$\partial_t W(\boldsymbol{k},\boldsymbol{x},t) + c_k \nabla_k W(\boldsymbol{k},\boldsymbol{x},t) + c_x \nabla_x W(\boldsymbol{k},\boldsymbol{x},t) = S_{qc} \tag{1}$$

where, $c_k = -\nabla_x \sigma(\boldsymbol{k},\boldsymbol{x}),\ c_x = \nabla_k \sigma(\boldsymbol{k},\boldsymbol{x})$ (2)

$$\sigma(\boldsymbol{k},\boldsymbol{x}) = \sqrt{g\boldsymbol{k}tanh\big(\boldsymbol{k}h(\boldsymbol{x})\big)} \tag{3}$$

$$S_{qc} = -i\int \Delta\hat{\Omega}^-(\boldsymbol{k},\boldsymbol{x},\boldsymbol{q})W(\boldsymbol{k}-\tfrac{1}{2}\boldsymbol{q},\boldsymbol{x},t)\,d\boldsymbol{q} + i\int \Delta\hat{\Omega}^+(\boldsymbol{k},\boldsymbol{x},\boldsymbol{q})W(\boldsymbol{k}+\tfrac{1}{2}\boldsymbol{q},\boldsymbol{x},t)\,d\boldsymbol{q} \tag{4}$$

$$\Delta\Omega^{\pm}(\boldsymbol{k},\boldsymbol{x},\boldsymbol{x}') = \Delta\sigma \pm \tfrac{i}{2}\partial_{\boldsymbol{k}}(\Delta\sigma)\widetilde{\boldsymbol{k}}\vec{\nabla}_x \tag{5}$$

$\Delta\hat{\Omega}^{\pm}$ represents the Fourier transform $\Delta\hat{\Omega}^{\pm} = \overline{F}_{x',q}\{\Delta\Omega\}$.

$\Delta\sigma$ is the difference between the local dispersion function value and its local plane approximation, multiplied by a Tukey Window Function, which approaches zero as $|\mathbf{x}'|$ approaches the maximum value $\xi_c = 2\pi/\Delta\mathbf{k}$, which essentially represents the de-correlation length of the wave field:

$$\Delta\sigma = TWF(\boldsymbol{x}')\big[\sigma(\boldsymbol{k},\boldsymbol{x}+\boldsymbol{x}') - \sigma(\boldsymbol{k},\boldsymbol{x}) - \boldsymbol{x}'\nabla_x\sigma|_{\boldsymbol{k},\boldsymbol{x}}\big] \tag{6}$$

The 2nd set of equations is derived from the 1st order Quasi-Coherent approximation variant prososed by Baltikas (2024):

$$\partial_t W(\boldsymbol{k},\boldsymbol{x},t) + c_x \nabla_x W(\boldsymbol{k},\boldsymbol{x},t) = S_{qc} \tag{7}$$

where, $c_x = a_k\widetilde{\boldsymbol{k}},\ \widetilde{\boldsymbol{k}} = \boldsymbol{k}/|\boldsymbol{k}|$ (8)

$$S_{qc} = -i\int \Delta\hat{\Omega}^-(\boldsymbol{k},\boldsymbol{x},\boldsymbol{q})W(\boldsymbol{k}-\tfrac{1}{2}\boldsymbol{q},\boldsymbol{x},t)\,d\boldsymbol{q} + i\int \Delta\hat{\Omega}^+(\boldsymbol{k},\boldsymbol{x},\boldsymbol{q})W(\boldsymbol{k}+\tfrac{1}{2}\boldsymbol{q},\boldsymbol{x},t)\,d\boldsymbol{q} \tag{9}$$

$$\Delta\Omega^{\pm}(\boldsymbol{k},\boldsymbol{x},\boldsymbol{x}') = \sigma(\boldsymbol{k},\boldsymbol{x}+\boldsymbol{x}') - \boldsymbol{a} \pm \tfrac{i}{2}\big[\sigma_{\boldsymbol{k}}(\boldsymbol{k},\boldsymbol{x}+\boldsymbol{x}') - \boldsymbol{a}_{\boldsymbol{k}}\widetilde{\boldsymbol{k}}\big]\nabla_{\boldsymbol{x}} \tag{10}$$

The coefficients α and α_k and consequently the spatial transport velocity c_x, as well as the pseudo-differential operator $\Delta\Omega^{\pm}$ are evaluated by the means of least squares plane approximations of $\sigma(\boldsymbol{k},\boldsymbol{x}+\boldsymbol{x}')$ and $\nabla_{\boldsymbol{k}}\sigma(\boldsymbol{k},\boldsymbol{x}+\boldsymbol{x}')$. The evaluation is performed within an area centered around $\boldsymbol{x}$ and with a radius of $\xi_c/2$ defined as:

$$\sigma^{lsq}(\boldsymbol{k},\boldsymbol{x},\boldsymbol{x}') = \boldsymbol{a} + \boldsymbol{b}\boldsymbol{x}',\ \sigma_{\boldsymbol{k}}^{lsq}(\boldsymbol{k},\boldsymbol{x},\boldsymbol{x}') = (\boldsymbol{a}_{\boldsymbol{k}} + \boldsymbol{b}_{\boldsymbol{k}}\boldsymbol{x}')\widetilde{\boldsymbol{k}} \tag{11}$$

and more specifically using the values $\sigma^{lsq}(\boldsymbol{k},\boldsymbol{x},\boldsymbol{x}')|_{\boldsymbol{x}'=0}$ and $\sigma_{\boldsymbol{k}}^{lsq}(\boldsymbol{k},\boldsymbol{x},\boldsymbol{x}')|_{\boldsymbol{x}'=0}$. It should be noted that W(**k**,**x**,t), which is being transported by Eqs (1-7), is not the regular wave variance density spectrum, but a more general Coupled Mode spectrum. It includes the complete 2nd order statistics of the wave field, accounting for its coherence and more accurate stochastic representation of wave interference. The CM spectrum is essentially a Wigner-Ville distribution, defined by the Fourier transform of the covariance function of the complex variable ζ. The real part is the free surface elevation, and its imaginary part is the Hilbert transform of the former.

$$W(\boldsymbol{k},\boldsymbol{x},t) = \tfrac{1}{2}\int \Gamma_{\zeta}(\boldsymbol{k},\boldsymbol{u},t)\exp[i\boldsymbol{u}\cdot\boldsymbol{x}]\,d\boldsymbol{u} = \tfrac{1}{2}\int\langle\hat{\zeta}(\boldsymbol{k}+{}^{\boldsymbol{u}}/_2,t)\hat{\zeta}^*(\boldsymbol{k}-{}^{\boldsymbol{u}}/_2,t)\rangle\exp[i\boldsymbol{u}\cdot\boldsymbol{x}]\,d\boldsymbol{u} \tag{12}$$

Both sets of equations can be obtained from equation

$$\partial_t W(\boldsymbol{k},\boldsymbol{x},t) = -i\int \hat{\Omega}\left(\boldsymbol{k}-\tfrac{i}{2}\nabla_x,\boldsymbol{q}\right)W\left(\boldsymbol{k}-\tfrac{1}{2}\boldsymbol{q},\boldsymbol{x},t\right)exp[i\boldsymbol{q}\cdot\boldsymbol{x}]\,d\boldsymbol{q} + \boldsymbol{C.C.} \tag{13}$$

where $\hat{\Omega}(\boldsymbol{k}\pm{}^{i}/_2\nabla_x,\boldsymbol{q}) = \left(\frac{\pm i}{2}\right)\frac{\partial\hat{\sigma}(\boldsymbol{k},\boldsymbol{q})}{\partial\boldsymbol{k}}\nabla_x$.

Eq. (14) is the 1st order Quasi-Coherent approximation of the general transport equation:

$$\partial_t W(\boldsymbol{k},\boldsymbol{x},t) = -i\big[\Omega(\boldsymbol{k}-{}^{i}/_2\nabla_x,\boldsymbol{x}+{}^{i}/_2\nabla_k) - \Omega(\boldsymbol{k}+{}^{i}/_2\nabla_x,\boldsymbol{x}-{}^{i}/_2\nabla_k)\big]W(\boldsymbol{k},\boldsymbol{x},t) \tag{14}$$

The CM spectrum is reduced to the variance density spectrum and Eq. (14) to the Radiative Transfer Equation of classic spectral wave models, when the wave field is quasi-homogeneous. This condition can be expressed by a parameter β, such that $\beta = \varepsilon/\delta = \xi_c/l_o/\varepsilon << 1$, where $\delta = \Delta k/k_o$ is a spectral width measurement parameter, $\varepsilon \ll 1$ a parameter associated with the slowly varying medium, k_0, l_0 a characteristic wave number and wave length of the wave field. When $\beta = O(1)$ the wave field becomes inhomogeneous, coherent effects become important and can only be accounted for by Eq.(13), its 1st order Quasi-Coherent approximation and the latter's variants, as shown in Smit & Janssen (2013); Smit et al. (2015a),(2015b); Baltikas & Krestenitis (2023), Baltikas (2024). Eqs (1) and (7) resemble the RTE, which is the backbone of classic spectral wave models, albeit augmented by the scattering term S_{qc}.

RESULTS

Results show that the QC modelling approach can reproduce wave interference patterns in the wave field, that RTE spectral wave models fail to resolve. This is the case for both sets of QC governing equations.

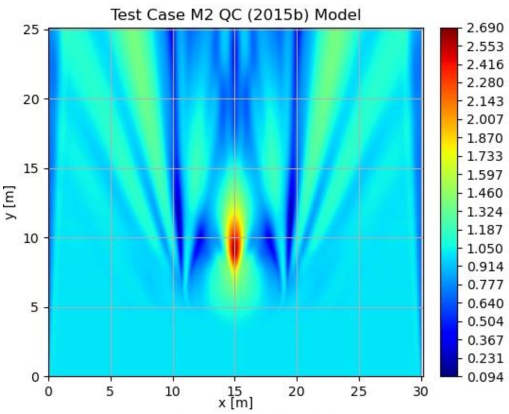

Figure 1. Normalized significant wave height. QC model results of Smit et al. (2015b).

However, simulations performed using the QC variant expressed by Eq. (7)-(10) yield more accurate results, which are closer to the experimental measurements of Vincent & Briggs (1989) and the simulations conducted by Smit & Janssen (2013) using Eq. (13). Moreover, local undershoots may appear when simulating the propagation of monochromatic or very narrow incident spectra using the QC variant of Eq. (1)-(5). Baltikas & Krestenitis (2023) have shown that these can be ameliorated by adjusting the smoothing effect of TWF in S_{qc} in combination with appropriate finite difference schemes. It must be noted that this problem does not arise when using the 2nd QC variant.

A closer examination of the derivation of the first QC variant reveals that Eq. (1) contains an internal contradiction. The transport velocities c_x and c_k are exposed from within the pseudo-differential operator $\hat{\Omega}\left(\boldsymbol{k} \pm \frac{i}{2}\nabla_{\boldsymbol{x}}, \boldsymbol{q}\right)$ of Eq. (14), under the assumption that the operator can be partially approximated by its version that corresponds to $\beta \ll 1$ (i.e. quasi-homogeneous wave field). Simultaneously, S_{qc} is derived from the remainder of $\hat{\Omega}$ that corresponds to $\beta = O(1)$ (i.e. inhomogeneous wave fields). This contradiction makes Eq. (1) partially inconsistent with the 1st order Quasi-Coherent approximation (Eq.14) of the general transport equation (Eq.15). On the other hand, the QC variant expressed by Eq. (7-10) is free of this contradiction, as its derivation employs an approximation of $\hat{\Omega}$ which assumes that it operates fully under the condition of $\beta = O(1)$ (Baltikas, 2024). That is also the case for other QC variants proposed in Smit et al. (2015a), and Akrish et al. (2020).

CONCLUSIONS

Variants of the 1st order QC approximation that resemble the classic RTE are easier to understand and implement than Eq.(14-15). However, such equations should be derived from Eq.(14) in a manner consistent with the underlying theory.

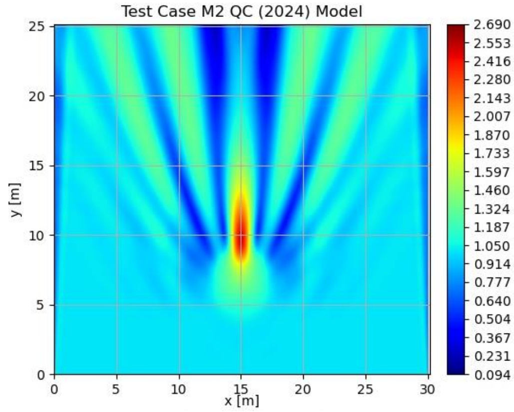

Figure 2. Normalized significant wave height. QC model results of Baltikas (2024).

Models based on the QC variant of Smit et al. (2015) contain an internal contradiction that makes partially inconsistent. They will be able to resolve the coherent interference patterns of waves induced by medium variations. However, in the limit of highly coherent and long-crested wave fields, they may give rise to local undershoots, that can be avoided with ad-hoc measures, while in general seem to be somewhat less accurate, than variants that do not share the same inconsistency regarding the QC theoretical approach. The latter, one of which is the one proposed in Baltikas (2024), perform without such problems under all conditions (i.e. from $\beta << 1$ to $\beta = O(1)$) producing results closer to experimental observations and the ones yielded by Eq.(13).

REFERENCES

Akrish, G., Smit, P., Zijlema, M., & Reniers, A. (2020). Modelling statistical wave interferences over shear currents. *J. Fluid Mech.* 891, A2.

Baltikas, V. & Krestenitis, Y. (2023). A Spectral Wave Model for Inhomogeneous Water Wave Fields Using the Quasi-Coherent Theory. *J Mar. Sci. Eng.* 11(11), 2066.

Baltikas, V. (2024). Investigation, extension, and application of the Quasi Coherent theory for the development of spectral wave models. Doctoral dissertation, AUTH, Thessaloniki.

Smit, P.B. & Janssen, T.T. (2013): The evolution of inhomogeneous wave statistics through a variable medium. *J. Phys. Oceanogr.* 43, 1741–1758.

Smit, P.B., Janssen, T., & Herbers, T. (2015a). Stochastic modelling of coherent wave fields over variable depth. *J. Phys. Oceanogr.* 45, 1139–1154.

Smit, P.B., Janssen, T., & Herbers, T. (2015b): Stochastic modelling of inhomogeneous ocean waves. *Ocean Model.* 96(1), 26–35.

Vincent, C.L. & Briggs, M.J. (1989): Refraction-diffraction of irregular waves over a mound. *J. Waterw. Port Coast. Ocean Eng.* 115(2), 269–284.

Real-Time Forecasting of Coastal Waves Using Neural Networks

Wright W.[1,*], Craske J.[1] and Karmpadakis I.[1]

[1] Department of Civil and Environmental Engineering, Imperial College London, SW7 2AZ, UK

*corresponding author:
e-mail: w.wright23@imperial.ac.uk

INTRODUCTION

Accurate real-time wave prediction is important for several different purposes. For example, wave-energy converters can optimise their energy production based on short-term forecasts (Li et al. 2012). The most basic model for prediction is linear wave theory (LWT). LWT decomposes the surface elevation into a superposition of harmonics of different wavelengths and frequencies, which evolve independently of each other. This can be generalised to include varying bathymetry, and some simple parametric breaking models, but fails to capture nonlinearities, such as interactions between the harmonics, which become important at high steepnesses.

Improvements upon LWT come from higher-order models, such as the choppy wave model (CWM) (Nouguier et al. 2009), second-order wave theory, or HOS (higher-order spectral) models. These sacrifice ease of computation in return for increased accuracy, but are still only approximations of the complex physics involved.

In recent years, there has been a surge of interest in using neural networks (NNs) to model all manner of wave-associated processes. While these don't usually offer any insights into the how the different physical processes work, the large number of parameters involved allows all of these processes to be encoded into the model, effectively 'learning' the dynamics. This study examines the accuracy of both convolutional neural networks (CNNs), and artificial neural networks (ANNs) for real-time wave prediction on a large set of laboratory data.

METHODOLOGY

For most of this study, the CNN being used is a variation of the U-Net model described by Ehlers et al. (2023), whilst the ANN being used is a simple MLP. Both networks have been implemented in Python using the Tensorflow package.

The networks are trained using the surface similarity parameter (SSP), which Wedler et al. (2022) proposed for this kind of data. It is defined as

$$\mathrm{SSP}(y_1, y_2) = \frac{\|y_1 - y_2\|}{\|y_1\| + \|y_2\|} \tag{1}$$

where $\|y\|^2 = y^T y$, with $\|\cdot\|$ denoting the standard ℓ^2-norm.

The laboratory data being analysed comes from Bellos et al. (2023). These consist of unidirectional waves propagating over 3 different uniform slopes, and being measured by an array of wave gauges along the length of the flume. We examine sea states generated from both Gaussian and JONSWAP spectra, with various peak periods and 6 different steepnesses.

For this work, an input time series (surface elevation) is taken from an initial gauge towards the start of the tank, and the NN models are used to predict the output time series at a gauge further down the tank. Each wave case has been run for at least 20 different seeds, providing ample data for use in both training and testing.

The length of the time series being predicted here is known as the predictability zone. This is the zone where neither fast- nor slow-moving waves observed outside of the initial time series have any significant effect at the prediction gauge.

Using linear theory, this zone spans up to around $4T_p$ into the future (roughly 50 seconds in field scale). The predictive ability of the networks will be compared against both LWT and the CWM, as these models are both easily run in real time.

DISCUSSION

Figure 1 depicts an example of the outputs from the NN models. In this case they are predicting waves of

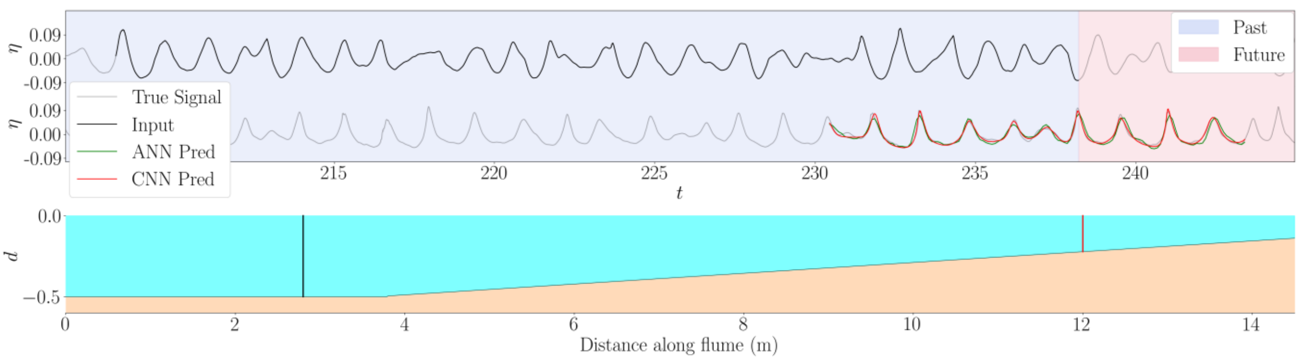

Figure 1. Prediction of surface elevation using the CNN model (red) and the ANN model (green). An input signal (black) is taken from the first gauge, and used to predict the surface elevation at a subsequent gauge. Gauge locations are shown in the bottom plot.

approximate steepness 0.05, propagating up a 1/15 slope. Here, steepness is defined as $s = 2\pi H_s/gT_p^2$, where H_s and T_p denote the significant wave height and peak period respectively.

This case is highly nonlinear, and includes a significant amount of wave breaking, thus falling far outside the range which LWT can accurately predict. As evidenced by the graph, the NN models are able to provide accurate predictions with a fast run time of about 50 milliseconds in total.

Figure 2 shows comparisons of the prediction error of the two NN models for a range of different spectra, with varying values of H_s and T_p, as well as varying shapes.

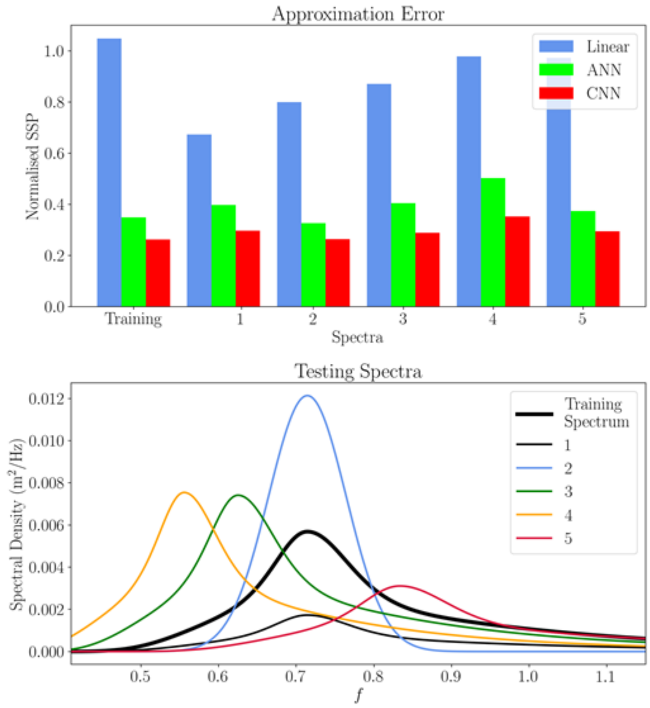

Figure 2. A comparison of the error metric for the NN models in estimating the time series produced by different initial spectra. The upper plot shows the different values of the error metric, and the lower plot demonstrates the different spectra on which they have been tested.

For the range of spectra shown, the error metric remains roughly constant for both networks. This demonstrates the ability of the models to generalise to out-of-distribution data - data generated from different spectra to the training spectrum (shown as the thick black line in figure 2). This property is of particular importance to field applications, where sea states are continuously changing - instead of having to train a network for each new sea state, one can make use of an already trained model.

REFERENCES

Li, G., Weiss, G., Mueller, M., Townley, S., & Belmont, M. R. (2012). Wave energy converter control by wave prediction and dynamic programming. *Renew. Energy* 48, 392–403

Nouguier, F., Guérin, C. A., & Chapron, B. (2009). "Choppy wave" model for nonlinear gravity waves. *J. Geophys. Res. Oceans* 114(C9).

Ehlers, S., Klein, M., Heinlein, A., Wedler, M., Desmars, N., Hoffmann, N., & Stender, M. (2023). Machine learning for phase-resolved reconstruction of nonlinear ocean wave surface elevations from sparse remote sensing data. *Ocean Eng.* 288, 116059

Wedler, M., Stender, M., Klein, M., Ehlers, S., & Hoffmann, N. (2022). Surface similarity parameter: A new machine learning loss metric for oscillatory spatio-temporal data. *Neural Netw.* 156, 123–134.

Bellos V., Swan C. & Karmpadakis I. (2023). Spatial evolution of wave height and crest height distributions of waves propagating over sloping coastal bathymetry. Proc. 2nd International Conference on Design and Management of Port, Coastal and Offshore Works (DMPCO, 2023), Thessaloniki, Greece.

Predicting Significant Wave Height Using Reservoir Computing

Karampas C.[1], Karambas T.[2,*]

[1] Department of Physics, Aristotle University of Thessaloniki, Greece,
[2] School of Civil Engineering, Aristotle University of Thessaloniki, Greece

*corresponding author:
e-mail: karambas@civil.auth.gr

INTRODUCTION

This study uses a neural network configuration referred to as reservoir computing to train a model that will be able to predict future significant wave height values. Reservoir Computing is a type of neural network called Recurrent Neural Network and is similar to LSTM (Thakur, 2018). RNN models are known for their capacity to have both long- and short-term memory and have shown successful results in time series analysis. We used a reservoir computing setup because training is significantly faster than other models, allowing us to optimize parameters like window size despite hardware limitations (Karampas et al., 2022).

METHODOLOGY -RESULTS

We used hourly data of significant wave height (150.000 values) and daily data of sea level (11.000 values) that we split in 60% of training data, 20% of validation data and 20% of test data. The window sizes (number of data the model trains on each iteration) were chosen based on which one gave the best results in the training set using a search space of 20-100 (step=20). In Figure 1 present methodology results are compared to COPERNICUS data (predictions 1 hour, 3 hours and 6 hours ahead respectively). The model predicts the wave height quite well.

After comparing results with the prediction of the training set and validation set and confirming that no overfitting has occurred, we present the metrics we achieved for each prediction of the validation set according to the target in table 1. Similarly, the methodology is applied to predict sea level variations 1 and 3 days ahead, using daily data. The results, together with COPERNICUS data are shown in Figure 2.

Had we access to more computational power we would work as such: Optimize window size regarding the results of the training set's predictions.

Table 1. RMSE and MAE.

Prediction Ahead	Window Size	RMSE	MAE
1h	20	0.056454	0.034949
3h	20	0.106349	0.066476
6h	40	0.174664	0.104114
12h	40	0.256616	0.152288
1 day	80	0.007245	0.005701
3 days	80	0.017090	0.013525
6 days	100	0.034558	0.026806

Optimize our reservoir's hyperparameters using both training and validation set as our new training set and confirm successful results in the last 20% of the data (the test set). Then since we have more data, we can optimize the training set's data quantity (number of observations used to train the model) and the model's prediction horizon (how long its predictions are accurate by using a larger set to check if the model's prediction capability decreases by reducing or growing the two data sets respectfully.

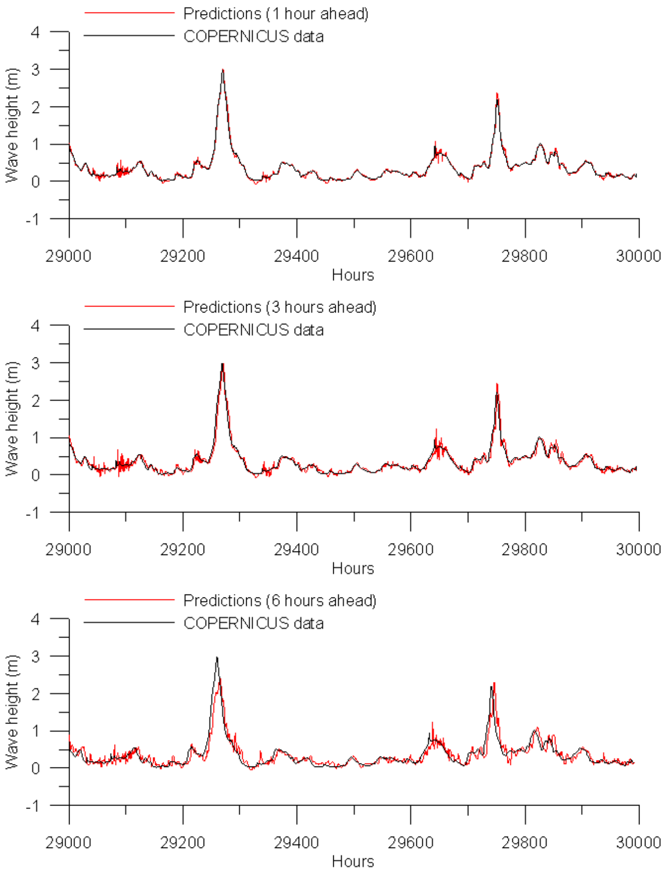

Figure 1. Comparisons between predictions and COPERNICUS data (Wave height).

RELATED WORKS AND COMPARISONS

Although mathematically, recurrent neural networks have been around since the 90's, only recently were people able to implement them on their home computer, a framework about how everything should be carried out hasn't been established which resulted in a lot of experimenting. Data preprocessing is mainly mentioned as mandatory but rarely are the dangers of its mishandling mentioned. Pushpam and Enio (2020) used the min-max preprocessing technique in their whole data set (both training and test sets) which means information from the future may have passed to previous data, and since it has been proven that min-max preprocessing achieves false successful results (Song et al., 2021) we did not use any preprocessing technique.

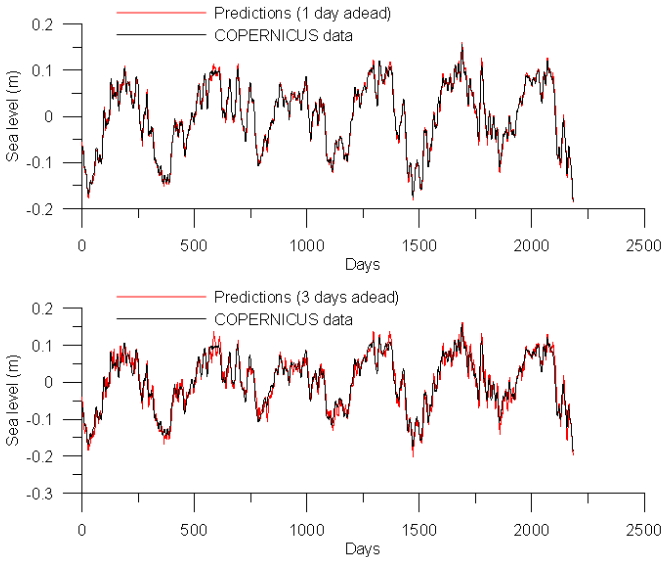

Figure 2. Comparisons between predictions and COPERNICUS data (Sea level).

CONCLUSION

In hopes of getting access to our institute's supercomputer we will be able to optimize both the data parameters like window size but also the networks parameters (hidden layer size, activation function, sparsity of neurons etc.) to achieve optimal results that will be used in real time predictions. These predictions could provide wave-energy production systems with information that would maximize their energy production. These predictions can also be used in marine traffic coordination so the algorithm of ships entering a harbor would be even more time efficient.

REFERENCES

Copernicus Marine Service. Available at: https://marine.copernicus.eu

Karampas K., I. P. Antoniades1, C.K. Volos and I.N. Stouboulos (2022) Forecasting Daily Foreign Exchange Market Trends Using Long-Short Term Memory Artificial Neural Network with Multiple Fourier Transform Pre-processing https://drive.google.com/file/d/1cCgzRKd5NDes9D09xRfbbDSbpB8zO4O3/view

Pushpam, M.M., & Enio, F. (2020). Forecasting Significant Wave Height using RNN-LSTM Models Proceedings of the International Conference on Intelligent Computing and Control Systems (ICICCS 2020) IEEE Xplore Part Number: CFP20K74-ART; ISBN: 978-1-7281-4876-2

Song, D., Chung Baek, A-D., & Kim, N. (2021). Forecasting Stock Market Indices Using Padding-Based Fourier Transform Denoising and Time Series Deep Learning Models, IEEE Access, 10.1109/ACCESS.2021.3086537.

Thakur, D. (2018). LSTM and its equations. www.medium.com

3D Simulation of Irregulars Waves in Harbor Using the Non-Hydrostatic Model SWASH

Koronakis T.[1], Karambas Th.[1,*]

[1] Laboratory of Maritime Engineering and Maritime works, Department of Civil Engineering, Aristotle University of Thessaloniki, Thessaloniki, Greece

*corresponding author:
e-mail: karambas@civil.auth.gr

ABSTRUCT

Ports are a very important coastal infrastructure in terms of the development of the respective area, as they facilitate navigation and maritime transportation. Their design is primarily based on the penetration of waves into the port and their interaction within it. The continuously changing motion of the waves, from the moment they enter the port, creates dynamic loads that must be considered in the design to ensure the smooth and safe operation of the port.

In the context of wave propagation, the computational program SWASH (**S**imulating **WA**ves till **SH**ore) was developed over the years by Delft University of Technology (TU Delft). This program is a model for the propagation of non-hydrostatic free surface flows, capable of performing realistic and accurate simulations in various and complex geometries, while utilizing wave interaction with porous structures. In this article, a three-dimensional simulation of wave interaction with porous structure, such as a harbor, is conducted.

NON-HYDROSTATIC MODEL - SWASH

The SWASH program is a computational tool designed to simulate non-hydrostatic, rotational free-surface flows and the propagation of phenomena in one, two, or even three dimensions. Based on the Navier-Stokes equations, the governing equations underlying the model are as follows:

$$\frac{\partial \zeta}{\partial t} + \frac{\partial hu}{\partial x} + \frac{\partial hv}{\partial y} = \emptyset \tag{1}$$

$$\frac{\partial u}{\partial t} + u\frac{\partial u}{\partial x} + v\frac{\partial u}{\partial y} + g\frac{\partial \zeta}{\partial x} + \frac{1}{h}\int_{-d}^{\zeta}\frac{\partial q}{\partial x}dz + c_f\frac{u\sqrt{u^2+v^2}}{h} = \frac{1}{h}\left(\frac{\partial h\tau_{xx}}{\partial x} + \frac{\partial h\tau_{xy}}{\partial y}\right) \tag{2}$$

$$\frac{\partial v}{\partial t} + u\frac{\partial v}{\partial x} + v\frac{\partial v}{\partial y} + g\frac{\partial \zeta}{\partial y} + \frac{1}{h}\int_{-d}^{\zeta}\frac{\partial q}{\partial y}dz + c_f\frac{u\sqrt{u^2+v^2}}{h} = \frac{1}{h}\left(\frac{\partial h\tau_{yx}}{\partial x} + \frac{\partial h\tau_{yy}}{\partial y}\right) \tag{3}$$

The parameter **t** represents time, while **x** and **y** are coordinates at the still water level, with the **z** axis directed upward. The variable **ζ(x, y, t)** denotes the surface elevation measured from the still water level, and **d(x, y)** represents the still water depth, or the bottom level measured downward. The total water depth, or depth **h**, is given by **h = ζ + d**, with **u(x, y, t)** and **v(x, y, t)** representing the depth-averaged flow velocities in the **x** and **y** directions, respectively. The term **q(x, y, z, t)** refers to the non-hydrostatic pressure, while **g** is the gravitational acceleration. Additionally, $\mathbf{c_f}$ is the dimensionless bottom friction coefficient, and $\boldsymbol{\tau_{xx}}$, $\boldsymbol{\tau_{xy}}$, $\boldsymbol{\tau_{yx}}$, and $\boldsymbol{\tau_{yy}}$ are the horizontal turbulent stress terms.

Equations [Eq.1], [Eq.2] and [Eq.3] constitute the shallow water equations and describe the non-hydrostatic free-surface flow at mean depth. To complete the system of equations in the computational domain, a weak reflection condition is applied at the open boundaries. The incoming non-harmonic waves are simulated by distributing their local velocity through the following [Eq.4]:

$$u_b(z,t) = \sum_{j=1}^{N} a_j\left[\omega_j\frac{\cosh k_j(z+d)}{\sinh k_j h} + \sqrt{\frac{g}{h}}\right]\cos(\omega_j t - a_j) - \sqrt{\frac{g}{h}}\zeta \tag{4}$$

where $\mathbf{k_j}$ and $\mathbf{a_j}$ are the wave number and the random wave phase of each frequency $\boldsymbol{\omega_j}$, respectively. Furthermore, the range of frequencies is defined through a step Δω (ω_j=Δω_j). The wave number and wave frequency are related through the dispersion equation of linear theory. Essentially, the velocity at a given depth can be calculated from the linear superposition of N harmonic waves, with amplitudes determined using the relationship $a_j = \sqrt{2E(\omega_j)\,\Delta\omega}$ for a given energy density spectrum.

A key role in the SWASH model is played by the dispersion equation. To approximate frequency dispersion, a scheme is applied for the vertical gradient of the non-hydrostatic pressure, combined with vertical discretization of the domain into layers down to the seabed. In the SWASH program, the linear dispersion equation is approximated using the Keller – Box scheme, which depends on the number of layers K into which the computational domain has been divided. The range of applications of the program, regarding the importance of the approximation of the linear dispersion equation in relation to the values of the dimensionless depth kd, particularly for primary waves, is illustrated in the table below.

Table 1. Range of application

K	Range	Error
1	kd ≤ 0,5	1%
1	kd ≤ 2,9	3%
2	kd ≤ 7,7	1%
3	kd ≤ 16,4	1%

SIMULATION PARAMETERS AND RESULTS

The simulation is conducted in an environment of 1000 x 1000[m^2] with a mean depth of 8[m]. At the western boundary, a JONSWAP energy density spectrum is applied with a peak period T_{peak} = 8[sec] and peak wave height H_{peak} = 2[m]. At the eastern boundary, a wave energy absorption layer is implemented to prevent reflections. Within this domain, a harbor basin with a depth identical to that of the domain has been placed. The simulations take into account porosity values for the core of the structure and its external protection. For porosity values **n < 0.1**, the structure is considered solid and acts as a vertical wall, while for values greater than 0.1, it allows a percentage of the waves to penetrate into the interior basin. For **n=0.45**, the structure is considered to be protected by an external layer of slopes. The results of these simulations are the water level and the significant wave height of the interaction between the waves and the harbor.

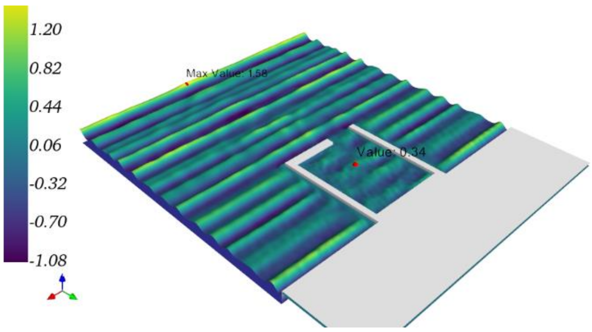

Figure 1. 3D-Water level with n = 0.05.

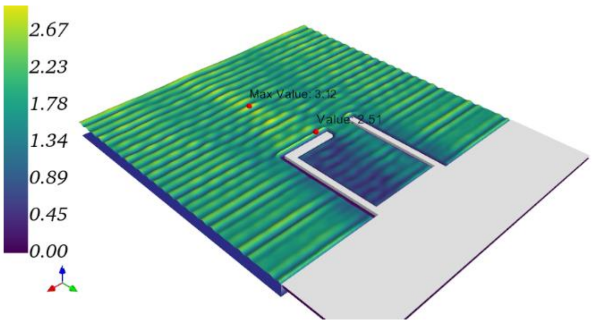

Figure 2. 3D-Hsignificant with n = 0.05.

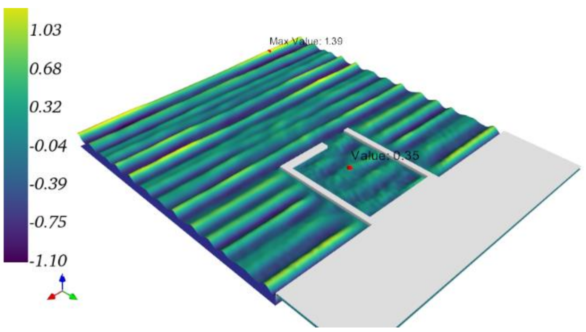

Figure 3. 3D-Water level with n = 0.45.

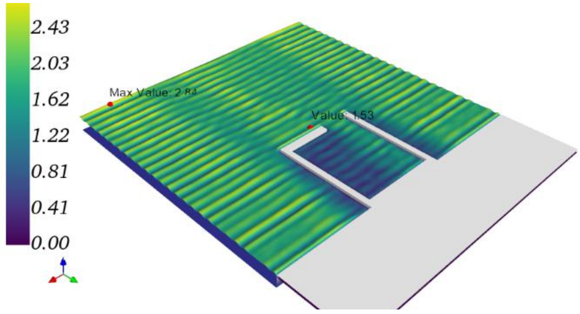

Figure 4. 3D-Hsignificant with n = 0.45.

Table 2. Results

	n = 0.05	**n = 0.45**
Water level (max)	1.58 m	1.39 m
Water level (value)	0.34 m	0.35 m
Hsignificant (max)	3.12 m	2.84 m
Hsignificant (value)	2.80 m	1.64 m

As shown in the results table (Table 2), the operation of the vertical front generates significant reflections on the face of the breakwater, and as a result, the significant wave height is greater. Regarding the water level, no noticeable difference in disturbances within the harbor is observed. The elevation of the water level appears to be slightly higher, which is logical since the breakwater allows wave inflow. These results are also illustrated in Figure 1, Figure 2, Figure 3 and Figure 4.

CONCLUSIONS

In conclusion, the SWASH model is capable of performing highly complex simulations with regard to the computational domain. Its main strength lies in its approach to solving the dispersion equation of wave velocity by discretizing the domain into K horizontal layers. This results in highly complex calculations, especially in shallow water domains or in fields with structural interactions where non-hydrostatic effects have a greater influence on the velocities of water particles. The application of this model can assist in the proper design of ports including porous flow through the breakwaters.

REFERENCES

Blayo, E., & Debreu, L. (2005). Revisiting open boundary conditions from the point of view of characteristic variables. *Ocean Model.* 9, 231–252.

Dailey, J.E. (1978). Stokes V Wave Computations in Deep Water. *J. Waterw. Port Coast. Ocean Div.* 104(WW4).

TEAM, S., n.d. SWASH USER MANUAL. SWASH version 10.01 ed. s.l.:s.n.

Vasarmidis, P., Stratigaki, V., Suzuki, T. & Zijlema, M. (2019). InternalWave Generation in a Non-Hydrostatic Wave Model. *Water* 11(986).

Vasarmidis, P., Stratigaki, V., Suzuki, T., Zijlema, M., & Troch, P. (2021). On the accuracy of internal wave generation method in a non-hydrostatic wave model to generate and absorb dispersive and directional waves. *Ocean Eng.* 219, 108303.

Hydrodynamic Forces on Sea-bed Structures: A Methodology Overview for South-Eastern Mediterranean Sea

Mylonas A.[1], Roupas I.[2,*], Memos C.[1]

[1] School of Civil Engineering, National Technical University of Athens, Zografos, 15780, Greece
[2] Department of Civil Engineering, Aristotle University of Thessaloniki, University Campus, Thessaloniki, 54 124, Greece

*corresponding author:
e-mail: roupas.yan@gmail.com

INTRODUCTION

Nowadays an increasing effort can be observed regarding energy transfer projects involving cables or conduits laid on the ocean floor over quite long distances. This activity is particularly noted in eastern Mediterranean basin. Therefore, it is imperative to study the hydrodynamics close to the sea bed to be able to evaluate the loading on the electric cables or other components of energy connection schemes.

SCOPE

The scope of this study is to present a methodology for evaluating the sea actions upon seabed structures taking into account: the influence of several hydrodynamic parameters; the impact on the design parameters due to climate change. To demonstrate the methodology, case studies will be presented here below, concerning real conditions in the eastern Mediterranean basin. Finally, insights will be given regarding the securing, against slipping and/or uplifting, of potential energy interconnections in the above area, in order to help engineers in optimizing their design.

METHODOLOGY APPLIED

General Considerations: In order to evaluate the actions upon the sea-bed structures considered herein, it is imperative to obtain the water kinematics at the area, especially their extreme values during the envisaged design life of the works.

Oceanic Circulation: The global movement of the planet's oceans provides a part of the total velocities at any considered site. To assess those, data from the Med MFC model were used. Results, including tidal currents, are for daily means and presently cover a period of around 35 years.

Local Contributions: a) *Wind-induced currents:* Relevant wind data from nearby meteo-stations were used. These can give the sea surface geostrophic velocity, CEM (2003). Following Ekman's theory, the current components at any depth in the open ocean can be obtained. In depths lower than the depth of frictional influence, a quadratic distribution of the velocity was used instead.

b) *Tsunamis:* Severe tsunamis or similar local processes of extreme intensity that could generate long waves are rare in eastern Mediterranean. However, for comparison reasons we estimate water velocities of tsunamis, assuming a surface superelevation characteristic for the site considered.

c) *Surface waves:* Satellite data were used for obtaining values of wave heights and periods of wind-generated waves (https://doi.org/10.25423/cmcc/medsea_multiyear_wav_006_012). The values cover a period of nearly 30 years. The most severe events during that period were accounted for extreme values analysis. The Weibull distribution was assumed for extrapolation of wave heights. The wave transformation from the given grid points to the site considered was evaluated through application of the SwanOne wave model.

Design Values: For the kinematics needed to calculate the hydrodynamic loading on the seabed structures, design values depend on the required reliability level. The procedure followed to derive a joint design value, involves the Gumbel-Hougaard copula and the correlation between the two actions.

Climate Change: Current climate trends can affect the parameters examined in this study. The direct impact of the above trends on our design parameters would be confined to marine growth and the met-ocean processes that drive seawater kinematics. Estimates of the climate change impact on the relevant kinematics at the locations considered, are based on Copernicus Climate Data Store, IPCC 2023 (Synthesis Report), and Makris et al. (2023). The adopted values averaged over the whole region studied are, for a reference period of the next 100 years: oceanic currents, increase by 14%; wind-induced currents, reduction by 12% of the return time; wind waves, 12% height increase.

APPLICATIONS

The above methodology was applied to two distinct structures, one light and one heavy. The environmental conditions tested were a semi-protected site of moderate depth and a site exposed to waves in shallow water, both in the Aegean. Also, cable stability was checked over a greater area of the basin.

Hydrodynamic Parameters: The parameters defined previously were evaluated including climate change for the two sites, at the following depths:
Site #1a (depth 38.3m); *Site #2a* (21.0m), for light structure.
Site #1b (depth 39.8m); *Site #2b* (22.8m), for heavy structure.

Hydrodynamic Actions: The above calculated values of hydrodynamic parameters can lead to the evaluation of actions upon objects placed on the seabed. Two such elements were studied: a light box cage protecting the electrode modules and a typical section of the electric cable itself. An additional parameter was considered, that of marine growth. This can severely alter the relevant design loading values, BS6349-1-2.

- **Protective Cage**: This structure had an orthogonal shape measuring 11.1m x 8.1m x 1.68m (height), and made of light material grid panels. The primary values used for the drag, inertia, and lift coefficients, in the open field, were based on current literature, e.g. Dean and Dalrymple (1991), DNV (2017). The resulting loads are:

Site #1a horizontal 5kN, uplift 1.5kN; *Site #2a* horizontal 60kN, uplift 18kN.
Sliding: A quick check of resistance against sliding leads to an underwater weight requirement for the cage of the order of 13kN and 150kN for sites #1a and #2a, respectively.
Vibrations: The possibility of vibrations developing on members of the cage can be ignored, because the natural frequency of the upper horizontal beams of the structure is an order of magnitude higher than that of surface waves.

- **Electricity cable**: A cylindrical cross section is assumed, with a diameter of 200mm and a weight of 150kg/m. The parameters defined previously were evaluated for *Site#1b* and *Site#2b*.

The primary values used in the applications for the drag, inertia, and lift coefficients, were determined through the recommended practice of DNV GL RP-F105 (2017). Results are as follows:
Site #1b: The most critical action comes from the combination of the general oceanic circulation with the wave action and the addition of the local wind-generated current. The total horizontal load was estimated to 0.01kN/m and the uplift to 0.0003kN/m.
Site #2b: The most critical action comes from the combination of wind waves with the local wind-generated current. The total horizontal load was estimated to 0.11kN/m and the uplift to 0.006kN/m.
Sliding: A quick check of resistance against sliding confirms that the weight of the electricity cable is enough to achieve stability at the aforementioned depths, without an external stabilization method.

Cable stability on a greater scale: To increase our insight on the parameters that affect the stability of the cable in open waters, the methodology was applied to multiple sites around Crete and offshore southwards, with depths ranging between 15m and 3.200m. Taking into account the prevailing wave conditions at the study area, we can deduce that the relationship between the oceanic circulation and the wind-wave particle velocity changes at around the -80m water mark. In shallower waters, the wind-wave induced particle velocities yield the most critical actions (Figure 1).

Figure 1. Spatial distribution of dominating hydrodynamic parameters.

DISCUSSION OF RESULTS

The comprehensive methodology applied in this study allows the identification of the critical hydrodynamic parameters upon which the design of seabed structures should be based. The presented results showed that it is advisable examining the full range of the said parameters instead of preselecting the "right" design criteria, based on local sea conditions. This is so since the associated amount of knowledge among the profession is still inadequate to support presumptive identification of those criteria. It can be seen from the applications given above that frequently the major interplay between hydrodynamic processes holds between oceanic circulation and wave-induced kinematics, governed by water depth. Such quantitative comparisons in terms of particle velocity can reveal that wind waves may be of primary importance in exposed sites of shallow or intermediate depths. There, anchoring of the structure onto the sea floor may be required, as showed in the previous applications. This depends obviously on the actual loading received by the structure, including hydrodynamic and actions of other origin. The former loading depends, as suggested by the results given above, on the shape of the structure considered; in this respect, the circular cylinder, commonly used in applications, offers a rather favourable shape. Also, the results show that the uplift forces should be taken into account, especially in light structures, where additional weight may be needed.

CONCLUDING REMARKS

Based on the above exposition, the following concluding remarks can be drawn:

(a) In order to address the hydrodynamic loading on seabed structures a comprehensive methodology should be applied, like the one presented herein, rather than an empirical approach.
(b) The effect of biofouling on the action values should be considered, especially in shallow and warm waters.
(c) The effect of flow induced vibrations can be negligible in the case of a protective cage, but should be considered in the case of a free spanning cable, especially in shallow waters, where the water particle frequency there can be comparable to the natural frequency of the cable.
(d) The approach presented here can also be applied to conduits of tubular shape sitting on the sea floor; in such cases hydrostatic actions should also be considered.
(e) In real life applications, loads due to processes of other origin, e.g. seismic excitations, should also be included.

The present study employs theories based on simplified assumptions. Thus, effects such as turbulence due to bed friction, upwelling in wind-generated flow, tidal contribution, interaction between the examined processes, etc. are not considered. Therefore, in design it is advisable to incorporate generous safety margins, especially in shallow water.

REFERENCES

Dean, R.G. & Dalrymple, R.A. (1991) Water Wave Mechanics for Engineers and Scientists, *Prentice-Hall Inc.*
DNV GL RP-F105 2017: Free spanning pipelines. Det Norske Veritas AS Codes and Standards.
Makris, Ch., Tolika, K., Baltikas, V., Velikou, K., & Krestenitis, Y. (2023). The impact of climate change on the storm surges of the Mediterranean Sea, *Ocean Model.* 181, 102149.
SwanOne User Manual V1.3 April 2018, TU Delft.
U.S. Army Corps of Engineers, Coastal Engineering Manual (CEM). Engineer Manual. Washington, D.C. (6 volumes).

Wave Loading on Slender Monopiles in the Vicinity of the Free Surface

Mao X.L.[1*], Ma L.[1] and Karmpadakis I.[1]

[1] Department of Civil & Environmental Engineering, Imperial College London, London, SW7 2AZ, UK

*corresponding author:
e-mail: xinlu-lucy.mao20@imperial.ac.uk

INTRODUCTION AND BACKGROUND

In recent years, due to increasing necessity to address climate change, there has been a shift towards more renewable energy generation methods, such as offshore wind. With the increasing adoption of offshore wind energy and, in particular, the deployment of floating offshore wind turbine (FOWT) designs, understanding wave loads near the free surface has become increasingly critical. While bottom-fixed structures experience total load as an integrated effect throughout the water column, floating structures are primarily influenced by the uppermost part of an incident wave, where nonlinear effects and uncertainties are most pronounced. The most commonly applied hydrodynamic loading model for the estimation of total incident wave loading on slender offshore structures is Morison's equation (Morison et al., 1960). The equation considers the total loading (f) as a sum of a drag term and an inertia term.

$$f \;=\; \frac{1}{2} C_d \,\rho\, D\, u \cdot |u| \;+\; C_m\, \rho\, \frac{\pi\, D^2}{4} \frac{\partial u}{\partial t} \qquad (1)$$

where C_d and C_m are the drag and inertia coefficients, respectively, D is the diameter, ρ is the fluid density and u is the fluid particle velocity normal to the structure.

Recent studies have suggested that Morison-type loading models do not consistently predict the wave loads on structures in the regions close to the wave crest when implementing design recommended coefficients (Vested et al., 2018, 2020; Wang et al., 2022). This study presents new experimental data specifically investigating the wave loads arising in the vicinity of the free surface.

METHODOLOGY

An experimental investigation has been conducted in the Long Wave Flume at the Imperial College London Hydrodynamics Laboratory. The experimental facility is 56.6m in length, 2.8m in width with nominal water depth 1.25m. Wave generation is achieved through a bottom-hinged flap-type paddle wavemaker. A slender cylindrical structure with 30mm outer diameter has been constructed, placed at a position 29.5m downstream from the wave paddles. The column is equipped with a single height-adjustable force measurement sensor, which allows for the local measurement of horizontal wave loading on a cylinder section of 20mm height. Force measurements are taken at 6 different elevations in the crest-to-trough zone. The measurements were conducted under wave conditions that reflect realistic design scenarios, including both non-breaking and breaking waves.

RESULTS

Comparison between measured loading and Morison's equation calculated loading using recommended design coefficients and the best possible representation of the underlying kinematics from a fully nonlinear Boundary Element Method (BEM) numerical wave simulation shows a consistent overestimation of the loading at elevations close to the free surface.

A re-calibration of the coefficients based on locally measured loading at different elevations has been done along with fully nonlinear BEM kinematics. Figure 1 shows the summary of the local drag coefficient in a number of breaking and non-breaking deterministic focused wave events as a function of the depth dependent Froude number (Fr_z), which can be defined as:

$$Fr_z \;=\; \frac{u_{max}(z)}{\sqrt{g z'}} \qquad (2)$$

where u is the maximum horizontal water particle velocity at z relative to still water level (SWL), g is the gravitational acceleration constant and z' is the relative distance to the free surface. C_d has also been normalised by $C_{d,av}$, which is the average local drag coefficient below SWL.

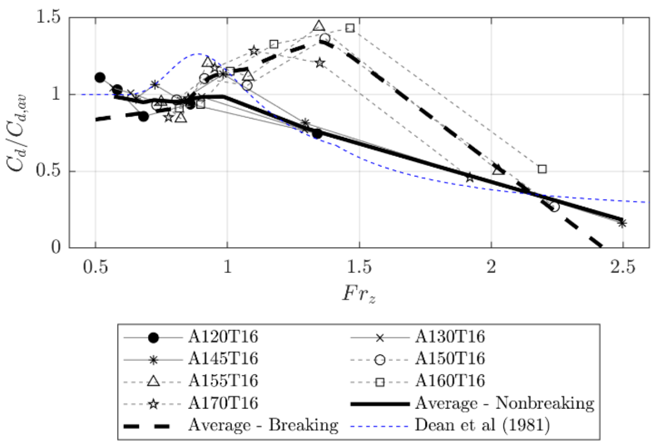

Figure 1. Variation of normalised local drag coefficient with depth-dependent Froude number and comparison to empirical trend identified by Dean et al. (1981)

In all cases, there is a decrease in the value of C_d at higher elevations, where the flow can be expected to be highly intermittent and disturbed by the presence of the structure. The loading clearly differs from that assumed by the Morison loading model, which assumes minimal disturbance to the flow and drag loading arising as a result of low-pressure wake formation in the downstream of the structure.

For wave cases with significant breaking, there is also an initial increase in the value of C_d at intermediate elevations above SWL. This may be attributed to a region of low pressure immediately beneath the free surface. Due to the flow around the column, a cavity region forms in the rear of the structure resulting in suction in the surrounding fluid. Overall, the results align well with the fitting of Dean et al. (1981), where wave breaking was not explicitly considered and therefore, the trends in breaking and non-breaking waves may have been averaged out. This may indicate a need to re-evaluate the suitability of using design coefficients calibrated for continually submerged conditions at higher elevations in the wave.

CONCLUSIONS

The results indicate both under- and over-predictions, confirming significant variations in the loads occurring close to the free surface. Importantly, a clear underlying trend was demonstrated in the applied loads, the latter dependent on proximity to the free surface and the onset of wave breaking. A refined, more physically representative set of loading coefficients was presented, obtained using the best possible fully nonlinear water particle kinematics. These coefficients were shown to be consistent with the key flow characteristics observed in the crest-to-trough region.

REFERENCES

Dean, R.G., Dalrymple R.A., & Hudspeth, R.T. (1981). Force Coefficients from Wave Project I and II Data Including Free Surface Effects. *Soc. Pet. Eng.* 21, 779–786.

Morison, J.R., Shaaf, S.A., & Johnson, J.W. (1950). The Force Exerted by Surface Waves on Piles. *J. Pet. Technol.* 2, 149–154.

Vested, M.H., Carstensen, S., & Christensen, E.D. (2018) Experimental Study of Wave Force Distribution on a Monopile Structure. Proc. 37th International Conference on Ocean, Offshore and Arctic Engineering (ASME 2018), Madrid, Spain.

Vested, M.H., Carstensen, S., & Christensen, E.D. (2020) Experimental Study of Wave Kinematics and Wave Load Distribution on a Vertical Circular Cylinder. *Coastal Eng.* 157, 103660.

Wang, L., Robertson, A., Jonkman, J., & Yu, Y.H. (2022) OC6 phase I: Improvements to the OpenFAST predictions of nonlinear, low-frequency responses of a floating offshore wind turbine platform. *Renew. Energy* 187, 282–301.

Focused Wave Impacts at a Rubble Mound Breakwater Crest Wall: A Physical Model Study

Sklia M.[1,2,*] and Hofland B.[1]

[1] TU Delft, Faculty Civil Engineering and Geosciences, Delft, the Netherlands
[2] Archirodon Group N.V., Engineering Department, Athens, Greece

*corresponding author
e-mail: m.sklia@archirodon.net

INTRODUCTION

Modelling and predicting the hydraulic response of coastal structures to wave loading – despite being studied since the 1940s, e.g. in Bagnold (1939), is still a matter that concerns coastal engineers today (e.g., Pedersen 1996, Hofland et al. 2010, Cuomo et al. 2010, Norgaard et al. 2013, Jacobsen et al. 2018, Chen et al. 2019 and van Gent et al. 2019). The numerical modelling tools to perform such predictions of wave loads have increased in number today, but physical models keep their position at the forefront of research.

Different types of wave signals can be forced in physical or numerical flumes so that the fluid-structure interaction can be studied, beyond the common practice of simulating random sea states comprising thousands of waves. Tromans et al. (1991) proposed an approach to model a deterministic extreme wave signal of transient nature derived from a predefined wave energy spectrum. In that sense, this extreme surface elevation is considered the most probable water level shape of an extreme wave in a given random wave field. Baldock et al. (1996) put the linear, two-dimensional focusing methodology of Tromans into a physical flume highlighting the importance of non-linear wave interactions for the formation of the extreme crest elevation that were neglected in the initially presented theory and compared measurements with first and second order solutions for the free surface elevation.

In recent studies, second order wave generation for focused wave groups was investigated (Mortimer et al. 2022). Several attempts have been made to use focused wave groups to generate extreme waves and consequently extreme hydraulic responses in terms of wave overtopping, runup and pressures on seawalls in recent years (Hofland et al. 2014, Whittaker et al. 2018). However, for the load on breakwater crest walls no such study is known to the authors. Therefore, in this study we treat the load on crest walls by extreme focused waves. These impacts are compared to the response under irregular seas with the same exceedance probability.

PHYSICAL MODEL TESTS

The experiments were performed in the wave flume of the Hydraulic Engineering Lab of TU Delft. The modelled structure was a rubble mound breakwater with seaward slope of 1:2, with basalt armour glued by epoxy to prevent displacements. At the armour crest, the thickness of the armour layer was 0.12 m, and the crest wall was placed with a retreat of 0.20 m. The crest wall, placed behind the armour, was 0.22 m high and 0.30 m wide (Figure 1). The test section was divided in two, i.e., two separate crest wall elements were placed in the flume, allowing for simultaneous measurements of pressures exerted on the crest wall and horizontal displacement. Pressure measurements were made by pressure sensors embedded in the fixed crest wall. The horizontal displacement of the loose crest wall element was measured with a proximity sensor placed behind the test section and was loaded with a critical weight depending on the hydraulic boundary conditions, to conduct a sliding failure test, with relevant criteria determined during the irregular wave tests (see de Vos 2024).

The foundation level of the crest wall under side was F_c = 0.03 m, relative to the still water level. The target focused wave height at the toe was set $H_{0.1\%}$ = 0.28 m of a Rayleigh distributed irregular sea state and target T_p = 2.53 s in a JONSWAP spectrum. The formulation of the extreme wave envelope followed the formulation of Tromans et al. (1991) with an additional wave celerity enhancement factor as implemented by Hofland et al. (2014). In the present tests (Figure 2) the wave celerity was enhanced by 2%. The gauged free surface at the toe of the structure is shown in Figure 3.

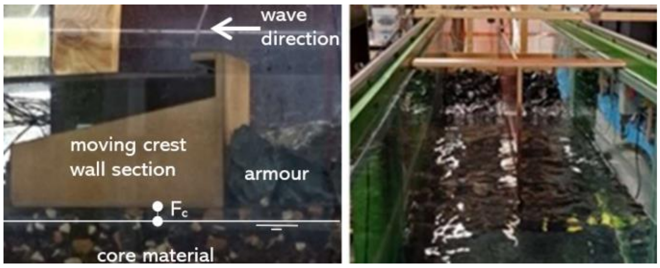

Figure 1. Side view of test section (left) and front view of split test sections (right).

Figure 2. Photo of a focused wave impact at the crest wall.

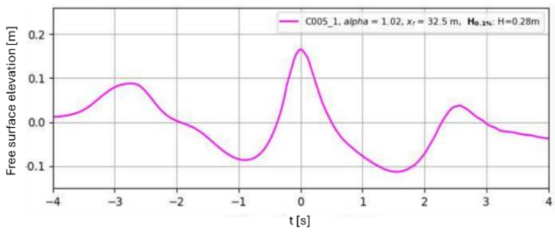

Figure 3. Focused wave signal measured at the toe, H=0.28 m, focal distance from the wave paddle, x_f =32.5 m.

RESULTS

The optimal focal distance to create a wave impact on the crest wall was found – via trial and error – to be $0.05\lambda_{op}$ seaward of the waterline on the armour layer. The wave impact during the forcing of a wave height equal to $H_{0.1\%}$ of a

Rayleigh distributed sea state, gauged near focus, at the toe of the structure, led the crest wall to a sliding failure, similarly to the failure that occurred during the forcing of an irregular sea state of a thousand waves with the same spectral characteristics (H_s = 0.15 m, T_p = 2.53 s). Comparison of the horizontal point pressure between irregular and focused wave test is illustrated in Figure 4, with measurements from the first sensor exposed to wave action – not sheltered by the armour (as indicated in Figure 4). The pressure shown corresponds to focused wave impact with a wave height H = 0.28 m, together with $p_{0.2\%}$, the second highest pressure recorded during the random wave test of a thousand waves with H_s = 0.15 m and T_p = 2.53 s and a critical weight of 20.2 kg including the weight of the crest wall.

Results from focused wave tests showed that the first pressure sensor located above the armour layer, thus more exposed to wave forces, consistently recorded higher pressures than the sensors placed at the sheltered part behind the armour. Regarding the uplift pressures (Figure 5), the first group of (lower) pressure peaks corresponds to the wave impacting the vertical crest wall. A second longer-duration group of peaks (Figure 5) corresponds to the pulsating load of the wave crest travelling through the breakwater core. Results confirmed the phenomenon as observed by De Vos (2024) that there is an increasing time lag between the upward and horizontal peak pressures, as well as the rapid decrease in the width of the uplift pressure distribution, with increasing foundation level.

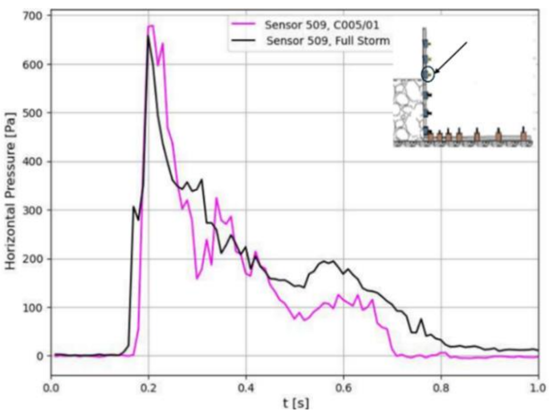

Figure 4. Horizontal pressure during focused wave impact (magenta) and full storm (black) for $p_{0.2\%}$.

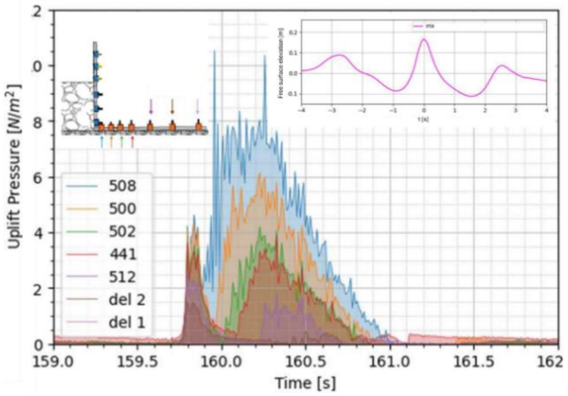

Figure 5. Uplift pressures on crest wall foundation during focused wave impact.

CONCLUSIONS AND RECOMMENDATIONS

Main results indicated that a focused wave signal with a wave height corresponding to the highest wave of a storm in an irregular sea state can drive the sliding failure of a crest wall relative to a rubble mound breakwater, with loads that are very similar to the extreme loads of an irregular sea state. This approach seems to be a promising tool that could potentially optimise the standard practice of costly simulations of random sea states comprising thousands of waves - needed to predict extreme hydraulic responses. Additional physical model experiments are recommended.

ACKNOWLEDGEMENTS

The author acknowledges the support of Archirodon N.V. in the paper presentation. Research was conducted at TU Delft.

REFERENCES

Bagnold, R.A. (1939). Interim Report on Wave-Pressure Research. ICE, 12 (7), 202–226.

Baldock, T.E., Swan, C., & Taylor, P.H. (1996). A laboratory study of non linear surface waves on water. *Phil. Trans. R. Soc. A.* 354, 649–676.

Chen, X., Hofland, B., Molenaar, W., Capel, A., & van Gent, M.R.A. (2019). Use of impulses to determine the reaction force of a hydraulic structure with an overhang due to wave impact, *Coastal Eng.* 147, 75–88.

Cuomo, G., Allsop, N.W. H., Takahashi, S., & Kortenhaus, A. (2010). Breaking wave loads at vertical seawalls and breakwaters. *Coastal Eng.* 57(4), 424–439.

De Vos, D. (2024). Experimental research into the stability of crown walls on a rubble mound breakwater, MSc Thesis, Delft University of Technology.

Hofland, B., Kaminski, M., & Wolters, G. (2010). Large Scale Wave Impacts on a Vertical Wall. Proc. ICCE 2018, Baltimore, USA.

Hofland, B., Wenneker, I., & van Steeg, P. (2014). Short Test Durations for Wave Overtopping Experiments. Proc. Coastlab 2014, Varna.

Mortimer, M., Calvert, R., Antonini, A., Greaves, D., Raby, A., & v.d. Bremer, T. (2023), Implications of second order wave generation for physical modelling of force and run-up on a vertical wall using wave groups, *Coastal Eng.* 180, 104259.

Nørgaard, J., Andersen, T.L., & Burcharth, H.F. (2013). Wave loads on rubble mound breakwaters crown walls in deep and shallow water wave conditions. *Coastal Eng.* 80, 137–147.

Pedersen, J., (1996) Wave forces and overtopping on crown walls of rubble mound breakwaters: an experimental study. PhD Thesis, Aalborg University, Denmark.

Tromans, P.S., Anaturk, A.R., & Hagemeijer, P. (1991). A new model for the kinematics of large ocean waves application as a design wave. Proc. ISOPE, Edinburgh.

Van Gent, M.R.A., & van der Werf, I.M. (2019). Influence of oblique wave attack on wave overtopping and forces on rubble mound breakwater crest walls. *Coastal Eng.* 151, 78–96.

Whittaker, C.N., Fitzgerald, C.J., Raby, A.C., Taylor, P.H., & Borthwick, A.G.L. (2018). Extreme coastal responses using focused wave groups: Overtopping and horizontal forces exerted on an inclined seawall, *Coastal Eng.* 140, 292–305.

Multimodal Machine Learning Approaches for Accurate Wave Overtopping Discharge Predictions

Sotireli Z.[1,*], Karambas T.[1]

[1] School of Civil Engineering, Aristotle University of Thessaloniki, Greece

*corresponding author:
e-mail: zsotire@civil.auth.gr

INTRODUCTION

Wave overtopping poses significant risks to coastal structures, requiring precise prediction methods for effective design and management. Traditional approaches like empirical formulas and numerical simulations, though useful, have limitations in accuracy and computational efficiency (Meer, 2009). Machine Learning (ML) techniques, such as Convolutional Neural Networks (CNNs) and Long Short-Term Memory Networks (LSTMs), address these challenges by leveraging large datasets and modeling nonlinear relationships. This study explores advanced ML models to predict wave overtopping discharge accurately using the EurOtop database.

DATA

This study utilized the EurOtop database, a global resource containing over 10,000 tests on wave overtopping discharge across various coastal structures. A filtered subset of 8,176 tests was selected by excluding unreliable records (e.g., RF=4, CF=4, q=0) using a weight factor WF = (4 - RF) · (4 - CF), which prioritized reliable and simpler configurations.

The dataset included three hydraulic parameters (e.g., wave steepness, relative water depth) and eleven structural parameters (e.g., relative crest freeboard, relative berm width), all normalized into dimensionless forms to ensure consistency across scales and applicability to real-world conditions (Formentin, 2017; Zanuttigh, 2016). To prepare the wave overtopping discharge (q) for training, it was normalized as:

$$q_s = \frac{\log_{10}(q_{ad}) - \min[\log_{10}(q_{ad})]}{|max[\log_{10}(q_{ad})] - min[\log_{10}(q_{ad})]|}, \qquad (1)$$

where q_{ad}, the dimensionless wave discharge, is defined as:

$$q_{ad} = \frac{q}{\sqrt{gH_{m0,t}^3}}, \qquad (2)$$

with g = 9.8 m/s². This normalization confined q_s to a range of 0–1, minimizing errors caused by scale differences and ensuring robust model performance.

METHODS

This study employed three advanced machine learning techniques —DNNs, CNNs and LSTMs— to predict wave overtopping discharge q_s by integrating hydraulic, structural, and environmental parameters. DNNs served as a baseline regression model (Nielsen, 2015). The architecture included an input layer, multiple hidden layers, and an output layer. Hidden layers were configured dynamically to capture hierarchical relationships. Each neuron in a hidden layer computed a weighted sum of its inputs:

$$z = \sum_i w_i x_i + b, \qquad (3)$$

where w_i are the weights, x_i are the inputs, and b is the bias term. Activation functions introduced non-linearity:

- RELU: $f(z) = \max(0, z)$ (4)
- Tanh: $\tanh(z) = \frac{2}{1+e^{-2z}} - 1$ (5)
- Sigmoid: $\sigma(z) = \frac{1}{1+e^{-z}}$ (6)

To prevent overfitting, dropout layers randomly deactivated neurons during training. The output layer consisted of a single neuron, and the mean squared error (MSE) was used as the loss function:

$$MSE = \frac{1}{N}\sum_{I=1}^{N}(y_i - \hat{y}_i)^2 \qquad (7)$$

CNNs extracted spatial features from the data using convolutional layers (Heaton, 2018; O'Shea, 2015). The convolution operation applied filters to input data to detect patterns:

$$x^{(t)}[t] = \sum_{\tau=0}^{T} w[\tau] x^{(l-1)}[t - \tau + \varphi] + b[t] \qquad (8)$$

where $w[\tau]$ represents the filter coefficients, $b[t]$ is the bias term, *t* is the input index, and ϕ denotes the shift. Residual connections simplified optimization and improved gradient flow by bypassing transformations:

$$y^{(l)} = F\left(x^{(l-1)}, W\right) + x^{(l-1)} \qquad (9)$$

where $F\left(x^{(l-1)}, W\right)$ represents the transformation applied by the block with learnable parameters W, and $y^{(l)}$ is the output of the residual connection. Attention mechanisms (Niu, 2021) assigned weights a_i to emphasize critical features:

$$a_i = \frac{\exp(e_i)}{\sum_j \exp(e_j)} \qquad (10)$$

where e_i represents the score assigned to feature *i*. Max pooling reduced the dimensions of feature maps:

$$y[i,j] = max_{(m,n)\epsilon W_{i,j}} x[m,n] \qquad (11)$$

where W_{ij} represents the window centered at position *(i, j)* in the input tensor x. LSTMs modeled temporal dependencies through memory cells and gates (Hafner, 2017). The input gate determined how much new information was added to the memory cell:

$$i_t = \sigma(W_i \cdot [h_{t-1}, x_t] + b_i) \qquad (12)$$
$$\widetilde{C}_t = tanh(W_C \cdot [h_{t-1}, x_t] + b_C) \qquad (13)$$

where W_i and b_i are the weights and biases for the input gate, $\widetilde{C}_t$ is the candidate cell state, representing the new information proposed to be added.

The forget gate controlled which parts of the previous cell state to retain:

$$f_t = \sigma\left(W_f \cdot [h_{t-1}, x_t] + b_f\right) \qquad (14)$$

where σ is the sigmoid activation function. The cell state was updated by combining the retained and new information:

$$C_t = f_t * C_{t-1} + i_t * \widetilde{C}_t \tag{15}$$

where ∗ represents element-wise multiplication. Finally, the output gate generated the hidden state:

$$o_t = \sigma(W_o \cdot [h_{t-1}, x_t] + b_o) \tag{16}$$
$$h_t = o_t * \tanh(C_t) \tag{17}$$

where W_o and b_o are the weights and biases for the output gate and h_t is the final hidden state at timestep *t*, modulated by the output gate and the transformed cell state. An attention mechanism improved LSTM performance by dynamically weighting important time steps.

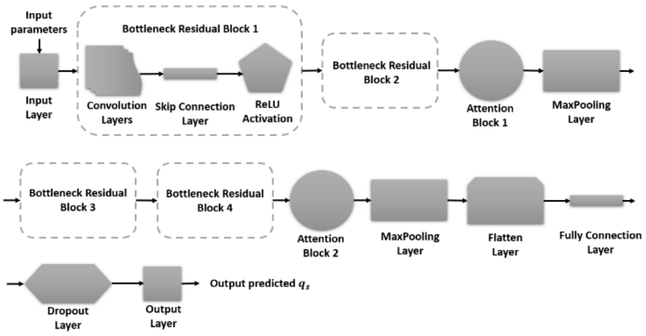

Figure 1. The proposed CNN architecture.

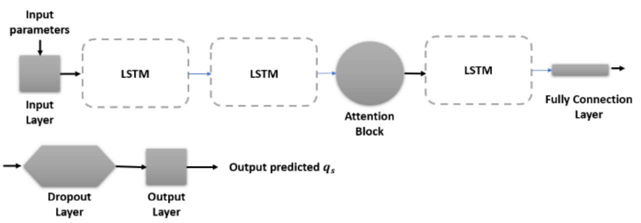

Figure 2. The proposed LSTM architecture.

RESULTS AND DISCUSSION

Models were trained using specified configurations for up to 5,000 epochs, with early stopping to prevent overfitting. The best model was saved based on validation performance. Implemented in Python with TensorFlow, the training used an 80/20 data split. Performance was evaluated using RMSE, R^2, and SI metrics.

CNNs effectively capture spatial features, and their performance improves significantly with attention mechanisms, as shown by an increase in R^2 from 0.7654 to 0.8434. However, they are less adept at modeling temporal dependencies compared to LSTMs. LSTMs consistently outperformed other models due to their ability to model sequential dependencies in time-series data, with the LSTM with attention achieving the best results (lowest RMSE of 0.0622 and highest R^2 of 0.8693) using the following parameters: 93 layers/units, 136 dense units, 0.154 dropout, 0.0014 learning rate, and a batch size of 16.

Attention mechanisms enhanced both CNNs and LSTMs by focusing on the most relevant features or time steps, improving predictive accuracy and reducing noise. Notably, the LSTM with attention showed incremental improvements over the standard LSTM, demonstrating its value.

Overall, DNNs are simple but struggle with complex spatiotemporal data. CNNs excel at capturing spatial patterns, while attention mechanisms further enhance performance. LSTMs, especially with attention, prove most effective for time-series forecasting.

Table 1. Performance Metrics for Machine Learning Models.

Model	RMSE	R^2	SI
DNN	0.1017	0.6509	0.1731
CNN w/attention	0.0681	0.8434	0.1160
CNN w/o attention	0.0834	0.7654	0.1419
LSTM w/attention	0.0622	0.8693	0.1059
CNN w/attention	0.0649	0.8580	0.1104

CONCLUSION

This paper presents advanced machine learning models, including CNNs and LSTMs, for accurate wave overtopping discharge prediction across diverse coastal structures and wave conditions. Architectural innovations like bottleneck residual blocks and attention mechanisms enhance feature extraction and sequence prioritization. Bayesian optimization and bootstrap resampling improve model robustness. The LSTM with attention achieved the highest accuracy, outperforming traditional methods in RMSE, R^2, and SI metrics. Additionally, this study lays the groundwork for a Unity-based real-time prediction tool for coastal engineers, aiding in the design and management of resilient coastal defenses.

ACKNOWLEDGEMENTS

The financial support of the Special Account for Research Funds of the Aristotle University of Thessaloniki is acknowledged.

REFERENCES

Formentin, S.M., Zanuttigh, B., & Meer, J.W. van der. (2017). A neural network tool for predicting wave reflection, overtopping, and transmission. *Coast. Eng. J.* 59(1), 1750006–1.

Hafner, D. (2017). Tips for training recurrent neural networks. Blog post.

Heaton, J. (2018). Ian Goodfellow, Yoshua Bengio, and Aaron Courville: Deep learning: The MIT Press, 2016, 800 pp. Genet. Program. Evolvable Mach. 19(1), 305–307.

Meer, J.W. van der, Verhaeghe, H., & Steendam, G.J. (2009). The new wave overtopping database for coastal structures. *Coastal Eng.* 56(2), 108–120.

Nielsen, M.A. (2015). Neural networks and deep learning, vol. 25, Determination Press, San Francisco, CA.

Niu, Z., Zhong, G., & Yu, H. (2021). A review on the attention mechanism of deep learning. *Neurocomputing* 452, 48–62.

O'Shea, K. (2015). An introduction to convolutional neural networks. arXiv preprint arXiv:1511.08458.

Zanuttigh, B., Formentin, S.M., & Meer, J.W. van der. (2016). Prediction of extreme and tolerable wave overtopping discharges through an advanced neural network. *Ocean Eng.* 127, 7–22.

Turbulence in Submerged Breakwaters under Regular and Irregular Surface Waves

Roupas I.[1], Repousis E.[2,*], and Memos C.[2]

[1] Department of Civil Engineering, Aristotle University of Thessaloniki, University Campus, PC 54 124 Thessaloniki, Greece
[2] School of Civil Engineering, National Technical University of Athens, Zografos, 15780, Greece

*corresponding author:
e-mail: elpirep@hotmail.com

INTRODUCTION AND SCOPE

In the realm of eco-hydraulic considerations, as applied to coastal structures, submerged detached breakwaters have become, under certain constraints, a shore protection alternative to their emerged counterparts. This is due to their capacity to allow for increased water renewal to their lee, safeguard an improved aesthetic value of the landscape, occupy smaller seabed area, when compared to traditional breakwaters. In addition to those environmental benefits, it has been observed that especially rubble mound submerged permeable breakwaters (SPBs) may function similarly to natural reefs in attracting marine life. The response of marine organisms to the presence of SPBs has not yet been investigated in-depth. However, hydrodynamic parameters as particle velocities and pore pressures are known to be significant factors in supporting marine life within and around these bars, in terms of, for example, distribution-species biodiversity and abundance (Siddon & Witman 2003). Acquiring information on the hydrodynamic field, including maximum wave-induced pore pressures, is important to assess SPBs' ecological potential (Kontaxi & Memos 2005, Moschella et al. 2005). Such an assessment may be different for each species considered but at this point it can be argued that water kinematics are the key hydraulic factors governing marine habitation levels (Hammond & Griffiths 2004). In addition to the mean values of those parameters, extreme ones are equally important in governing the said levels. The present paper deals with the latter variable mentioned, namely the turbulence related to particle velocities and pressures in SPBs due to the presence of regular and irregular waves, in terms of Turbulent Kinetic Energy (TKE) and Reynolds stresses. Experimental measurements were used for quantifying the turbulence levels inside a series of SPBs physical models. Finally, the correlation is provided of these quantities with the associated wave transmission coefficient K_t and wave breaking mode, in such a way that a complete framework for eco-technical design of SPBs be readily available.

EXISTING KNOWLEDGE

Although several studies on processes around submerged breakwaters can be found in the literature, the kinematics inside a SPB is a field of relatively less research. Regarding particle velocities and pressure in such structures due to regular waves results can be found in Metallinos and Memos (2012) and Metallinos et al. (2014). Both studies dealt with mean values of the variables involved. Perturbations around those mean values were quantified in Repousis et al. (2023), again for regular waves. Additionally, most numerical models deal with mean quantities, due to the complexity of the phenomenon that makes numerical simulation a very consuming undertaking. Models predicting the hydrodynamic field under wave propagation inside a SPB have been proposed in terms of mean values by Lara et al. (2006), Chan et al. (2007), Metallinos et al. (2014). Systematic research on porous flow through rubble mounds, including measurements of velocity and its turbulent component for oscillatory streaming flow conditions, yielded a model proposed by Van Gent (1995). However, in that work the porous models were restrained into a U-tube channel and turbulence produced should be considered as restricted to smaller scales as compared to an SPB physical model under wave action. In the following, turbulence will be evaluated in terms of TKE and Reynolds stresses induced by regular and irregular wave trains interacting with submerged permeable breakwaters.

METHODOLOGY

Within this work, the hydrodynamic field inside SPBs under regular and irregular waves was studied through experimental data of (i) orbital velocities' time series, in two and three dimensions, developing inside physical SPB models, focusing on turbulence levels and (ii) the hydrodynamic pressure component evolving inside these SPB models, also including fluctuation levels. To this end laboratory measurements were taken in the Laboratory of Fluid Mechanics of TU Delft. The data obtained were analysed and processed, by constructing velocity spectra where the inertial range can be detected with application of the reference Kolmogorov slope. Thus, the turbulent content can be calculated in terms of its intensity, TKE, and Reynolds stresses. The above specific tasks were implemented for both regular and irregular wavetrains.

The hydraulic experiments associated with the present study were conducted in a wave flume of 42m length, 0.8m width and 1.0m height, equipped with a piston type wave generator, able to produce both regular and irregular waves. Two physical models of submerged breakwaters of uniform natural stones, with porosity close to 0.4 were made; their crest width (B) varied from around $4d_{n50}$ to $6d_{n50}$, namely SPB1 with d_{n50} around 0.12m and B = 0.40m and SPB2 with d_{n50} around 0.12m and respective B = 0.65m. Testing scale was around 1:10 following Froude scaling similarity and the submerged bars were designed as statically stable. Both structures were assessed for regular and irregular waves of incoming wave height (H_i) ranging from 0.06m to 0.23m and peak wave period (T_p) from 1.0s to 2.5s. As for the hydrodynamic field around SPBs, to be able to provide additional data to the measurements for a more inclusive study, a weakly-nonlinear Boussinesq-type model with improved linear dispersion characteristics (Madsen and Sørensen 1992) was used to describe the wave motion in the fluid regions outside the breakwater. In the structural region the between model incorporates two extra terms accounting for the interaction the said motion and the flow within the rubble mound (Avgeris et al. 2004). This model was executed in conjunction with a depth-averaged Darcy-Forchheimer momentum equation describing the flow inside the porous medium. The one-dimensional form used assumes that the local wavelength is much higher than the dimensions of the structure, i.e. it reduces to the so-called nonlinear long-wave equation for porous medium. Finally, to simulate the depth-induced wave breaking, the governing equations of the core model were enriched by a simple eddy viscosity-type term. Finally, a relationship was established between representative variables of turbulence and the technical efficiency of the structure denoted by K_t. Thus the correlation between ecological and hydraulic characteristics can be obtained for each case and support a sustainable design of SPBs.

PHYSICAL MODELLING RESULTS

The experimental data gathered were filtered (Goring & Nikora, 2002) and turbulent statistics along with mean values for orbital velocities and hydrodynamic pressures were assorted. Specifically, the power spectrum was computed to define the inertial range (frequency range between f_1 and f_2 in Figure 1) where the Kolmogorov power law can apply and the so-called intermittence and viscous ranges (higher frequencies than f_2 in figure). The frequency threshold of the inertial range f_1 was defined for each wave scenario at various locations in the sea- and lee-side of the structure, in order to estimate the average amplitude of the components of turbulent fluctuations (*u', v', w'*), utilizing the amplitude spectra of *u*, *v*, *w* velocity components, that were also computed. Additionally, a reference spectrum was computed from the surface elevation measurements, by applying the linear potential wave theory, to estimate the TKE of each wave scenario at the locations where velocity measurements were available. The same methodology was adopted to estimate the pore pressure perturbations *p'* inside the permeable body of the submerged structures. Examples of data processing are given in the following Figure 1 for regular waves. Results for irregular waves show similar behaviour to those for regular waves but with a Kolmogorov line of lower steepness, in the order of -5/3.5. Comparisons were then conducted between the results.

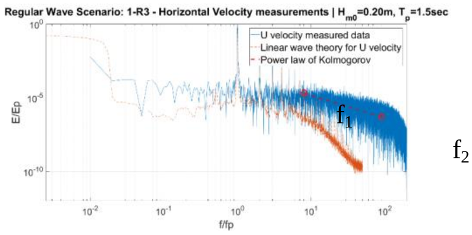

Figure 1. Power spectrum of horizontal velocity - Regular wave scenario.

NUMERICAL MODELLING RESULTS

The Boussinesq-type solver was applied for both regular and irregular wavetrains mainly for obtaining the relevant energy spectrum based on the surface elevation at the required station of the experiments. For irregular wave trains a simple input algorithm was used that provided a randomly constructed sequel of representative individual waves.

RELATION BETWEEN TURBULENCE AND K_t

This step relates representative variables of turbulence to the technical efficiency of the structure denoted by the wave transmission coefficient, K_t. In this way the correlation between ecological and hydraulic characteristics can be obtained for each case considered and support a sustainable design of SPBs.

CONCLUSIONS

In this study, measurements in physical models of submerged permeable breakwaters were analysed in an effort to quantify the turbulent content of orbital velocities and pressures inside these structures. A new methodology is proposed that can be utilized to estimate the three components of turbulent fluctuations (*u', v'* & *w'*) for both regular and irregular waves. Information on turbulent intensity, TKE, and Reynolds stresses under the action of irregular waves would be of great value in relevant studies of marine life habitation in submerged structures, since the real hydrodynamic conditions in such structures might be described in a more accurate way. Moreover, the provided relation between turbulent content and K_t would help designing those structures through a robust eco-hydraulic approach.

ACKNOWLEDGEMENTS

H.J. Verhagen and the Hydraulics Laboratory personnel at TUDelft are kindly acknowledged for providing support with the experiments. Additionally Dr Georgios Klonaris is acknowledged for assisting with numerical modelling.

REFERENCES

Avgeris, I., Karambas, T.V., & Prinos, P. (2004). Boussinesq modeling of wave interaction with porous submerged breakwaters. Proc. 29th ICCE, Lisbon, Portugal, 604–616.

Chan, H.C., Leu, G.M., & Lai, C.J. (2007). Velocity and turbulence field around permeable structure: comparisons between laboratory and numerical experiments. *J. Hydraulic Res*. 45(2), 216–226.

Goring, D. & Nikora, V. (2002). Despiking Acoustic Doppler Velocimeter Data. *J. Hydraulic Eng*. 128(2), 117–126.

Hammond, W., & Griffiths, Z.C.L. (2004). Influence of wave exposure on South African mussel beds and their associated infaunal communities. *Mar. Biol.* 144, 547–552.

Kontaxi, C. & Memos, C.D. (2005). Submerged breakwaters as artificial habitats. 31st IAHR Congress, Seoul, 3967–3975.

Lara, J.L., Garcia, N., & Losada, I.J (2006). RANS modelling applied to random wave interaction with submerged permeable structures. *Coast. Eng*. 53(5-6), 395–417.

Madsen, P.A., & Sørensen, O.R. (1992). A new form of the Boussinesq equations with improved linear dispersion characteristics. Part 2. A slowly-varying bathymetry. *Coast. Eng*. 18(3-4), 183–204.

Metallinos A., Emmanoulidiou M.E., & Memos, C.D. (2014). Wave-induced pore pressures in submerged rubble-mound breakwaters simulated by a compound Boussinesq model. *J. Hydraulic Res*. 52 (1), 24–35.

Metallinos, A.S., & Memos, C.D. (2012). Wave-induced kinematics inside submerged porous structures. *J. Hydr. Res.* 50(4), 388–394.

Moschella, P.S., et al. (2005). Low-crested coastal defence structures as artificial habitats for marine life: Using ecological criteria in design. *Coast. Eng*. 52, 1053–1071.

Repousis, E., Diplarakos, N., Roupas, I., & Memos, C. (2023). Kinematic Perturbations in Submerged Breakwaters under Waves. Proc. DMPCO 2023, Thessaloniki, Greece.

Siddon, C.E., & Witman, J.D. (2003). Influence of chronic, low-level hydrodynamic forces on subtidal community structure. *Mar. Ecol. Prog. Ser.* 261, 99–110.

Van Gent, M.R.A. (1995). Wave interaction with permeable coastal structures, PhD Thesis. Delft University, Delft, NL.

Numerical Investigation of Wave Interaction with Porous Artificial Reef Units

Leftheriotis G.[1,*], Sibetheros I.[1,2], and Dimas A.[3]

[1] Hellenic Open University, Patras, Greece
[2] Department of Civil Engineering, University of West Attica, Greece
[3] Department of Civil Engineering, University of Patras, Greece

*corresponding author:
e-mail: gleytheriot@upatras.gr

INTRODUCTION

Coastal regions are known for their substantial economic value and high population density. However, they are highly vulnerable to risks such as coastal erosion and flooding. With the accelerating impacts of climate change, these threats are expected to worsen. Therefore, it is crucial to develop both effective and sustainable protective measures, capable t withstand extreme events while minimizing environmental impact. Sustainable coastal development emphasizes the adoption of eco-friendly and cost-effective strategies. In this context, Nature-Based Solutions (NBS) have gained significant recognition in recent years. NBS utilize natural processes to mitigate risks and hazards while enhancing biodiversity. One such approach is the use of Artificial Reefs (ARs) placed on the seabed to replicate the functions of a natural reef. The implementation of ARs is increasingly being explored due to their multiple benefits, which include biodiversity conservation, enhancement of fishery resources, and improved shoreline protection (Lee et al., 2018).

The aim of this work is to further develop an advanced numerical model that integrates high-precision 3D flow algorithms with high-performance parallel computing techniques. The primary focus is on understanding the impact of ARs on wave propagation and energy dissipation. By evaluating various deployment strategies, we aim to deepen our understanding of the physical mechanisms driving wave interactions with ARs. The results of this research will provide valuable insights into the role of ARs in coastal areas, facilitating the design of ARs that serve two essential purposes: strengthening coastal protection against erosion and storm surges, while simultaneously enhancing marine habitats for biodiversity conservation.

METHODOLOGY

An in-house hydrodynamic numerical model (Chalmoukis et al., 2023) is employed to simulate the wave-induced free-surface flow, utilizing an efficient parallel implementation. The model is built on the Navier-Stokes equations, and applies a Large-Eddy Simulation approach for turbulence modeling. It treats the combined water and air flow as a single-fluid flow, enabling the simulation of porous media flow with constant porosity, as outlined by Liu et al. (1999):

$$\frac{\partial u_i}{\partial x_i} = 0 \tag{1}$$

$$\frac{1+c_A}{n}\frac{\partial u_i}{\partial t} + \frac{1}{n^2}\frac{\partial}{\partial x_j}\left(u_i u_j\right) = -\frac{1}{\rho}\frac{\partial p}{\partial x_i} + \frac{\delta_{i3}}{\mathrm{Fr}^2} - \frac{1}{n}\frac{\partial \tau_{ij}}{\partial x_j} +$$
$$+\frac{1}{n}\frac{1}{\mathrm{Re}}\frac{1}{\rho}\frac{\partial}{\partial x_j}\left(\mu\left(\frac{\partial u_i}{\partial x_j} + \frac{\partial u_j}{\partial x_i}\right)\right) - a_p\frac{\left(1-n^2\right)}{n^3}\frac{v}{D^2}\frac{1}{\mathrm{Re}}u_i - \tag{2}$$
$$-\beta_p\left(1+\frac{7.5}{\mathrm{KC}}\right)\frac{1-n}{n^3}\frac{1}{D}u_i\sqrt{u_i u_i} + f_i$$

In the above equations, u_i represent the velocity components, x_i are the Cartesian coordinates, n is the porosity, c_A is the added mass coefficient, t is the time, ρ is the fluid density, p is the total pressure, and δ_{ij} is the Kronecker's delta function. Additionally, Fr denotes the Froude number, Re is the Reynolds number, τ_{ij} are the sub-grid scale stresses, and μ and v are the dynamic and kinematic viscosity. Moreover, D is the characteristic dimension of the solids in the porous medium, a_p and β_p are empirical coefficients, KC is the Keulegan-Carpenter number and f_i represents an external forcing term associated with the implementation of the 3D Immersed Boundary method (Dimas & Chalmoukis, 2020) to enforce the no-slip boundary condition on the bed surface. The water-air interface is tracked using the level-set method, where a scalar variable φ is introduced. This variable represents the signed perpendicular distance from any given point to the interface. The evolution of the free-surface is computed by the following advection equation, with $\varphi = 0$ at the free surface.

$$\frac{\partial \varphi}{\partial t} + u_i \cdot \nabla \varphi = 0 \tag{3}$$

The effect of the ARs is modeled by incorporating a porous medium approach to account for flow resistance within the AR field. In this approach, an equivalent porosity value, n_{eq}, is used in place of the traditional porosity n in Eq. (2). The value of n_{eq} depends on the density of the AR shell. In this study, we focus on one of the most popular types of artificial reefs, the Reef Ball™, a hemispherical-shaped AR unit made of concrete, characterized by a large internal void space and a thin shell. This specific design is particularly well-suited for deep water areas and locations prone to extreme wave conditions. Reef Balls™ were originally developed for biological enhancement of marine life. However, when arranged in rows, they can function as submerged breakwaters, thereby extending their application to shoreline protection (Buccino et al. 2013).

A time-splitting projection approach is employed for the temporal discretization, where only the pressure term in Eq. (2) is treated implicitly. For the computation of an intermediate velocity field, a 2nd order Adams–Bashforth scheme is applied. In the second stage the final velocity field is derived from the pressure gradient, which is calculated by solving the corresponding Poisson equation. For parallel implementation, the numerical code utilizes a hybrid MPI+OpenMP approach, allowing it to fully utilize the capabilities of modern supercomputing resources. The code demonstrates nearly linear scalability using up to 1200 CPU cores, achieving high performance with a parallel efficiency of 79%. In terms of the physical model, various AR layouts have been explored, considering factors such as the number of AR rows and the streamwise distance between individual AR units.

RESULTS

Numerical simulations of wave propagation over a beach with a constant slope tanβ = 1/15 were conducted both with and without the presence of AR units. A total of three cases were simulated. The first case (Case 1) represents the scenario before the deployment of AR units, and the other two cases involve the deployment of one row (Case 2) and two rows (Case 3) of AR units, respectively. For all cases, the Reynolds number based on the water depth at the position of the wavemaker is set to $Re_d = 1.5\times10^6$. The incident wave characteristics correspond to laboratory scale dimensions of H = 0.15 m and T = 1.53 s. The simulations are initialized with the fluid at rest. The first 10 wave periods are required for waves to reach fully developed conditions, and another 10 wave periods are used for results sampling and averaging.

Figure 2 illustrates the streamwise velocity field on the cross-shore vertical plane at the center of the AR units for Case 1 (one row of ARs) and Case 2 (two rows of ARs). The presence of the artificial reefs is modeled incorporated using the porous medium approach. The streamwise velocity contours clearly show an increase in velocity at the wave crest. However, within the AR field, the porous medium approach significantly? reduces the velocity magnitudes. Figure 3 presents the phase-averaged cross-shore vertical (2DV) envelope of the free-surface elevation for all cases. The wave breaking position is marked with a vertical dashed line in each case. In Case 1 (no ARs), the wave height distribution over the sloped bed follows the typical shoaling process of wave height reduction as the waves approach the shore, followed by an increase in wave height and eventual breaking. In Cases 2 and 3 (with ARs), the wave breaking is delayed compared to Case 1, and the breaking height is slightly reduced. The wave breaking depth is decreased by about 9% in Case 2 and by approximately 18% in Case 3 compared to Case 1.

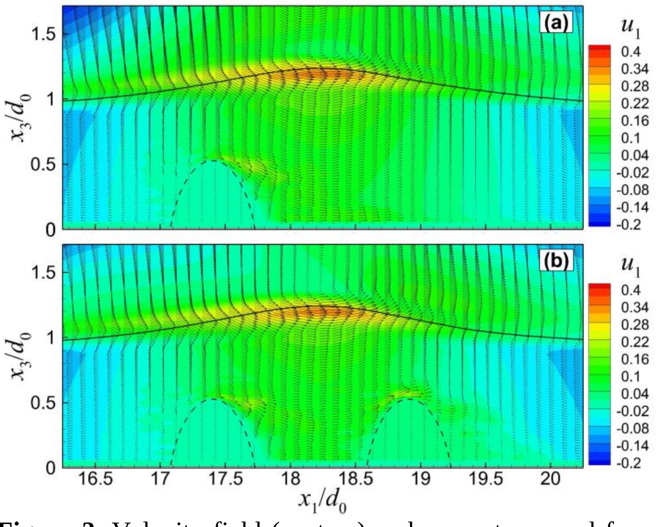

Figure 2. Velocity field (vectors) and u_1 contours and free-surface elevation over AR units (dashed lines) for (a) Case 2 and (b) Case 3.

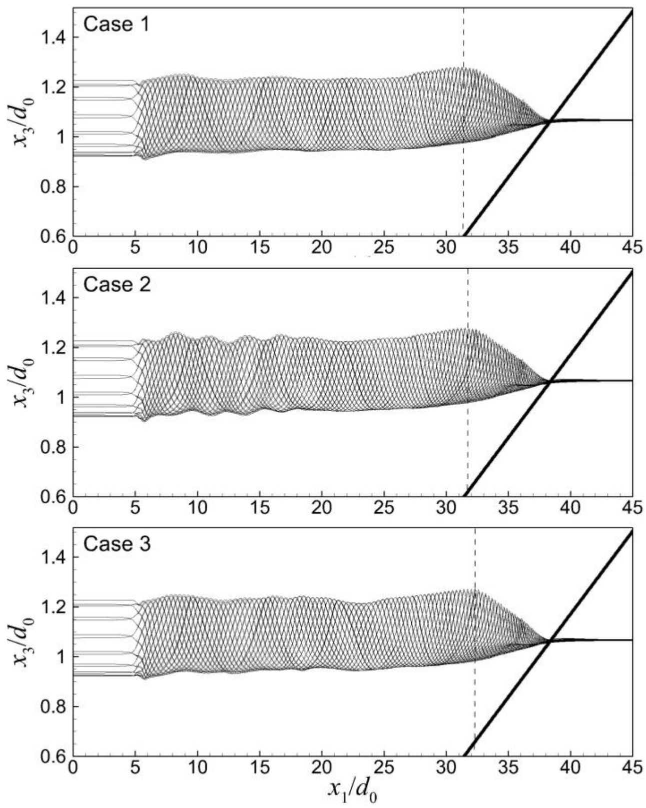

Figure 3. Phase-averaged 2DV envelope of the free-surface elevation of waves propagating for Cases 1-3. Note that the axes are in scale x_1/x_3 = 0.05 for clarity of the exposition.

ACKNOWLEDGEMENTS

This work is funded by the Hellenic Open University under the research project CoastPRO and is supported by computational time granted by the Greek Research & Technology Network at the National HPC facility – ARIS.

REFERENCES

Buccino, M., Del Vita, I., & Calabrese, M. (2013). Predicting wave transmission past Reef Ball™ submerged breakwaters. *J. Coast. Res.* 65, 171–176.

Chalmoukis, I.A., Leftheriotis, G.A., & Dimas, A.A. (2023). Large-Eddy Simulation of Wave Attenuation and Breaking on a Beach with Coastal Vegetation Modelled as Porous Medium. *J. Mar. Sci.Eng*. 11(3), 519.

Dimas, A.A., & Chalmoukis, I.A. (2020). An adaptation of the immersed boundary method for turbulent flows over three-dimensional coastal/fluvial beds. *Appl. Math. Model*. 88, 905–915.

Lee, M.O., Otake, S., Kim, J.K. (2018) Transition of artificial reefs (ARs) research and its prospects. *Ocean Coast. Manag.* 154, 55–65.

Liu, P.L.F., Pengzhi, L., Chang, K., & Sakakiyama, T. (1999). Numerical modeling of wave interaction with porous structures. *J. Waterw. Port Coast. Ocean Eng*. 125(6), 322–330.

Numerical Study on the Efficiency of Geotube Breakwaters for Coastal Protection during Extreme Storms

Petalas S.[1,*], Kokkos N.[1] and Sylaios G.[1]

[1] Laboratory of Ecological Engineering and Technology, Department of Environmental Engineering, Democritus University of Thrace, 67100 Xanthi, Greece

*corresponding author:
e-mail: spetalas@affil.duth.gr

INTRODUCTION

The impacts of wave action on coastal regions during extreme storm events have become a critical area of research, particularly in the context of climate change and rising sea levels (Williams et al. 2018). Coasts and beaches vulnerable to erosion due to extreme waves can benefit from classical coastal engineering solutions like the installation of breakwaters (either submerged or emerged). In recent decades, however, Nature-based Solutions (NbS) using new materials and ways of constructing breakwaters have emerged, allowing for a lower environmental footprint and reduced construction costs while providing a final product more integrable with the local ecosystem. An example is using geotubes as building blocks for low-crested breakwaters by stacking long cylindrical sand-filled tubes in a pyramid shape.

This study uses numerical modeling to examine the efficiency of geotube breakwaters as wave-energy reducers during two specific storm events that occurred in the coastal area of Kalamitsa beach near Kavala, Northern Greece. The storms are selected based on a former analysis of the offshore wave field collected from the CMEMS reanalysis database. These storms are considered typical examples of the predominant wave direction and wave characteristics of extreme waves in the area, causing significant transformations in coastal morphology and the incident wave energy field reaching the shoreline (Sylaios and Kokkos 2022). The first storm lasted from 30/11/2017 to 03/12/2017 and was characterized by significant wave height exceeding 2.3 meters originating predominantly from the southeastern direction. It affected the coastal infrastructure due to high wave periods and energy concentrations along the shoreline. Similarly, the second storm on the 26th of February 2018, with its distinct northeastern orientation, highlighted the susceptibility of the coast to severe weather patterns.

METHODOLOGY

Several numerical experiments were set-up for the coastal area of Kalamitsa Beach using the REEF3D numerical model. The REEF3D is a hydrodynamic simulation platform, offering numerical simulation capabilities with CFD and wave models (Wang et al. 2022). In this application, the NHFLOW (Non-Hydrostatic Flow) solver was used, which is a 3D non-hydrostatic wave simulator that uses a Godunov-type scheme for shock-capturing properties, with WENO flux reconstruction (Bihs and Wang 2025). The model may reproduce the dynamic wetting and drying processes in the swash zone, even for complex shorelines, and can numerically solve the transition of waves from deep to shallow water and their breaking along the surf zone.

For the Kalamitsa beach, realistic bathymetry was used to construct a numerical grid with a horizontal resolution of 2 meters and a size of 350 x 378 grid cells (Figure 1). On the vertical axis, the model uses a non-uniform vertical grid layout in sigma coordinates, which varies in time according to the model requirements (depending on the depth and wave period) to reach the lowest possible number of vertical layers necessary to maintain numerical stability. The integrations performed for the three sub-cases (see below) lasted 240 seconds each. The wave field input at the open boundary followed a JONSWAP spectrum assumption of a fully developed sea, and the wave characteristics (significant wave height, period, direction) for typical cases of severe storms in the area, as recorded in November 2017 and February 2018 (Table 1).

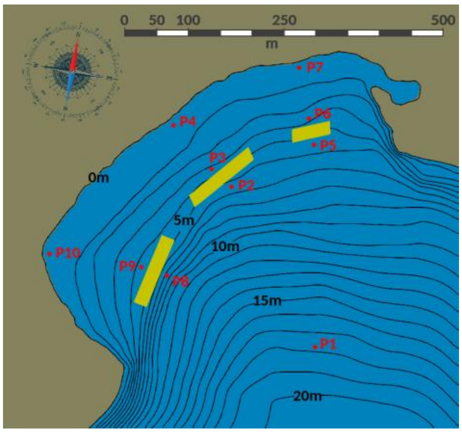

Figure 1. Kalamitsa beach coastline with bathymetry in black contour lines every 1m. The placement and geometry of the three breakwaters is shown in yellow. Points P1-10 (red) represent numerical sea-level gauges used in the analysis as monitoring points (see Results).

Table 1. Wave spectrum characteristics for the two storms.

Storm	Significant Wave Height	Mean Wave Period	Wave front mean origin. direction
30/11/2017	2.30 m	8.7 sec	170°
26/02/2018	1.66 m	8.4 sec	82°

The direction of wavefront input was set from the SE direction (170 deg) for the first storm and from the NE direction (82 deg) for the second storm. Simulations were performed for three sub-cases: (a) control simulation without shore protection structures, (b) simulation using three submerged breakwaters with their crest at 1m below mean sea level, and (c) simulation using three emerging breakwaters extending to 1m above mean sea level. The breakwaters were placed in front of parts of the coast that were identified by previous studies as erosion hotspots, and were constructed using trapezoidal cross-sections with a 1:3 slope, a crest width of 15 meters and a length of 120 meters for the central and western breakwaters, and 60 meters for the eastern one. The water depth at the place of installation is ~4.5 meters. In order to obtain a comparable sea state in all experiments, the same forcing of the control experiment is applied to all subsequent experiments.

RESULTS & DISCUSSION

The wave field as calculated for the storm of November 2017 for the three numerical experiments (i.e., control without breakwater, with crest at 1 meter below surface, and with crest one meter above surface) can be seen in Figure 2, and the one for the storm of February 2018 in Figure 3. In both storms, the control experiments (a), demonstrate wave fields subject to wave shoaling and refraction due to the bottom slope.

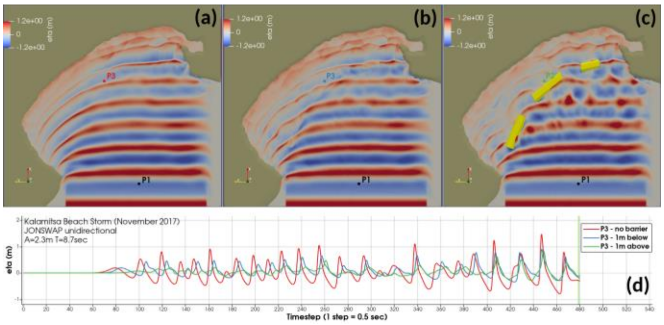

Figure 2. Simulated wave field of the storm of November 2017 for: (a) the control case with no breakwaters, (b) with submerged breakwater, and (c) with emerged breakwater - 1m. Time-series of the water level gauges at points P1 and P3 is shown in (d).

In the case of the submerged breakwater (b), the wave field is similar to the control experiment, with signs of wave diffraction appearing due to the breakwaters. The wave height at the shoreline is reduced at several locations while increased at others due to wave interference. Several wave reflections are visible at the location of the breakwaters. An exaggerated image of the above holds for the cases with the emerged breakwater (c), where both wave diffraction and reflection become more prominent, while the attenuation of wave height at the shoreline is highly reduced overall compared to the control case.

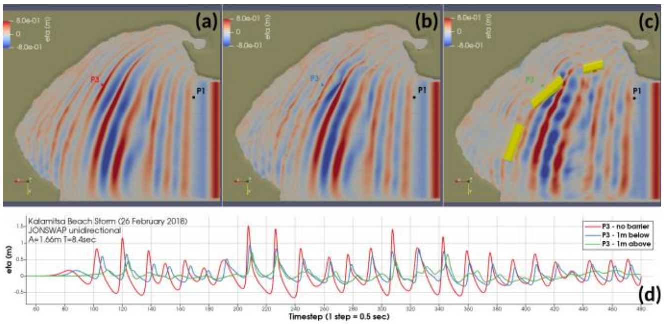

Figure 3. As in Figure 2, for the storm of February 2018.

In the time series of water level at gauge P3 (lee-side of the central breakwater), a reduction of up to 30% in wave height is observed for the submerged breakwater and a reduction of up to 80% for the emerged breakwater. An approximation of the potential sediment transport can be obtained using the velocity field at the bottom to calculate shear stresses. Additionally, applying the sediment transport algorithm of the model would more effectively showcase the impact of such a wave height reduction on shoreline erosion compared to the unprotected control case, and is part of the future steps in this study.

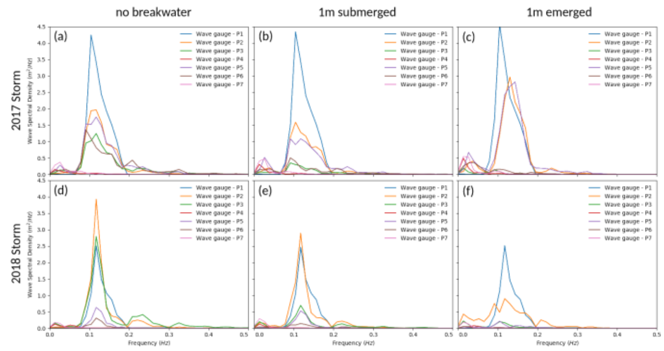

Figure 4. Wave spectral density at control points P1-P7 (see Fig. 1), for the two storms and the three sub-cases

The spectral density for both storms and all cases can be seen in Figure 4 for all gauges. It is observed that the peak wave frequency near the forcing boundary (gauge P1) has a slight dispersion around the dominant wave period of Table 1 (this is expected because the imposed JONSWAP spectrum is comprised of 24 different frequencies in this study). Closer to the breakwaters (gauges P2, P5), there is an attenuation of the dominant frequency and a larger dispersion toward lower and higher frequencies. Moving past the breakwaters (gauges P3, P4, P6, P7), an almost complete attenuation of the dominant frequency is observed, while a transfer of energy towards the lower wave frequencies (with T~30 sec) is seen.

ACKNOWLEDGEMENTS

This research was funded by the EU Horizon 2021-2027 Research and Innovation Program (DesirMed-Demonstration and mainstreaming of nature-based solutions for climate resilient transformation in the Mediterranean, Grant Agreement No. 101112972). The article reflects only the authors' view, and the Commission is not responsible for any use that may be made of the information it contains.

REFERENCES

Bihs, H., & Wang, W.W. (2025). Reef3d:Nhflow – A High-Performance Non-Hydrostatic Solver for Coastal Wave Propagation (SSRN Scholarly Paper 5145387). Social Science Research Network.

Sylaios, G., & Kokkos, N. (2022). Wave and Coastal Engineering Study for the Restoration and Protection Works of "Kalamitsa" Beach. Final Technical Report for the Municipality of Kavala. Democritus University of Thrace.

Wang, W., Pákozdi, C., Kamath, A., Martin, T., & Bihs, H. (2022). Hydrodynamic Coupling of Viscous and Nonviscous Numerical Wave Solutions within the Open-Source Hydrodynamics Framework Reef3d. *J. Offshore Mech. Arct.* 144(041903).

Williams, A.T., Rangel-Buitrago, N., Pranzini, E., & Anfuso, G. (2018). The management of coastal erosion. *Ocean Coast. Manag.* 156, 4–20.

Evaluation of RANS Turbulence Models for Weak Breaking Wave Simulations with a Moving Boundary using the InterFoam Solver

Pasias G.[1,*], Barajas G.[2], Lara L. J.[2], Grigoriadis D.G.E.[1], and Stagonas D.[3]

[1] Affiliation and address: Department of Mechanical and Manufacturing Engineering University of Cyprus, 1 Panepistimiou Avenue 2109 Aglantzia, Nicosia, Cyprus
[2] Affiliation and address: IHCantabria—Instituto de Hidráulica Ambiental, C. Isabel Torres, 15, 39011 Santander, Cantabria, Spain
[3] Affiliation and address: Department Civil and Enviromental Engineering University of Cyprus, 1 Panepistimiou Avenue 2109 Aglantzia, Nicosia, Cyprus

*corresponding author:
e-mail: gpasia01@ucy.ac.cy

INTRODUCTION

Numerical wave modelling is vital in marine and coastal engineering, offering critical insights into wave dynamics, energy dissipation, and coastal processes. However, accurately simulating breaking waves remains challenging due to their turbulence, nonlinear interactions, and significant energy loss factors essential for wave energy assessments, sediment transport studies, and hazard mitigation. Recent advancements have improved wave-breaking simulations. Lin and Liu (1998) underscored the importance of turbulence modelling in capturing breaking wave profiles and dissipation. Jacobsen et al. (2012) highlighted how grid resolution and solver setup in OpenFOAM influence wave propagation and breaking. Higuera et al. (2013) introduced enhanced wave generation and absorption methods, enabling more realistic simulations of wave breaking and energy loss. Yet, the comparative performance of RANS turbulence models $k-\epsilon, k-\omega,$ and $k-\omega-\ SST$ in simulating energy evolution and dissipation during breaking remains underexplored.

This study evaluates the impact of Reynolds Averaged Navier–Stokes (RANS) turbulence models $k-\epsilon, k-\omega,$ and $k-\omega-\ SST$ for simulating weak breaking waves using OpenFOAM's interFoam solver. Waves are generated using a dynamic mesh to simulate a piston-like motion, effectively replicating the process in a numerical wave flume. The primary objective is to identify the most suitable turbulence model and simulation setup for accurately capturing the dynamics of weak breaking waves.

To achieve this, pre- and post-breaking wave elevations and the energy evolution of a focusing wave group are compared against experimental data from a small-scale physical model. Wave decomposition is applied to analyse wave profiles and energy dissipation for both linear and nonlinear components. The decomposition employs a harmonic separation approach, as described by Buldakov, Stagonas, and Simons (2017), which isolates nonlinear superharmonics for the first (linear), second, and third orders, along with a second-order minus-component (subharmonics). For a detailed visualisation, refer to Figure 1.

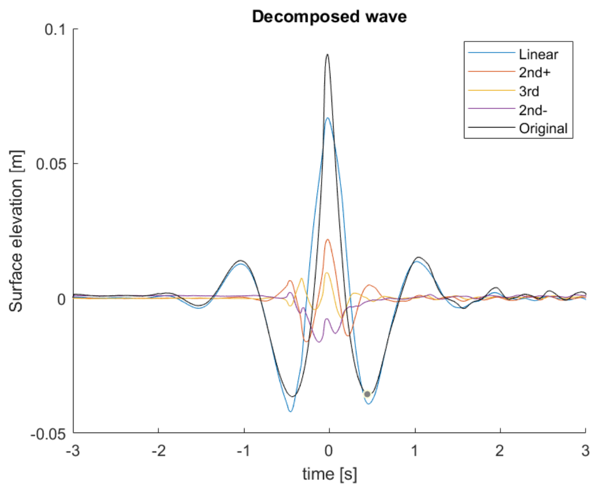

Figure 1. Decomposed Focussed Wave

OBJECTIVES AND METHODOLOGY

A focused breaking wave was generated $6.5\ m$ from the wavemaker at a predefined location and time, following the methodology proposed by Buldakov et al. (2017). The wave was produced using a Gaussian target spectrum with a peak frequency of $1\ Hz$ and a focus amplitude of 7.2 cm. The focusing time was set to 64 seconds, with a repeat interval of 128 seconds, corresponding to a frequency spacing of $1/128\ Hz$, which defines the increment between consecutive wave frequencies in the spectrum.

Building on this setup, the key parameter under investigation include:

- **Free-Surface Elevation:** The accuracy of turbulence models in predicting wave profiles is evaluated by comparing simulation outputs with experimental measurements.

- **Energy Dissipation:** Two complimentary approaches are used to quantify energy dissipation during wave breaking:

  1. **Local Energy Analysis at Probes**: Energy is evaluated locally at probe points before and after the breaking point. Linear and the full nonlinear wave energy is determined using spectral density analysis:

$$E_{lin} = \rho g \int \frac{S_{lin}(f)}{2}\, df, \tag{1}$$

$$E_{total} = \rho g \int \frac{S_{total}(f)}{2}\, df, \tag{2}$$

where S_{lin} and S_{total} represent the power spectral densities of the linear component and the full nonlinear wave, respectively. The spectra are obtained from the Fourier transform of the surface elevations for both the full nonlinear and decomposed linear wave components at designated probe locations. Energy loss associated with the linear and nonlinear components is quantified by comparing the wave energy of these components before and after breaking. These results are subsequently compared with data from the physical experiment to examine which model performs better in this scenario.

2. **Total Energy Evolution**: The kinetic and potential energy of the waves are calculated for each computational cell using the method of Clous and Abadie (2019). These energy components are summed over all cells using,

$$E_p = \sum_{i=1}^{Nx}\sum_{j=1}^{Ny}\sum_{k=1}^{Nz} a\,\rho g z(i,j,k)\,\Delta V, \tag{3}$$

$$E_k = \sum_{i=1}^{Nx}\sum_{j=1}^{Ny}\sum_{k=1}^{Nz} a\,\frac{\rho U^2(i,j,k)}{2}\,\Delta V. \tag{4}$$

Here, a is the volume fraction, U the velocity, z the cell height, and ΔV the cell volume. This approach gives as a comprehensive view of the total energy evolution across the entire tank, the time the wave breaking occurs and the total energy loss from the wave breaking.

RESULTS AND DISCUSSION

This study assessed the performance of RANS turbulence models $k-\epsilon, k-\omega$, and $k-\omega-SST$ in simulating weak wave breaking, with a focus on free-surface dynamics, energy dissipation, and wave energy decomposition. The simulations were performed using the interFoam solver, which solves the Navier–Stokes equations and employs the Volume of Fluid (VOF) method to capture the free surface. Discretisation was carried out using the finite volume method, with an Euler scheme (first-order accurate) for time integration and Gauss upwind/linear schemes (first/second-order accurate) for convection and diffusion. A detailed convergence analysis of grid resolution and Courant number confirmed the numerical accuracy, with deviations of less than 5% from experimental results.

Among the models tested, the $k-\omega-SST$ turbulence model demonstrated the best performance, providing a strong balance between pre-breaking accuracy and reliable turbulence representation post-breaking. In contrast, the laminar model was effective in the pre-breaking phase but struggled to capture the energy dissipation driven by turbulence after breaking.

The analysis of wave energy dynamics confirmed that weak wave breaking involved limited energy transfer from linear to nonlinear components, with dissipation predominantly affecting the nonlinear energy. Overall, the results validated the suitability of the $k-\omega-SST$ model for simulating weak wave breaking, offering accurate predictions of free-surface elevations, energy dissipation, and overall wave behaviour. These findings provide a solid foundation for future studies of breaking waves in numerical wave flumes.

ACKNOWLEDGEMENTS

The authors would like to express their gratitude to the ONISILOS Fellowship, which has received funding from the European Union's Horizon 2020 research and innovation program under the Marie Skłodowska-Curie Grant Agreement No 101034403.

REFERENCES

Buldakov, E., Stagonas, D., & Simons, R. (2017). Extreme wave groups in a wave flume: Controlled generation and breaking onset. *Coastal Eng.* 128, 75–83.

Clous, L, & Abadie, S (2019). Simulation of Energy Transfers in Waves Generated by Granular Slides. *Landslides* 16, 1663–1679.

Higuera, P., Lara, J.L, & Losada, I.J. (2013). Realistic Wave Generation and Active Wave Absorption for Navier–Stokes Models: Application to OpenFOAM®. *Coastal Eng.* 71, 102–118.

Jacobsen, N.G., Fuhrman, D.R., & Fredsøe, J. (2012). A Wave Generation Toolbox for the Open-Source CFD Library: OpenFOAM®. *Int. J. Numer. Method. Fluids* 70(9), 1073–1088.

Lin, P., & Liu, P.L.F. (1998). A Numerical Study of Breaking Waves in the Surf Zone. *J. Fluid Mech.* 359, 239–264.

Numerical Investigation of Scour Evolution around Monopile Structures using sedInterFoam

Tiwari N.[1,*], Knaapen M.[1], Haeri S.[1] and Attili T.[1]

[1] HR Wallingford, Howbery Park, Wallingford, OX10 8BA, UK

*corresponding author
e-mail: n.tiwari@hrwallingford.com

INTRODUCTION

Scour around monopile structures critically affects offshore engineering by destabilizing foundations of wind turbines and marine installations. It results from complex wave and current interactions with the structure and seabed, creating intense flow patterns and turbulence that elevate bed shear stress, particularly upstream, forming a horseshoe vortex that initiates scour holes.

Accurate prediction of scour depth and morphology is vital for effective protection measures and structural integrity. This study uses sedInterFoam, an open-source OpenFOAM solver introduced by Mathieu (2024), to simulate sediment transport under combined wave and current conditions. By integrating multiphase flow dynamics with sediment equations, it analyses processes like bed shear stress, sediment entrainment, and deposition. Preliminary results show accuracy in predicting scour evolution, providing insights into sediment transport mechanisms and emphasizing the importance of advanced numerical tools for enhancing offshore foundation resilience against scour.

METHODOLOGY

Sediment transport and scour evolution around monopile structures are modelled using sedInterFoam, a three-phase OpenFOAM solver. Building on the two-phase Eulerian model sedFoam (Chauchat (2017)), it incorporates an air phase for free-surface dynamics, making it suitable for wave-driven coastal sediment transport. Governing equations are based on mass and momentum conservation principles applied to sediment and fluid phases (water and air). A k-ω SST turbulence model captures flow transitions, while the Volume of Fluid (VOF) method, coupled with waves2Foam, simulates wave generation, propagation, breaking, and seabed interaction. Advanced rheological models, including the Kinetic Theory of Granular Flows and μ(I) Rheology (Jop (2006)), ensure accurate sediment behaviour under varying flow conditions.

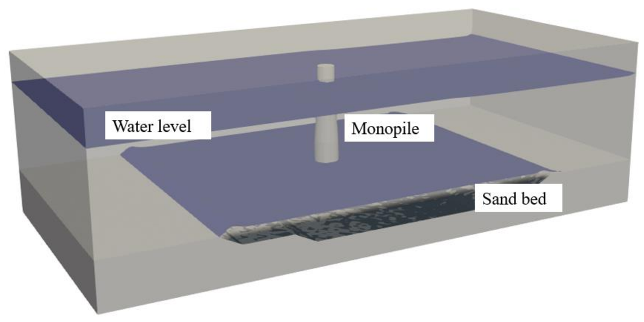

Figure 1. Computational Domain

Validation used experimental data from HR Wallingford's Fast Flow Facility, where a 1.75 m monopile was placed in a flume with a 0.3 m sand bed and 1.4 m water depth. The physical setup was meticulously replicated in OpenFOAM (Figure 1) using a computational mesh of approximately 0.4 million hexahedral cells, ensuring high-resolution modelling of flow fields and sediment processes. Simulations were conducted under steady currents of 0.2 m/s over 600 seconds, comparing scour evolution and sediment transport against experimental results. Additional simulations explored higher current velocities (0.3 m/s, 0.4 m/s) and wave-current interactions, incorporating realistic wave parameters such as height, period, and direction to assess hydrodynamic and sediment transport responses under varied conditions.

RESULTS

Post-processing of the 600-second simulation results (Figure 2) involved extracting a contoured surface from the volume fraction field to represent the water-sediment interface. This interface accurately captures morphological changes due to scour and deposition, enabling detailed characterization of scour depths and sediment accretion patterns around the monopile. The approach provides a clear depiction of the evolving sediment bed, facilitating quantitative analysis of erosion and deposition mechanisms near the structure.

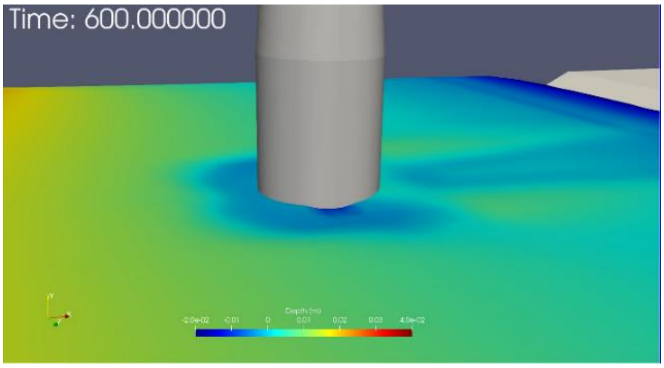

Figure 2. Scour Depth (m) around the monopile geometry using sedInterFoam.

ACKNOWLEDGEMENTS

The project has received funding from Horizon Europe Marie Skłodowska-Curie Actions, Grant Agreement no. 101072443 - SEDIMARE. Experimental data is taken from the Fast Flow Facility at Froude Modelling Hall, HR Wallingford Ltd.

REFERENCES

Chauchat, J., Cheng, Z., Nagel, T., Bonamy, C., & Hsu, T.J. (2017). SedFoam-2.0: a 3-D two-phase flow numerical model for sediment transport. *Geosci. Model Dev.* 10(12), 4367–4392.

Jop, P., Forterre, Y., & Pouliquen, O. (2006). A constitutive law for dense granular flows. *Nature* 441(7094), 727–730.

Mathieu, A., Kim, Y., Hsu, T.J., Bonamy, C., & Chauchat, J. (2024). sedInterFoam 1.0: a three-phase numerical model for sediment transport applications with free surfaces. *Geosci. Model Dev. Discuss.* 1–20.

Numerical Analysis of Particle Trajectories Driven by Currents and Waves in an Idealized Estuarine Model

Soori N.[1,*], Brocchini M.[1] and Postacchini M.[1]

[1] Università Politecnica delle Marche, Ancona, Italy

*corresponding author:
e-mail: n.soori@staff.univpm.it

ABSTRACT

Estuaries, which serve as critical transitional zones between riverine and marine ecosystems, are subject to complex hydrodynamic processes due to the combined influences of river inflows, tidal forces, and oceanic currents. Understanding particle trajectories within these environments is crucial for assessing the transport of sediments, pollutants, and other materials. This study utilizes a numerical modeling approach to examine nearshore circulation generated by currents around an idealized inlet configuration. The primary objective is to compare trajectories of water particles extracted using the Delft-3D software with the results obtained from a 2DH Nonlinear Shallow Water Equation (NSWE) solver. Both modeling approaches reveal dominant circulation patterns around the inlet, yet differences emerge in the particle distribution. Using a tailored Lagrangian tracker, the NSWE solver results are also used to investigate the fate of non-neutral units, with the objective to mimic the motion of plastic particles with different densities. These findings contribute to a better understanding of the hydrodynamic processes in estuarine environments, particularly in terms of pollutant particle retention and dispersion.

INTRODUCTION

Estuarine environments are characterized by complex and dynamic water movements, driven by the interplay of riverine inflows, tidal fluctuations, and oceanic currents. These interactions result in variable particle trajectories that influence critical processes, such as sediment deposition, nutrient dispersion, and contaminant transport (Özsoy and Ünlüata, 1892). Estuaries play a pivotal role in regulating the transport of sediments and nutrients, which can either be retained within these zones or exported to the open ocean, depending on the prevailing hydrodynamic conditions (Fontes et al., 2014). The dynamic interplay of forces within estuaries creates constantly fluctuating conditions that affect sediment transport, nutrient cycling, and ecosystem health (Jay and Musiak, 1994).

Accurately predicting particle trajectories in such environments is essential for effective estuarine management. This is particularly critical for addressing issues like sedimentation or pollution, where understanding transport pathways can inform mitigation strategies. Numerical modeling has proven to be a valuable tool for simulating the complex processes governing particle movement, providing insights that aid in the development of strategies to manage and protect these sensitive coastal areas. In this study, a particle-tracking model integrated within a hydrodynamic framework is employed to simulate particle trajectories in a simplified estuarine environment. The primary goal is to compare two distinct methods for tracking particle movement: Delft-3D, a sophisticated hydrodynamic modeling software, and a MATLAB-based script, utilizing the hydrodynamic simulation computed by the NSWE solver's velocity field and wave as an input. This comparison evaluates the capabilities of each approach in simulating particle trajectories, highlighting their respective strengths and limitations within a controlled estuarine domain.

MATERIALS AN METHODS

Model setup – Delft-3D

To simulate the effects of currents and waves on a simplified inlet, a series of numerical simulations were conducted to examine nearshore circulation patterns. The Delft-3D software was employed for this study, providing a basis for comparison with the work of Olabarrieta et al. (2014), which offers a robust framework for understanding hydrodynamic and sediment transport processes in estuarine environments. Delft-3D, developed by Delft Hydraulics (now Deltares), is a versatile numerical modeling system capable of simulating hydrodynamic processes driven by waves, tides, rivers, winds, and coastal currents (Delft-3D, 2024).

The primary objective of this study was to explore the effects of river currents entering the sea and wave effects on particle tracking, leveraging Delft-3D's robust hydrodynamic and particle transport modeling capabilities. For the simulations, the computational grid was created in Delft-3D, with bathymetry data sourced from an in-house NSWE solver (Brocchini et al., 2001; Melito et al., 2018) that employs a 2DH formulation suitable for shallow-water conditions. The grid dimensions were $300 \times 151\,[M \times N]$ with $\Delta x = 20, \Delta y = 10\,m$, covering a domain of $3 \times 3\,km$ in the cross-shore and alongshore directions. The estuarine window accounted for the current velocity, while Reimann boundary conditions were applied at the seaward boundaries.

According to Figure 1, the model domain features a maximum water depth of ≈ 9 m at the offshore boundary. This bathymetric profile aligns well with the findings of Olabarrieta et al. (2014), further validating the model's accuracy in replicating key dynamics, such as flow circulation and particle trajectory patterns.

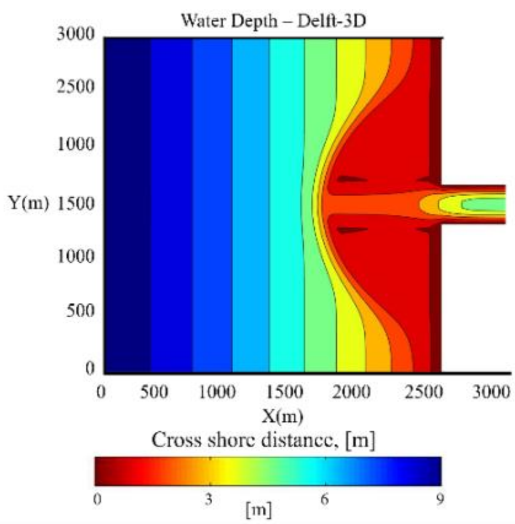

Figure 1. Water depth, Delft-3D.

Figure 2 presents depth-averaged velocities simulated using Delft-3D. This simulation compares well with NSWE simulation (Melito et al., 2018) and shows that the flow is primarily directed downstream, with velocity decreasing laterally as the distance from the centerline increases. Delft-3D results display smoother and more symmetric velocity fields, characterized by a distinct jet spreading uniformly downstream. In contrast, the solver captures more intricate and turbulent flow features, including eddies and mixing zones, which become more pronounced at higher flow rates. The differences highlight the contrasting approaches of the models in resolving flow dynamics, particularly in regions with complex flow behaviour. Releasing particles from the estuary into the sea is a common method for studying particle transport dynamics in coupled estuarine-coastal systems. To simulate particle transport, the Delft-3D model separates motion into two components: advection (representing large-scale flow) and dispersion (random spreading). Advection is solved analytically using a linearly interpolated velocity field, while dispersion is computed using Euler-type numerical scheme that incorporates wind-driven effects and settling processes (Delft3D-Part, 2024). In this study, to focus on horizontal transport mechanisms, particle settling is excluded in this analysis. This approach isolates the effects of flow velocity on particle trajectories, emphasizing the critical role of flow dynamics in controlling particle distribution and spread.

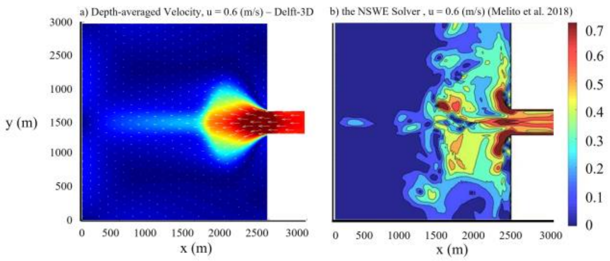

Figure 2. Comparison of depth-averaged velocity obtained using Delft-3D (left panel) and NSWE solver (right panel).

Model Setup- MATLAB Script

A custom MATLAB script has been implemented to simulate particle trajectories. This script tracks the particle movement by interpolating flow fields around particles. The hydrodynamic input data was sourced from the NSWE solver to analyze the effects of combined waves and current actions on particle pathways. Executing the NSWE solver requires the prior generation of a meshing domain. This process utilizes the code developed by Melito et al (2018), specifically designed for this purpose. The meshing domain is the same as that for Delft-3D. A series of numerical simulations were performed using the NSWE solver to investigate nearshore circulation induced by current around an idealized inlet configuration. The simulation results were then utilized as input for a MATLAB script. In this study, a single particle is transported by the flow velocity field derived from hydrodynamic simulations, with river-imposed current velocities of 0.6 and 1.6 m/s and no waves, weak waves and strong waves regime ($H_s = 0, 0.5\ , 1.5\ m$).

RESULTS AND CONCLUSION

In both models a single particle is released at different locations, allowing it to move according to the local flow field for 3600 seconds. Initially, the estuarine flow primarily governs the particle's motion. However, as the particle reaches the open sea, coastal currents become the dominant force. Increased momentum transfer from the river to the sea, driven by velocity, significantly influences the transport pathways. Figure 3 displays the positions of a single particle with a time interval of 600 seconds and a flow velocity of 0.6 m/s at four different release points. As can be observed in Figure 2, the estuary channel has higher velocity, indicating strong flow. The Delft-3D simulation indicates that momentum drives the particle further into the coastal ocean, highlighting a strong influence on coastal dynamics. In contrast, the NSWE simulation shows that circulation limits greater particle dispersion, resulting in more localized transport. In Figure 3-a, the particle is released at (x,y)=(270,75)m within the estuary channel, where the velocity is moderate to high. Based on the velocity field, the particle is expected to move seaward toward the estuary mouth. Upon reaching the high-velocity jet at the estuary mouth, it may be carried further offshore into the open sea.

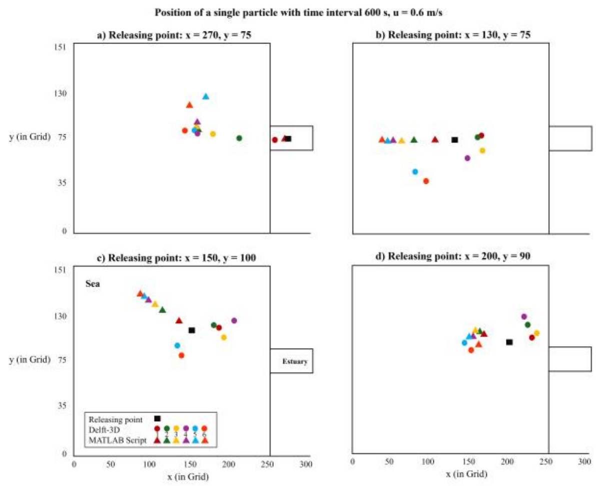

Figure 3. Comparison of single-particle trajectories in Delft-3D and MATLAB script: Influence of release location

ACKNOWLEDGEMENTS

This project has received funding from the European Union's (EU) Horizon Europe Framework Programme (HORIZON) under Grant Agreement No 101072443 as a MSCA Doctoral Network (HORIZON-MSCA-2021-DN-01) of SEDIMARE.

REFERENCES

Özsoy, E., & Ünlüata, Ü. (1982). Ebb-tidal flow characteristics near inlets. *Estuar. Coast. Shelf Sci.* 14(3), 251-IN3.

Fontes, R.F.C., & Miranda, L.B, F.P.A. (2014). Estuarine Circulation, Springer Science +Business Media Dordrecht.

Olabarrieta, M., Geyer, W.R., & Kumar, N. (2014). The role of morphology and wave-current interaction at tidal inlets: An idealized modeling analysis. *J. Geophys. Res. Oceans*. 119(12), 8818–8837.

Delft3D-Flow and WAQ PART User Manual. (2024). Deltares, Delft, The Netherlands.

Melito, L., Brocchini, M., Darvini, G., & Lenci, S. (2018). On the hydro-morphodynamics of river mouths: the role of waves, Università Politecnica delle Marche. Faculty of Engineering, Civil Engineering Department.

Brocchini, M., Bernetti, R., Mancinelli, A., & Albertini, G. (2001). An efficient solver for nearshore flows based on the WAF method, *Coastal Eng*. 43(2), 105–129.

Impact of Flow and Sediment Parameters on the Morphodynamic Evolution of Vortex Ripples

Leftheriotis G.[1,*], and Dimas A.[1]

[1] Department of Civil Engineering, University of Patras, Greece
[*]corresponding author:
e-mail: gleytheriot@upatras.gr

INTRODUCTION

Wave-generated flows interacting with the sand bed in coastal waters lead to the generation of sand ripples, known as vortex ripples, forming due to flow vortices on the leeside of ripple crests. Ripples are significant for nearshore processes, including wave attenuation and sediment transport, with their size affecting bottom friction and the wave boundary layer. The aim of the present work is to numerically examine how non-dimensional parameters influence the morphodynamic development of vortex ripples. The analysis focuses on three non-dimensional parameters: the mobility parameter (ψ), the ratio of wave orbital amplitude to grain diameter (a_o/D_g), and the Reynolds number, Re. The study investigates how these parameters affect ripple evolution, particularly the ripple characteristics, i.e. the non-dimensional ripple length (L_r/a_o) and the non-dimensional ripple height (h_r/a_o) over time. Moreover, the vortical flow structures and the corresponding sediment transport are explored.

METHODOLOGY

The governing flow equations in the developing boundary layer are the continuity equation and the Navier-Stokes (NS) equations, which are made dimensionless using U_o and a_o, under the LES formalism:

$$\frac{\partial u_i}{\partial x_i} = 0 \tag{1}$$

$$\frac{\partial u_i}{\partial t} + \frac{\partial}{\partial x_j}\left(u_i u_j\right) = -\frac{\partial p}{\partial x_i} - \frac{\partial \tau_{ij}}{\partial x_j} + \frac{1}{\mathrm{Re}}\frac{\partial^2 u_i}{\partial x_j \partial x_j} + f_i \tag{2}$$

where u_i are the velocity components, x_i are the spatial coordinates, t is the time, p is the dynamic pressure, τ_{ij} are the subgrid-scale (SGS) stresses, which are modelled using the standard eddy-viscosity model in Smagorinsky (1963), and f_i is the Immersed Boundary (IB) method term (Dimas and Chalmoukis, 2020) for the imposition of the non-slip velocity boundary condition on the bed surface. The NS equations are spatially discretized using second-order, central, finite differences on a staggered Cartesian grid. For the time discretization of the NS equations, a fractional time-step approach is followed. An intermediate velocity field is computed in the first stage, using a 2nd order Adams-Bashforth scheme. Then, the dynamic pressure is computed by the solution of a Poisson equation in order to satisfy the continuity equation. Finally, in the second stage of the time-step, the final velocity field is computed by an implicit scheme based on the dynamic pressure correction. Regarding the sediment transport, both bed and suspended sediment transport are taken into account. The bedload transport rate, q_{bi}, is calculated following the semi-empirical formula in Engelund and Fredsøe (1976), while an advection-diffusion equation is used for the computation of the suspended sediment concentration. The coupling between the evolution of bed level and the sediment transport fluxes is implemented by the numerical solution of the sediment continuity (Exner) equation.

RESULTS

The numerical model has been validated in terms of fluid flow, sediment transport and bed morphodynamics in Dimas and Leftheriotis (2019), while validation results for the morphological evolution of the bed have been presented in Leftheriotis and Dimas (2022). Regarding the simulation cases, two values of ψ (= 20, 50) and two values of a_o/D_g (= 500, 1000) have been considered, which correspond to orbital vortex ripples according to Clifton and Dingler (1984). The bed sediment porosity was set to n = 0.4, a typical value for coastal environments, and the bed sediment corresponds to typical fine quartz sand with specific gravity equal to S = 2.65. In total, four cases were simulated, and the flow and sediment parameters are presented in Table 1. All simulations started with the fluid and the sediment at rest, around 200-1500 wave periods (depending on the case) were required for the bed geometry to reach equilibrium conditions and another 20 wave periods were simulated for results sampling and averaging.

Table 1. Flow and sediment parameters of the four cases

#	ψ	a_o/D_g	U_o (m/s)	a_o (m)	T (s)	D_g (mm)	Re
1	20	500	0.22	0.075	2.139	0.15	14500
2	20	1000	0.22	0.150	4.278	0.15	29000
3	50	500	0.35	0.075	1.354	0.15	23000
4	50	1000	0.35	0.150	2.708	0.15	46000

In Figure 1, ripple creation for Case 1 is presented. Due to the small value of the mobility parameter, the net sediment transport rate is small, especially in the beginning of the simulation. It takes almost 100 wave periods for the initial hump to grow and cause the creation of ripples. Then, the computational domain is almost fully covered with small ripples that grow slowly and begin to present spanwise two-dimensionality. After about 200 wave cycles, the bed geometry consists of five consecutive ripples. During the next 200 waves, phenomena of ripple merging occur, with ripple number 3 (at 200T) slowly dividing and merging with ripples number 2 and 4. After 400 wave cycles, the bed geometry consists of four consecutive ripples, which is close to the predicted final form. During the next 500 waves, phenomena of ripple annihilation occur, with ripple number 4 slowly vanishing, due to the larger vortices generated by ripples 1 and 3. After about 900 wave cycles the bed finally converges to its equilibrium geometry, composed of three consecutive ripples, with lengths equal to $1.25 \cdot a_o$ and heights equal to $0.188 \cdot a_o$. For the next 500 wave periods the ripples retain these equilibrium dimensions.

The spatio-temporal evolution of the spanwise-averaged ripple profile is presented in Figure 2 for all cases of Table 1.

The initial perturbations grow fast in height for all cases. In time, small structures are generated and grow (ripple creation and growth), while others get smaller until they disappear (ripple annihilation). Phenomena of ripple merging are observed with ripple crests approaching each other, until they finally merge into one, see for example at about 400T and 900T in Figure 2a, at 500T and 1500T in Figure 2b, and at 400T in Figure 2d. In all cases, the bed converges to its equilibrium geometry composed of 3 ripple lengths, but at different time for each case.

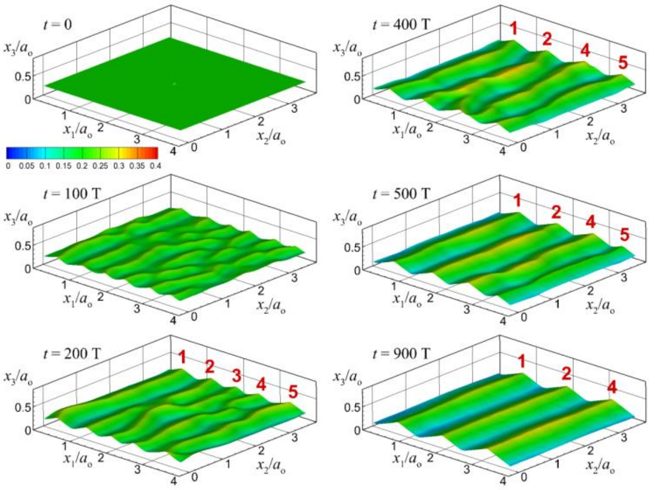

Figure 1. Numerical result of ripple creation from a flat bed for ψ = 20 and a_o/D_g = 500. The equilibrium conditions are reached after about 900 wave cycles.

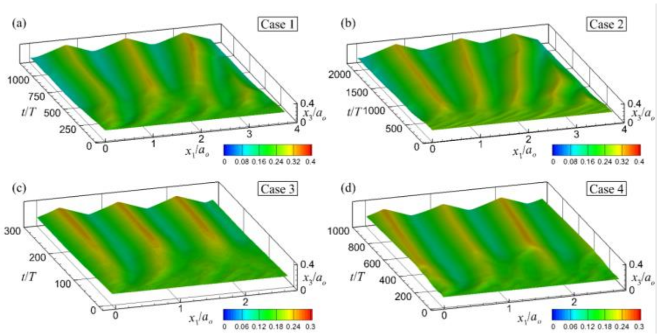

Figure 2. Ripple creation and evolution in time and space for all cases examined. The phase-averaged ripple profile is presented in each wave period.

Regarding the turbulent field in the vicinity of the ripples, the phase- and spanwise-averaged velocity field (vectors) and turbulent kinetic energy, k, (contours) are presented in Figure 3 for all cases in Table 1. Two phases of the wave period are shown, one at $2T/8$, i.e., at the maximum onshore free-stream velocity, and one at $6T/8$, i.e., at the maximum offshore free-stream velocity, when k acquires its maximum values. In general, a similar qualitative behavior is observed for all four cases. The turbulence development in the specific phases is highly associated with periodic vortex shedding phenomena which occur during each half-cycle of the flow. In the first two cases (ψ = 20), the turbulent kinetic energy is present both onshore and offshore of the ripple crest at both phases, due to flow separation at the ripple crest and slow dissipation due to the large ripple dimensions. As expected, the same value of ψ in the first two cases results in a similar ripple shape, which in turn results in a similar behavior of k, with equal maximum values. In the last two cases (ψ = 50), the turbulent kinetic energy is mostly generated onshore of the ripple crest in both phases, due to flow separation on the onshore flank. The turbulent kinetic energy is in general higher for all cases during maximum onshore free-stream velocity ($2T/8$) than during maximum offshore free-stream velocity ($6T/8$), due to the external flow skewness.

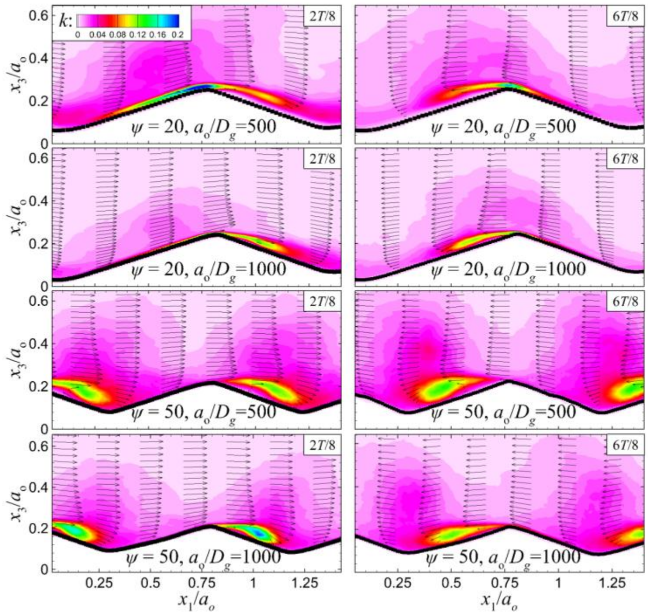

Figure 3. Phase- and spanwise-averaged velocity field (vectors) and turbulent kinetic energy, k/U_o^2 (contours), at two phases for Cases 1-4 in Table 1, respectively.

ACKNOWLEDGEMENTS

This work is supported by computational time granted by the Greek Research & Technology Network at the National HPC facility – ARIS.

REFERENCES

Clifton, H.E., & Dingler, J.R. (1984). Wave-formed structures and paleoenvironmental reconstruction. *Mar. Geol*. 60 (1-4), 165–198.

Dimas, A.A., & Chalmoukis, I.A. (2020). An adaptation of the immersed boundary method for turbulent flows over three-dimensional coastal/fluvial beds. *Appl. Math. Model*. 88, 905–915.

Dimas, A.A., & Leftheriotis, G.A. (2019). Mobility parameter and sand grain size effect on sediment transport over vortex ripples in the orbital regime. *J. Geophys. Res. Earth Surf.* 124 (1), 2–20.

Engelund, F., & Fredsøe J. (1976). A sediment transport model for straight alluvial channels. *Hydrol. Res.* 7(5), 293–306.

Leftheriotis, G.A., & Dimas, A.A. (2022). Morphodynamics of vortex ripple creation under constant and changing oscillatory flow conditions. *Coastal Eng.* 177, 104198.

Smagorinsky, J. (1963). General circulation experiments with the primitive equations I. The basic experiment. *Mon. Weather Rev*. 91(3), 99–165.

Large-Eddy Simulation of Turbulent Oscillatory Flow and Mixed-Grain Sediment Transport over Fixed Bed Ripples

Tsipas I.G.[1,*], Leftheriotis G.A.[1] and Dimas A.A.[1]

[1] Department of Civil Engineering, University of Patras, 26500, Patras, Greece

*corresponding author:
e-mail: up1054975@ac.upatras.gr

INTRODUCTION

Mixed-grain sand significantly impacts sediment transport by influencing hydrodynamic interactions, bedform evolution, and sediment mobility. Natural sediment beds contain varying grain sizes, leading to complex transport mechanisms that affect bedload and suspended sediment flux, complicating sediment transport predictions. Grain-specific critical shear stress varies due to differences in particle protrusion, drag forces, and near-bed turbulence.

Studies highlight the importance of considering these variations when modeling sediment transport, as they directly impact the initiation and movement of different grain sizes. Bed roughness, influenced by grain-size heterogeneity, plays a crucial role in sediment mobilization. Coarser grains increase flow resistance, enhancing transport rates and altering wave-boundary layer dynamics. These interactions significantly impact ripple formation in oscillatory flows, where vortex structures shape the seabed. The mobility parameter ψ and the normalized sediment size a_o/D_g control ripple evolution, affecting sediment transport efficiency.

This study examines the impact of mixed-grain sediments on transport processes, integrating numerical simulations to assess the influence of grain-size variability on sediment dynamics in coastal and offshore environments.

METHODOLOGY

In realistic sediment transport problems, one has to deal with a grain-size distribution curve that follows a log-normal distribution (Fredsøe and Deigaard, 1992), which is discretized in "k" number of fractions. This study employs Large-Eddy Simulation (LES) to investigate the dynamics of mixed-grain sand transport under oscillatory wave-induced flow over fixed bed ripples. The governing fluid equations, rendered dimensionless, are the continuity and the Navier-Stokes, and they are solved numerically, incorporating the Smagorinsky eddy-viscosity model for the subgrid-scale (SGS) stresses. The immersed boundary (IB) method (Dimas and Chalmoukis, 2020) is applied to enforce the non-slip boundary condition on the seabed.

Bedload transport is computed using the formulation in Engelund and Fredsøe (1976), adapted for grain-size fractions, while suspended sediment evolution follows an advection-diffusion equation, with settling velocities calculated separately according to Hallermeier (1981) for each sediment fraction "k". A hide-exposure factor (Wu et al., 2002) refines the critical Shields parameter, accounting for size-dependent entrainment thresholds by calculating the probabilities of each "k" fraction being hidden or exposed by the other fractions. Numerical discretization in time utilizes a two-stage time-splitting scheme combined with second-order Adams-Bashforth method. External wave forcing follows a second-order Stokes wave model, ensuring realistic flow boundary conditions. Numerical discretization in space is based on a 2nd-order central finite-difference scheme; a typical computational domain is shown in Figure 1.

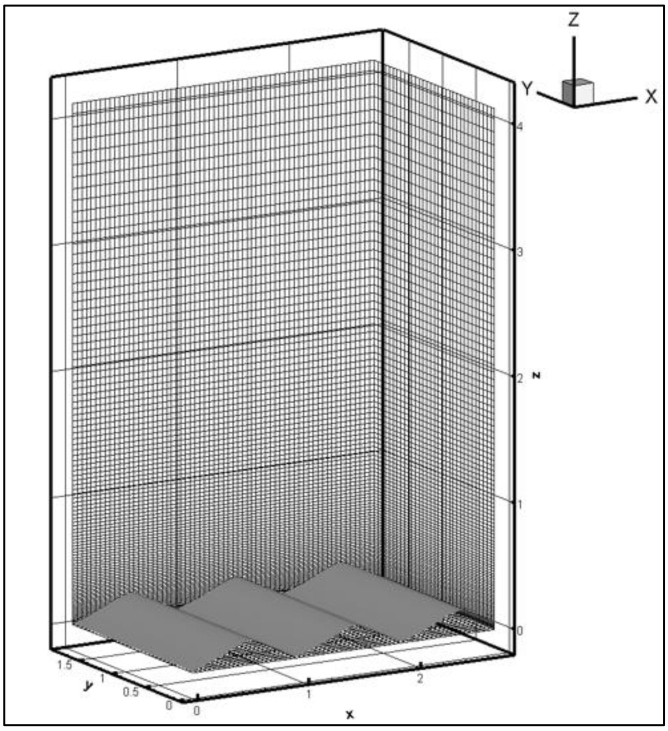

Figure 1. Sketch of a typical computational domain with Cartesian grid for the simulation of oscillatory flow over ripples. The rippled bed is immersed in the Cartesian grid.

The mixed grain-sand (comprising 5 fractions with diameters D_{10}=0.25 mm, D_{30}=0.35 mm, D_{50}=0.44 mm, D_{70}=0.53 mm, and D_{90}=0.66 mm) and the flow parameters in the experiments by Van der Werf et al. (2007) were used and out model was validated by comparison with the corresponding experimental data of sediment transport rates, vorticity structures, and concentration profiles. Results provide insights into size-selective sediment transport, phase-lag effects, and morphodynamic responses under varying hydrodynamic conditions.

RESULTS AND DISCUSSIONS

The LES simulations reveal distinct transport mechanisms for mixed-grain sediment under oscillatory flow, with bedload and suspended load exhibiting strong size-selective behavior. Analysis of Shields parameter variations shows that incorporating the hiding-exposure factor (Wu et al., 2002) significantly alters entrainment thresholds: finer grains require higher shear stress to mobilize, while coarser grains experience reduced thresholds due to preferential exposure. The velocity and vorticity fields (Figure 2) demonstrate strong vortex structures that peak near the bed during flow reversal, enhancing sediment uplift and entertainment (Figure 3).

Fine-grained fractions (D_{10}–D_{30}) experience prolonged suspension due to turbulence, whereas coarser fractions (D_{70}–D_{90}) primarily contribute to bedload transport, particularly at ripple crests where shear stress peaks. The suspended load is highest at flow reversal phases, with vortex-induced uplift enhancing sediment entrainment. Period-averaged velocity (Figure 2) and sediment flux profiles demonstrate that suspended transport is dominated by fine fractions, while coarser grains display onshore-directed bedload transport, reinforcing morphodynamic stability of ripple formations (Figure 4). The comparison with van der Werf et al. (2007) experimental data shows strong agreement, validating the numerical approach. These findings highlight the role of grain sorting in transport dynamics, with turbulence-driven phase-lag effects altering net transport rates. The results have implications for coastal morphodynamics modeling, improving predictions of sediment redistribution in natural environments.

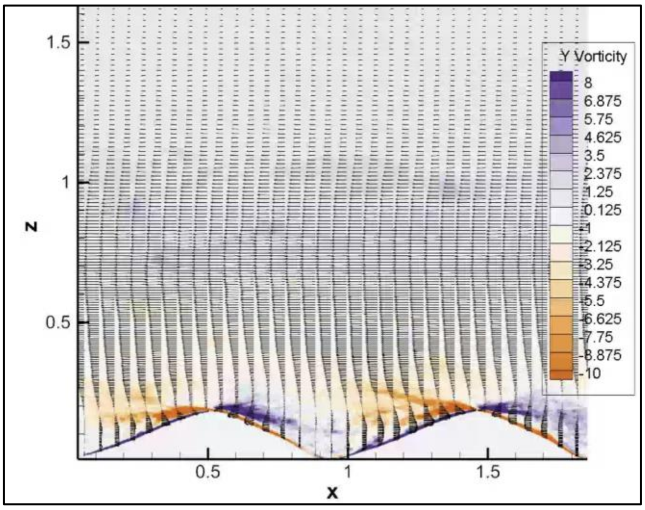

Figure 2. The period- and spanwise-averaged velocity field (vectors) and Y vorticity field.

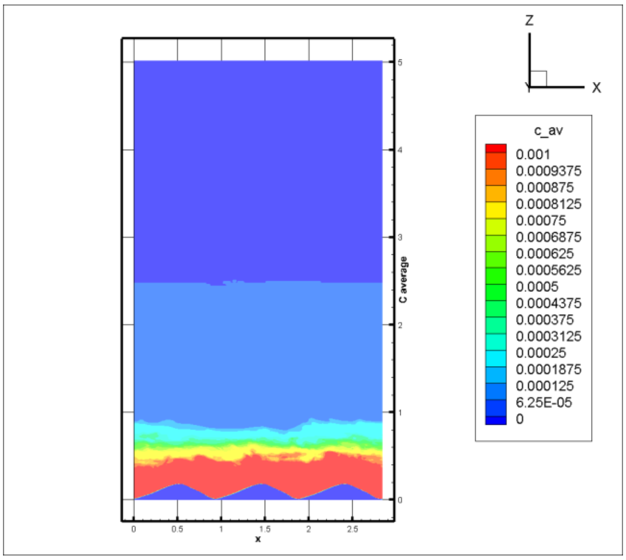

Figure 3. Period-average suspended sediment (c) of the smallest sediment fraction of diameter size 0.25 mm.

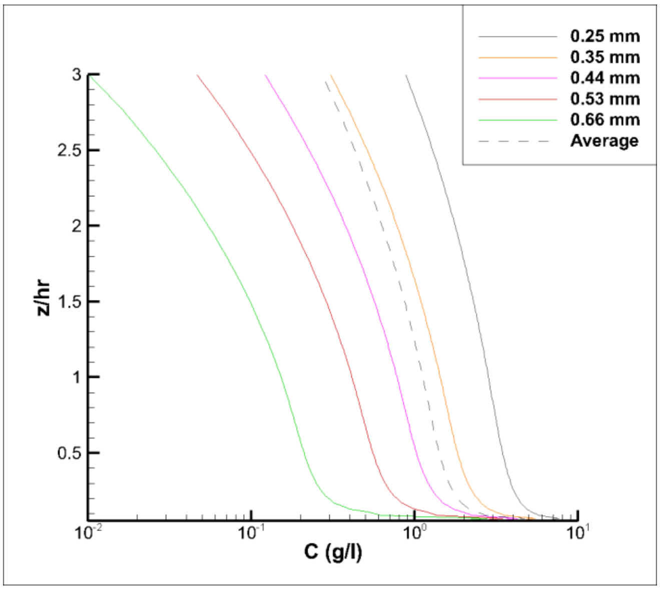

Figure 4. Profiles of the mean suspended sediment concentration of each sediment size fraction up to 3 hr.

ACKNOWLEDGEMENTS
This project has received funding from the European Union's (EU) Horizon Europe Framework Programme (HORIZON) under Grant Agreement No. 101072443 as a MSCA Doctoral Network (HORIZON-MSCA-2021-DN-01). The work was also supported by computational time granted by the Greek Research & Technology Network at the National HPC facility – ARIS.

REFERENCES
Dimas, A.A., & Chalmoukis, I.A. (2020). An adaptation of the immersed boundary method for turbulent flows over three-dimensional coastal/fluvial beds. *Appl. Math. Model.* 88, 905–915.
Dimas, A.A., & Leftheriotis, G.A. (2019). Mobility parameter and sand grain size effect on sediment transport over vortex ripples in the orbital regime. *J. Geophys. Res. Earth Surf.* 124(1), 2–20.
Fredsøe, J., & Deigaard, R. (1992). Mechanics of Coastal Sediment Transport. World Scientific.
Hallermeier, R.J. (1981). Terminal settling velocity of commonly occurring sand grains. *Sedimentology* 28(6), 859–865.
van der Werf, J.J., Doucette, J.S., O'Donoghue, T., & Ribberink, J.S. (2007). Detailed measurements of velocities and suspended sand concentrations over full-scale ripples in regular oscillatory flow. *J. Geophys. Res. Earth Surf.* 112, F02012.
Wu, W., Wang, S.S.Y., & Jia, Y. (2000). Nonuniform sediment transport in alluvial rivers. *J. Hydraul. Res.* 38(6), 427–434.

Ultimate Limit State Mooring System Design for a 10 MW Semi-submersible Offshore Wind Turbine in the Aegean Sea

Konstantaras T.[1] and Loukogeorgaki E.[1,*]

[1] Department of Civil Engineering, Aristotle University of Thessaloniki, Thessaloniki, Greece

*corresponding author:
e-mail: eloukog@civil.auth.gr

INTRODUCTION

Floating Offshore Wind Turbines (FOWTs) present nowadays a keystone in the renewable energy sector towards a low-carbon energy prospect in Europe. Aiming to operate at large water depths, where stronger and more consistent winds exist, FOWTs boost the deployment of large capacity WTs. Hence, floaters suitable for supporting those WTs along with relevant mooring systems have to be designed and assessed (e.g., Zhao et al., 2021). A mooring system provides adequate station-keeping to the whole floating structure, with its design process being driven by requirements related to strength, fatigue life and floater's offset. In this paper, we propose a spread catenary mooring system for a 10 MW semi-submersible FOWT deployed in the Aegean Sea and we assess the moored FOWT's dynamic behaviour under extreme environmental conditions focusing on the mooring system's Ultimate Limit State (ULS) design.

METHODOLOGY

The mooring system is designed for the semi-submersible platform (Figure 1) developed by Vagenas et al. (2023). The platform (35 m draft) supports the DTU 10 MW reference WT (Yu et al., 2017), with the tower being suitably modified to be adjusted to the platform's geometry. The FOWT is taken to be deployed east of Crete at 100 m water depth.

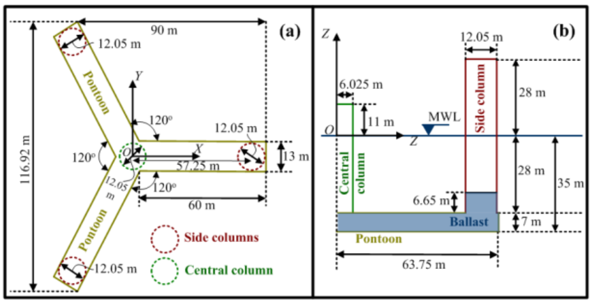

Figure 1. Examined platform's top **(a)** and side **(b)** view (ballast height adjusted to the present mooring system).

The ULS design process of Figure 2 is applied consisting of five stages (S1~S5). Initially (S1), the Mooring Lines' (MLs) characteristics (i.e., number, material, diameter, length and configuration) are determined and a preliminary analysis is conducted to calculate the FOWT's static equilibrium position (S2), including potential ballast height adjustments, and the platform's natural periods (S3). A fully-coupled, integrated time-domain dynamic analysis of the moored FOWT follows (S4), where floater's responses and MLs' tensions are evaluated for specific Design Load Cases (DLCs) related to extreme environmental conditions. Finally, the mooring system is assessed for specific ULS design requirements (S5). S5.2 requirement is achieved by ensuring that a portion of each ML always lies on the seabed. As for S5.1, this requirement indicates that the ML's design tension, T_{DES}, should be smaller than its characteristic strength, S_c. This condition is described by Eq. 1 (DNV, 2021), where $T_{c,mean}$ and $T_{c,dyn}$ are the characteristic mean and dynamic tension, *MBS* is the minimum breaking strength, while Y_{mean} and Y_{dyn} are the mean and dynamic load factors respectively equal to 1.5 and 2.2 (ULS, consequence class 2).

$$SF = T_{DES} / S_c < 1.0 \Rightarrow \left(Y_{mean}T_{c,mean} + Y_{dyn}T_{c,dyn}\right) / \left(0.95MBS\right) < 1.0 \qquad (1)$$

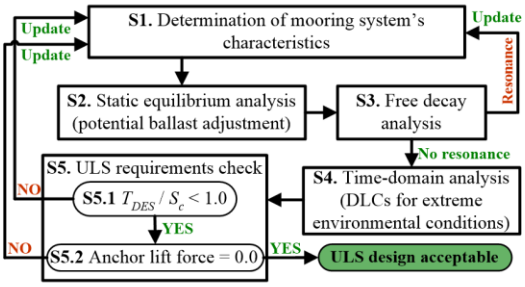

Figure 2. ULS mooring system design process.

MOORING SYSTEM CHARACTERISTICS

Starting with S1 (Figure 2) and based on the geometry of the examined platform, a 3-leg spread catenary mooring system is proposed. The system consists of three identical MLs made of Grade R4 studless chain. The chain nominal diameter is selected equal to 132 mm with breaking and proof load of 15,965 kN and 11,187 kN respectively. The axial stiffness and the submerged weight per unit length have been calculated equal to 1.488E+06 kN and 2.9403 kN/m. By deploying the well-known catenary equations and assuming the chain proof load as the maximum tension at the top of each ML for minimum required length calculations, the total length of each ML is selected equal to 771.30 m. The MLs fairleads are placed 21 m below the MWL and a pretension of 708 kN is applied leading to ~164 m hanging length. The mooring system's layout is shown in Figure 3.

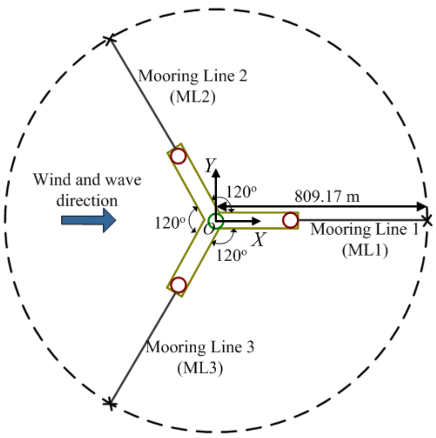

Figure 3. Layout of the examined mooring system.

RESULTS AND DISCUSSION

The static equilibrium analysis (S2, Figure 2) of the FOWT moored with the proposed mooring system led to an 0.10 m reduction of the ballast height inside the platform's columns compared to Vagenas et al. (2023) for achieving the 35 m draft. Accordingly, the surge, heave and pitch static offsets have been calculated equal to 0.433 m, 0.0 m and -0.0818 deg respectively, indicating good stability. As for the free decay simulations (S3, Figure 2), the platform's natural frequencies equal to 0.0055 Hz (surge & sway), 0.0433 Hz (heave), 0.0403 Hz (roll & pitch) and 0.0061 Hz (yaw) do not fall close to the 1P and 3P frequencies (i.e., no resonance phenomena occur).

The moored FOWT's dynamic analysis (S4, Figure 2) is performed for different DLCs (Table 1) related to extreme environmental conditions based on DNV (2021). For all DLCs, we consider stochastic wind and waves of 0 deg direction (Figure 3) and 5400 s total simulation time. Wave conditions have been calculated for a 50 years return period. The mean wind velocity at the hub height (U_{hub}) for DLC1~DLC5 corresponds to this return period. For the rest DLCs, U_{hub} has values along the WT's power curve range, where 11.4 m/s and 24.0 m/s are the rated and cut-out speed.

Table 1. Examined DLCs.

No	Yaw misalignment (deg)	H_s (m) & T_p (s)	U_{hub} (m/s)	WT
DLC1	0	7.58 & 11.82	32.3	Parked
DLC2	8			
DLC3	-8			
DLC4	180			
DLC5	90			
DLC6	0	7.58 & 11.82	8.0	Normal operation
DLC7			11.4	
DLC8			18.2	
DLC9			24.0	

Figure 4a shows part of the surge time-series indicatively for DLC1, DLC2 and DLC5 (parked WT) as well as for DLC6~DLC7 (operational WT). The 90 deg yaw misalignment (DLC5) results to a larger static offset of the FOWT along *OX* and, thus, to larger surge values compared to DLC1~DLC2. This trend is more pronounced for DLC6~DLC7 due to the WT's operation that leads to a substantial increase of the rotor thrust. As for ML2, which corresponds to the most heavily loaded ML (Figure 3), the tension at the top (T_{top}) of this ML (Figure 4b) follows the variation pattern of the surge responses. Under operational conditions (DLC6~DLC7) larger T_{top} values and a more intense T_{top} time variation are observed compared to the DLCs, where the WT is parked.

Finally, regarding the MLs' assessment according to the ULS design requirements (S5, Figure 2), Table 2 includes relevant results for ML2 and for the DLCs of Figure 4. Eq. 1 has been applied for $T_{c,mean}$ and maximum $T_{c,dyn}$ at the top of ML2, and *MBS* equal to the proof load. It can be seen that for all DLCs both ULS design requirements are well satisfied. Similar conclusions can be drawn for the rest MLs.

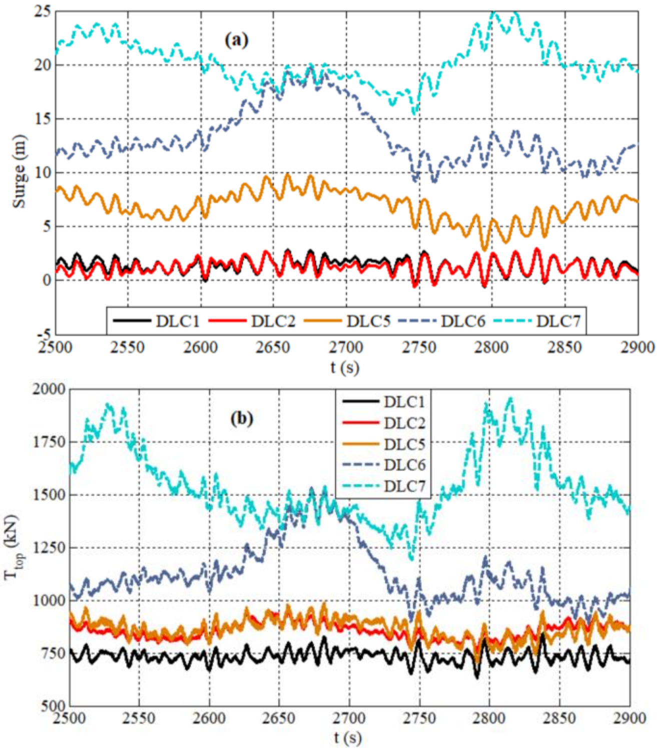

Figure 4. Time variation of FOWT's surge **(a)** and T_{top} of ML2 **(b)** for DLC*i*, *i*=1, 2, 5, 6 & 7.

Table 2. ULS assessment results for ML2 (L_{bot} (m): Length of ML on the seabed).

	DLC1	DLC2	DLC5	DLC6	DLC7
SF	0.1344	0.1723	0.1910	0.4294	0.3552
L_{bot}	600.0	585.0	570.8	493.6	478.2

CONCLUSIONS

The results of the present paper indicate an efficient ULS MLs' design for a 10 MW semi-submersible FOWT deployed in the Aegean Sea that satisfies relevant design requirements. Further work is required including fatigue assessment of the proposed mooring system, as well as enhancement of its design considering cost-related issues additionally to pure structural performance requirements.

REFERENCES

DNV (2021). Floating wind turbine structures. DNV-ST-0119.

Vagenas, L.A., Panagiotidou, M., Loukogeorgaki, E., & Michailides, C. (2023). Design and time-domain analysis of a 10 MW semi-submersible floating offshore wind turbine. Proc. 2nd International Conference on Design and Management of Port, Coastal and Offshore Works (DMPCO 2023), Thessaloniki, Greece, 121–125.

Yu, W., Müller, K., Lemmer, F., et al. (2017). D4.2 Public definition of the two LIFES50+ 10MW floater concepts. Deliverable of LIFES50+ project.

Zhao, Z., Shi, W., Wang, W., Qi, S., & Li, X. (2021). Dynamic analysis of a novel semi-submersible platform for a 10 MW wind turbine in intermediate water depth. *Ocean Eng*. 237, 109688.

Design and Assessment of Three Catenary and Hybrid-Catenary Mooring Systems for a Semi-Submersible Wind Turbine

Manolas D.[1], Konispoliatis D.[2,*], Mavrakos S.[2] and Meleddu M.[3]

[1] iWIND Renewables S.A., Greece
[2] School of Naval Architecture and Marine Engineering, National Technical University of Athens, Greece
[3] Teufelberger-Redaelli Tecna S.p.A., Italy

*corresponding author:
e-mail: dkonisp@naval.ntua.gr

INTRODUCTION

Station-keeping systems are essential for floating Wind Turbines (WT) to limit their excursion and maintain the orientation of the structures under the action of the combined effects of wave, current, and wind induced environmental loading. In recent years, numerous studies have been presented in the literature focusing on the design, analysis, and simulation of various mooring system types, aiming to enhance both safety and cost-effectiveness. This study examines the design and assessment of three mooring system configurations: a conventional catenary mooring system with chains and two hybrid catenary systems incorporating steel wire ropes (**SWR**) and polyester ropes (**PR**). These systems are evaluated for a semi-sub floater operating under harsh weather conditions (offshore class OA) in the North Sea at a water depth of 200 m. The semi-submersible floater (Figure 1) employed (Yu et al,. 2021) supports the DTU 10MW reference wind turbine (Bak et al., 2013) and is an up-scaled version of the semi-submersible platform originally defined in the OC4 project (Robertson et al., 2012). Table 1 provides an overview of the platform's main structural characteristics, while Table 2 shows the lower natural frequencies of the coupled system.

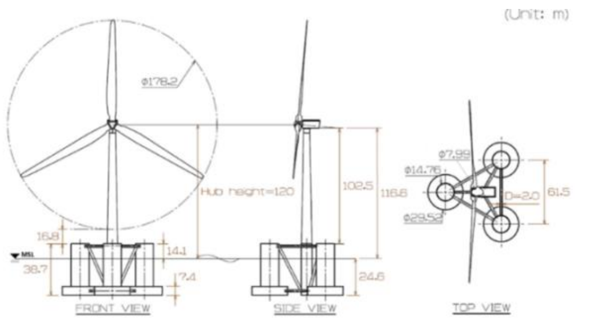

Figure 1: Schematic representation of the 10MW semi-submersible platform (Yu et al. 2021)

DESIGN SPECIFICATIONS

The following design specifications were considered: (a) The design process is based on the ABS-195 standard, using the same numerical tools and methodology for all three designs. (b) A redundant mooring system layout consisting of three pairs of lines (3x2 layout) with an 8° angle between the lines within each pair, anchored using drag embedded anchors (Figure 2). (c) Each pair of mooring lines is connected to the bottom of the floater at the platform corners, with fairleads located 24.6 m below the still water level, and oriented at angles 0°, 120°, and 240°. (d) Each mooring line has a length of 700 m. (e) The design lifetime is 25 years. (f) A design (quasi-static) offset of 15 m is considered for intact conditions under a horizontal design load of 2000 kN. (g) The minimum tension of the polyester ropes is required to be greater than 5% of the minimum breaking load (MBL). (h) The rope-chain connection must not touch the seabed under intact conditions (mandatory for synthetic ropes).

Table 1: Structural characteristics of the 10MW semi-submersible platform

Total mass (inlc. ballast)	24977 t
Platform IPx/IPy about CM	$1.92 \cdot 10^7$ tm^2
Platform IPz about CM	$3.75 \cdot 10^7$ tm^2
Platform CM location below SWL	16.56 m
Platform Draft/Freeboard	24.6 / 14.1 m
Diameter of main/outer upper/lower column	8.0 / 14.8 / 29.5 m
Column Spacing	61.5 m

Table 2: Lower natural frequencies of the coupled system

Floater surge / sway rigid body mode	0.010 Hz
Floater yaw rigid body mode	0.014 Hz
Floater roll / pitch rigid body mode	0.036 Hz
Floater heave rigid body mode	0.053 Hz
Tower 1st side-side bending mode	0.326 Hz
Tower 1st fore-aft bending mode	0.333 Hz

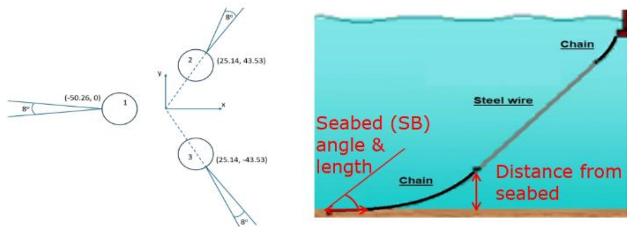

Figure 2: Top view of the 3x2 mooring system layout (left) and schematic representation of the hybrid catenary mooring system consisting of chain and steel or polyester rope (right).

HYDRODYNAMIC ANALYSIS

The hydrodynamic loads acting on the floater-including the exciting wave loads, hydrodynamic parameters (added mass and damping coefficients), and mean drift forces- were determined using theoretical formulations (Mavrakos, 1995) and the numerical software ANSYS AQWA. Figure 3 presents the horizontal exciting force and the mean drift force on the structure. Predictions by the two methods show very good agreement.

MOORING SYSTEM DESIGN

The mooring line design process is based on a global hydro-servo-aero-elastic analysis of the coupled system in the time domain using hGAST solver (Manolas, 2020), supplemented by quasi-static and frequency domain dynamic analyses. The following technical details, in accordance with ABS-195, are considered in the design process: (a) Three Limit states are evaluated: Fatigue (FLS), Ultimate (ULS), and Accidental (ALS). (b) An annual diameter reduction of 0.4 mm due to corrosion and wear is accounted for; (c) Marine growth is considered with a density of 1300 kg/m^3 and a thickness of 50 mm. Table 3 presents the finalized mooring system designs that meet the specified design specifications. The table includes the length of a single mooring line (i.e. chain-rope-chain) from anchors to fairleads, as well as the nominal diameter, linear mass density in air for both the chain and the rope, and the applied pretension. In all cases, studless chain grade R3 was used. Figure 4 shows the quasi-static offset motion of the floater as a function of the pretention per mooring line for the three finalized designs under a design load of -2000kN. The horizontal, dashed black line at a 15m offset represents the specified design criterion. Table 4 provides the Ultimate, Accidental and Fatigue limit states considered in the design of the chain and the rope. Additionally, it includes the supplementary design specifications for the ropes, namely the minimum dynamic tension under ULS (intact) conditions normalized by MBL (T_{MIN}) and the minimum distance of the chain-rope connection from the seabed under ULS and ALS (Z_{SB}).

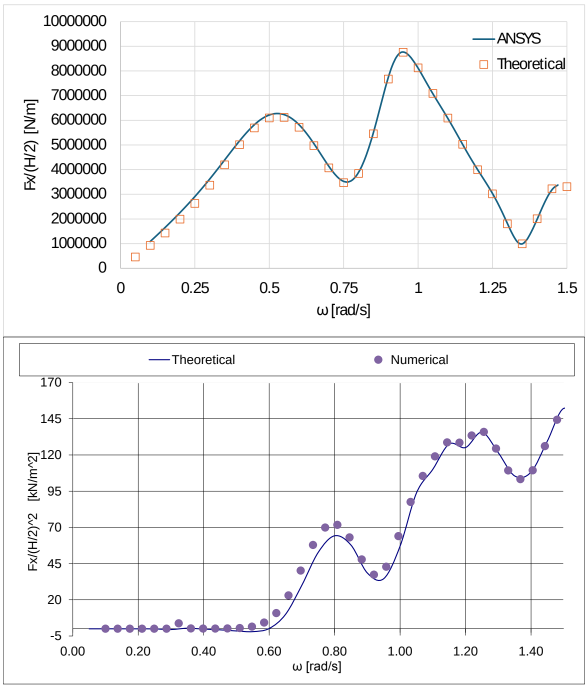

Figure 3: Horizontal exciting force (top) and mean drift force (bottom) acting on the structure.

CONCLUSIONS

Based on the developed mooring design and analysis for a semi-submersible floater under harsh weather conditions (Offshore Class OA) at a water depth of 200 m, suitable for supporting a 10MW WT, the following technical conclusions were drawn:

(a) All three mooring system designs considered - namely, the conventional catenary system with chains and the two hybrid catenary systems with steel wire or polyester ropes - are viable solutions, leading to similar dynamic behavior of the coupled floating structure. Both rope materials can be effectively used for the stationkeeping of the semi-submersible floater.

(b) In all cases, the design of chains is driven by fatigue, whereas both types of rope are governed by extreme loading conditions, being in-line with findings from other studies.

(c) For the considered (quasi-static) design offset of 15 m under intact conditions, the use of ropes in the hybrid systems reduces both fatigue and extreme loading on the mooring lines. This is reflected in the smaller chain diameters required in the hybrid systems. Specifically, the concluded chain diameter for the hybrid system with steel wire ropes is 147 mm, while for polyester ropes, it is 152mm. In contrast, the conventional catenary system requires a chain diameter of 162 mm for the same design lifetime of 25 years.

Table 3: Finalized mooring system designs

Mooring System	Length [m]	Chain d [mm]	Chain Linear dens [kg/m]	Rope d [mm]	Rope Linear dens [kg/m]	Preten-sion [kN]
Hybrid-SWR	400-270-30	147	430.0	80	32.6	689
Hybrid-PR	400-270-30	152	459.8	131	11.3	1030
Catenary	700	162	522.3	-	-	2043

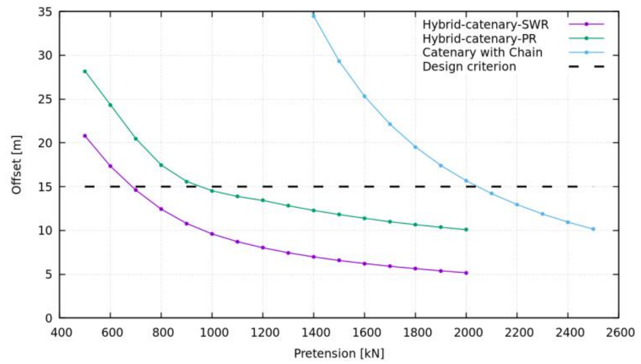

Figure 4: Floater offset motion vs pretention per mooring line for the static horizontal design load of -2000kN.

Table 4: Limit state equations and design criteria of the finalized mooring system designs

Mooring system	Chain FLS	Chain ULS	Chain ALS	Rope FLS	Rope ULS	Rope ALS	T_{MIN}	Z_{SB}
Hybrid-SWR	0.95	0.31	0.34	0.06	0.87	0.96	1.9%	2.5
Hybrid-PR	0.90	0.27	0.27	0.01	0.93	0.89	7.6%	10.7
Catenary	0.98	0.34	0.38	-	-	-	-	-

REFERENCES

ABS 195. (2021). Guide for building and classing floating offshore wind turbines.

Bak, C., Zahle, F., et. al. (2013). Description of the DTU 10 MW Reference WT, DTU Wind Energy Report-I-0092.

Manolas, D.I., Riziotis, V.A., Papadakis, G.P., Voutsinas, S.V. (2020). Hydro-Servo-Aero-Elastic Analysis of Floating Offshore Wind Turbines. *Fluids* 5(4), 200.

Mavrakos, S.A. (1995). User's manual for the software HAMVAB. School of Naval Architecture and Marine Engineering, Laboratory for Floating Structures and Mooring Systems, Athens, Greece.

Robertson, A., Jonkman, J., et al. (2014). Definition of the Semisubmersible Floating System for Phase II of OC4. Offshore Code Comparison Collaboration Continuation (OC4) for IEA Task.

Yu, Y., Pham, T.D., Shin, H., Ha, K. (2021). Study on the motion characteristics of 10MW superconducting floating offshore wind turbine considering 2nd order wave effect. *Energies* 14, 6070.

3rd International Conference on
Design and Management of Port, Coastal and Offshore Works

Patras, Greece, May 7-9 2025

Comparison of CFD Simulations and Experimental Results for Floating Tension-Leg Platforms

Tsakalomatis D.[1,*], Papadopoulou S.[1], Trompouki A.[1], Mouzakis F.[1], and Peppas A.[1]

[1] ETME S.A, Offshore BU, Kritis 2, N. Psychico, Athens, Greece

*corresponding author:
e-mail: d.tsakalomatis@etme.gr

INTRODUCTION

In recent years, the offshore wind industry has experienced significant growth, with floating platforms emerging as crucial solutions for deep-water installations. This paper conducts a comparative analysis of computational fluid dynamics (CFD) simulations and experimental results for floating tension leg platforms (TLPs), with a specific focus on the FloatMast platform deployed in the Aegean Sea.

PLATFORM DESCRIPTION

FloatMast® is an innovative floating tension leg platform (TLP) designed to optimize wind resource assessment for Offshore Wind Parks (OWPs). The platform integrates a meteorological mast with remote sensing devices to deliver high-accuracy wind measurements. Beyond wind data collection, the system supports environmental monitoring, met-ocean measurements, and marine space surveillance, providing comprehensive ocean environment observation capabilities. The platform's structural design consists of a main vertical central pontoon surrounded by four radially arranged pontoons, all rigidly interconnected. Tethers secure the peripheral pontoons to concrete block anchors, creating the tension leg system. For enhanced deployment and transportation flexibility, all five vertical pontoons and portions of the lower connecting beams incorporate pressure-controlled ballasting systems. The platform measures 22m x 22m x 25m, with a deck positioned 10m above mean sea level (AMSL) atop the central pontoon. This deck houses electrical cabinets, power production equipment, and other operational systems. The platform achieves energy autonomy and environmental sustainability through an integrated power system combining fuel cells, wind turbines, and solar panels.
Crowning the deck is a specially designed 30m Carl-C A/S self-supporting lattice meteorological mast, which extends to a total height of 44.0m AMSL. This robust mast configuration ensures stable and accurate measurement capabilities throughout the platform's deployment.

NUMERICAL MODEL

The numerical simulations were conducted using Flow-3D CFD software, a Volume of Fluid (VOF)-based multi-physics computational fluid dynamics package with proven reliability across various industries, from aerospace to marine applications. Prior to the final analysis, multiple preliminary assessments evaluated different geometries by varying critical parameters such as weight and depth, leading to the current optimized design. The selection of appropriate domain cell sizes proved crucial for balancing computational accuracy with efficiency. The mesh strategy incorporated a refined near-body region using 0.40m cubic cells surrounding the TLP body, applied both upstream and downstream to enable high-accuracy simulation of motion and fluid responses. In the intermediate region, cell sizes gradually increased from 0.80m to 1.60m, designed to capture wave energy absorption by the TLP while reducing volume of fluid instabilities in the physical model. The far-field region utilized 10.0m cells at the domain boundaries, with an extended domain length that prevented wave reflections and eliminated computational distortions. The results of the CFD simulation are shown in Figure 2 for the case of: Water depth= 65.0m, Regular wave height H = 10.40m and wave period T = 13.0sec.

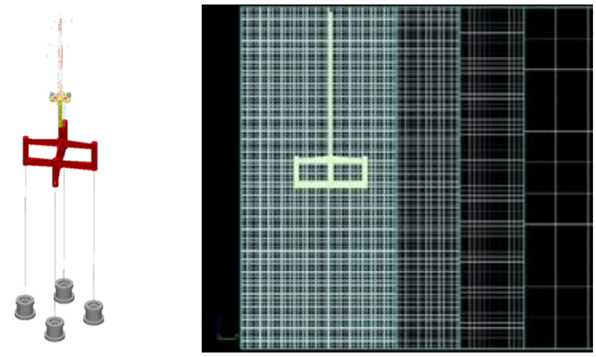

Figure 1. Model of FloatMast (left) and computational mesh (right).

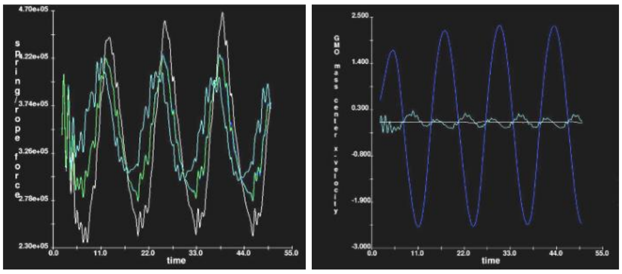

Figure 2. Numerical Model Results – Translations (m) (left) Rope Tension (N) (right).

EXPERIMENT

The experimental campaign utilized a 1:25 scale model based on Froude scaling methodology. Tests were conducted in a purpose-built tank with dimensions of 25m length, 1.60m width, and variable depth of 2.00m to 1.60m. The tank maintained a water depth of 1.20m, with a wave travel length of 15.00m and a wave dissipation beach length of 3.90m.To accurately simulate wind loading effects on the TLP structure, including the mast, top platform, and associated equipment (anemometers, antennas, Lidar), the team installed a "wind resistance" disc atop the TLP center pylon.

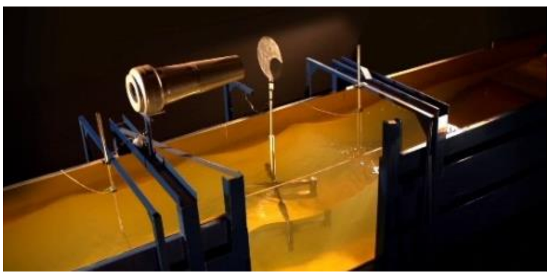

Figure 3: FloatMast tank experiment

Wind forces were generated using a fan with a nozzle system, producing a model-scale velocity of 6 m/sec in the same direction as the waves, corresponding to full-scale winds of 30 m/sec. Initial testing confirmed that wind effects were negligible compared to strong wave forces, aligning with theoretical predictions.

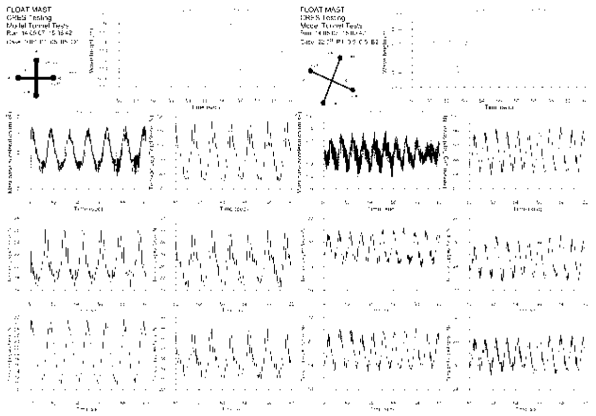

Figure 4: Example Sheets for experiment results

COMPARISON

Indicatively, CFD simulations have been performed for a wave (Height=6.5m |Period=7.85sec), corresponding to CRES experiment No. 22.50_P1_05_05_C4, in order to compare the tension forces on the wires.

Table 1: Maximum observed accelerations comparison.

Max Excitation Accelerations			
Wave Characteristics (Full-scale)	Model tests (m/s^2)	CFD Simulation (m/s^2)	Difference (%)
2.72m (H) |5.5sec (T)	0.60	0.70	14.3
3.57m (H) | 4.0sec (T)	0.50	0.40	-25.0
5.62m (H) | 7.95sec (T)	1.20	1.50	20.0
5.93m (H) | 6.8sec (T)	1.40	1.60	12.5
7.48m (H) | 8.1sec (T)	1.00	0.90	-11.1

Table 2: Maximum observed roll/pitch comparison.

Max Excitation roll/pitch			
Wave Characteristics (Full-scale)	Model tests (º)	CFD Simulation (º)	Difference (%)
2.72m (H) |5.5sec (T)	0.40	0.20	-100
3.57m (H) | 4.0sec (T)	0.30	0.25	-20
5.62m (H) | 7.95sec (T)	0.80	0.94	14.9
5.93m (H) | 6.8sec (T)	1.50	1.62	7.4
7.48m (H) | 8.1sec (T)	1.30	1.34	3.0

Table 3: Maximum Tendon Force comparison.

Max Loads on Tendons (kN)				
No. of rope	Model scale (λ = 1:25)	Full scale (x λ^3)	Full Scale CFD Simulation	Difference %
1	25.00	390,6	395	-1.1
2	32.50	507,8	450	11.4
3	29.30	457,8	425	7.2
4	33.00	515,6	430	16.6

CONCLUSIONS

The deviation in quantitative results between the CFD simulations and the tank test measurements remains within reasonable limits. Both experimental and numerical calculations not only yield identical qualitative dynamic behavior of the TLP but also demonstrate that the TLP's excitation angles remain extremely small, even under the most extreme environmental conditions.

The observed small deviations may be attributed to:

- Differences regarding the inability of the current CFD to simulate the wire rope accordingly (simulated as a spring with constant k)
- Experimental inaccuracies, such as minor variations in wave characteristics and slight differences in the initial lengths of the four strings (since tension force is highly sensitive to uneven string lengths).
- Large-scale viscous effects that are not accounted for by Froude similarity.

For most experiments and simulations, the recorded excitation angles are less than 1°. Furthermore, it is also expected that the TLP's excitation behavior will remain largely unchanged in higher waves with longer periods. A similar convergence was observed between the numerically calculated and experimentally measured tendon forces. The maximum recorded value at full scale was 515.6 kN (52.6 tons). Any differences in tendon forces can largely be accommodated by the tendons' high safety factors.

DEPLOYMENT – NEXT STEPS

As part of the FloatMastBlue Project, ETME (Coordinator) and STREAMLINED successfully delivered the first-of-its-kind offshore mini-TLP mast for offshore measurements, reaffirming the European Union's technological leadership in Offshore Wind Energy. The project fully implemented the FloatMast patent, demonstrating both the validity of the concept—through the provision of certified wind measurements—and its technical feasibility, as the platform successfully completed a 12-month operational campaign. The demonstration took place off the coast of Makronisos Island in the Aegean, Greece, at a water depth of 65 meters, marking a significant milestone for offshore wind development in the Mediterranean. Building on this demonstration, we will conduct new comparisons, leveraging both our extensive CFD expertise and our investment in SESAM, the specialized software for hydrodynamic and structural analysis of floating platforms developed by DNV. Over the years, we have gained significant experience in CFD simulations, and with the addition of SESAM, we have further expanded our technical capabilities. These tools will allow us to analyze the collected data in greater depth, validating our findings against tank tests and refining our predictive models for offshore platform behavior.

Figure 5: FloatMast during operation.

REFERENCES

Foussekis, D., & Mouzakis, F. (2021). Wind resource assessment uncertainty for a TLP-based metmast. *J. Phys. Conf. Ser.* 012018.

Peppas, A., Papatheodorou, T., & Tsakalomatis, D. (2015). An Innovative TLP platform for combined reliable and bankable offshore Cup Anemometer – Lidar wind measurement. Proc. European Offshore Wind Energy, EWEA Offshore 2015, Denmark, Copenhagen.

Analysis of the VolturnUS-S 15 MW Offshore Wind Turbine under Extreme Environmental Conditions in Greek Seas

Tsoukleri G.[1,*] and Dimas A.A.[1]

[1] Department of Civil Engineering, University of Patras, 26500, Patras, Greece

*corresponding author:
e-mail: up1047364@ac.upatras.gr

INTRODUCTION

The number of installed floating offshore wind turbines (OWTs) is expected to increase significantly in the upcoming years due to several key factors: (a) they are renewable energy projects compatible with the European Union's European Green Deal (EC, 2020), (b) they perform better compared to fixed-bottom OWTs as they are deployed in deeper waters where wind conditions are more consistent and stronger, leading to higher overall performance, and (c) they have milder environmental impact, in terms of visual and acoustic disturbance, as they are located far from coastal areas. These advantages are significant for Greece where the offshore wind energy potential is substantial (Spyridonidou et al., 2020). In the present study, OpenFAST was used to model the 15 MW wind turbine supported by a VolturnUS-S floating platform under environmental conditions, including extreme ones, representative of Greek seas.

METHODOLOGY

Numerical model

OpenFAST is an open-source simulation tool for the coupled dynamic response of OWTs developed by the National Renewable Energy Laboratory (NREL). OpenFAST combines aerodynamic, hydrodynamic, control and structural dynamic models to enable a coupled nonlinear aero-hydro-servo-elastic simulation (NREL, 2025). The modules used in this study are AeroDyn, HydroDyn, ElastoDyn, ServoDyn, InflowWind and MoorDyn. The turbulent wind loads were generated using TurbSim (Jonkman and Buhl 2006). Aerodynamic loads on the blades and tower are calculated using AeroDyn (NREL, 2025). The calculation is based on the blade element momentum (BEM) theory, under the assumption that blades are divided into elements whose aerodynamic forces are summed to calculate the total forces and moments on the turbine (Moriarty and Hansen, 2005). AeroDyn uses wind-inflow data generated by TurbSim and processed by InflowWind. These date are distributed at each grid point of a vertical rectangular grid including the OWT geometry above the sea surface (Platt et al., 2016). HydroDyn is a time-domain hydrodynamics module whose input is the position, orientation, velocities, and accelerations of the offshore structure, calculates the hydrodynamic loads and returns them back to OpenFAST. HydroDyn models regular or irregular waves and computes hydrodynamic forces using three main approaches: potential flow theory, strip theory (Morison’s equation), or a combination (NREL, 2025). ElastoDyn is a structural dynamic module that models the system geometries, sets the initial conditions for the floating system (NREL, 2025) and calculates displacements, velocities accelerations and reaction loads (Jonkman, 2017). MoorDyn, is used for solving the mooring line dynamics, using a lumped mass model where each mooring line is divided into equal segments. MoorDyn takes into account buoyancy, hydrodynamic and damping forces, weight, spring-damper forces from seabed contact and inner axial stiffness (Hall, 2015).

Floating system description

In the present study, the floating system consists of the University of Maine (UMaine) VolturnUS-S steel semi-submersible floater (Allen et al., 2020) supporting the IEA 15-MW reference wind turbine (Gaertner et al., 2020). The reference platform has a draft of 20m and consists of four columns, three-radial and one central. The outer columns are connected to the central column via three rectangular bottom pontoons and three radial struts as shown in Figure 1. The floating system is deployed in 200m water depth and is maintained in location by the use of three chain catenary mooring lines. Each mooring line has unstretched length of 850m and is connected to the fairleads located on the outer columns at 14 m below the still water level. The design parameters of the Umaine VolturnUS-S semi-submersible platform and its mooring system are summarized in Table 1.

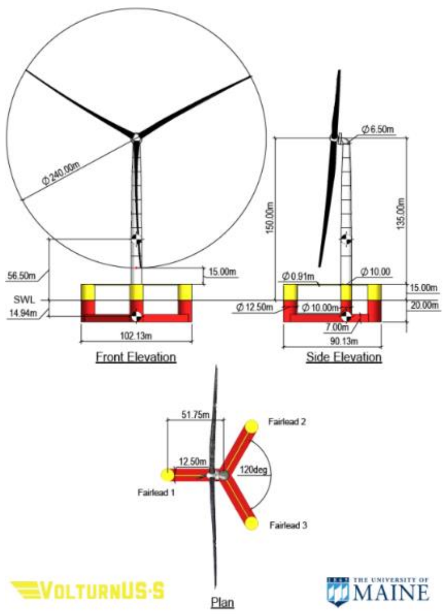

Figure 1. VolturnUS-S platform (Allen et al., 2020).

Table 1. Parameters of the VolturnUS-S semi-submersible platform and properties of the mooring system

Parameter	Value
Hull Displacement	20.206 m^3
Draft, Freeboard	20m, 15m
Mooring System Type	Chain Catenary
Depth of Anchor	200m
Depth of Fairlead	14m
Dry Line Linear Density	685 kg/m
Unstretched Length of line	850m
Nominal Chai Diameter	185m

The reference wind turbine has a three-bladed upwind design and is a Class IB direct-drive machine with a 240m rotor diameter, a hub height of 150m and a rated rotor speed of 7.56 rpm. The control system of the wind turbine is managed by the Reference Open-Source Controller (ROSCO) (Abbas et al, 2022). The main parameters for the IEA 15 MW reference wind turbine are presented in Table 2.

Table 2. Parameters of the IEA Wind 15-MW Turbine

Parameter	Value
Turbine rating	15 MW
Cut-in and cut-out wind speed	3 m/s, 25 m/s
Minimum rotor speed	5.0 rpm
Maximum rotor speed	7.56 rpm
Hub height	150m
Tower mass	1.263t

RESULTS AND DISCUSSION

In the present study, irregular wave time series were considered using the JONSWAP spectrum for environmental conditions representative of the Greek marine environment. The examined significant wave height (H_s), peak spectral period (T_p) and hub velocity (V_{hub}) values are presented in Table 3. Extreme conditions, including the extreme wave height (H_{s50},) with a return period of 50 years, are examined according to the IEC 61400-3 design standard (IEC 61400-3, 2009) and the corresponding critical Design Load Cases (DLCs) are shown in Table 4 where V_{50}, V_{e50}, V_{red50} are the 50-year return period wind velocity, extreme wind velocity averaged over three seconds and reduced extreme velocity, respectively, while H_{50}, is the extreme wave height and H_{red50} is the reduced wave height with a return period of 50 years.

Table 3. Details of environmental conditions.

V_{hub}	H_s	T_p	Return Period	Situation
25 m/s	2.92 m	5.58 s	1 year	operational
39.5 m/s	5.05 m	9.64 s	50 years	parked

Table 4. Selected DLCs

Situation	DLC	Wind	Waves
Operational	1.2	V_{hub}	H_s, T_p,
Parked	6.1a	V_{hub}= 0.95 V_{50}	H_s=1.09 H_{s50}
Parked	6.1b	V_{hub}=V_{e50}	H= H_{red50}
Parked	6.1c	V_{hub}=V_{e50}	H= H_{50}

In this study, the motions (translational and rotational) of the wind turbine under the combined action of wind and waves were analyzed. Typical results for the surge motion are shown in Figures 2 and 3. In Figure 2, the surge motion for DLC 6.1a (Table 3) is shown where the hydrodynamic loads were evaluated under both 1st and 2nd order approximations. It is observed that the 2nd order approximation results, in general, into higher excursions. In Figure 3, the surge motions for DLCs 1.2 and DLC 6.1a are compared. When the wind turbine is operational (DLC 1.2), the values of the surge motion vary between 0 m and 18.5 m with a mean value of 11.5 m, while when the wind turbine was parked (DLC 6.1a) due to high wind velocity, the maximum value of the surge motion is 13 m and the mean value is 7.3 m.

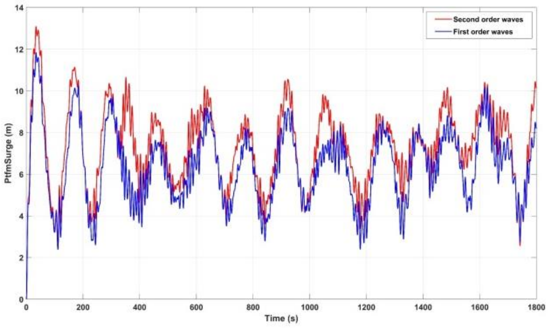

Figure 2. Surge motion for 1st & 2nd order waves (DLC 6.1a)

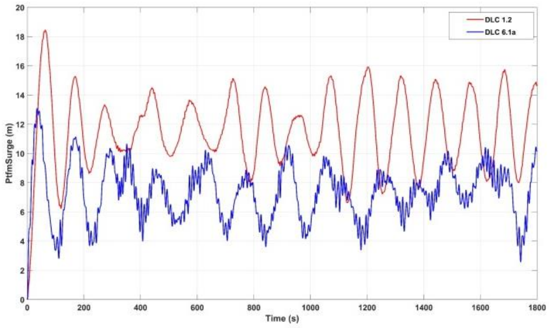

Figure 3. Surge motion for operational and parked condition

ACKNOWLEDGEMENTS

Author Georgia Tsoukleri was financially supported by the «Andreas Mentzelopoulos Foundation».

REFERENCES

Abbas, N., Zalkind, D., Pao, L., & Wright, A. (2022). A reference open-source controller for fixed and floating offshore wind turbines. *Wind Energy Sci.* 7 (1), 53–73.

Allen, C., Viscelli, A., Dagher, H., Goupee, A., Gaertner, E., Abbas, N., Hall, M., & Barter, G. (2020). Definition of the UMaine VolturnUS-S Reference Platform Developed for the IEA Wind 15-Megawatt Offshore Reference Wind Turbine.

Gaertner, E., Rinker, J., Sethuraman, L., Zahle, F., Anderson, B., Barter, G., Abbas, N., Meng, F., Bortolotti, P., Skrzypinski, W., Scott, G., Feil, R., Bredmose, H., Dykes, K., Shields, M., Allen, C., & Viselli, A. (2020). Definition of the IEA 15-Megawatt Offshore Reference Wind.

European Commission (2020). An EU Strategy to Harness the Potential of Offshore Renewable Energy for a Climate Neutral Future, COM/2020/741 final, Brussels.

Hall, M. (2015). MoorDyn User's Guide.

IEC 61400-3 (2009). Wind turbines - Part 3: Design requirements for offshore wind turbines

Jonkman, B., & Buhl, M., (2006). TurbSim user's guide.

Jonkman, J. (2017). FAST: An Open-Source Platform for Wind Turbine Multi-Physics Engineering Modeling. NAWEA 2017 Symposium. Ames, IA

Moriarty, P., & Hansen, A. (2005). AeroDyn Theory Manual

NREL (2025). OpenFAST – Documentation. Available from: https://openfast.readthedocs.io/en/main/.

Platt, A., Jonkman, B., & Jonkman, J. (2016). InflowWind User's Guide.

Spyridonidou, S., Vagiona, D.G., & Loukogeorgaki, E. (2020). Strategic Planning of Offshore Wind Farms in Greece. *Sustainability* 12(3), 905.

A Numerical Wave Tank for Evaluating Dynamic Response of Floating Wind Platforms

Dimakopoulos A.S.[1,*], Daskalothanasi L.[1], Paradeisiotis A.[2] and Stagonas D.[2]

[1] Laboratory of Hydraulic Engineering, Department of Civil Engineering, University of Patras, Rio Patras, 26500, Greece
[2] Department of Civil and Environmental Engineering, University of Cyprus, Nicosia, Cyprus

*corresponding author:
e-mail: a.dimakopoulos@upatras.gr

INTRODUCTION

Harvesting wind energy from floating wind turbines is an emerging technology which is expected to mature over the next decade, for example, according to McCoy et al (2024), global floating wind power output is expected to grow from <1GW currently to ~14GW until 2029 – and keep increasing thereafter. Floating wind infrastructure is already in planning / pre-licensing state in various states around the world and, notably, in Greece, there are already offshore sites considered for licensing and construction (Stefatos et al., 2024). Floating wind platforms encounter significant challenges in seakeeping, along with licensing and construction as ensuring that floating platforms remain in place throughout the design life of the offshore wind farm is crucial for keeping them in operation and securing return of investment. These challenges comprise the design and of platforms that will withstand hostile environmental conditions (extreme wave climate, currents and wind forcing) while maintaining a minimal response against wave excitation and mooring systems that will be capable of restraining the platform over several decades with minimum requirements for maintenance. Addressing these critical challenges requires accurate prediction of the moored floating platform motions, to estimate resonant frequencies, response amplitude operators as well as loads to the platform elements and mooring systems. This work presents a viable methodology for providing such estimates, relying on a validated numerical wave flume able to represent motion of floating structures restrained by a mooring system.

METHODOLOGY AND RESULTS

Computational Fluid Dynamics (CFD) models are an established tool for simulating flows around moving structures and have been applied to model prototype floating wind platforms (de Lataillade et al 2021, Aliyar et al 2024). The work of de Lataillade, 2019 greatly resolved numerical instability issues in CFD models relating to spurious added mass effects encountered in explicit partitioned schemes for two-way coupling of wave structure interaction processes, and was implemented in the finite-element based Proteus CFD toolkit (https://proteustoolkit.org/). More recently, Roenby et al (2023) used a similar approach to tackle these issues within the context of the finite-volume based OpenFOAM CFD toolkit, which is widely used in academia and industry as a numerical wave tank framework. Along with fluid structure interaction modelling capabilities, the OpenFOAM toolkit has built-in capabilities for reliable generation of realistic sea states (Jacobsen et al., 2012; Higuera et al., 2013; Dimakopoulos et al., 2016; Dimakopoulos and Higuera, 2021). In this work, we develop a numerical wave tank which is based on the OpenFOAM toolkit to perform free-oscillation tests and wave excitation tests on a floating wind platform which is under development (Figure 1). The approach uses the built-in dynamic mesh motion in OpenFOAM, which relies on deforming the mesh of the finite volume mesh to follow the motion of the rigid platform and subsequently correcting the Eulerian finite volume cell fluxed to account for the movement of the cell in a Lagrangian frame.

A series of tests were performed comprising free-oscillation and wave excitation tests. Free oscillation tests include heave and roll tests by displacing the platform from initial position of balance by 1m and 2 degrees, respectively (note that due to the axisymmetric layout, rotational oscillations do not depend on wave directions). Wave excitation tests were performed using a white noise spectrum to extract the response amplitude operator (RAO) across a range of periods from 6 to 18s, which is typical for wind-generated waves. Following extraction of natural periods, several tests were performed using shortened wave groups (Dimakopoulos et al 2025), to provide estimates of extreme loads on the platform and the mooring system. Results were compared with experimental data showing a good comparison between the two approaches.

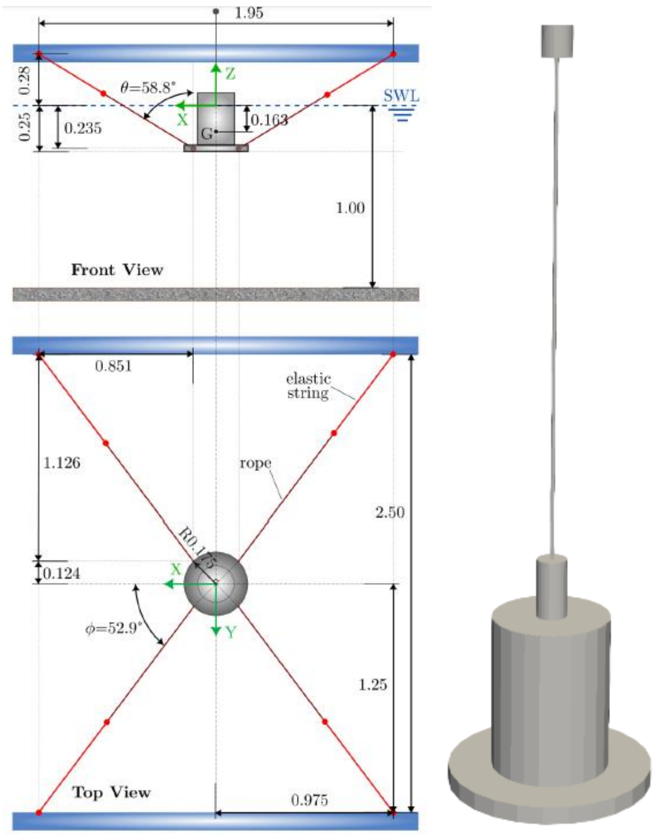

Figure 1. Left panel: experimental set-up (plan view and side view). Right panel: 3D CAD model used in the numerical wave tank

ACKNOWLEDGEMENTS

Andreas Paradeisiotis has received funding from the European Union's Horizon 2020 research and innovation programme under the Marie Sklodowska-Curie Grant Agreement No 101034403. We would also like to thank UCL's CEGE and Mechanical Engineering departments for allowing use of their experimental facilities.

REFERENCES

McCoy, Angel, et al. Offshore Wind Market Report: 2024 Edition. No. NREL/TP-5000-90525. National Renewable Energy Laboratory (NREL), Golden, CO (United States), 2024.

Stefatos et al. (2023) National Programme for Offshore Wind Energy (in Greek).

de Lataillade, T., Dimakopoulos, A., Kees, C., & Johanning, L. (2021). A coupling strategy for modelling dynamics of moored floating structures. Advanced Numerical Modelling of Wave Structure Interaction, CRC Press, 203–247.

Aliyar, S., Bredmose, H., Roenby, J., Tomaselli, P.D. & Sarlak, H. (2024). Directional focused wave group response of a Floating Wind Turbine: Harmonic separation in experiment and CFD. *arXiv preprint arXiv:2412.16718*.

de Lataillade, T. (2019). High-fidelity computational modelling of fluid–structure interaction for moored floating bodies.

Jacobsen, N.G., Fuhrman, D.R. & Fredsøe, J. (2012). A wave generation toolbox for the open-source CFD library: OpenFoam®. *Int. J. Numer. Methods Fluids* 70(9),1073–1088.

Higuera, P., Lara, J.L. & Losada, I.J. (2013). Realistic wave generation and active wave absorption for Navier–Stokes models: Application to OpenFOAM®. *Coastal Eng.* 71, 102–118.

Dimakopoulos, A.S., Cuomo, G. & Chandler, I. (2016). Optimized generation and absorption for three-dimensional numerical wave and current facilities. *J. Waterw. Port Coast. Ocean Eng.* 142(4), 06016001.

Dimakopoulos, A. & Higuera, P., 2021. Wave generation and absorption techniques. In *Advanced Numerical Modelling of Wave Structure Interaction*, CRC Press, 1–35.

Dimakopoulos A., Paradeisiotis A., Heracleous A., Daskalothanasi L, & Stagonas D. (2025). CFD and Experimental Validation of a Wave Event Reconstruction Approach with Focused Gaussian Wave-Groups on a Model Floating Offshore Wind Turbine. Accepted in Wind Energy Science Conference 2025, Nantes 24-27 June 2025.

Simulating Floating Bodies using Smooth Particle Hydrodynamics

Boufidi I.[1,*], Martínez-Estévez I.[2], Crespo A.J.C.[2] and Loukogeorgaki E.[1]

[1] Department of Civil Engineering, Aristotle University of Thessaloniki, Thessaloniki, Greece
[2] Environmental Physics Laboratory, Universidade de Vigo, Ourense, Spain

*corresponding author:
e-mail: ibouf@civil.auth.gr

INTRODUCTION

The increase in electricity demand over the past decades, combined with the need to reduce fossil fuel dependence, highlights the importance of renewable energy sources. The marine environment provides an abundance of energy that can be harnessed by offshore wind turbines and wave energy converters. Offshore winds are stronger and less variable, allowing wind turbines to operate at maximum capacity for longer periods of time. On the other hand, wave energy is characterized by fewer energy losses, high predictability and higher energy density. Still, high construction and operating costs remain a challenge that can be addressed in various ways including the efficient design of the floating device.

The accurate simulation of floating moored bodies under wave action is essential for overcoming the aforementioned challenges. Traditional Computational Fluid Dynamics (CFD) relying on mesh-based methods have difficulties simulating efficiently highly nonlinear flows that exist in extreme wave conditions. Meshless methods such as Smooth Particle Hydrodynamics (SPH) overcome those limitations by representing fluids as distinct particles and, thus, omitting the drawback of properly representing the mesh distortion in nonlinear flows. DualSPHysics (Domínguez et al., 2022) is an open-source SPH-based code particularly suited for those simulations due to its ability to efficiently model violent wave-structure interactions, while leveraging GPU acceleration for high computational efficiency (Crespo et al., 2015). A coupling of DualSPHysics with the mooring library MoorDynPlus, presented in Domínguez et al. (2019), allows the simulation of floating moored offshore structures. This capability has been successfully demonstrated in studies such as Tagliafierro et al. (2022). The aim of this work is to develop and validate an SPH-driven numerical wave tank capable for simulating moored floating bodies of typical geometries (e.g. cylinders and rectangular boxes) under the action of regular and extreme waves.

NUMERICAL MODELLING

The numerical configuration includes a 3D numerical wave flume with a width W, length $L1$ and an initial water depth d (Figure 1). On the left side of the numerical wave tank, there is a piston-type wave generator of height Hw (Figure 1a), capable of generating regular and extreme waves. A wave-dissipative beach is positioned on the opposite side to reduce reflected waves in the flume, starting at a distance $L2$ from the wave generator (Figure 1b). The floating cylinder is held in place by three Mooring Lines (MLs) arranged symmetrically at 120°, with one ML being positioned on the leeward side in line with the incident wave direction (Figure 1). The cylinder is positioned at a distance $L3$ from the wave generator (Figure 1b). The coupling between DualSPHysics and MoorDynPlus enables accurate predictions of numerical mooring tensions and floating body responses under extreme wave conditions, as validated through experimental studies (Wu et al., 2018).

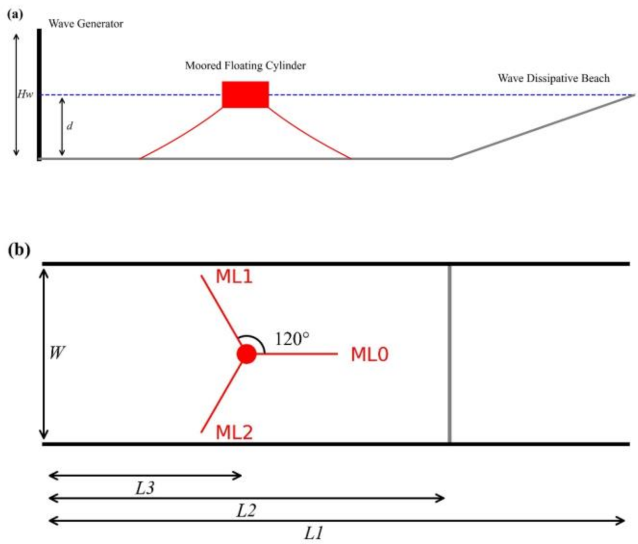

Figure 1. (a) Side and (b) top view of a moored cylinder in the numerical wave tank.

RESULTS AND DISCUSSION

To validate the numerical wave tank used for wave simulations, experimental data are utilized. In Paredes et al. (2015), a generic buoy is tested in a 0.9 m deep tank of $W = 2$ m and $L1 = 22.5$ m, under the action of regular waves with $H = 0.04$ m and $T = 1.2$ s. The buoy corresponds to a vertically truncated cylinder with mass of 35.85 kg, diameter of 0.515 m, moment of inertia (I_{yy}) of 0.9 kg·m² and center of gravity 0.0758 m above the tank bottom. Those parameters, slightly modified by Palm (2016), have been adopted for the present numerical model, along with MLs' (cables) properties derived from Paredes et al. (2015) and Bergdahl et al. (2016) as detailed in Palm (2016). The moored body is positioned at a distance $L3 = 2.5$ m from the piston-type wave generator ($Hw = 1.4$ m), while the wave-dissipative beach is situated at a distance $L2 = 5.5$ m from the wave generator. To produce the numerical setup in DualSPHysics, an initial inter particle distance, dp, is defined to discretize the fluid and boundary particles. In this investigation, the number of particles per wave height, H/dp, is set equal to 8, which is appropriate for large 3D simulations (Altomare et al., 2017).

Figure 2 shows a comparison of the time series for the heave, surge and pitch motions of the moored cylinder obtained from the present SPH simulation with the corresponding experimental data. It can be seen that the heave and surge motions are well captured by the SPH numerical model and are close to the experimental data, while the pitch motion is a bit underestimated by the present numerical approach.

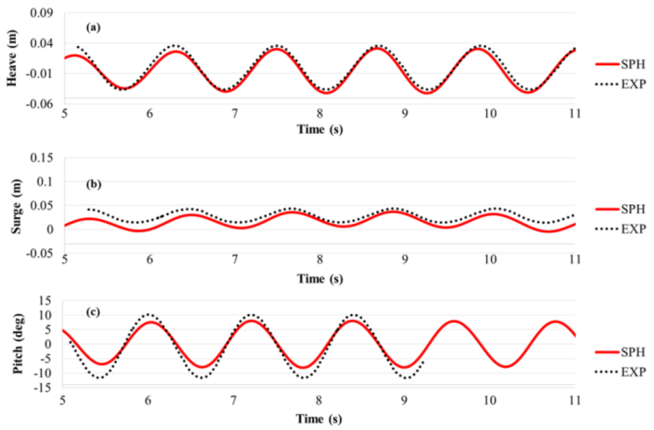

Figure 2. Comparison between numerical (SPH) and experimental (EXP) time series of heave (a), surge (b) and pitch (c).

Additionally to the above and in order to validate the mooring solver, a comparison of the numerically calculated tensions at the top (fairlead) of two mooring lines with the relevant experimental data is made. Specifically, the tension force time series of ML0 (leeward ML, Figure 1b), and ML1 (one of the two seaward MLs, Figure 1b) are included in Figure 3. Due to symmetry the results for ML2 are identical with those of ML1 and are not shown.

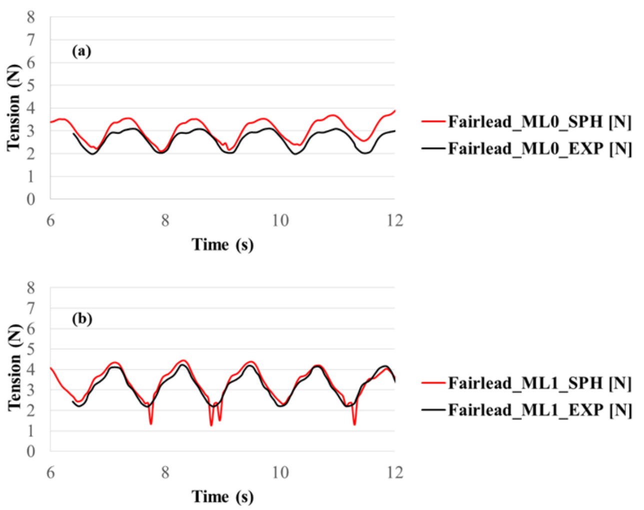

Figure 3. Comparison between numerical (SPH) and experimental (EXP) time series of tension at the top of ML0 (a) and ML1 (b).

The SPH calculated tensions match well with the experimental data. Still, it can be seen that the tension at the top of ML0 (Figure 3a) is on average higher in the SPH simulation compared to the experiments.

CONCLUSIONS

The agreement between the numerical and experimental results, despite some discrepancies in the peak forces of the floating body’s responses and MLs tensions, demonstrates that the present SPH-driven numerical wave tank is a reliable tool for further simulations involving moored floating bodies. Next steps will include validation of not only for regular waves but also for extreme waves, as well as the modeling and investigation of other geometries different to the moored cylinder, such as boxes with four catenary chains.

ACKNOWLEDGEMENTS

Results presented in this work have been produced using the Aristotle University of Thessaloniki (AUTh) High Performance Computing Infrastructure and Resources. The authors would like to acknowledge the support provided by the IT Center of the Aristotle University of Thessaloniki (AUTh) throughout the progress of this research work.

REFERENCES

Altomare, C., Domínguez, J., Crespo, A., González-Cao, J., Suzuki, T., Gómez-Gesteira, M., & Troch P. (2017). Long-crested wave generation and absorption for SPH-based DualSPHysics model. *Coast Eng.* 127, 37–54.

Bergdahl, L., Palm, J., Eskilsson, C., & Lindahl, J. (2016). Dynamically scaled model experiment of a mooring cable. *.J Mar. Sci. Tech.* 4(1), 5.

Crespo, A.J.C., Domínguez, J.M., Rogers, B.D., Gomez-Gesteira, M., Longshaw, S., Canelas, R., Vacondio, R., Barreiro, A., & García-Feal, O. (2015). DualSPHysics: opensource parallel CFD solver on smoothed particle hydrodynamics (SPH). *Comput. Phys. Commun*. 187, 204–216.

Domínguez, J. M., Crespo, A. J. C., Hall, M., Altomare, C., Wu, M., Stratigaki, V., Troch, P., Cappietti, L., & Gómez-Gesteira, M. (2019). SPH simulation of floating structures with moorings. *Coastal Eng*. 153, 103560.

Domínguez, J. M., Fourtakas, G., Altomare, C., Canelas, R. B., Tafuni, A., García-Feal, O., Martínez-Estévez, I., Mokos, A., Vacondio, R., Crespo, A. J. C., Rogers, B. D., Stansby, P. K., & Gómez-Gesteira, M. (2022). DualSPHysics: From fluid dynamics to multiphysics problems. *Comput. Part. Mech.* 9(5), 867–895.

Palm, J., Eskilsson, C., Paredes, G.M., & Bergdahl, L. (2016). Coupled mooring analysis for floating wave energy converters using CFD: Formulation and validation. *Int. J. Mar. Energy* 16, 83–99.

Paredes, G., Palm, J., Eskilsson, C., Bergdahl, L., & Taveira-Pinto, F. (2015). Experimental investigation of mooring configurations for wave energy converters. Proc. 11th European Wave and Tidal Energy Conference (EWTEC 2015), Nantes, France.

Tagliafierro, B., Martínez-Estévez, I., Domínguez, J.M., Crespo, A.J.C., Göteman, M., Engström, J., & Gómez-Gesteira, M. (2022). A numerical study of a taut-moored point-absorber wave energy converter with a linear power take-off system under extreme wave conditions. *Appl. Energy* 311, 118629.

Wu, M., Stratigaki, V., Verbrugghe, T., Troch, P., Altomare, C., Crespo, A., Kisacik, D., Cappietti, L., Domínguez, J.M., Hall, M., Gomez-Gesteira, M., Stansby, P., & Canelas, R.B. (2018). Experimental study of motion and mooring behavior of floating oscillating water column wave energy converter. Proc. 7th International Conference on the Application of Physical Modelling in Coastal and Port Engineering and Science (Coastlab 2018), Santander, Spain.

FORCYS; A 15 MW Floating Offshore Wind Turbine Conceptual Design

Michailides C.[1,*], Loukogeorgaki E.[2], Shi W.[3], Tsani S.[4], Tsipou C.[1], Mantadakis N.[2,1], Boufidi I.[2,1], Chytou C.[5,1] and Tsaousis T.[6,1]

[1] Department of Civil Engineering, International Hellenic University, Serres, Greece
[2] Department of Civil Engineering, Aristotle University of Thessaloniki, Thessaloniki, Greece
[3] Dalian University of Technology, Deepwater Engineering Research Center, Dalian, China
[4] National Kapodistrian University of Athens, Department of Economics, Athens, Greece
[5] Department of Economics, University of Ioannina, Ioannina, Greece
[6] School of Naval Architecture and Marine Engineering, National Technical University of Athens, Athens, Greece

*corresponding author:
e-mail: cmichailides@ihu.gr

INTRODUCTION

The advancement of the offshore wind energy sector is crucial to achieving the goals of the European Green Deal. According to the Offshore Energy Strategy (European Commission, 2020), the installed offshore wind capacity in EU was 14.6 GW in 2021 and is projected to grow significantly, reaching 60 GW by 2030 and expanding at least 25-fold by 2050, leveraging the vast potential of all EU sea basins. The technology of Floating Offshore Wind Turbines (FOWTs) has advanced rapidly in recent years. Since the initial research concepts proposed in the late 20th century, the past decade has seen significant progress aiming to the commercialization of the technology, with various research groups contributing to the field. Of the approximately 100 concepts introduced, around 90 rely on steel as the primary platform material. While the use of concrete for FOWT platforms has been explored and validated, it has only been implemented in a limited number of demonstration projects. Concrete platforms offer several potential advantages, including reduced ballast requirements, smaller floater size, improved stability, local manufacturing feasibility, an accessible material supply chain, and enhanced constructability and adaptability for port infrastructures.

The Research Project 'FORCYS – An alternative Floating OffshoRe wind turbine Concept technologY deSign' seeks to offer novel insights, based on physical and computational modelling and analysis, aiming to develop, design and promote an alternative, concrete-based FOWT, as an innovative energy conversion system that can be used in coastal and offshore locations off the Mediterranean coasts. FORCYS brings together an interdisciplinary team of experts in computational analysis of FOWTs, physical and environmental modelling, techno-economic analysis and business key players. The project will deliver the computational and experimental modeling of the FORCYS FOWT and the achievement of a TRL4 technology level at the end of the project based on techno-economic studies (http://www.forcys.civil.ihu.gr/). The FORCYS methodology is shown in Figure 1.

This paper introduces a conceptual design for a concrete FOWT supporting a large rated 15 MW wind turbine. Additionally, it examines the influence of design parameters related to FOWT's platform geometry on intact stability and hydrodynamic response in the frequency domain.

FORCYS PRELIMARY CONCEPTUAL DESIGN

The conceptual design of the concrete FORCYS platform is illustrated in Figure 2 below, including a concept sketch, along with the structural model of the platform and the panel model mesh. The proposed design consists of a braceless semi-submersible platform with five cylindrical columns and four rectangular pontoons. Each cylindrical column has a diameter of 12 m, while the rectangular pontoons measure 12 by 7 m. The platform has a draft of 22 m and a freeboard of 15 m. The central column is designed to support the 15 MW reference WT (Evan et al., 2020). A crucial design parameter of the concept is the center-to-center spacing of the columns (*D*). Hence, different values of *D* have been considered to analyse the impact of this design parameter on the stability and the hydrodynamic response of the FORCYS platform. A shown in Table 1, the change of *D* introduces modifications to the platform's mechanical characteristics (e.g. weight, buoyancy, CoG, CoB and natural periods).

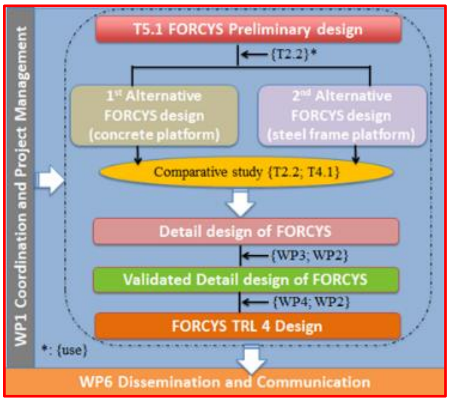

Figure 1. FORCYS Methodology work flow

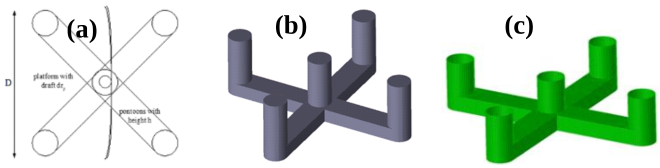

Figure 2. Conceptual design of the concrete-based FORCYS FOWT concept: **(a)** FOWT's sketch, **(b)** structural 3D model and **(c)** panel model for frequency domain hydrodynamic analysis.

Table 1. Characteristics of the FORCYS platform (natural periods have been calculated using analytical equations).

Design No.	D (m)	Displacement (tonnes)	CoB (m)	Heave (sec)	Pitch (sec)
D_86	86	27258	-15.01	20,84	25,67
D_96	96	29694	-15.29	21,88	23,37
D_106	106	32129	-15.53	22,98	21,24

Analyzing the intact stability of FOWTs is essential to guarantee their ability to withstand environmental forces and maintain stability in various operational conditions (e.g. large inclination of the FOWT and fully submergence of FOWT's outer columns). In order to study the FORCYS FOWT's capacity to resist capsizing or tilting over due to external forces such as wind and waves, the hydrostatic stability of the platform is assessed. The latter assessment requires evaluating both the wind heeling moment, M_{wh}, and the righting moment, M_R, at various platform heeling angles. M_{wh} represents the tilting effect caused by wind forces on the FOWT, while M_R reflects the platform's ability to resist external forces and maintain stability. M_{wh} is typically calculated based on the maximum wind thrust force acting on the WT. In this work, it is assumed constant at 460,000 kNm under rated wind load conditions, corresponding to a mean wind speed of 11.4 m/sec. In the intact stability design of a column-stabilized platform, the area under the M_R curve up to the downflooding angle is compared to the area under the wind heeling moment curve over the same angle range. Stability regulation criteria generally require this ratio to exceed 130%. The intact stability analysis' results for wind direction angles β between 0° and 45° (due to symmetry) for various platform's heeling conditions are illustrated in Figure 3. The results show that only the D_96 and D_106 designs meet the stability criterion, as their M_R curve areas from equilibrium to the downflooding angle exceed 130% of the wind heeling moment area. Additionally, M_R remains positive from equilibrium to the second intercept angle, fulfilling the required criterion.

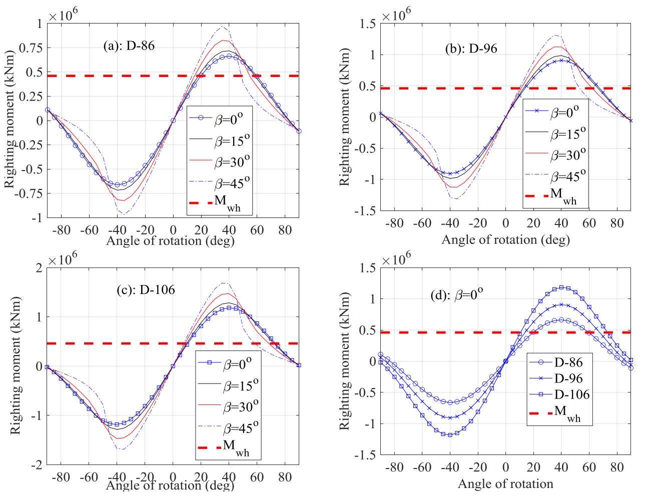

Figure 3. M_R curves of D-86 **(a)**, D-96 **(b)** and D-106 **(c)** for platform's heeling direction β=0°, 15°, 30° and 45°, and comparison of M_R curves for β=0° **(d).**

The hydrodynamic analysis of the platform subjected to regular waves is conducted in the frequency domain and is based on a 3D linear wave diffraction theory. In this linear analysis, the platform is assumed to undergo small oscillations in all six degrees of freedom corresponding to surge, sway, heave, roll, pitch and yaw, with complex amplitudes ξ_j, j=1,…, 6, respectively. Hydrodynamic coefficients are calculated based on solution of the 1st order boundary value problem and ξ_j, j=1,…, 6, are obtained by solving the following linear system of equations, where M_{ji}, A_{ji}, B_{ji} and C_{ji} are respectively the mass, added mass, radiation damping and hydrostatic-gravitational stiffness coefficients, while and F_j are the wave exciting forces:

$$\sum_{j=1}^{6}\left[-\omega^2\left(M_{ij}+A_{ij}\right)+i\omega B_{ij}+C_{ji}\right]\xi_j=F_i,\ i=1\sim6 \quad (1)$$

For all designs, all responses' curves up to a period equal to 20 sec follow the same pattern with small changes in the relevant local peaks (Figure 4). Heave and pitch natural periods are close to the 20 sec and agree well with the values calculated with analytical equations (Table 1). The increase of the *D* value results to the shifting of the heave RAO peak in larger wave periods, while, for pitch motion the opposite holds true.

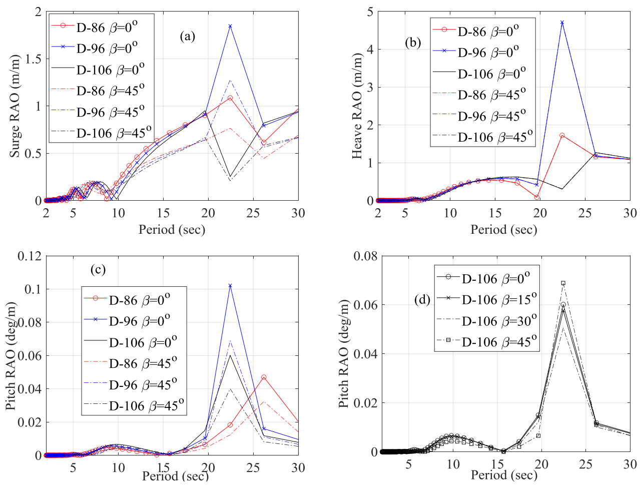

Figure 4. RAOs of examined designs: **(a)** surge, **(b)** heave , **(c)** pitch and **(d)** comparison of pitch RAO for D-106 under different wave directions.

CONCLUSIONS

In this paper, we introduced an efficient conceptual design for a concrete FOWT supporting a large rated 15 MW WT, as developed within FORCYS project. Additionally, the influence of critical design parameters related to the FOWT's platform geometry on intact stability and frequency-based hydrodynamic response were presented.

ACKNOWLEDGEMENTS

This research was funded through the FORCYS research project which is implemented in the framework of H.F.R.I call "Basic research Financing (Horizontal support of all Sciences)" under the National Recovery and Resilience Plan "Greece 2.0" funded by the European Union – Next Generation EU (Implementation body: H.F.R.I. Project Number:14966).

REFERENCES

European Commission. An EU Strategy to Harness the Potential of Offshore Renewable Energy for a Climate Neutral Future, COM/2020/741 final, Brussels, 2020.

Evan, G., Rinker, J., Sethuraman, L., Zahle, F., et al. 2020. Definition of the IEA 15-Megawatt Offshore Reference Wind. Golden, CO: National Renewable Energy Laboratory. NREL/TP-5000-75698.

Preliminary Assessment of FORCYS FOWT combined with TALOS Wave Energy Converter

Michailides C.[1,*], Loukogeorgaki E.[2], Aggidis G.[3] and Shi W.[4]

[1] Department of Civil Engineering, International Hellenic University, Serres, Greece
[2] Department of Civil Engineering, Aristotle University of Thessaloniki, Thessaloniki, Greece
[3] School of Engineering, Lancaster University, Lancaster, UK
[4] Dalian University of Technology, Deepwater Engineering Research Center, Dalian, China

*corresponding author:
e-mail: cmichailides@ihu.gr

INTRODUCTION

Among ocean-based renewable energy solutions, Offshore Wind Turbines (OWTs) currently dominate the sector. Floating Offshore Wind Turbines (FOWTs) technology is advancing rapidly, gaining increasing recognition as a viable and scalable solution for deep-water energy production. This progress has captured the interest of key stakeholders (e.g. governments, investors, and energy developers) who see its potential to unlock vast offshore wind resources in previously inaccessible regions worldwide. In contrast, Wave Energy Converters (WECs), despite four decades of intensive research, remain in a phase of methodological reevaluation, particularly regarding commercialization and design standardization. Over the years, researchers have proposed a large number of WECs designs; yet, the technology has not achieved the same level of commercial maturity as offshore wind. Given this disparity, a promising pipeline lies in combining FOWTs and WECs to harness wind and wave energy simultaneously. Such combined systems could leverage shared marine infrastructure, significantly reduced costs and optimizied ocean space utilization. Active or passive integration of WECs with FOWTs could enhance system efficiency and energy yield, while, furthermore, passive WEC configurations might serve a dual purpose: (a) damping of OWTs components' critical structural vibrations, improving their stability and integrity and (b) concurrent wave energy capture, even if the produced wave energy is not comparable with the produced energy by the WT.

The FORCYS FOWT concept (Figure 1a) consists of a 15 MW WT, a mooring line system and a concrete braceless semi-submersible platform. The latter component consists of five cylindrical columns of 12 m diameter and four rectangular pontoons of 12 m length and 7 m width. With a freeboard of 15 m, the platform's central column ables to support the 15 MW reference WT. The centre to centre distance between the central and rest columns is 47 m.

A groundbreaking multi-mode point absorber called the TALOS WEC (Figure 1b) has been developed at Lancaster University over recent years and its efficient performance has been evaluated with the use of different numerical analysis models (Michailides et al., 2017). The TALOS design includes a rigid floater that operates with six Degrees of Freedom (DoFs) and a Power Take-Off (PTO) mechanism housed within the floater. This internal PTO system consists of an inertial mass (a sphere) linked to the floater through springs and dampers (such as hydraulic cylinders) and facilitates power capture through the relative movements between the sphere and the floater. As a result, TALOS can efficiently generate power by utilizing the relative motions between the sphere and floater across all six DoFs, depending on the configuration of the spring-damper system.

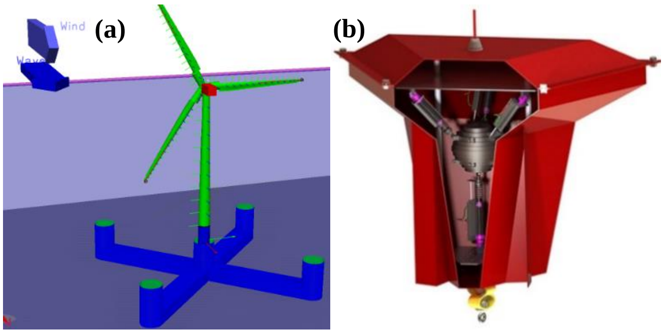

Figure 1. Conceptual design of: **(a)** concrete FORCYS FOWT concept and **(b)** TALOS WEC (floater and PTO)

The present study focuses on the performance of the FORCYS FOWT combined with the TALOS PTO addressing wave-structure interaction effects in time domain. The TALOS PTO is integrated within the existing pontoon structure of the FORCYS platform, enabling passive energy absorption. The PTO is connected to the platform via a spring-damper system, and power is extracted through the relative motion between the PTO and the platform. A comprehensive evaluation of the PTO's power output under varying environmental conditions provides preliminary insights into the system's energy harvesting potential and response reduction. To assess the hydrodynamic response and quantify wave power generation, a dedicated numerical model has been developed and applied.

NUMERICAL MODELLING

The governing equation of motion is derived from Newton's second law using the Cummins time-domain formulation (Cummins, 1962). This framework captures the coupled dynamics of wave exciting forces and radiation forces (often termed fluid memory effects) induced by the floating structure's motion. For the present system, where the FORCYS platform exhibits N DoFs and the TALOS PTO's internal sphere operates with M DoFs, the equation of motion takes the following form:

$$(\mathbf{M}+\mathbf{A}_{\infty})\ddot{\mathbf{x}}(t)+\int_{-\infty}^{t}\mathbf{B}(t-\tau)\dot{\mathbf{x}}(\tau)d\tau+(\mathbf{C}+\mathbf{K})\mathbf{x}(t)=\mathbf{F}_{\mathbf{exc}}(t)+\mathbf{F}_{\mathbf{PTO}}(t) \quad (1)$$

In Eq. 1 $\mathbf{x}$, $\dot{\mathbf{x}}$ and $\ddot{\mathbf{x}}$ are the displacement, velocity and acceleration vectors of the platform and sphere, $\mathbf{M}$ is the structural mass matrix, $\mathbf{A}_{\infty}$ is the added mass matrix at infinite frequency, $\mathbf{B}$ is the matrix of impulse response functions (retardation functions), $\mathbf{C}$ is the hydrostatic-gravitational stiffness matrix, $\mathbf{K}$ is the mooring lines stiffness (assuming linear springs in this paper), $\mathbf{F}_{\mathbf{exc}}$ is the wave loading vector, $\mathbf{F}_{\mathbf{PTO}}$ is the vector of forces resulting from the PTO mechanism, t is time, while τ is a dummy variable. The maximum dimensions of the above matrices and vectors correspond to (N+M) X (N+M) and (N+M) X 1 respectively.

The hydrodynamic coefficients and wave exciting forces are computed in the frequency domain using the boundary integral equation method. The analysis employs 3D linear potential flow theory. Adopting the assumptions of inviscid, incompressible fluid and irrotational flow, the fluid motion is described through the velocity potential theory. The radiation and diffraction potentials satisfy Laplace's equation and are constrained by linearized boundary conditions on the free surface, the sea bottom, and the floater's wetted surface. This first-order boundary value problem is numerically solved through the 3D panel method, applying Green's theorem.

RESULTS AND DISCUSSION

The FORCYS platform, integrated with the internal TALOS PTO, has a total draft of 22 m. The TALOS PTO comprises a mass of 200,000 kgr along with a system of springs and dampers. Two operational cases, OC1 and OC2, have been analyzed. In OC1, a single-mode PTO mechanism is considered, allowing the PTO's sphere to oscillate in heave relative to the platform while constraining all other DoFs of the internal mass. Consequently, Eq. 1 is solved for M=1. In OC2, a two-mode PTO mechanism is examined, permitting the PTO's sphere to oscillate in both surge and heave relative to the platform, while keeping the remaining DoFs of the internal mass restrained. Thus, Eq. 1 is solved for M=2. In both cases the PTO mechanism is modelled as a linear, 1- and 2-DoFs, respectively, spring-damper system with equivalent heave and surge PTO stiffness, K_{PTO}, equal to 3,400,000 N/m and equivalent heave and surge PTO damping, B_{PTO}, equal to 1,750,000 Ns/m.

The wave power absorbed by the combined system is calculated using Eqs. 2 and 3 for OC1 and OC2, respectively:

$$\mathrm{Power}(t) = B_{PTO,h}\left(\dot{x}_{hP}(t) - \dot{x}_{hm}(t)\right)^2 \qquad (2)$$

$$\mathrm{Power}(t) = B_{PTO,s} + B_{PTO,h}\left(\dot{x}_{hP}(t) - \dot{x}_{hm}(t)\right)^2 \qquad (3)$$

In the above equations, $\dot{x}_{sP}$, $\dot{x}_{hP}$ are the velocities of the FORCYS platform in surge and heave respectively, while, $\dot{x}_{sm}$, and $\dot{x}_{hm}$ are the corresponding quantities for the TALOS PTO's sphere as obtained from the solution of Eq. 1. The preliminary assessment for both OC1 and OC2 is implemented under the action of both regular and irregular waves. For the regular wave condition (EC1), the wave height, H, is taken equal to 1.5 m, while the period, T, is set equal to 5.0 s. For the irregular wave condition (EC2), the Jonswap spectrum with peakedness factor of 1.0 has been used with significant wave height, H_s = 1.5 m and peak period, T_p, =5.0 s. The total simulation time is 400 s and 3,600 s for the regular and irregular conditions, respectively.

Regarding EC2, the comparison of the FORCYS platform's motion for the two OCs (Fig. 2a) reveals an insignificant effect on the operation of the TALOS PTO on the motion response of the FORCYS platform; similarly for regular wave conditions the response is identical (Fig. 2e). Moreover, the relative motion of the surge and heave between the sphere and the platform (Fig. 2b) remains in a rational range avoiding the utilization of the end stop mechanism placed for avoiding the collision between the two bodies. As for the wave power absorbed by the combined concept (Figs. 2c and 2d), the mean values for OC1, OC2 are equal to 33.8 kW, 78,13 kW, respectively. At the same time, the motion responses of the platform (Fig. 2f) are damped since the TALOS PTO behaves dually as a passive damper.

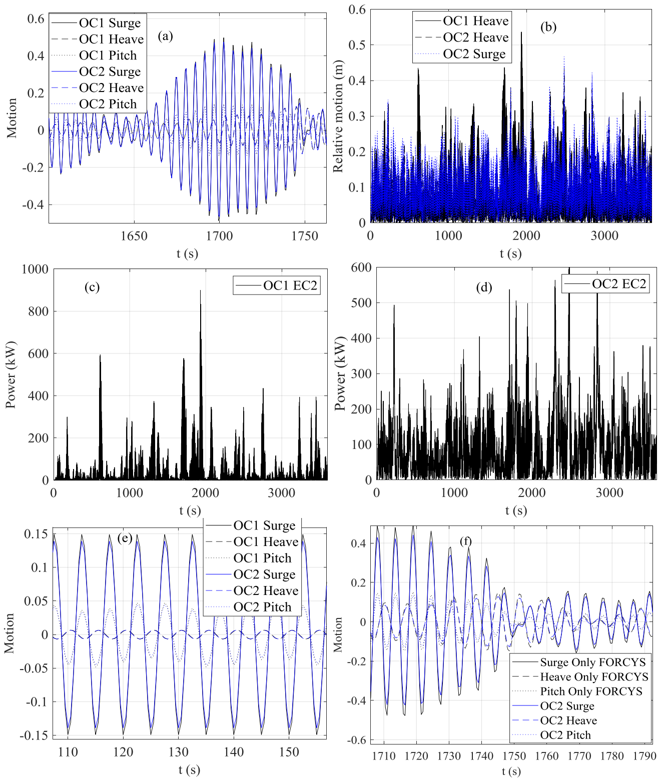

Figure 2. (a) Surge, heave and pitch of FORCYS platform for OC1 and OC2, **(b)** Relative motions for OC1 and OC2, **(c)** Produced power for OC1 and EC2, **(d)** Produced power for OC2 and EC2, **(e)** Platform's motions of OC1 and OC2 for EC1 and (f) Comparison of platform's motions for EC2.

CONCLUSIONS

In this paper, we introduced the FORCYS FOWT combined with the TALOS WEC PTO serving as a passive damper. The effect of the TALOS PTO on the response of the FORCYS platform is insignificant, while a rational amount of additional produced power exists. The proposed combined concept should be further optimized while the effect of the aerodynamic loads should be accounted in future studies.

ACKNOWLEDGEMENTS

This research was funded through the FORCYS research project which is implemented in the framework of H.F.R.I call "Basic research Financing (Horizontal support of all Sciences)" under the National Recovery and Resilience Plan "Greece 2.0" funded by the European Union – Next Generation EU (Implementation body: H.F.R.I. Project Number:14966).

REFERENCES

Michailides, C., Loukogeorgaki, E., Sheng, W. & Aggidis, G. (2024). Response and Power Absorption Assessment of the TALOS Wave Energy Converter in Time Domain, *Int. J. Offshore Polar Eng.* 34(1), 29-36.

Cummins, W.E. 1962. The Impulse Response Function and Ship Motions, Report 1661, Department of the Navy David Taylor Model Basin, 12.

Optimal Siting of Offshore Wind Farms in Greece: Methodology, Cost Surface & Results; The Case of Patraikos State-Proposed Development Area

Tsiara C.[1], Katsardi V.[1,*], Spiliotopoulos G.[1] and Vasiliades L.[1]

[1] Department of Civil Engineering, University of Thessaly, Pedion Areos, Volos, 38334, Thessaly, Greece

*corresponding author:
e-mail: vkatsardi@civ.uth.gr

INTRODUCTION

The global energy crisis dictates the need to adopt a comprehensive approach to the sustainable exploitation of renewable energy sources at the national level. Spatial planning practices with long-term viability emerge as a strategic pathway toward energy security. Wind energy, in particular, has been globally validated as a realistic alternative to non-renewable sources, offering both environmental and economic advantages. Notably, Ram (2018) suggested that the recent decline in the costs of wind and solar energy systems reflects a broader trend across all renewable energy sources, which are anticipated to surpass fossil fuels in economic competitiveness by 2030. Menendez (2013) and many researchers since, have identified the Aegean Sea as a prime location for offshore wind development in the Mediterranean. However, offshore wind farm (OWF) projects have yet to be established in Greece, highlighting the need to harness this untapped potential. Spyridonidou (2020) published a guide on spatial planning practices for OWF projects, and Serpetsidaki (2024) highlighted common methodological approaches within the site selection paradigm.

This research enhances the OWF siting approach for Greece by conducting a detailed analysis of location-specific cost indices for eligible offshore locations, based on both exclusion and prioritization criteria. Specifically, these sites were evaluated using the Levelized Cost of Energy (LCOE) method, generating spatial maps that illustrate the life-cycle cost, projected annual energy output, and LCOE values. The research primarily contributes to improving decision-making by offering cost-based visual tools for optimal OWF site selection. Furthermore, it includes an assesment of the Greek state's offshore wind development program, focusing on the OWF Organized Development Area (OWFODA) ‘Patraikos’.

PRIMARY ASSUMPTIONS

Given the extent of the study area, well-defined assumptions had to be established in an attempt to limit arising uncertainties. Namely:

- The floating platform setup selected was the WindFloat model.
- The reference farm consisted of 14, Vestas V236-15MW wind turbines, arranged in two rows of 5 and one row of 4.

DETERMINATION OF VIABLE OFFSHORE SITES

This study identifies eligible locations for offshore wind farms by considering multiple location-dependent factors, including legislative, techno-economic, and environmental constraints. Using an ArcMap model, exclusion zones — areas unsuitable for development due to technical or environmental limitations— were determined based on legal frameworks and best practices. After identifying viable sites, their suitability was assessed by quantifying key technical attributes, such as wind potential, depth, and proximity to the coast. In this context, the prioritization of offshore sites for the development of OWFs occured in two stages: first, unsuitable sites were horizontally excluded and then the remaining viable locations were classified through the cost assessment methodology. This approach ensured that the uncertainties arising from arbitrarily weighing criteria of different nature would be limited. Thus, three categories of constraints wre enforced: techno-economic, environmental and nuisance criteria.

TECHNO-ECONOMIC CRITERIA

The techno-economic criteria ensure the financial viability of potential OWF projects, their overlap with compatible only land uses, and compliance with the prevailing legal framework. For instance, this category of constraints excluded offshore sites that did not meet mean wind speed requirements, overlapped with high-traffic ship routes, or were not located within Greek territorial waters.

ENVIRONMENTAL CRITERIA

The environmental criteria were applied to preserve protected sites of natural importance and biodiversity sanctuaries. Unfortunately, the existing legislation does not cover all environmentally sensitive areas and, under specific circumstances, allows development in their vicinity. In this study, Natura 2000 regions, bird migration corridors, wildlife refuges, and other ecologically significant areas were fully excluded from the viable offshore sites for wind energy projects, following best practices in relevant literature.

NUISANCE CRITERIA

The nuisance criteria were enforced to preserve areas important for human activities. Examples of excluded areas include UNESCO World Heritage Sites, the 1NM coastal zone, Blue Flag beaches, and other culturally or recreationally significant locations.

COST ASSESSMENT METHODOLOGY

The next logical step was the prioritization of the eligible offshore points via location-specific parameters (i.e. wind potential, depth, proximity to shore) integrated into the cost assessment methodology. Castro-Santos (2016) proposed a comprehensive guide to blue energy costing, which was adapted for OWFs and implemented in the present research. Specifically, using Matlab software, the first index calculated was the life-cycle cost. This parameter pertains to the sum of the individual expenditures generated during each phase of development (i.e. concept & definition, design & management, construction, installation, operation, dismantling). The life-cycle cost (LCS_n) is the dimensionless total cost of an OWF project in € and fluctuates depending on the year of operation (n) examined. On the other hand, the LCOE measured in €/MWh is constant throughout the life-cycle (N_{farm} in years) and introduces the annual estimated energy produced by an OWF (E) and the capital cost (r) as shown in equation (1):

$$LCOE = \frac{\sum_{n=0}^{N_{farm}} \frac{LCS_n}{(1+r)^n}}{\sum_{n=0}^{N_{farm}} \frac{E}{(1+r)^n}} \tag{1}$$

The annual estimated energy yield (E) is a product of the annual estimated energy produced by a single wind turbine (E_1), the number of devices in the farm, and constants related to the availability of the electrical grid. In more detail, E_1 in MWh/year is a function of the wind turbine's power curve ($P_{CP}(v)$) multiplied by the probability density function assuming a Weibull wind distribution with unique scale (c) and shape (k) parameters for each eligible offshore point ($p_{Weibull}(v; c, k)$). The product is integrated over the spectrum of viable wind speeds ($v \in$ [0, cut-out speed]) and multiplied by the number of hours in a year ($NHAT$) as shown in equation (2):

$$E_1 = NHAT * \int_0^{v_{cut-out}} P_{CP}(v) * p_{Weibull}(v; c, k) dv \tag{2}$$

The following map was produced using the calculated LCOE values as input in the ArcMap model.

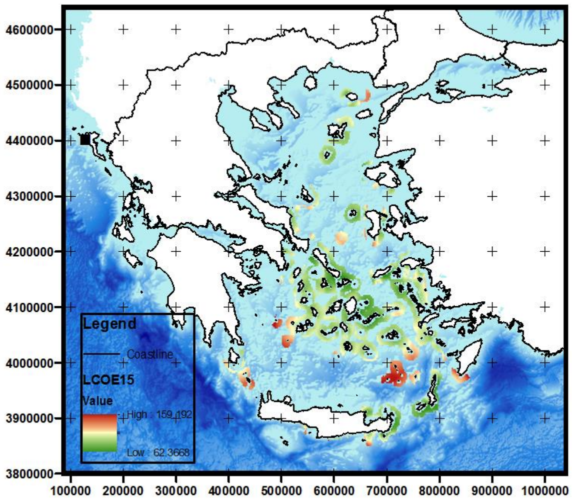

Figure 1. LCOE values for eligible offshore sites.

NATIONAL DEVELOPMENT FOR OFFSHORE WIND FARMS – THE OWFODA 'PATRAIKOS'

The Hellenic Hydrocarbons & Energy Resources Management Company SA oversaw the state-leased study on offshore wind potential. This resulted in the National Development Program for Offshore Wind Farms (NDP-OWF) and its supplementary Strategic Environmental Impact Assessment (SEIA). The reports propose 23 potential OWFODA, categorized by development timeline and foundation type. Ten are medium-term projects (2030-2032), including seven floating and three fixed wind turbine sites, while 13 are long-term (post-2032), comprising 12 floating and one fixed project. The purpose of this section was the evaluation of the OWFODAs on the same basis as this study. Generally, a substantial percentage of the proposed plots retains significant overlap with the viable sites for OWF development produced in this research. Namely, 16 out of 23 OWFODAs present over 70% overlap. However, some plots were met with harsh critique, mainly due to the deprioritization of environmental exclusion criteria. Regrettably, the pilot projects 'Evros' and 'Samothraki' as well as 'Diapontia Nisia' and 'Patraikos' OWFODAs rank last in agreement percentage with zero or near zero values. The relevant legislation does not identify Patraikos Gulf as an enclosed bay. Nevertheless, it still constitutes a narrow passage characterized by high traffic due to the port of Patras. Furthermore, the proposed plot is in proximity to Messolonghi lagoon and Acheloos' delta. These are sites of natural importance classified under both the Natura2000 area 'GR2310015' and important areas for birdlife. Additionally, the wind potential is not particularly encouraging, with wind speeds averaging lower than 9m/s at 100 m above sea level.

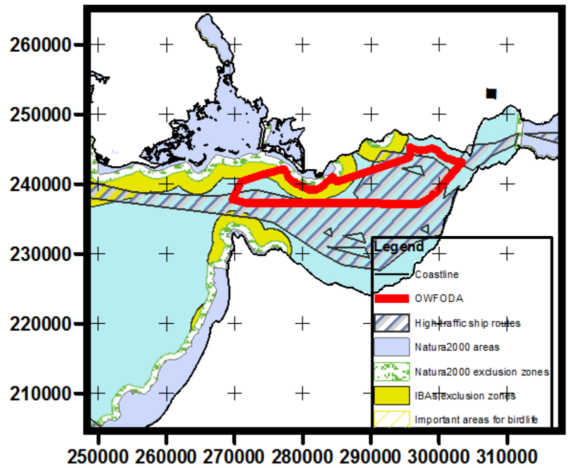

Figure 2. 'Patraikos' OWFODA – overlap with environmental criteria.

REFERENCES

Ram, M., Child, M., Aghahosseini, A., Bogdanov, D., Lohrmann, A, & Breyer, C. (2018). A comparative analysis of electricity generation costs from renewable, fossil fuel and nuclear sources in G20 countries for the period 2015-2030. *J. Clean. Prod*. 199, 687–704.

Menendez, M.D.C.R., García-Díez, M., Fita, L., Fernández, J., Méndez, F.J., & Gutiérrez, J.M. (2014). High-resolution sea wind hindcasts over the Mediterranean area. *Clim. Dyn.* 42, 1857–1872.

Spyridonidou, S., Vagiona, D.G., & Loukogeorgaki, E. (2020). Strategic planning of offshore wind farms in Greece. *Sustainability* 12(3), 905.

Gkeka-Serpetsidaki, P., Skiniti, G., Tournaki, S., & Tsoutsos, T. (2024). A review of the sustainable siting of offshore wind farms. *Sustainability* 16(14), 6036.

Castro-Santos, L., Martins, E., & Soares, C.G. (2016). Cost assessment methodology for combined wind and wave floating offshore renewable energy systems. *Renew. Energy* 97, 866–880.

Evaluation of the Proposed Offshore Wind Farm in the Gulf of Patras

Kontoe S.[1,*], Dimakopoulos A.[1], Pappas C.[1] and Georgoutsou K.F.[1]

[1] Department of Civil Engineering, University of Patras, Greece

*corresponding author:
e-mail: skontoe@upatras.gr

INTRODUCTION

The Greek National Plan (GNP) for offshore wind installations was issued in October 2023 (Stefatos et al 2023) aiming to identify suitable locations in Greece and ultimately to contribute to the EU targets of at least 60 GW of installed capacity from Offshore Wind Farms (OWF) by 2030 and 300 GW by 2050. Through a series of exclusion and evaluation criteria the GNP proposes 23 potential locations which are grouped in 10 medium-term development areas (until 2030-2032) of 4.9 GW capacity and 13 long-term development areas (after 2030-2032) of 6.9 GW capacity.

The present study focuses on one of the medium-term areas of priority at the gulf of Patras, Western Greece, aiming to provide some insights regarding the technical feasibility of the proposed OWF considering the site-specific characteristics of the marine area and the current best practice in the development of OWFs at international level.

BRIEF DESCRIPTION OF THE PROPOSED OFFSHORE WIND FARM

The GNP envisages the development of an offshore wind farm in the Gulf of Patras with an estimated capacity of 695 MW and a total area of 139 km^2 as depicted in Figure 1, with its main characteristics summarised in Table 1.

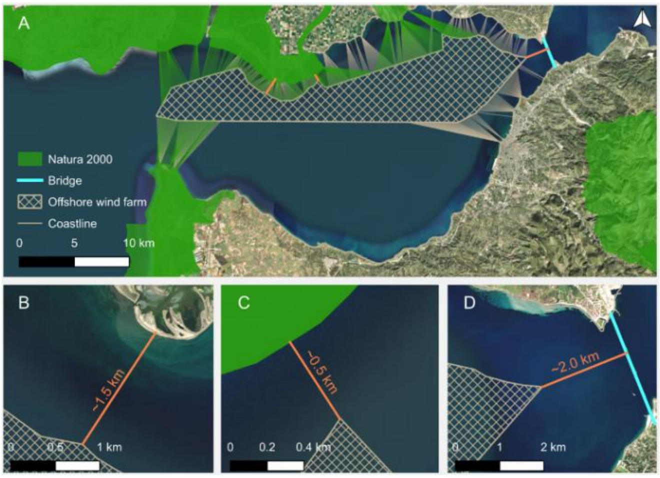

Figure 1. (A) An overview of the Gulf of Patras, Western Greece, with the polygon outlining the proposed OWF (from Stefatos et al 2023, and minimum distances from (B) the Evinos river delta, (C) Natura 2000 protected areas (GR2310015 site), and (D) Rio–Antirrio bridge.

Table 1. Main features of the proposed OWF as outlined in Stefatos et al (2023).

Average water depth (m)	Average Wind speed (m/s)	Stated minimum distance from the shore (m)
69.5	7.3	1,852

TECHNICAL CHALLENGES

The GNP assumes a density capacity of 5 MW/km^2 and an average distance between two consequent wind turbines of 10D (where D is the diameter of the rotor) in both directions (i.e. along its length and breadth). Therefore, the estimated capacity of 695 MW at the envisaged marine area of 139 km^2 at the Gulf of Patras requires in principle, 46-47 wind turbines of 15 MW. The proposed OWF is a polygon (Figure 1), which can be simplified to a rectangle with ~26 km x 5.4km edges. The GNP assumes 15 MW wind turbines, requiring grid spacing 10 times the turbine diameter (2,400m). Hence it is possible to use a grid of ~12 x 3 i.e. 36 wind turbines in total. This is based on a rather optimistic scenario, assuming that the wind turbines can be installed at the edges of the rectangle area. These simple considerations demonstrate that the estimated capacity of 695 MW appears too ambitious and that a more realistic estimate would be 22 % lower, corresponding to 540 MW. The final allocation of wind turbines in the polygon will be determined with site-specific wind capacity studies. The optimum arrangement for power output may eventually fit less than 36 turbines in the (irregularly shaped) polygon, due to limitations emerging from future wind climate studies in the area and the consideration of other activities (e.g. shipping), thus reducing further power output.

The type of foundation (bottom fixed) for the proposed OWF is set as the main criterion in the GNP for prioritising its development in the medium-term, as floating solutions present challenges in terms of their technological readiness. The exact layout of the foundation (i.e. monopile, jackets, caisson) is not specified. Generally, the most common foundation type is the monopile (about 80 % of the foundations), which is used at water depths up to 40-50 m, followed by jackets supported by piles that reach 50-80 m water depths. Table 1 shows that the average water depth in the area is 69.0 m, which makes the implementation of a bottom fixed foundation technically challenging. Statistical data of Musial et al (2023) show that there are few bottom fixed operating wind farms in depths >50 m , while only one wind farm from those in planning stage exceeds 70 m depth. Therefore, international experience shows that it is extremely challenging to implement a bottom fixed foundation in the Gulf of Patras, given that the global technological readiness for installing deep (~70 m) offshore wind foundations does not appear to be at an established level for commercial use. Therefore, international experience indicates that it would be rather challenging to implement a bottom fixed foundation in the Gulf of Patras, given that the global technological readiness for installing deep (~70 m) offshore wind foundations does not appear to be at an established level for commercial use.

Internationally, the development of OWF is characterised by an upward trend in the size of offshore wind turbines, accompanied by an upward trend in the distance from the coast. Data from Musial et al (2023) for bottom fixed OWFs show that the vast majority of OWF are located at a distance >10 km from the coast. Furthermore, the majority of OWFs greater than 250 MW are located > 20 km from the coast.

The GNP has set a wind potential criterion for including marine areas as suitable for power generation, defined as having annual average wind speed at 100 m above sea level greater than 6.5 m/s. It should be noted a higher wind velocity threshold is specified in the GNP for floating OWFs (>8 m/s). The average speed in the Gulf of Patras is 7.3 m/s (Table 1), being the second to last wind speed amongst the 23 potential locations proposed by the GNP. It should also be emphasized that the average wind speed at the Gulf of Patras is significantly lower than the optimal speed (rated wind speed) of operation of the 15 MW Vestas 236 reference wind turbine (11.1 m/sec). Finally, the stability of the wind potential has not been considered, which is an important parameter for the sustainability of a wind farm. Stability issues may emerge due to the proximity of the proposed OWF to steep topographic features (e.g. Paliovouna / Klokova mountain complex) which may affect local wind flow patterns. Further investigation is required to ensure that wind potential stability is not compromised by the landscape topography.

A preliminary investigation of the required electrical infrastructure is required for the planning phase of an OWF. The GNP considers the possibility of an interconnection to the existing grid as a prioritisation parameter for the potential locations of the OWFs, but it does not further examine the electrical infrastructure (e.g. need of offshore substations for each OWF). As stated in the GNP, the Patraikos OWF is the only one of the proposed OWFs in Greece not having an existing grid interconnection point. Given the low wind potential of the Patraikos OWF compared to the other sites, it is evident from the GNP report that the main reason for the medium-term prioritisation is the provision of a bottom fixed foundation which is considered advantageous over a floating one. However, as previously indicated, a bottom fixed foundation would not, most likely, be viable due to the excessive water depth. On the other hand, a floating solution would not meet the minimum wind speed requirement of 8 m/s set by the GNP. Therefore, there are no reasons to prioritise the Patraikos OWFs as there are severe technical challenges which raise serious concerns about its viability.

VISUAL IMPACT

The GNP has specified the 1 NM (~1.85 km) as the minimum distance from the coastline. This minimum distance of 1 NM is a high priority exclusion criterion for all proposed sites in Greece, stemming from the European Water Framework Directive 2000/60/EC. The footprint of the proposed Patraikos OWF sits at this marginal distance from the coast (1 NM) at several places, especially in its northern part (Figure 1). Musial et al (2023) show that there is no historical precedent of a large-capacity OWF, either constructed or planned, in such close proximity to the coast. Furthermore, Diaz & Guedes Soares (2020) show that the distance from the coast for OWFs of 600-700 MW capacity exceeds 50 km. Moreover, as illustrated in Figure 1B, the footprint of the proposed Patraikos OWF is at a 1.5 km distance from the delta of the Evinos River which is less than the 1 NM limit, while being also close to the GR2310015 Natura 2000 site (about 0.5 km, Figure 1C) and to the Rio-Antirrio bridge (about 2.0 km, Figure 1D), a recognised landmark of international interest.

CONCLUSIONS

The present study demonstrates that there are significant technical and economic challenges for the implementation of the proposed offshore wind farm in Patraikos Gulf. The envisaged capacity of 695 MW is probably not feasible in the Gulf of Patras due to limitations in the layout of the wind turbines and the irregular shape of the proposed marine area. International experience shows that a bottom-fixed foundation would be very challenging to implement in this area due to the large average water depth (69.0 m). The disadvantages of the proposed site also include the low wind potential of the area, with an average wind speed of 7.3 m/s, which may be higher than the threshold of 6.5 m/s set by the GNP for bottom fixed OWFs, but it is the second lowest of the proposed sites in Greece and significantly lower from rated wind speeds for 15 MW wind turbines. Also, the Patraikos OWF is the only proposed OWF in Greece without existing interconnection point in the grid. All these factors combined, put the economic viability of the OWF in further question, and it could be argued that the particular OWF, in the way that is envisaged, is likely to be a relatively costly endeavor with potentially little (if any) return of investment.

The proximity of the OWF to the coast is also a significant obstacle. The proposed high capacity OWF, would involve enormous wind turbines located at about 2 km from the coast, within an enclosed marine area, which is unprecedent in international practice. The visual impact is expected to be severe for all adjacent areas on both the north and south side of Patraikos and the scheme will face the opposition of environmental stakeholders and the local communities. The literature shows that high-capacity offshore wind farms are located in distances of at least 10 km from the coast. It would be therefore recommended to reconsider the feasibility of the Gulf of Patras OWF and perhaps consider alternatives, such as moving it further away from the shore, as per international practice, or to prioritize another site.

REFERENCES

Díaz, H., & Guedes Soares, C. (2020). Review of the current status, technology and future trends of offshore wind farms, *Ocean Eng.* 209, 107381.

Gaertner, E. et al (2020). Definition of the IEA 15-Megawatt Offshore Reference Wind. Golden, CO: National Renewable Energy Laboratory. NREL/TP-5000-75698.

Musial, W., et al. (2023). Offshore Wind Market Report: 2023 Edition.

Νικολόπουλος, Κ., et al. (2023) Στρατηγική Μελέτη Περιβαλλοντικών Επιπτώσεων.

Στεφάτος, Α., et al. (2023) Εθνικό Πρόγραμμα Ανάπτυξης Υπεράκτιων Αιολικών Πάρκων (ΥΑΠ).

Environmental Contours of Wind and Wave Actions in Thracian Sea for the Development of Offshore Wind Farms

Kostaki E.[1], Michailides C.[1*] and Panagopoulos G.[1]

[1] Department of Civil Engineering, International Hellenic University, Serres, Greece

*corresponding author:
e-mail: cmichailides@ihu.gr

INTRODUCTION

The growing global demand for renewable energy has accelerated the expansion of Offshore Wind Farms (OWFs), which outperform onshore wind installations in several ways, such as access to stronger and more consistent winds, minimized land-use disputes, and greater energy generation potential. By 2023, the EU's offshore wind capacity reached 19.38 GW out of a global total of 34.24 GW, (Wind Europe 2024). With the vast wind resources of the EU's five sea basins, capacity is projected to surge to 60 GW by 2030 and multiply 25-fold by 2050, underscoring offshore wind's pivotal role in the energy transition globally. Offshore Wind Turbines (OWTs) are the leading technology in the marine renewable energy sector, having evolved into a reliable, mature, and fully industrialized solution.

Greece, a Mediterranean country with exceptional offshore wind energy potential, possesses abundant wind resources ideal for large-scale exploitation (Kardakaris et al., 2021). Although plans for Offshore Wind Farms (OWFs) in the Aegean Sea were proposed over a decade ago, none have progressed beyond the planning stage. However, offshore wind development has recently regained momentum as Greece accelerates towards a multisource energy mix.

Recently, the Hellenic Hydrocarbons and Energy Resources Management Company unveiled the National Offshore Wind Farm Development Program (NDP-OWF), a strategic roadmap identifying viable offshore wind zones across Greek seas (HEREMA, 2023). The program divides Greece's maritime territory into six sectors, each with predefined installation capacities, and defines 23 Offshore Wind Farm Organized Development Areas based on exclusion criteria and multi-stage assessments. These areas are temporally prioritized for medium-term (up to 2032) and long-term (up to 2050) OWF projects. Notably, three medium-term development zones—including one in the Thracian Sea—have been designated as suitable for fixed-bottom offshore wind turbines (OWTs), representing a pivotal milestone in Greece's offshore wind energy strategy.

The proposed Thracian Sea development area is divided into two distinct zones: the Alexandroupoli (425.5 km²) and the Samothraki zone (390.7 km²) (Figure 1). The two zones can support the development of fixed bottom OWFs. While previous studies have identified suitable marine areas for OWF deployment in the Thracian Sea (Vagiona and Kamilakis, 2018), successful project implementation necessitates a thorough understanding of local environmental conditions; particularly the complex wind-wave interactions. To address this critical knowledge gap, this study presents the joint probability distributions of wind and wave conditions at specific Thracian Sea locations, and the environmental contour plots derived from a probabilistic model that captures the interdependence of metocean parameters. The developed contour surface ensures that exceedance probabilities correspond to engineering-standard return periods, while, providing essential generic use data for different purposes in future engineering studies.

DATA ANALYSIS AND ARITHMETICAL MODELLING

This study utilizes publicly available datasets on bathymetry, wind, and wave conditions from the two zones in the Thracian Sea. For each zone, 28 years of high-resolution metocean data were analyzed at representative locations to ensure robust statistical modeling and representativeness. Data set covers hourly the period between January 1, 1993 to January 1, 2020. Figure 1 displays the boundaries of the two zones, along with bathymetric data and 28-year mean wind speed isocontours (at 10 m height). The figure also indicates the two study locations, ALE (Alexandroupoli) and SAM (Samothraki), for which environmental contours were calculated. As far as the wind resource, an increase is obtained as we move towards southeast; ALE location has a mean wind speed equal to 6,24 m/sec while SAM 7,04 m/sec. In Figure 2 ALE time series of significant wave height (H_s) and hub-height wind speed (u_W) are presented.

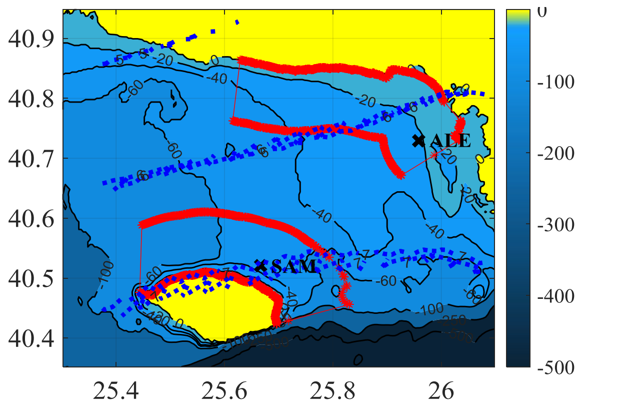

Figure 1. Bathymetry, wind speed contours and metocean analysis locations (ALE, SAM) in the Offshore Wind Farm Organized Development Areas in Thracian sea.

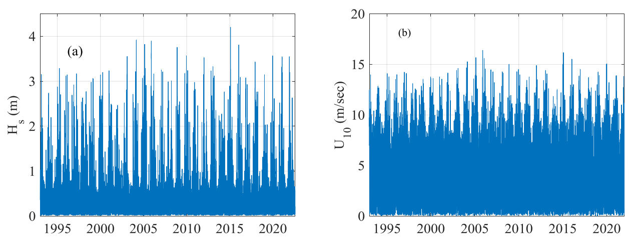

Figure 2. (a) H_s and (b) U_{10} series for ALE location

For the two locations under assessment, the joint probability distribution of H_s, u_W and T_p (peak wave period) is calculated. In constructing the joint distribution, H_s is selected as the primary governing variable in the analysis. Consequently, the joint distribution framework consists of a marginal distribution for H_s, a conditional distribution of u_W given H_s, and a conditional distribution of T_p given H_s. The resulting joint probability function is formulated as follows:

$$f_{H_s,\bar{u}_W,T_p}(h,u,t) = f_{H_s}(h) \cdot f_{\bar{u}_W|H_s}(u|h) \cdot f_{T_p|H_s}(t|h) \quad (1)$$

Regarding the marginal distribution of H_s, the values of H_s are predicted to follow a hybrid Lonowe model. The probability density function (PDF) is given as follows:

$$f_{H_s}(h) = \begin{cases} \frac{1}{\sqrt{2\pi}\sigma_{HM} h} \exp\left[-\frac{1}{2}\left(\frac{\ln(h)-\mu_{HM}}{\sigma_{HM}}\right)^2\right], h \le h_0 \\ \frac{\alpha_{HM}}{\beta_{HM}}\left(\frac{h}{\beta_{HM}}\right)^{\alpha_{HM}-1} \exp\left[-\left(\frac{h}{\beta_{HM}}\right)^{\alpha_{HM}}\right], h > h_0 \end{cases} \quad (2)$$

where the parameters α_{HM} and σ_{HM} define the lognormal distribution and correspond to the mean and standard deviation of the natural logarithm of significant wave height, ln(h), rather than of h itself. These parameters effectively describe the statistical behavior of smaller wave heights. Conversely, the parameters α_{HM} and β_{HM} represent the shape and scale of the two-parameter Weibull distribution, which governs the tail behavior associated with higher wave conditions. Also, h_0 is the shifting point of H_s from the lognormal distribution to the Weibull distribution.

The conditional distribution of u_W for given H_s is modeled using a two-parameter Weibull probability density function, characterized by the shape parameter α_{UC} and the scale parameter β_{UC}:

$$f_{\bar{u}_W|H_s}(u|h) = \frac{\alpha_{UC}}{\beta_{UC}}\left(\frac{u}{\beta_{UC}}\right)^{\alpha_{UC}-1} \exp\left[-\left(\frac{u}{\beta_{UC}}\right)^{\alpha_{UC}}\right] \quad (3)$$

To perform the analysis, the dataset is first stratified by discrete wave height intervals. Specifically, for values of H_s up to 1.0 m, where the dataset is densely populated a small bin size is employed, while for larger values we use larger represengative classes.

The subsequent step involves the estimation of the conditional distribution of peak wave period T_p given significant wave height H_s. This conditional distribution is modeled using a lognormal probability density function, defined by two parameters: μ_{TC} and σ_{TC} , which represent the mean and standard deviation of the natural logarithm of the variable:

$$f_{T_p|H_s}(t|h) = \frac{1}{\sqrt{2\pi}\sigma_{TC} t} \exp\left[-\frac{1}{2}\left(\frac{\ln(t)-\mu_{TC}}{\sigma_{TC}}\right)^2\right] \quad (4)$$

As previously outlined in the classification of H_s, the same binning approach is applied here to segment the dataset into discrete wave height classes.

Figure 3 presents the environmental contours and key results for a 50-year return period, as recommended by relevant standards, for the two examined locations. It is always very critical the reporting of the maximum conditions; for ALE those conditions correspond to: (i) H_s=4.92 m, T_p=9.49 s and U_W=13.26 m/s and (ii) H_s=1.23 m, T_p=4.97 s and U_W=24.44 m/s, while, for SAM are: (i) H_s=4.85 m, T_p=6.95 s and U_W=22.92 m/s and (ii) H_s=2.48 m, T_p=5.32 s and U_W=25.57 m/s.

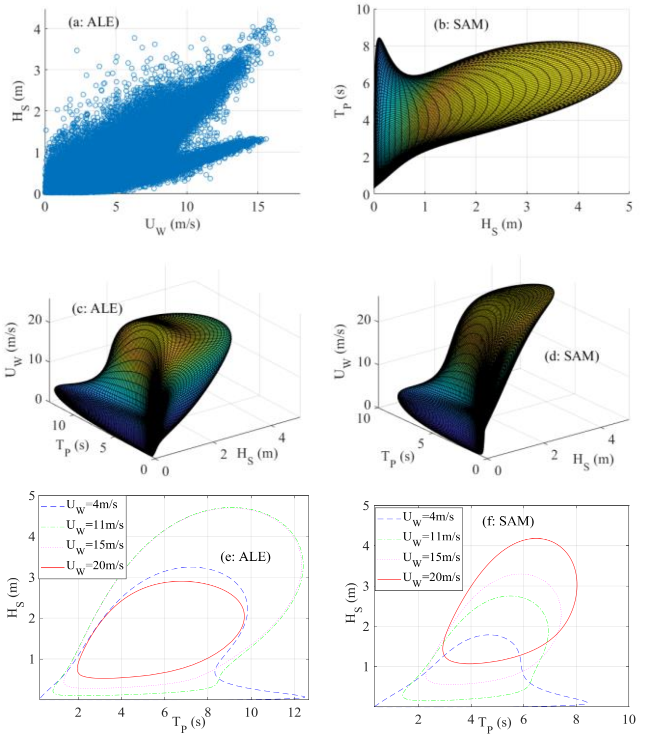

Figure 3. (a) H_s and U_W scatter plot of ALE, (b) H_s and T_p 2D environmental contour of SAM, 3D environmental contours of (c) ALE and (d) SAM, and environmental contours of H_s and T_p for different U_W values of (e) ALE and (f) SAM.

CONCLUSIONS

In this paper, the joint probability distributions of wind and wave conditions at two specific Thracian Sea locations are estimated and the environmental contour surfaces for 50 years returning period are calculated and presented for generic use.

ACKNOWLEDGEMENTS

This research was funded by the grant titled "Resilience of large-rated fixed bottom offshore wind turbines in Thracian Sea (XL-ALEX)" (Grant No. 81843), awarded by the Special Account for Research Funds of the International Hellenic University. It falls under task 2 of the program "Measures to Promote Research through Financial Support to Laboratories and Institutes of the International Hellenic University" (Code No. 81843).

REFERENCES

Hellenic Hydrocarbons and Energy Resources Management (HEREMA) 2023. National Offshore Wind Farm Development Plan, Athens, Greece.

Kardakaris, K., Boufidi, I. & Soukissian, T. 2021. Offshore wind and wave energy complementarity in the Greek seas based on ERA5 data. *Atmosphere* 12: 1360.

Vagiona, D.G. & Kamilakis, M. 2018. Sustainable Site Selec-tion for offshore wind farms in the South Aegean-Greece. *Sustainability* 10: 749.

Wind Europe 2024. Wind energy in Europe 2023: Statistics and the Outlook for 2024-2030.

Türkiye's Offshore Wind Energy Potential and Suitable Offshore Wind Power Plant Site Selection in YEKA Zones

Güral H.B.[1,*] and Akkurt G.G.[2]

[1] Ateş Wind Power, 35720, Bergama, Izmir, Turkey
[2] Izmir Institute of Technology, Energy Systems Engineering Department, Urla, Izmir, Turkey

*corresponding author:
e-mail: berrugural@atescelik.com

INTRODUCTION

The development of offshore wind energy is gaining significant attention due to its potential to contribute to renewable energy targets. Türkiye has identified several YEKA (Renewable Energy Resource Areas) for offshore wind development as shown in Figure 1, but site selection remains a critical challenge. This study presents a comprehensive feasibility analysis for offshore wind site selection within YEKA regions, integrating wind resource assessment, seabed characterization, environmental impact considerations, and economic feasibility studies.

Figure 1. Türkiye's Candidate Offshore YEKA Zones (Google Maps, 2024)

METHODOLOGY

The study employs a GIS-based approach to assess offshore wind feasibility in YEKA regions. the offshore wind farm selection criteria were investigated within the scope of candidate YEKA zones. Criteria were classified to three section as technical, social and accessibility. Firstly, the evaluation criteria and the study areas were determined, later the gathered data were processed through a Geographic Information System (GIS) tool called QGIS. There are some restrictions and qualifications that must be applied for site selection. During data processing the literature were reviewed and the legislation was inspected to determine the required limitation zones. Several criteria were evaluated, including wind speed, water depth, military restrictions, territorial waters, proximity to airports, fault lines, ports, and other environmental constraints. The site evaluation criteria and limitation zones are given in Table 1.

Wind Speed: According to Global Wind Atlas (2023), Bozcaada has the highest wind energy potential, followed by Gelibolu. Areas with wind speed over 7 m/s at 100-meter hub height were considered.

Water Depth: Fixed-bottom foundations were assessed for depths up to 50 meters, while floating platforms were considered for depths up to 200 meters.

Military & Territorial Waters: Restricted military zones were mapped from official notices. Türkiye's territorial waters extend 6 nautical miles on the western coast, but this does not significantly impact offshore feasibility.

Regulatory Constraints: Offshore wind farms must be at least 3 km away from airports and 3 km away from fault lines. Ports near YEKA zones were identified to optimize logistics.

Environmental & Infrastructure Factors: Wind Farms must be located outside of any bird migration paths. Additionally, submarine pipelines, and cables require a 750-meter buffer. These constraints were integrated into the site selection.

Table 1. Offshore Wind Farm Site Selection Criteria and Limitation Zones

Technical		
Criteria	**Limitation Zone**	**Data Source**
Wind Speed	≥ 7 m/s	Global Wind Atlas (2023)
Water Depth	≤ 50 m & ≤ 200 m	Global Wind Atlas (2023)
Social		
Criteria	**Limitation Zone**	**Data Source**
Military Regions	Outside	SHODB (2018)
Territorial Waters	Inside	Marine Regions (2023)
Airports	≥ 3 km	Our Airports (2023)
Fault Lines	≥ 3 km	MTA (2021)
Bird Migration Paths	Outside	Birdmap.5dvision (2013)
Key Biodiversity Areas	≥ 1 km	BirdLife International (2023)
Accessibility		
Criteria	**Limitation Zone**	**Data Source**
Shipwrecks	≥ 1 km	EMODnet (2023)
Submarine Cables	≥ 1 km	TeleGeography (2021)
Ship Route Density	≥ 3 km	EMODnet (2020)
Telecommunication cables	≥ 750 m	EMODnet (2017)
Submarine Pipeline	≥ 750 m	EMODnet (2023)

RESULTS & DISCUSSIONS

WIND RESOURCE ANALYSIS

Wind speed data indicates that YEKA regions possess high wind potential, with mean wind speeds exceeding 8 m/s at 100m hub height. Capacity factor estimations suggest values above 40% in optimal locations, making offshore wind a viable energy solution. However, wake losses due to turbine spacing and wind farm layout optimization must be considered.

SEABED AND BATHYMETRY ASSESSMENT

The bathymetric survey reveals that fixed-bottom foundations are feasible in depths up to 50m, particularly near Bozcaada and Gelibolu. However, deeper waters in other YEKA sites necessitate floating wind technology, increasing CAPEX but enabling deployment in high-wind zones.

ENVIRONMENTAL AND REGULATORY CONSIDERATIONS

Marine protected areas and busy maritime routes pose constraints on site selection. The study identifies zones with minimal environmental conflicts while ensuring regulatory compliance. Further environmental impact assessments (EIA) will be required before deployment.

GRID CONNECTION FEASIBILITY

Proximity to existing energy infrastructure is a key determinant of economic viability. The study identifies YEKA sites within 50 km of onshore substations, minimizing transmission losses and grid connection costs.

The results for suitable areas are shown in Figure 2 and Figure 3 for the fixed-bottom and floating platform scenarios, respectively.

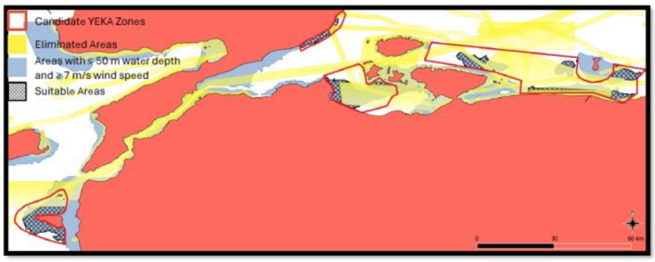

Figure 2. YEKA regions fixed-bottom scenario suitable areas map.

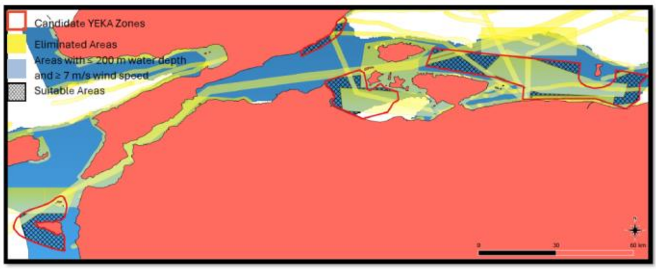

Figure 3. YEKA regions floating platform scenario suitable areas map.

CONCLUSION

The site selection for offshore wind farms in YEKA zones was evaluated using 14 criteria, categorized as technical, social, and accessibility factors. Areas with ≥7 m/s wind speed were deemed feasible, and water depth was analysed for fixed-bottom (≤50m) and floating (≤200m) foundations.

Bozcaada has the highest wind energy potential and shallow water depth, making it the most suitable for fixed-bottom foundations. However, high maritime traffic and tourism must be considered.

Gelibolu ranks second in wind potential but experiences turbulence and is located between two high-traffic straits.

Bandırma is close to active fault lines and military zones, limiting fixed-bottom feasibility but offering potential for floating platforms.

Karabiga has military restrictions but benefits from proximity to a port, reducing installation and maintenance costs.

While this study focused on YEKA regions, a broader assessment of Türkiye's western coastline is recommended due to its high wind potential. Future studies can enhance accuracy by incorporating seabed conditions, radar zones, and tourism impact.

ACKNOWLEDGEMENTS

The authors acknowledge the support of İzmir Institute of Technology and Ates Wind Power for providing data and technical guidance.

REFERENCES

Caceoğlu, E., Yildiz, H.K., Oğuz, E., Huvaj, N., & Guerrero, J.M. (2022). Offshore wind power plant site selection using Analytical Hierarchy Process for Northwest Turkey. *Ocean Eng.* 252, 111178.

Genç, M.S., Karipoğlu, F., Koca, K., & Azgın, Ş.T. (2021). Suitable site selection for offshore wind farms in Turkey's seas: GIS-MCDM based approach. *Earth Sci. Inform.* 14(3), 1213–1225.

Karipoğlu, F., Genç, M.S., & Koca, K. (2021b) Determination of the most appropriate site selection of wind power plants based Geographical Information System and Multi-Criteria Decision-Making approach in Develi, Turkey. *Int. J. Sustain. Energy Plan. Manag.* 30, 97–114.

Assessment Framework for Integrating Socioeconomic Impacts in Maritime Spatial Planning

Politopoulou C.[1,*], Papathanasiou A-F.[1], Mitropoulos L.[2], Vassi A.[2] and Giantsi T.[1]

[1] Department of Civil Engineering, National Technical University of Athens, Iroon Polytechniou 5, 15780 Athens, Greece
[2] Department of Rural Surveying and Geoinformatics Engineering, National Technical University of Athens, Iroon Polytechniou 5, 15780 Athens, Greece

*corresponding author:
e-mail: politopouloux@outlook.com

INTRODUCTION

Climate change refers to alterations in the climate directly or indirectly caused by human activities, leading to changes in the composition of the global atmosphere. This change is beyond the natural variability of the climate observed over comparable timeframes (United Nations Framework Convention, 1992). Maritime Spatial Planning (MSP) balances competing activities and protects marine ecosystems. MSP is a tool for managing the use of seas and oceans in a coherent, efficient, safe, and sustainable way. This study proposes a framework to integrate socioeconomic impacts in MSP, offering practical steps for sustainable resource use and environmental resilience under the European Union's (EU) sustainable development strategy.

MSP SYSTEM IN GREECE

Greece's MSP framework governs territorial waters up to 6 nautical miles, addressing ecological, economic, and geopolitical challenges. It focuses on marine boundaries with Italy, Turkey, Egypt, and Albania (Figure 1). Although Greece lacks a national MSP, it has sectoral frameworks addressing aquaculture and tourism. Key activities include fishing, aquaculture, energy production, transportation, and underwater cables.

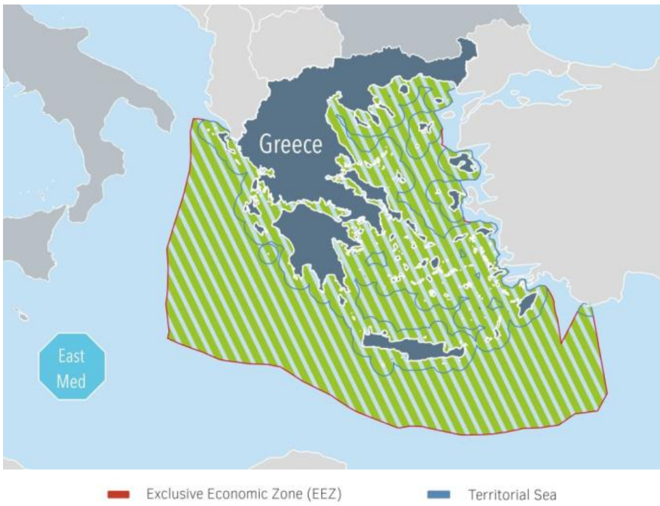

Figure 1. Territorial sea and Exclusive Economic Zone of Greece.

The coastal environment also supports tourism (e.g., cruises, sailing, surfing) and protected areas like Natura 2000, highlighting the balance between economic development and environmental protection. The concept of MSP emerged in Greece in 2000 but was not implemented until the 2014/89 EU Directive made it mandatory. Different maritime spatial units exhibit varying development patterns and pressures, requiring tailored management approaches. These areas possess diverse natural and cultural resources with unique exploitation potential and risks. Given their high vulnerability to climate change, an integrated, holistic strategy is crucial for sustainable maritime policy formulation and implementation.

MSP PRACTICES AND FRAMEWORKS

The evaluation of MSP is in early stages with no standardized process, relying on isolated efforts. EU Member States must analyze MSP's impacts using various criteria to assess its effectiveness. Human activities often have similar impacts, making this process challenging. Effective MSP requires interdisciplinary teams with expertise in spatial planning, maritime science, law, and stakeholder engagement. Though few studies assess MSP's effectiveness, there is growing recognition of its socio-economic benefits. Evaluation should involve clear criteria, addressing environmental, social, and economic issues with both qualitative and quantitative assessments. Six evaluation categories are suggested: ecosystem functioning, integration, spatial boundaries, adaptation, strategic goals, and stakeholder participation.

MSP ASSESSMENT METHODOLOGIES

Recent emphasis is on environmental protection and costbenefit analysis of MSP, with methods like Willingness to Pay and Input-Output Analysis used to quantify economic impacts. These methodologies evaluate trade-offs between economic benefits and costs, including opportunity costs and external impacts. In general, the socioeconomic data used in MSP are mostly missing or limited to descriptive information and it usually focuses on the short term.

OBJECTIVES AND IMPACTS IN MSP

MSP ensures the sustainable management of maritime resources. The step after defining the goals of the MSP is the identification of indicators that can measure progress in achieving these goals. The indicators for eight activities are listed in Table 1 as part of the general objectives of Blue Growth. While these are not described in detail, they are set outside the scope of the MSP and can be partially supported by the long-term indicators proposed for MSP. Objectives are set at three spatial levels, which correspond to specific timeframes are broad objectives (Blue Growth), longterm objectives and short-term objectives. Success depends on well-defined goals and indicators that track progress and effectiveness. These indicators assess long-term impacts like biodiversity conservation, sustainable fisheries, and renewable energy growth (e.g., offshore wind farms). They also evaluate the health of coastal industries and tourism, and protect cultural heritage. By using these indicators, MSP authorities can make informed decisions, minimizing negative ecosystem impacts. This monitoring fosters sustainable maritime sector growth, enhances ecosystem resilience, and supports coastal region development, contributing to blue growth and climate change mitigation.

Table 1. Indicators for Sustainable Management and Development of Marine and Coastal Activities.

Activity	Indicator and description
Marine and coastal protected areas	• Biodiversity: Increase indicators in protected areas. • Protected Areas: Percentage with effective management and regulation compliance. • Research Projects and Monitoring Programs: Number of projects conducted in protected areas.
Fisheries and aquaculture	• Fish Stock at Sustainable Levels: Percentage managed at sustainably. • Adoption of Sustainable Practices: Adoption rate in aquaculture technologies. • Profit and Employment Rates: Profit margins and employment rates in fisheries and aquaculture.
Coastal and marine tourism	• Certified Tourist Operators: Eco-certified operators. • Coastal and Marine Tourism Revenue: revenue from tourism activities. • Cultural Heritage Sites: Sites integrated into tourism and education programs.
Underwater cultural heritage	• Underwater Cultural Heritage Sites: Protected and preserved sites. • Public Awareness: Levels measured via surveys and participation rates. • Tourism Activities Related to Underwater Monuments: Activities featuring heritage with sustainable access.
Shipping	• Ship Processing Time: Average port processing time and reduction in shipping costs. • Maritime Shipping Emissions: Emission reductions. • Maritime Accidents: Annual number of accidents and incidents. • Indicators for Port operations
Coastal industries	• Coastal Industrial Projects Following Sustainable Development: Percentage complying with environmental regulations. • Investment in Research and Development: Funding for sustainable industrial technologies. • GVA from Coastal Industry: Contribution to local and national economy.
Oil, natural gas and minerals	• Oil Spills and Environmental Incidents: Number and volume of reported cases. • Investment in Renewable Energy by Oil Companies: Funding for renewable energy projects. • Investement in minerals mining
Renewable Energy Sources	• Installed Capacity (MW) of Renewable Energy Projects: Capacity of renewable energy in coastal areas. • Investment in Renewable Energy: Offshore renewable energy investments. • Energy Produced from Renewable Sources: Share of marine renewables in national energy mix.

CONCLUSION

MSP is key for sustainable maritime resource management. Its implementation involves structured phases, evaluating socioeconomic impacts through comparisons of hypothetical and real data. Proposed frameworks focus on measurable, relevant indicators. Continuous data collection and evaluation, alongside national and European collaboration, ensure effective decision-making and adaptation to challenges.

REFERENCES

European Commission. (2020). Study on the Economic Impact of Maritime Spatial Planning, Final Report. European MSP Platform.

European Commission. (n.d.). Maritime Spatial Planning. Retrieved from oceans-and-fisheries.ec.europa.eu /ocean/blue-economy/maritime-spatial-planning_en

Ehler, C., & Douvere, F. (2007). Visions for a Sea Change. UNESCO/IOC.

Guerry, A.D., et al. (2012). Modeling benefits from nature: using ecosystem services to inform coastal and marine spatial planning. *Int. J. Biodivers. Sci. Ecosyst. Serv. Manag.* 8(1-2), 107–121.

Kelly, C., Gray, L., Shucksmith, R.J., & Tweddle, J.F. (2014). Investigating options on how to address cumulative impacts in marine spatial planning. *Ocean Coast. Manag.* 102, 139–148.

Santiago, J. L., Ballesteros, M., Campillos-Llanos, M., Cervera-Núñez, C., LeTissier, M., & Menegon, S. (2023). Guidelines for the Integration of the Socioeconomic Impact of MSP. European Commission, Technical Expert Group on Data for MSP, Socioeconomic Subgroup.

The Provision of Water Supply and Sanitation for Coastal Zones and Marine Infrastructure in Georgia: Challenges and Key Issues

Kavelashvili L. [1,*], Tsinadze Z.[1] and Gordeziani K.[1]

[1] Georgian Technical University, 77 Kostava Str., 0160Tbilisi, Georgia

*corresponding author:
e-mail: l.kavelashvili7@gmail.com

ABSTRACT
The provision of sustainable water supply and sanitation in Georgia's coastal zones presents significant challenges due to climate change, rapid urbanization, expanding tourism, and environmental degradation. Rising sea levels, saltwater intrusion, and extreme weather events threaten freshwater availability, while increased population growth and tourism place additional pressure on water infrastructure. Many existing systems are outdated and insufficient, leading to inefficiencies, water losses, and pollution. Inadequate wastewater treatment contributes to marine ecosystem degradation and public health risks. Addressing these issues requires comprehensive strategies, including infrastructure investment, sustainable water management, climate adaptation measures, and improved governance. Implementing desalination, rainwater harvesting, and smart water technologies can enhance water security and resilience. Strengthening regulations and adopting sustainable tourism practices will be crucial for long-term environmental and economic sustainability. This study highlights the critical need for an integrated approach to water management to ensure a reliable and clean water supply for Georgia's coastal communities.

INTRODUCTION
Georgia, a country with a rapidly developing coastline along the Black Sea, faces significant challenges in providing sustainable water supply and sanitation for its coastal zones and marine infrastructure. Climate change, increasing urbanization, expanding tourism, and environmental degradation contribute to the complexity of ensuring safe and efficient water management in these areas. Addressing these challenges requires a comprehensive and resilient approach to safeguard public health, the environment, and economic development.

KEY ISSUES FOR WATER SUPPLY AND SANITATION IN COASTAL ZONES

1. Climate Change and Water Resources
One of the most pressing challenges affecting coastal water supply is climate change. Rising sea levels and changing precipitation patterns threaten freshwater sources in Georgia's coastal regions. Saltwater intrusion into groundwater, a key drinking water source, is becoming more frequent, reducing water availability and quality. Additionally, increased temperatures and droughts lead to water scarcity, stressing supply systems. Extreme weather events, such as storms and heavy rainfall, further challenge water management by causing infrastructure damage, flooding, and contamination of water sources. Storm surges can lead to higher salinity levels in coastal aquifers, requiring advanced treatment methods to make water potable. Additionally, the unpredictability of climate conditions makes long-term planning for water resource management increasingly difficult. Georgia relies on a mix of surface water and groundwater sources for its coastal water supply. The Rioni and Chorokhi rivers, along with smaller tributaries, are essential surface water sources, while underground reservoirs provide groundwater. However, pollution from industrial discharge, agricultural runoff, and untreated sewage frequently compromises water quality. Over-extraction of groundwater also exacerbates the problem, as it can lead to land subsidence and further intrusion of saline water into freshwater reserves.

To combat these issues, investment in modern desalination plants and enhanced water treatment facilities is necessary. Additionally, promoting rainwater harvesting and water reuse initiatives can help mitigate water scarcity. Technological advancements, such as smart water management systems, can improve efficiency by detecting leaks and optimizing distribution networks.

2. Rapid Urbanization and Population Growth
Coastal cities like Batumi, Poti, and Kobuleti have experienced rapid urban expansion, increasing demand for water supply and sanitation services. The infrastructure in these regions often struggles to keep pace with growing populations, leading to inefficiencies, water losses, and inadequate sewage treatment. Informal settlements, in particular, suffer from limited access to clean water and proper sanitation facilities. The lack of proper zoning regulations and urban planning in some areas leads to uncontrolled development, placing additional stress on water infrastructure. Informal settlements that develop without proper connection to municipal water and sewer systems can contribute to pollution and public health hazards, increasing the risk of waterborne diseases such as cholera and dysentery. Expanding infrastructure to serve these rapidly growing populations is a key challenge that requires significant investment and strategic planning.

Additionally, urban water demand is rising due to increased household consumption, industrial activity, and commercial use. Many older distribution networks suffer from leakages, resulting in high non-revenue water losses. Implementing water conservation programs, upgrading pipelines, and introducing tiered water pricing structures can help manage demand and reduce waste. Coastal cities like Batumi, Poti, and Kobuleti have experienced rapid urban expansion, increasing demand for water supply and sanitation services. The infrastructure in these regions often struggles to keep pace with growing populations, leading to inefficiencies, water losses, and inadequate sewage treatment. Informal settlements, in particular, suffer from limited access to clean water and proper sanitation facilities.

3. Expanding Tourism and Seasonal Demand Fluctuations

Georgia's coastal areas are key tourist destinations, especially during the summer months. Seasonal fluctuations place additional pressure on water supply and wastewater management systems. During peak seasons, water demand surges, overwhelming infrastructure designed for lower, year-round populations. This can lead to water shortages, contamination risks, and increased discharge of untreated wastewater into the Black Sea, harming marine ecosystems.

In tourist-heavy regions, hotels, resorts, and restaurants require large amounts of water for daily operations, which can deplete resources for local residents. Additionally, many older wastewater treatment systems are not equipped to handle the increased load, leading to untreated sewage being released into the environment. Sustainable tourism policies, including water conservation initiatives and improved treatment capacity, are essential to mitigating these impacts.

Introducing sustainable tourism measures, such as low-flow fixtures, water-efficient landscaping, and greywater recycling in hotels, can help alleviate pressure on local water systems. Furthermore, developing alternative water sources, such as desalination plants tailored for peak demand periods, can ensure a reliable supply without overexploiting natural resources.

4. Aging and Insufficient Infrastructure

Many coastal water supply and sanitation systems in Georgia are outdated and in need of modernization. Old pipelines and wastewater treatment facilities often suffer from leaks, inefficiencies, and breakdowns, leading to water losses and environmental pollution. Insufficient investment in upgrading and maintaining these systems exacerbates the problem, posing risks to both human health and the local economy.

In some cases, infrastructure that was originally built to serve small populations is now overwhelmed due to rapid urban growth. The lack of redundancy in many water treatment plants means that any failure in the system can lead to prolonged service disruptions. Additionally, limited funding for maintenance and expansion has resulted in suboptimal operations, further straining the already fragile system.

Encouraging public-private partnerships for infrastructure funding and integrating smart water technologies can improve efficiency and ensure long-term sustainability. Governments must also prioritize regular maintenance and timely upgrades to prevent costly breakdowns.

5. Environmental Pollution and Marine Ecosystem Degradation

Improper wastewater disposal and untreated sewage discharge into the Black Sea have led to significant marine pollution. This not only affects aquatic ecosystems but also threatens public health, fisheries, and tourism. Industrial activities and agricultural runoff further contribute to water contamination, increasing the need for robust environmental management strategies. Coastal areas serve as vital habitats for diverse marine life, and pollution from human activities can lead to declining biodiversity, algal blooms, and contamination of seafood. The destruction of natural buffers such as wetlands and mangroves further exacerbates pollution risks, as these ecosystems play a crucial role in filtering pollutants. Strengthening regulations and enforcing proper wastewater treatment measures is necessary to protect the long-term sustainability of Georgia's coastal environment.

Strategies for Addressing Water Supply and Sanitation Challenges

To overcome these challenges, Georgia must adopt a multi-faceted approach, including:

- **Infrastructure Investment:** Upgrading water supply and sanitation facilities to improve efficiency and resilience**.**
- **Sustainable Water Management:** Implementing desalination, rainwater harvesting, and water recycling technologies.
- **Climate Adaptation Measures**: Enhancing flood protection, monitoring saltwater intrusion, and promoting water conservation.
- **Tourism-Sensitive Planning**: Developing infrastructure that accommodates seasonal demand without overburdening local resources.
- **Strengthening Regulations and Governance**: Enforcing stricter wastewater treatment regulations and encouraging public-private partnerships for infrastructure development.

CONCLUSION

Ensuring reliable water supply and sanitation in Georgia's coastal zones is crucial for public health, environmental sustainability, and economic growth. Addressing the challenges posed by climate change, urbanization, tourism, and infrastructure limitations requires coordinated efforts from government agencies, local communities, and international partners. By implementing strategic investments and sustainable water management practices, Georgia can build a resilient and efficient coastal water supply and sanitation system for the future.

REFERENCES

UNDP (2021). *Strengthening Climate Resilience in Georgia's Coastal Zones.* https://www.undp.org.

World Bank (2020). *Georgia: Water Sector Diagnostic and Policy Recommendations.* https://www.worldbank.org.

Kavelashvili, L., Tsinadze, Z., & Gordeziani, K. (2024). Concept of water loss risk assessment in the water supply network of Georgia. Proc. 4th International Conference "Problems of Engineering Sciences", Batumi, Georgia

L. Kavelashvili, K. Gordeziani, Z. Tsinadze, (2024). Modern methods of wastewater treatment. The 3rd forum dedicated to World Water Day, Georgian Technical University.

Kavelashvili, L., Gordeziani, K., & Tsinadze, Z. (2023). Water management model using water accounting method. ISSN 1512-0287, Georgian Engineering News 3'23.

An Integrated Approach to Coastal Protection of Navagio (Shipwreck) Beach in Zakynthos, Greece

Tsoukala V.[1,*], Papadimitriou A.[1], Sartampakos P.[2], Metallinos A.[1], Ziros A.[1] and Chondros M.[1]

[1] Laboratory of Harbour Works, NTUA, 9 Iroon Polytechniou Str., 15780 Zografou, Greece
[2] Nireas Engineering, Katsikogianni 8, 34132 Chalkis, Greece

*corresponding author:
e-mail: tsoukala@mail.ntua.gr

INTRODUCTION

Navagio Beach, located on the northwest coast of Zakynthos, Greece (37.859362°, 20.624931°), is one of the most iconic tourist destinations globally, renowned for the shipwreck of "MV Panagiotis", which was carried ashore by wave action back in 1980. The beach is characterized by its steep cliffs, crystal-clear waters, and the historic shipwreck, which has become a cultural landmark. However, the site faces significant challenges due to intensive wave action and rising sea levels, which threaten the structural integrity of the shipwreck while rockfalls pose a direct threat to the safety of visitors. To address these challenges, this study employs an integrated approach combining advanced field measurements and state-of-the-art numerical modeling to propose an optimal coastal protection measure. The primary objective is to protect the shipwreck from wave action, mitigating the coastal erosion, while preserving at the same time the natural beauty and ecological balance of the area.

METHODOLOGY

This study adopts a comprehensive methodology to understand the complex coastal processes at Navagio Beach and to design an effective protection measure. The key steps include:

Data Collection: Retrieval of data from reputable oceanographic databases and operational wind stations.

Field Measurements: Bathymetric and geophysical surveying of the whole bay and concurrent field measurements of waves and currents in deep intermediate and shallow waters using advanced and reliable equipment.

Numerical Modelling: Application of Scientia Maris models (Scientia Maris, 2023) for hydrodynamic and sediment transport simulations for the longshore coastal processes.

Model Calibration & Validation: Numerical model validation and calibration with field measurements to ensure accuracy.

Coastal Profile Evolution: Simulation using the CSHORE model (Kobayashi, 2009) to evaluate the profile shoreline evolution and wave run-up.

Selection of Protection Measure: Selection of the proper protection scheme (beach nourishment in this case)

Optimization of Protection Measure: Optimization of nourishment layout and volume to enhance coastal resilience and prevent erosion & degradation of "MV Panagiotis".

FIELD MEASUREMENTS

To gain valuable insights about the prevalent conditions at the study area, extensive field measurements were carried out utilizing state of the art instrumentation, regarding:

Bathymetric and Geophysical Surveying: High-resolution bathymetric (with multibeam echosounders) and geophysical surveys were conducted to map the seabed in detail and provide crucial information on the bed layer composition and width, something unique in coastal engineering applications.

Concurrent Wave and Current Measurements: Waves and currents were measured simultaneously in deep, intermediate, and shallow waters via advanced instrumentation, i.e. wave buoys and current profilers, connected on a web dashboard, providing critical data for model calibration and validation.

Sediment Sampling: to determine grain size distributions and assess potential sediment compatibility for the nourishment.

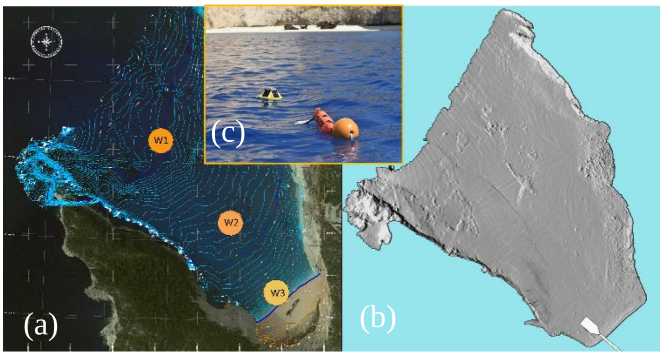

Figure 1: (a) Locations of wave (W1, W2, W3) measurements in the study area; (b) backscatter survey by the multibeam echosounder, (c) W2 wave spotter buoy.

NUMERICAL MODELLING

The study employed cutting-edge numerical modeling tools to analyze wave propagation, hydrodynamic field, sediment transport processes and coastal profile evolution at Navagio Beach. The models applied include long-shore and cross-shore processes. Specifically:

Longshore Coastal Processes: The longshore Coastal Processes were simulated by using the advanced models of Scientia Maris (Scientia Maris 2023). Specifically, wave propagation was defined by applying the numerical model Maris HMS, a nonlinear model that solves the hyperbolic form of the mild-slope equations. This model accurately simulates the transformation of complex wave fields and accounts for various coastal phenomena, including nonlinear irregular wave propagation, shoaling, refraction, diffraction, partial or total reflection, and energy dissipation due to bottom friction and wave breaking. The hydrodynamic field was simulated using Maris HYD, modelling the nearshore wave generated currents and subsequently, the simulation of sediment transport field was performed by implementing the Maris SDT model. To reduce the sheer number of simulations several wave input reduction methods were examined to assess their performance in both predicting accurately the morphological bed evolution in the study area but also reducing the computational effort.

Coastal Profile Evolution: The analysis of coastal profile evolution involved extracting the bed level in representative coastal profiles to assess sediment dynamics. Numerical modeling entailed nearshore wave transformation as well as estimation of wave runup. The coastal profile evolution was simulated using the CSHORE model developed by USACE (Kobayashi, 2009). Additionally, the effectiveness of the proposed beach nourishment scheme was evaluated by simulating the response of the new beach profile under different hydrodynamic conditions, ensuring long-term stability without frequent renourishment of the shoreface.

RESULTS & DISCUSSION

The obtained results highlight the significant role of wave-induced hydrodynamics in shaping the coastal morphology of Navagio Beach. Without intervention, wave runup (even for waves with return periods lower than 1 year), reaches the shipwreck of MV Panagiotis accelerating corrosion and structural degradation. Field measurements of wave characteristics confirm that the main wave propagation direction is from WNW to NNW, leading to direct wave attack to the beach and dominant cross-shore dynamics. Figure 2 showcases the concurrent measurements of significant wave height at the three buoy locations. As expected, wave height decreases as the waves approach shallower water but not significantly, due to the low energetic sea-states and refraction coefficients close to 1. The field campaign was also crucial in calibrating the hydrodynamic models (Figure 3), with numerical results well within acceptable limits (< 10% difference in shallow water). To eliminate the effect of wave runup and considering the ecological and cultural implications of “hard” protection measures, beach nourishment was considered the optimal solution. The Scientia Maris models were employed in order to focus on longshore processes ensuring the optimized design that maximizes energy dissipation and minimizes sediment loss over time. The sea-surface elevation comparison between the existing beach and the nourished configuration is shown in Figure 4. The mild shoreface slope of the envisaged nourishment enhances wave energy dissipation by expanding the surf zone width and effectively reducing wave run-up.

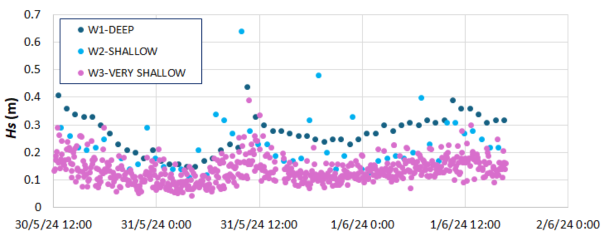

Figure 2. Wave height field measurements.

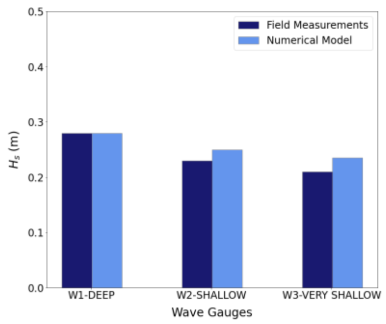

Figure 3. Comparison of wave model results with field measurements.

The simulations with the CSHORE coastal profile model indicate a seasonal variability of the shoreface with higher erosion volumes during winter. A berm is formed above the waterline offering another means of reducing wave runup. The implementation of beach nourishment is shown to serve the purpose of reducing wave run-up, expanding the beach width, with small loses of sand even for extreme events (Figure 5).

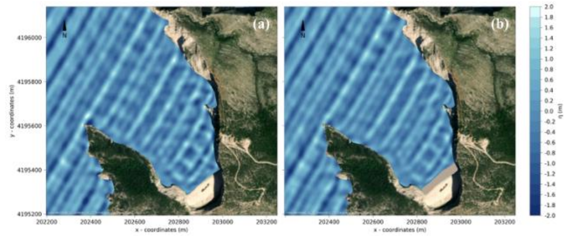

Figure 4. Sea surface elevation with incoming wave characteristics H_s = 2.35 m, T_p = 7.84 s, MWD = 300^o N for (a) current situation; (b) proposed nourished beach.

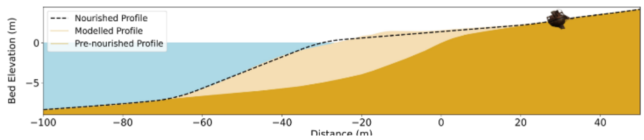

Figure 5. Modelled nourished profile evolution after a year of wave action – CSHORE model.

While the obtained results for the nourished beach profile evolution indicate a general stability of the newly formed beach, it is crucial to establish a monitoring system and further conduct field measurements of waves & currents to ensure proper recovery in case of storm events.

CONCLUSIONS

This study underscores the effectiveness of an integrated approach to coastal protection, incorporating field measurements of oceanographic data and bed composition, validated numerical modeling, and environmentally friendly protection measures. Beach nourishment proves to be a viable intervention, creating a buffer zone for waves while preserving the site's aesthetic and cultural value. It also emerges as a dual-purpose solution, increasing beach width while also mitigating wave runup, reducing the impact of wave action on the historic shipwreck. This measure not only helps preserve the cultural landmark but also enhances beach stability, as well as promoting sustainable tourism with increasing the beach width.

ACKNOWLEDGEMENTS

The authors express their gratitude to Assoc. Prof. A. Kalimeris of the Ionian University for the provision of wind measurements and Assoc. Prof. P. Tsakiridis of NTUA for his contribution to the field measurements.

REFERENCES

Kobayashi, N. (2009). Documentation of Cross-Shore Numerical Model CSHORE 2009. Research Report No. CACR-09-06. Newark, Delaware.

Scientia Maris (2023). User Guides v03.2023 for Maris HMS, HYD, SDT

Assessment of Property Exposure to Coastal Flooding in Urban Areas: Application in Miami (FL, USA)

Makris C.[1,*], Mallios Z.[2], Androulidakis Y.[3] and Kourafalou V.[4]

[1] Department of Civil Engineering, Democritus University of Thrace, Xanthi, 67100, Greece
[2] School of Civil Engineering, Aristotle University of Thessaloniki, Thessaloniki, 54124, Greece
[3] Department of Marine Sciences, University of the Aegean, Mytilene, Lesvos Island, 81100, Greece
[4] Rosenstiel School of Marine Atmospheric and Earth Science, University of Miami, Miami, Florida, 33149-1031, USA

*corresponding author:
e-mail: cmakris@civil.duth.gr

INTRODUCTION

The fluctuations in nearshore Sea Level Elevation (SLE) are a crucial indicator of climate change, significantly affecting low-lying coastal regions (Williams & Gutierrez, 2009). South Florida (USA) is one of the world's most vulnerable areas, frequently experiencing extreme sea levels due to hurricanes and tropical storms. Miami, with its urban infrastructure exposed to the Atlantic Ocean, is facing risks from such climate-induced adversities (Palm & Bolsen, 2020). Storm surges have inundated coastal areas during past cyclonic weather events, leading to urban disruptions with important socio-economic and environmental impacts.

SCOPE OF STUDY

This study explores new ways to estimate the exposure of properties (at the plot holding level) to coastal flooding based on highly detailed inundation hazard maps (Makris et al., 2024). These are produced by a recent version of the CoastFLOOD model (Makris et al., 2023), specifically designed for high-resolution (1-2 m grid-scale) simulations of coastal inundation driven by extreme SLE scenarios along South Florida's shorelines over a 30-year timeframe (1994-2023). The primary aim is to analyze the interannual variability of urban flooding impacts on key residential areas in Miami while evaluating the building-level exposure to seawater floods along the Biscayne Bay coast and Miami Beach. The study also investigates long-term SLE trends and extremes using historical tide gauge records to minimize the uncertainty of environmental parametric inputs. The goal is to improve understanding of seawater inundation impacts and support coastal flood risk assessment at the building and property levels using detailed GIS flood maps.

METHODOLOGY

Study Area – Sea Level Data

Miami-Dade County (MDC), located in southeastern Florida, is highly susceptible to storm surges, particularly during hurricanes and King Tide events (Chao et al., 2021). The study area (Figure 1) was chosen based on its diverse Land Use and Land Cover (LULC) while considering several local socio-economic factors (e.g., dense population and valuable real estate). The extents of the study area and its simulation domain were defined based on the computational feasibility for flood modelling (~$15 \cdot 10^3$ grid cells). It includes the northern Biscayne Bay coasts and Miami Beach, representing both naturally sheltered regions and highly exposed urban shorelines. SLE data were sourced from NOAA's hourly tide gauge records in Virginia Key (central Biscayne Bay), covering the 1994–2023 period. The highest recorded SLE (=1.172 m >244-year return value) occurred during Hurricane Irma, a devastating Category 5 tropical cyclone in early September 2017.

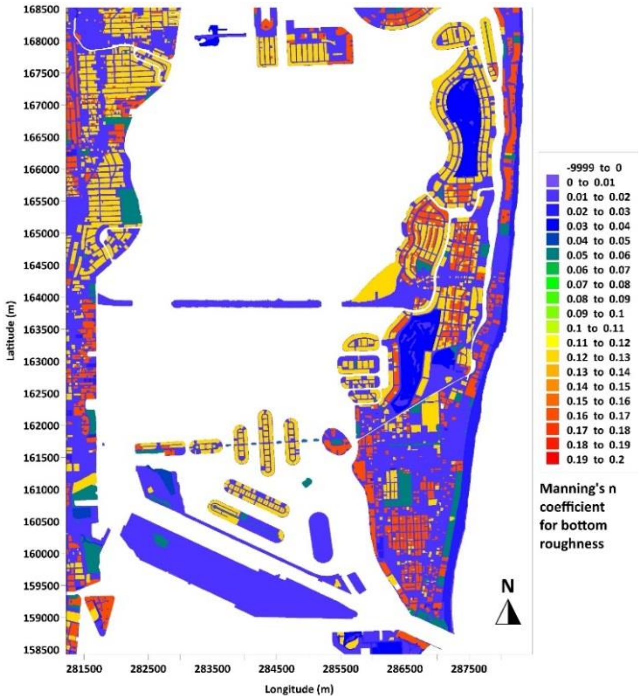

Figure 1. Chorochromatic-type map of the Miami study area's Manning *n* coefficient of terrain bottom roughness based on NLCD's LULC data, overlaid on NOAA's 2-m resolution Digital Surface Model (DSM) for land elevation, measured from North American Vertical Datum 1988.

Numerical Model – Extreme Value Analysis

CoastFLOOD is a high-resolution, raster-based, two-dimensional flood routing simulation model that tracks seawater propagation using mass balance equations (Makris et al., 2023). It integrates Manning's roughness coefficients to represent terrain friction and is calibrated using NOAA datasets (Makris et al., 2024). The model is applied to assess urban flood exposure under various SLE scenarios. Our analysis identifies 2-, 5-, 10-, …, 100-, …, 1000-, … 10000-year return values of SLEs (Table 1), based on a GEV distribution fit of annual block maxima, using the *extRemes* package of R-studio. Thresholds and long-term trends are estimated by applying statistical models such as Empirical Mode Decomposition and Pettit Homogeneity tests.

Property-Level Exposure to Coastal Flooding

The impact of the coastal inundation hazard was estimated based on a generic Flood Cover Percentage (FCP%; Androulidakis et al., 2023). The assessment components of property-level exposure to coastal inundation comprise very high-resolution analyses of both building-level and elements-at-risk impact metrics to manage seawater flooding in coastal cities and their adverse effects (Iliadis et al., 2023). For example, the quantifiable metrics include inundation probability measures per property by number of flooded cells, min-max, standard deviation, median, and high-order percentiles of hazard magnitudes in terms of flooded area, maximum floodwater height and velocity, mean encroached floodwater depth, vicinity of buildings to flood boundaries, etc., defined per discrete property by an effective buffer zone around its bounds, regarding a diverse sample of owners and stakeholders. A classification scheme to categorize buildings and properties by a 5-level Likert-scale ranking formulates a cumulative exposure index for each element at risk.

Table 1. Extreme coastal SLE scenarios at MDC study area.

A/A	Return Period (-years)	SLE_{extr} (m)	A/A	Return Period (-years)	SLE_{extr} (m)
1	2	0.520	7	200	1.126
2	5	0.651	8	500	1.249
3	10	0.741	9	1000	1.344
4	20	0.829	10	2000	1.441
5	50	0.945	11	5000	1.572
6	100	1.035	12	10000	1.674

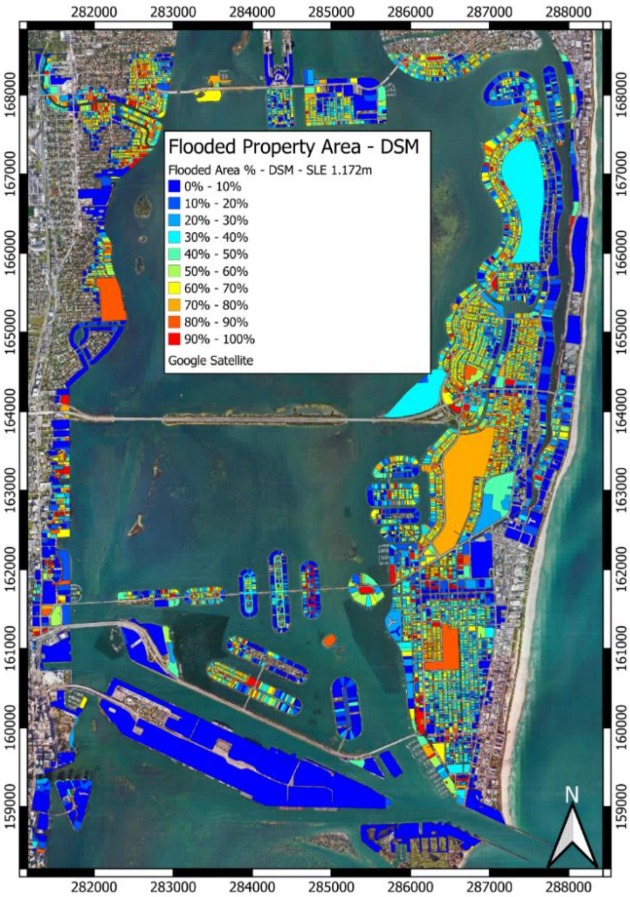

Figure 2. Choropleth-type map of flooded properties portraying the percentage of inundated area within each discrete plot holding over the study region, based on CoastFLOOD simulations for Hurricane Irma (SLE = 1.172 m).

RESULTS

Model Validation - Coastal Inundation Assessment

The model's performance was evaluated by comparing it with NOAA's Sea Level Rise (Bathtub) Viewer outputs, which assess flooded areas under similar SLE conditions. The results revealed a quite high correlation between CoastFLOOD simulations and NOAA estimations, with a Goodness-of-Fit, GoF>0.8. Differentiations are plausible since CoastFLOOD model considers the flow dynamics due to bottom friction. Flood heights are analyzed for significant storm surge events (e.g. Hurricane Irma) and 12 extreme scenarios (Table 1). CoastFLOOD simulations indicate that areas with land elevation up to 2 m above mean sea level are particularly exposed, corroborating the FEMA (2018) reports of surge-induced inundation in downtown MDC.

Property-Level Exposure Analysis

The key findings of flood exposure assessment at the property level using GIS-based spatial analyses (Figure 2) include:

- Low-lying residential areas exhibit high flood exposure, particularly in southwestern Miami Beach and island barriers.
- Properties near Indian Creek and Biscayne Bay's western coastlines are highly exposed to inundation events.
- Coastal infrastructure, such as the port and highways, demonstrates flood pooling due to impermeable surfaces.

CONCLUSIONS

This research presents a high-resolution numerical approach for simulating coastal flooding in Miami-Dade County. We estimate detailed GIS-based impacts by incorporating long-term *in-situ* observations and proper extreme value analysis of SLE, providing insights into property-level exposure to flood hazards. The findings highlight the need for enhanced urban planning and adaptation strategies to mitigate future coastal hazards from hurricane-induced storm surges.

REFERENCES

Androulidakis, Y., Makris, C.V., Mallios, Z., & Krestenitis, Y. (2023). Sea level variability and coastal inundation over the northeastern Mediterranean Sea. *Coast Eng J.* 65(4), 514–545.

Chao, S.R., Ghansah, B., & Grant, R. (2021). An exploratory model to characterize the vulnerability of coastal buildings to storm surge flooding in Miami-Dade County, Florida. *Appl Geogr*. 128, 102413.

FEMA (2018). *Mitigation assessment team report: Hurricane Irma in Florida*. FEMA P-2023.

Iliadis, C., Galiatsatou, P., Glenis, V., Prinos, P., & Kilsby, C. (2023). Urban Flood Modelling under Extreme Rainfall Conditions for Building-Level Flood Exposure Analysis. *Hydrol.* 10(8), 172.

Makris, C. et al. (2023). CoastFLOOD: A High-Resolution Model for the Simulation of Coastal Inundation Due to Storm Surges. *Hydrol*, 10(5), 103.

Makris C.V., Mallios, Z., Androulidakis, Y., & Krestenitis, Y. (2024). On Modeling the Coastal Floods and Assessing the Impacts on Inundated Urban Areas of Miami (FL, USA). Proc. 34th International Ocean and Polar Engineering Conference (ISOPE 2024), Rhodes, Greece.

Palm, R., & Bolsen, T. (2020). Climate change and sea level rise in South Florida, Vol. 34, Springer.

Williams, S.J., & Gutierrez, B.T. (2009). Sea-level rise and coastal change: Causes and implications for the future of coasts and low-lying regions. *Shore Beach* 77(4), 13.

Risk Management of Commercial Ports, Methodology and Application to the Port of Palermo

Maresca F.[1,*], Scala A.[1], De Cristofano V.[1], Viviano A.[2] and Cuomo G.[1]

[1] SPERI Società di Ingegneria e di Architettura SpA , Via Lungotevere delle Navi, 19, Rome, Italy
[2] Autorità del Sistema Portuale del Mare di Sicilia Occidentale, Via Piano dell'Ucciardone, 4, Palermo, Italy

*corresponding author:
e-mail: fmaresca@sperispa.com

ABSTRACT

Marine traffic play a vital role in global trade, transportation, and coastal communities, but it is increasingly exposed to risks arising from extreme metocean conditions, including extreme storms, and related surges, as well as sea level rise. Thirty percent (30%) worth of all world marine traffic passes through the Mediterranean Basin for a total of 200,000 ships every year. The efficiency of marine traffic is deeply linked to safe access and operability within ports, that can be compromised in the case of extreme metocean conditions. Identifying the thresholds above which port operability might be compromised is of crucial importance in order to inform port risk management, minimise downtime and improve safety of real time port operations. It can also inform planning and middle to long term port management investment strategies. This research is part of a work conduted within the framework of the SeaSmartEye project funded by Regione Puglia, and aims to develop a support decision framework to prioritize investments and to implement resilient harbour management practices within the context of escalating metocean conditions driven by climate hange. As part of this work, this paper describes a general framework for port risk assessment which allows to identify metocean critical conditions (waves, wind and tidal variations) that can pose risk to port integrity and safe port operability. The outcome of this study, combined with a chain of predictive models, enables informed real-time decision making and operability forecast. Where the risk is significant in fact, mitigation strategies can be evaluated, that include structural interventions or real time management strategies. The methodology is applied to key elements of the Port of Palermo, for which a number of failure modes have been identified enabling to define both operational (i.e. excessive overtopping or wave agitation at the quays) and integrity (i.e. structural and geotechnical instability) related thresholds as a function of metocean and seismic hazard at the site. The results show the importance of real time informed management and adaptive strategies, including modern breakwater designs, continuos monitoring systems and scenario-based emergency plans.

METHODOLOGY

Risk can be defined as an indicator resulting from a multidisciplinary analysis that allows the assessment of the effects in terms of damage (loss of life, monetary, structural) that extreme events (e.g. storm surge or earthquake) may cause in a given structure or system.

A number of methodologies exist that have been developed over the past 50+ years, whilst their comprehensive review is outside of the scope of this paper, it is worth remembering that risk can be considered as the product of three components:

- Hazard: the probability that an event with a given return period will occur during the assessment period;
- Exposure: the quantity and value of the assets and activities present on the site of interest that may be affected directly or indirectly by the events;
- Vulnerability: the susceptibility to damage of the structure due to actions of different intensity.

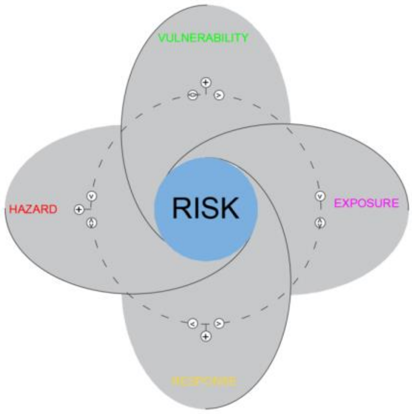

Figure 1. Risk assessment framework.

In this paper the risk assessment has been conducted through a matrix analysis involving metocean conditions, the structural end dynamic characteristics of the port infrastructure, geotechnical properties of their foundation soils and the characteristics of the vessels expected to berth and moor at the port.

CASE STUDY

The port of Palermo is the main access route to Sicily for passengers and goods. Thanks to its favourable geographical position, Palermo is a strategic port of call for navigation in the Mediterranean. The port is oriented to North East and it is characterised by two distinct basins, the first, external, is dedicated to shipbuilding, the second, internal, represents the tourist and commercial port.

Figure 2. Port of Palermo.

Metocean conditions at the site were reconstructed by analysing 80 years of wind and wave data (Figure 3), a site specific tide analysis was also performed. Residual wave agitation was assessed by means of the Artemis model (Aelbrecht, 1997), which is part of the multipurpose hydrodynamic Telemac modelling suite (EDF R&D, 2010), and solves the mild slope equation (Berkhoff, 1976) using a finite element approach. Seismic scenarios were identified based on the regional characterization of the site.

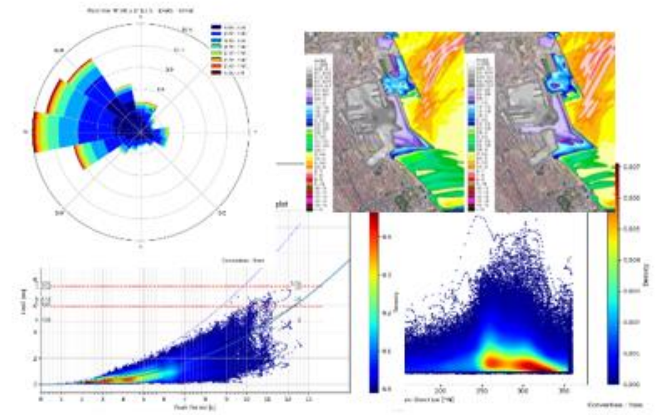

Figure 3. Metocean conditions at the site

Through a preliminary analysis and consultation with the Port Authority, the following failure modes were identified:

- Structural damage;
- Local stability (caissons sliding, overturning);
- Global stability;
- Bearing capacity;
- Excessive overtopping;
- Excessive wave agitation.

For each failure mode, the response of the port element was assessed under both frequent and extreme conditions, example result obtained as part of the global stability and residual wave agitation analysis are given in Figure 4 and Figure 5 respectively.

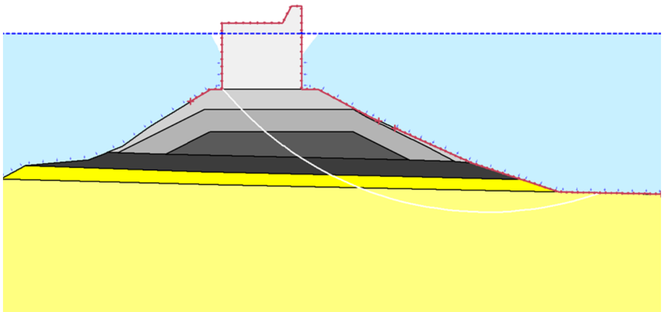

Figure 4. Global stability analysis.

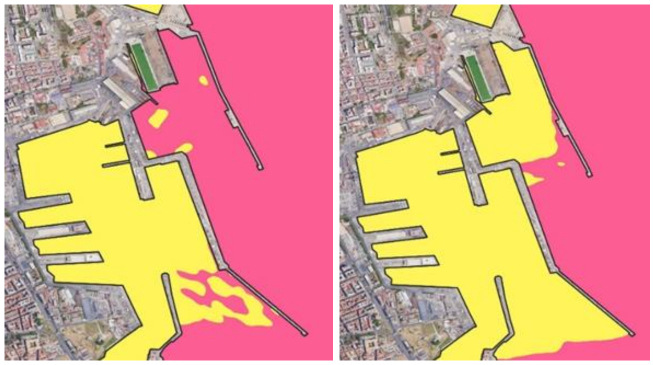

Figure 5. Residual wave agitation for selected offshore wave conditions.

For each element of the port and failure mode, five (5) levels of hazard and vulnerability were identified; the exposure levels were defined in base of structures, vessels or workers involved in the mode. Hazard, vulnerability and exposure were combined to identify the corresponding risk levels, as illustrated in the general matrix of Figure 6.

V4 E4	5	6	7	8	10
V3 E3	4	5	6	7	9
V2 E2	3	3	4	6	8
V1 E1	1	2	2	3	6
V0 E0	0	0	0	0	0
Risk matrix	H5	H4	H3	H2	H1

Figure 6. Risk matrix.

CONCLUSION

A general framework for the assessment and the management of risk of commercial ports has been developed and applied to the Port of Palermo. The risk assessment has highlighted as wave high and direction are the leading condition for the most of the risk indicators together with geotechnical conditions of the foundation soils.

ACKNOWLEDGEMENTS

This paper is part of the work performed within the framework of the SeaSmartEye Project funded by Regione Puglia. The authors wish to thank the many other colleagues and friends at SPERI SpA who have contributed to this work.

REFERENCES

Aelbrecht, D., 1997. ARTEMIS 3.0: a finite element model for predicting wave agitation in coastal areas and harbours including dissipation. Computer modelling of seas and coastal regions III. International conference. Eds.: J.R. Acinas, C.A. Brebbia, 343–352.

EDF R&D, 2010. Agitation d'un plan d'eau par la houle. Logiciel ARTEMIS. Version 6. Notice théorique et manuel utilisateur. 134 pp.

Berkhoff, J.C.W. (1976). Mathematical models for simple harmonic linear water waves. Wave diffraction and refraction. s.l.: Delft Hydraulics Lab Publication. 163.

Determination of the Optimal Location of Commercial Ports for Sustainable Development: The Case of Elefsis Port

Kyriazi N.[1], Chatzimarkaki G.[2] and Giantsi Th.[3,*]

[1] Department of Business Administration, UNIWA, 250 Thivon & P. Ralli Str, Egaleo, Greece
[2] Independent Researcher (Senior Full Stack Software Engineer), Elefsis, Greece
[3] Laboratory of Harbour Works, NTUA, Iroon Polytechniou 5, Zografou, 15780, Greece

*corresponding author:
e-mail: dgiantsi@central.ntua.gr

INTRODUCTION

Ports play a critical role in the economic development of coastal regions, serving as key nodes in global trade and logistics networks. The decision-making process regarding the optimal location for commercial ports must consider multiple factors, including economic viability, environmental sustainability, and social acceptance. The port of Elefsis, located in the Attica region of Greece, has been facing challenges related to congestion, environmental concerns, and urban integration. This study aims to determine the optimal location of commercial ports, focusing on their sustainable development and socio-economic impact on local communities. The study evaluates the relocation of the Elefsis port through a multi-criteria decision analysis (MCDA), utilizing the Analytic Hierarchy Process (AHP) to assess various relocation scenarios. The results indicate that the optimal choice is relocating the port to the "Halyvourgiki" area, which presents significant challenges regarding jurisdiction and implementation.

METHODOLOGY

The methodology employed in this study is based on the MCDA framework, specifically using the AHP technique (Saaty, 1980). The study is structured in the following stages:

1. **Data Collection:** Primary data were collected through interviews with key stakeholders of the Elefsis port, while secondary data were obtained from official reports and databases, (UNCTAD 2018).
2. **Analysis of Current Situation:** A SWOT analysis was conducted to identify the strengths, weaknesses, opportunities, and threats associated with the current port location (Pietrzykowski & Gucma, 2019).
3. **Criteria Definition and Weighting:** Evaluation criteria were established based on socio-economic, environmental, technical, and spatial factors (Vego et al., 2016) (Table 1).
4. **Scenario Evaluation:** Three relocation scenarios were assessed using the AHP method, with criteria weighted using expert opinions and sensitivity analysis (Macharis et al., 2004).
5. **Final Decision:** The scenario with the highest priority score was selected as the optimal relocation choice.

AHP Steps:

The AHP methodology involves the following steps:

1. **Problem Definition:** Clearly define the problem and the goal of the decision-making process.
2. **Hierarchy Structure:** Break down the problem into a hierarchical structure consisting of the goal, criteria, sub-criteria, and alternatives.
3. **Pairwise Comparisons:** Conduct pairwise comparisons of criteria and alternatives using a scale of relative importance (Table 2).
4. **Weight Calculation:** Calculate the weights of criteria and alternatives using eigenvalue methods (Figure 1).
5. **Consistency Check:** Assess the consistency ratio to ensure logical coherence in the pairwise comparisons.
6. **Aggregation of Priorities:** Combine the criteria weights and alternatives scores to determine the best option (Figure 2).
7. **Sensitivity Analysis:** Analyze how changes in criteria weights affect the final decision (Figure 3).

The evaluation criteria included factors such as accessibility, environmental impact, economic benefits, social acceptance, and operational feasibility. The AHP method allowed for a comprehensive prioritization of these factors, ensuring an objective decision-making process.

Table 1. Scenario evaluation criteria and sub-criteria.

Criteria	No	Sub-criteria
Social	1.1	Development of the wider area
	1.2	Creation of job opportunities
	1.3	Social acceptance
	1.4	Accessibility to the waterfront
Economic	2.1	Generation of income for the local economy
	2.2	Increase in revenue for the Port Authority
	2.3	Enhancement of the port's competitiveness
	2.4	Attraction of new investments
Technical	3.1	Feasibility of implementation (Port Infrastructure, equipment)
	3.2	Development of infrastructure networks (electricity, water, sewage, etc.)
	3.3	Development of transport networks (highways, railways, airports)
	3.4	Improvement of land accessibility
Spatial	4.1	Allocation of public spaces
	4.2	Integration into urban and spatial planning
	4.3	Ownership status of facilities
Environmental	5.1	Water pollution
	5.2	Visual pollution - Aesthetic degradation
	5.3	Air pollution
	5.4	Risk to the local ecosystem
	5.5	Nuisance - Noise
	5.6	Land traffic congestion
	5.7	Marine traffic congestion
	5.8	Increase in port and ship waste
	5.9	Impacts on Climate Change
	5.10	Energy Consumption and Sustainable Sources

Table 2. Pairwise comparison matrix of criteria

	Social	Economic	Technical	Spatial	Environmental	CR	Weight
Social	1	1/3	2	1/2	3	0,015	0,16
Economic	3	1	4	2	5		0,419
Technical	1/2	1/4	1	1/3	2		0,097
Spatial	2	1/2	3	1	4		0,263
Environmental	1/3	1/5	1/2	1/4	1		0,062

ANALYSIS - RESULTS

The analysis of the three proposed relocation scenarios for Elefsis port revealed the following key findings:

• **Scenario 1:(S1)** Expansion within the existing location – Despite its feasibility, this scenario was found to have significant limitations related to environmental concerns and urban congestion.

- **Scenario 2:(S2)** Relocation to the "Blycha" area – This option showed moderate scores across most criteria but lacked the necessary connectivity and stakeholder support.
- **Scenario 3:(S3)** Relocation to the "Halyvourgiki" area – This option ranked highest in the AHP analysis, offering the best balance between accessibility, economic growth, and sustainability; however, it faces legal and administrative constraints.

The sensitivity analysis confirmed that the "Halyvourgiki" area remains the most viable option under varying weighting scenarios, emphasizing its potential for sustainable port development (Figure 4).

Social 0,160	1.1	1.2	1.3	1.4	CR	Sub-criteria Weight
1.1	1	2	1/3	3	0,027	0,216
1.2	1/2	1	1/5	3		0,137
1.3	3	5	1	7		0,582
1.4	1/3	1/3	1/7	1		0,065

Economic 0,4185	2.1	2.2	2.3	2.4	CR	Sub-criteria Weight
2.1	1	4	1/3	4	0.097	0,272
2.2	1/4	1	1/5	4		0,121
2.3	3	5	1	7		0,553
2.4	1/4	1/4	1/7	1		0,054

Technical 0,0973	3.1	3.2	3.3	3.4	CR	Sub-criteria Weight
3.1	1	5	2	3	0.0078	0,477
3.2	1/5	1	1/4	1/2		0,081
3.3	1/2	4	1	2		0,288
3.4	1/3	2	1/2	1		0,154

Spatial 0,0973	4.1	4.2	4.3	CR	Sub-criteria Weight
4.1	1	1/5	1/7	0.012	0,075
4.2	5	1	1/2		0,333
4.3	7	2	1		0,592

Environmental 0,0973	5.1	5.2	5.3	5.4	5.5	5.6	5.7	5.8	5.9	5.10	CR	Sub-criteria Weight
5.1	1	8	2	1/2	3	4	4	6	7	5	0.057	0,209
5.2	1/8	1	1/7	1/9	1/6	1/2	1/2	1/3	1/2	1/4		0,020
5.3	1/2	7	1	1/3	2	3	3	5	6	4		0,148
5.4	2	9	3	1	4	5	5	8	7	6		0,288
5.5	1/3	6	1/2	1/4	1	2	2	4	5	3		0,103
5.6	1/4	2	1/3	1/5	1/2	1	1	3	4	2		0,064
5.7	1/4	2	1/3	1/5	1/2	1	1	3	4	2		0,064
5.8	1/6	3	1/5	1/8	1/4	1/3	1/3	1	2	1/2		0,032
5.9	1/2	2	1/6	1/7	1/5	1/4	1/4	1/2	1	3		0,033
5.10	1/5	4	1/4	1/6	1/3	1/2	1/2	2	1/3	1		0,039

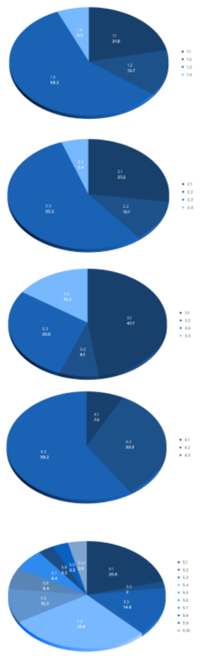

Figure 1. Weight calculation results using the eigenvalue method.

4.1 Allocation of public spaces 0,075	S1	S2	S3	CR	Weights of Alternatives
S1	1	1/5	2	0,012	0,167
S2	5	1	7		0,740
S3	1/2	1/7	1		0,094

4.2 Integration into urban and spatial planning 0,333	S1	S2	S3	CR	Weights of Alternatives
S1	1	1/6	4	0,093	0,176
S2	6	1	9		0,763
S3	1/4	1/9	1		0,061

4.3 Ownership status of facilities 0,592	S1	S2	S3	CR	Weights of Alternatives
S1	1	1	1/9	0	0,091
S2	1	1	1/9		0,091
S3	9	9	1		0,818

(a)

Sub-criteria	Sub-criterion Weight	S1	S2	S3
Allocation of public spaces	0.075	0.167	0.740	0.094
Integration into urban and spatial planning	0.333	0.070	0.763	0.167
Ownership status of facilities	0.592	0.091	0.091	0.818

(b)

Scenario	Weight	Position
S1	0,08971	3rd
S2	0,36339	2nd
S3	0,54692	1st

(c)

Figure 2. Aggregation of priorities for relocation scenarios. (a) Scenario Evaluation by Spatial Sub-Criteria, (b) Aggregate Scenario Evaluation, (c) Final Scenario Evaluation.

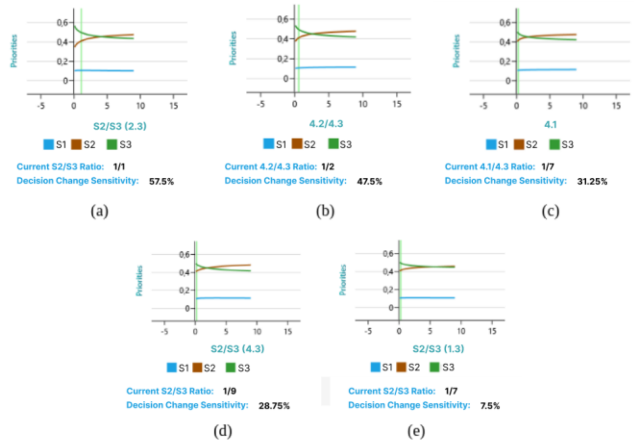

Figure 3. Sensitivity analysis of criteria weights.

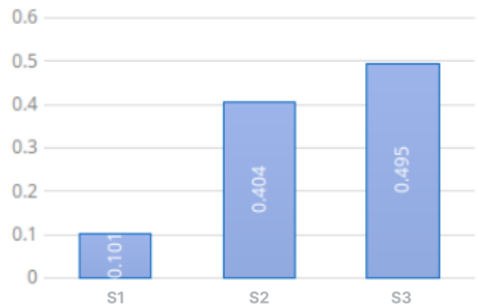

Figure 4. Scenario Ranking.

CONCLUSION

This study provides a robust framework for evaluating commercial port relocation strategies using MCDA methods. The findings support the relocation of Elefsis port to the "Halyvourgiki" area as the optimal solution, provided that jurisdictional challenges can be addressed. The methodology can be applied to similar cases globally, offering a strategic approach to port planning and development.

ACKNOWLEDGEMENTS

The authors acknowledge the support of the Elefsis Port Authority and all stakeholders who contributed to the data collection and analysis.

REFERENCES

Macharis, C., De Witte, A., & Ampe, J. (2004). The multi-actor, multi-criteria analysis methodology (MAMCA) for the evaluation of transport projects: Theory and practice. *J. Adv. Transp.* 43(2), 183–202.

Notteboom, T., & Rodrigue, J.P. (2005). Port regionalization: Towards a new phase in port development. *Marit. Policy Manag.* 32(3), 297–313.

Pietrzykowski, Z., & Gucma, L. (2019). Decision support for port development planning.

Saaty, T.L. (1980). The analytic hierarchy process. McGraw-Hill, New York.

Sirimanne, S.N., Hoffman, J., Juan, W., et al. (2018). Review of Maritime Transport 2018, United Nations conference on trade and development (UNCTAD), Geneva, Switzerland.

Vego, D., Nikitakos, N., & Stefanakos, C. (2016). Multi-criteria decision making for port selection.

Harbour Layout Design in a Changing Climate Based on Advanced Numerical Models and Machine Learning: Incorporating Downtime and Upgrading Costs

Samaras A.G.[1,*], Iliadis, L.[1] and Karambas T.V.[2]

[1] Department of Civil Engineering, Democritus University of Thrace, University Campus - Kimmeria, 67100 Xanthi, Greece
[2] Department of Civil Engineering, Aristotle University of Thessaloniki, University Campus, 54124 Thessaloniki, Greece

*corresponding author:
e-mail: achsamar@civil.duth.gr

INTRODUCTION

Port operability is increasingly challenged by the impacts of a changing climate, as shifts in metocean conditions affect port infrastructure, navigation, and cargo handling, compromising operational efficiency and safety (Winckler et al., 2022). Addressing these challenges involves significant costs, including infrastructure upgrades, maintenance, and operational downtime. Accordingly, decision-makers must balance these financial burdens with long-term resilience strategies, leveraging adaptive engineering solutions (Camus et al., 2019; Wiegel et al., 2021). Considering the critical role of harbour layout in addressing these challenges, Samaras et al. (2023) proposed a novel methodology for harbour layout design in a changing climate based on Advanced Numerical Models (ANM) and Machine Learning (ML). Samaras et al. (2024) applied this method-ology to a case study in Greece. This work enhances previous research by introducing downtime and upgrading costs into the Performance Score used for the development of ML models based on ANM applications.

THE NOVEL METHODOLOGY

Briefly presented, the novel methodology comprises the following components: (A) Marine Data Analysis, (B) Harbour Layout Analysis, (C) ANM Applications and (D) ML Applications (see Figure 1). Component (A) involves the acquisition and analysis of marine data in order to define a series of Design Scenarios (DS) for past, present and future (climate change) conditions. Component (B) involves the acquisition, analysis and classification of harbour layout data and port information in order to identify Typical Harbour Layouts (THL).

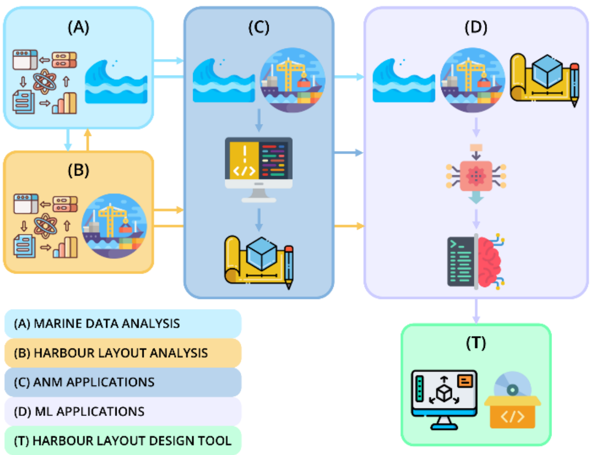

Figure 1. Components and flowchart of the novel method-ology for harbour layout design in a changing climate (Samaras et al., 2023).

Component (C) involves the adaptation, testing and eventual implementation of ANM to the THL defined in Component (B), using as forcings the DS defined in Component (A). Models results are evaluated on the basis of changes in wave agitation at selected critical locations inside harbour basins and around harbour entrances, and Design/Redesign Solutions (DRS) are proposed for each THL. Component (C) in this work is based on in-house models for the simulation of coastal/harbour wave dynamics and hydrodynamics developed by the authors (Karambas and Samaras, 2017; Karambas et al., 2023). Finally, component (D) involves the preprocessing of the data from Components (A), (B) and (C) and the development of robust ML models, capable to correctly classify THL to the optimal DRS based on the change in DS (McClarren, 2021; Prakash et al., 2021). The final output of this methodology will be a tool (T), whose users will be able to select one (or more) of the THL that better fit their project, load their DS for past/present/ future conditions, and run the ML models for the input dataset, getting as results the optimal DRS without the need of running an advanced wave and hydrodynamics model, as well as full reporting on the ML models' performance.

INCORPORATING DOWNTIME AND UPGRADING COSTS

After analysis of relevant literature within the context of the present work, the Performance Score (PS) was structured as:

$$PS = f\left(H_{max}, H_{crit1}, H_{crit2}, freq, UC_u, DDC_u\right) \tag{1}$$

where H_{max} is the maximum wave agitation inside the harbour basin as resulted from ANM applications, $H_{crit1,2}$ are values of critical wave agitation (upper/lower) related to port operability, $freq$ is the frequency of occurrence of the DS in time units, UC_c is the upgrading cost per unit length of construction, and DDC_u is the downtime cost per unit time of port operations disruption. The dimensionless PS follows:

$$PS = \frac{(UC + DDC)_i}{(UC + DDC)_{max}} \tag{2}$$

where UC is the upgrading cost, DDC is the downtime cost, i refers to each DS for each layout (THL or DRS) and max refers to the entire set of applications for the same layout. It is noted that in Eq. (2) UC is the annualised upgrading cost (thus also a function of the design life of the upgrade and a given interest rate) and DDC the annual downtime cost, calculated by:

$$DDC = a\left(DDC_u\, freq\right) \tag{3}$$

where a is a downtime multiplier, i.e. a=0 for $H_{max} \leq H_{crit1}$, a follows a smooth saturation function for $H_{crit1} < H_{max} < H_{crit2}$, and $a=1$ for $H_{max} \geq H_{crit2}$.

THE CASE STUDY

The case study presented in this work regards a coastal area located in the East Macedonia and Thrace (EMT) Region in Greece. Data from Copernicus Marine Service and Climate

Change Service were analyzed for a representative coastal location in the selected Region. In-depth combined analysis of all collected data, resulted to the definition of DS for combinations of varying wave height (up to 3.5m), wave direction (225°/NW – 135°/NE), wave period (6s-12s), and annual frequency of occurrence (up to 0.4%). Analysis of the natural (morphological, meteo-marine, climatic) and developmental characteristics of the EMT Region regarding port infrastructure led to the identification of the typical layout of a medium-sized harbour (180m x 100m harbour basin) schematically represented in the top left panel of Figure 2, along with three indicative design/redesign solutions: DRS 1 and 2 suggesting extension of the wind-ward breakwater at an angle (by 40m and 70m, respectively), and DRS 3 suggesting construction of a detached breakwater (length: 100m) near the harbour entrance.

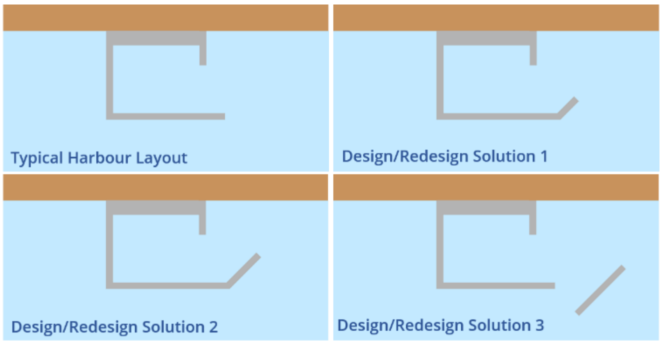

Figure 2. Schematic representations of the Typical Harbour Layout (THL) and Design/Redesign Solutions (DRS).

Applications of the ANM were run for all DS for the four harbour layouts (THL and DRS presented in Figure 2). ANM results were analysed using an in-house algorithm for H_{max} extraction. Regarding the downtime and upgrading costs, values for all parameters included in Eqs. (1) to (3) were properly assigned based on the characteristics of the case study. Finally, ML models were developed based on DS and PS for each of the THL and DRS. Over 50 models were tested; Figure 3 presents results for the optimal model for each harbour layout.

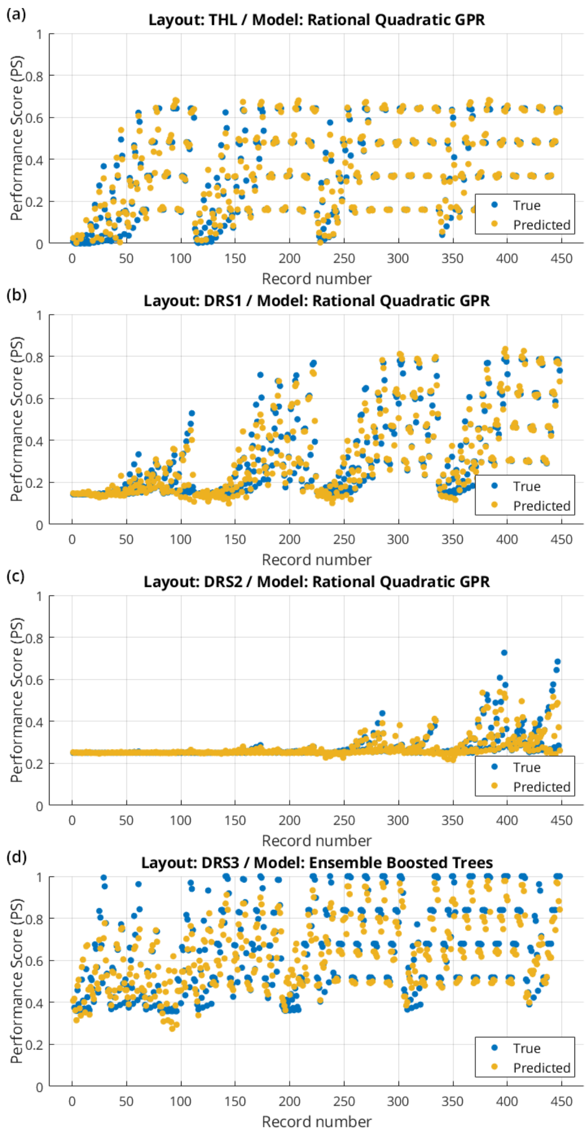

Figure 3. Response plots for the optimal ML models developed for the: (a) THL, (b) DRS1, (c) DRS2, (d) DRS3.

CONCLUSIONS

This work improves previous research by the authors on the combined use of ANM and ML for harbour layout design, by investigating cost aspects that are critical for addressing port operability challenges in a changing climate. Furthermore, the incorporation of novel methods into existing port design practice provides valuable insights about the informed use of ML in coastal engineering applications.

REFERENCES

Camus, P., et al. (2019). Probabilistic assessment of port operation downtimes under climate change. *Coast. Eng.*, 147, 12–24.

Karambas, T.V., & Samaras, A.G. (2017). An Integrated Numerical Model for the Design of Coastal Protection Structures. *J. Mar. Sci. Eng.*, 5(4), 50.

Karambas, T.V., et al. (2023). A new time-dependent irregular wave propagation model. Proc. 2nd International Conference Design and Management of Port, Coastal and Offshore Works, Thessaloniki, Greece.

McClarren, R.G. (2021). Machine Learning for Engineers. Cham, Switzerland: Springer.

Prakash, K.B., et al. (2021). Advanced Deep Learning for Engineers and Scientists. Cham, Switzerland: Springer.

Samaras, A.G., et al. (2023). A methodology for harbour layout design based on Machine Learning. Proc. 40th IAHR World Congress, Vienna, Austria.

Samaras, A.G., et al. (2024). Harbour layout design in a changing climate based on Advanced Numerical Models and Machine Learning: A case study. Proc. 38th Int. Conf. Coastal Eng. (ICCE 2024), Rome, Italy.

Wiegel, M., et al. (2021). Global Mapping of Seaport Operability Risk Indicators Using Open-Source Metocean Data. *J. Mar. Sci. Eng.*, 9(7), 695.

Winckler, P., et al. (2022). Impacts in ports on a tectonically active coast for climate-driven projections under the RCP 8.5 scenario: 7 Chilean ports under scrutiny. *Coast. Eng. J.*, 64(3), 387–405.

Navigating the Integration of Digital Twins into Smart Ports: Processes, Interconnections, and Evolution

Tsaimou C.N.[1,*] and Tsoukala V.K.[1]

[1] Laboratory of Harbour Works, Department of Water Resources and Environmental Engineering, School of Civil Engineering, National Technical University of Athens (NTUA), Zografou, 15780, Greece

*corresponding author
e-mail: ctsaimou@central.ntua.gr

BACKGROUND AND OBJECTIVES

The maritime port sector is undergoing a significant transformation driven by advancements in automation and digital technologies. The integration of technologies such as the Internet of Things (IoT), Artificial Intelligence (AI), and big data analytics has marked the ongoing evolution of “Industry 4.0” laying the foundation for smart port (SP) development and expansion (Paraskevas et al., 2024). In this context, Digital Twin (DT) technology emerges as a key enabler, strengthening the SP initiatives (Almeida, 2023).

DTs are increasingly being implemented across various industries, including ports, to enable dynamic, real-time representations of infrastructure and operations (Klar et al., 2023). These virtual models facilitate predictive analytics, allowing potential issues to be identified and addressed before they occur in the real world, thereby enhancing decision-making processes (Neugebauer et al., 2024). Their effectiveness is significantly enhanced when integrated into established SPs with real-time data streams from sensors, IoT, and wearable technologies used by staff. This continuous data flow enables DT models to mimic, analyze, and iteratively refine interactions between physical assets and human operators (Wang et al. 2021).

The digital transformation of SPs is closely linked to the broader context of smart cities. According to Klar et al. (2023), SPs function as both supply chain nodes and integral parts of smart cities, influencing three key dimensions of smart development: smart energy, smart mobility, and smart infrastructure. Their study underscores the need for DT solutions capable of processing data from large-scale systems to digitize the physical twin and provide analytics for management and maintenance. Since smartness extends beyond technological efficiency to encompass socio-economic and environmental aspects, it becomes essential to analyze in which sectors DTs contribute most significantly to SPs. Identifying these key areas will provide deeper insight into how digital twins align with the broader smart city objectives of urban growth and sustainability.

In light of these considerations, this study aims to analyze the integration of DTs to SPs, focusing on the chronological development of both smart and digital ports and their key areas of integration. To achieve this, the study employs a literature review and a thematic analysis of research trends, offering insights into the digital transformation of port systems, benefiting both theoretical understanding and practical applications.

LITERATURE TRENDS

To systematically analyze the academic evolution of SPs and DTs, three literature investigations were conducted using the Scopus database. The search focused on peer-reviewed journal articles and conference papers to ensure the reliability of findings. Given the multidisciplinary nature of SPs, the following three Boolean queries were designed to capture relevant publications:

- Search A: (("smart port*") AND ("port industry" OR "maritime" OR "harbor" OR "seaport")), retrieved a total of 191 documents (Figure 1). The earliest two publications appeared in 2012, with contributions from the Netherlands and South Korea. The most active author was affiliated with Universitat Politècnica de València, Spain, with six documents.
- Search B: (("digital twin*") AND ("port industry" OR "maritime" OR "harbor" OR "seaport")) retrieved a total of 250 documents (Figure 1). The first publication in this category appeared in 2018, with research from the United States. The most active contributors in this field were from Norway, with seven documents.
- Search C: (("smart port*") AND ("digital twin*") AND ("port industry" OR "maritime" OR "harbor" OR "seaport")) retrieved a total of 13 documents (Figure 1). The earliest two publications in this category were recorded in 2021, originating from China. The most frequently contributing authors (with two documents) were affiliated with institutions in Edinburgh (United Kingdom), Canada, and Turkey (representing the same documents as those from Edinburgh).

The queries were structured to ensure relevance to the maritime industry by incorporating terms like "port industry," "maritime," "harbor," and "seaport." Moreover, the research covers the timeframe from the first identified document to 2024.

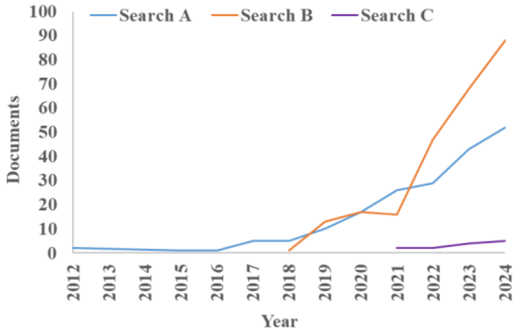

Figure 1. Analysis for documents per year -Search A, Search B, and Search C.

Despite the later emergence of DTs in ports, the number of documents discussing DTs in the maritime sector surpasses those on SPs, reflecting the increasing significance of this technology. Moreover, while SPs first appeared in academic literature in 2012, and DTs for port applications were introduced in 2018, the intersection of these two concepts was first documented in 2021. A limited number of publications addresses both SPs and DTs, with the study of Wang et al. (2021) being the most cited document. This indicates that the integration of DTs within SP frameworks is both a growing trend and a research perspective.

KEY AREAS OF INTEGRATION OF DTS INTO SPS

According to Klar et al. (2023), port DTs significantly contribute to making ports more intelligent and self-learning. Given their dual function as supply chain nodes and smart city components, DTs enhance threat detection, energy efficiency, cost reduction, performance optimization, and collaboration. Through a Scopus-based investigation of the most cited documents (>10 citations), the following key areas of the integration of DT into SP were identified.

DT-driven management in SP processes plays a crucial role in optimizing cargo transportation, container storage, real-time data sharing, predictive optimization, and environmental sustainability. The integration of DTs enables the development of 5th generation SPs, characterized by intelligence, virtualization, and sustainability. IoT sensors provide real-time interactive feedback, facilitating data fusion, visualization platforms, and enhanced decision-making in port operations (Wang et al., 2021).

Moreover, DTs within SPs assist in ensuring accurate ship navigation, which is essential in congested seaport areas to prevent delays, downtime, and collisions that could result in significant property damage and loss of life. The TwinPort architecture, integrating DT technology with drone-assisted data collection, enhances ship maneuvering, docking precision, and navigation safety, reducing operational risks and improving overall efficiency (Yigit et al., 2023).

As digital infrastructures expand, SPs face growing cybersecurity threats. DTs provide an essential cybersecurity layer by integrating honeypot-based security mechanisms. The study by Yigit et al. (2023) successfully simulated internal and external cyber threats, demonstrating how DTs enhance security resilience in smart ports.

Further to the above, automated terminals are a cornerstone of SPs, and DTs help to optimize terminal operations. Geographic Information Systems (GIS) and Building Information Modeling (BIM) approaches enhance DTs by perceiving 3D data and capturing temporal and spatial changes in all directions (Haiyuan et al. 2021).

Several ports worldwide have implemented DT technologies to enhance various SP functions. The Port of Valencia has successfully utilized DT technology to improve cargo handling efficiency. The Port of Singapore has integrated a transport traffic monitoring system to enhance the flow of cargo. At the Port of Rotterdam, DTs are employed to streamline cargo handling and transportation logistics. In Mawan Port, DT applications have improved operation and storage efficiency in container terminals. The Port of Barcelona and Port of Hamburg have leveraged DTs for enhanced data communication and sharing, ensuring seamless port operations. In Livorno Port, DTs are used to optimize storage space visualization and risk prediction. Additionally, the Port of Oulu has incorporated DTs for environmental protection and sustainability initiatives (Wang et al., 2021). Ports such as Shanghai Yangshan Port have implemented DT solutions to optimize automated terminal construction (Yao et al., 2021).

DISCUSSION AND COCLUSIONS

While port design and modeling remain fundamental to infrastructure development, the field has reached a level of maturity that has shifted research focus toward the automation and digitalization of port systems. Modeling approaches remain valuable, particularly in optimizing digital workflows that help real-time decision-making. As ports continue to embrace digitalization, the integration of DTs will play an increasingly critical role in shaping the future of SP operations. The primary aspects of this integration relate to logistics, ship navigation, construction stages for automated facilities, and cybersecurity. Beyond these, the widespread adoption of DTs should also extend to other dimensions of port smartness, such as smart maintenance of port facilities through intelligent Structural Health Monitoring (SHM) approaches, as discussed in Tsaimou et al. (2024).

REFERENCES

Almeida, F. (2023). Challenges in the digital transformation of ports. Businesses 3(4), 548–568.

Klar, R., Fredriksson, A., & Angelakis, V. (2023). Digital twins for ports: Derived from smart city and supply chain twinning experience. IEEE Access 11, 71777–71799.

Neugebauer, J., Heilig, L., & Voß, S. (2024). Digital Twins in the context of seaports and terminal facilities. *Flex. Serv. Manuf. J.* 36, 821–917.

Paraskevas, A., Madas, M., Zeimpekis, V., & Fouskas, K. (2024). Smart Ports in Industry 4.0: A systematic literature review. *Logistics* 8(1), 28.

Tsaimou, C.N., & Tsoukala, V.K. (2024). Towards a guide for building digital twins of port infrastructure. In Monitoring of Mediterranean Coastal Areas: Problems and Measurement Techniques (pp. 1019–1029). Firenze University Press.

Wang, K., Hu, Q., Zhou, M., Zun, Z., & Qian, X. (2021). Multi-aspect applications and development challenges of digital twin-driven management in global smart ports. *Case Stud. Transp. Policy.* 9(3), 1298-1312.

Yao, H., Xue, T., Wang, D., Qi, Y., & Su, M. (2021). Development direction of automated terminal and systematic planning of smart port. (2021) IEEE 2nd International Conference on Big Data, Artificial Intelligence and Internet of Things Engineering, Nanchang, China.

Yigit, Y., Kinaci, O.K., Duong, T.Q., & Canberk, B. (2023). TwinPot: Digital twin-assisted honeypot for cyber-secure smart seaports. 2023 IEEE International Conference on Communications Workshops: Sustainable Communications for Renaissance, Rome, Italy.

Yigit, Y., Nguyen, L.D., Ozdem, M., Kinaci, O.K., Hoang, T., Canberk, B., & Duong, T.Q. (2023). TwinPort: 5G drone-assisted data collection with digital twin for smart seaports. *Sci. Rep.* 13(1), 12310.

Enhancing Seismic Resilience of Port Infrastructures Using BIM Technology: A Case Study of the Port of Patras

Tsikas P.[1] and Chassiakos A.[1,*]

[1] Department of Civil Engineering, University of Patras, Greece

*corresponding author:
e-mail: a.chassiakos@upatras.gr

ABSTRACT

Infrastructure Building Information Modeling (I-BIM) enables the digital modeling of large infrastructure projects, accurately reflecting their real-world conditions. It serves as a powerful tool for supporting management decisions throughout the project life cycle. This study focuses on the vulnerability of port infrastructures to seismic activity, which can cause significant disruptions, leading to both direct and indirect losses. Effective maintenance management plays a crucial role in mitigating earthquake impacts. I-BIM technology facilitates vulnerability assessment and strategic planning for both preventive and restorative measures. By integrating advanced analyses, I-BIM enhances port resilience and ensures operational continuity. The findings of this study highlight the potential of I-BIM as a valuable framework for managing port facilities, reducing seismic risks, and optimizing maintenance strategies.

INTRODUCTION

Port facilities are large-scale infrastructure projects with significant technological, economic, and environmental importance. They require specialized design and maintenance while serving as critical hubs in global trade. Disruptions can severely impact multiple industries.

Building Information Modeling (BIM) has modernized construction, improving infrastructure planning, asset maintenance, and operational efficiency. Through 3D modeling and simulation, BIM optimizes port layouts, identifies design conflicts early, and streamlines cargo flow. Integrated with IoT, it enables real-time monitoring and predictive maintenance. BIM also enhances sustainability by optimizing energy use and assessing climate resilience. Additionally, it strengthens security, disaster preparedness, and regulatory compliance. As a centralized hub, BIM fosters collaboration, reducing costs and improving decision-making.

Infrastructure BIM (I-BIM) can further enhance seismic risk management in ports. It enables digital twins to simulate seismic effects, support post-earthquake recovery, and enhance resilience. Real-time monitoring and risk scenario simulations help minimize operational disruptions and economic losses.

Ports in seismic regions are highly vulnerable. Events like the Kobe (1995) and Chile (2010) earthquakes caused severe quay damage, soil liquefaction, and crane destruction, leading to major delays and increased costs. These disasters highlight the need for systematic, technology-driven solutions. Werner et al. (2008) note a lack of systematic seismic risk management in ports, while Conca et al. (2020) emphasize the poor seismic performance of piers, where single-component failures can disrupt entire systems. This study addresses this gap by proposing an I-BIM-based framework for seismic vulnerability assessment and risk mitigation in ports.

METHODOLOGY

The methodology in this study utilizes I-BIM for seismic risk management in seismically active regions (GEM, https://www.globalquakemodel.org/).

Figure 1. 3D-BIM model of the port of Patras (SNP) (location 38°13'42.2"N 21°43'15.5"E google map)

The process begins with the creation of a 3D digital model of the port infrastructure (Figure 1). Next, a seismic vulnerability analysis is conducted, assessing the interdependencies among critical infrastructure elements. The primary objective is to develop mitigation and restoration strategies. Finally, the results are visualized, providing valuable insights for optimizing maintenance and restoration procedures, thus ensuring the continuity of port operations following seismic events.

The proposed data management framework integrates seismic risk assessment with BIM visualization, enabling organizations to make informed decisions, reduce potential losses, and enhance infrastructure safety. The seamless, real-time flow of information is crucial for effective task execution. Moreover, the interoperability of BIM software through I-BIM enhances comprehensive seismic risk analysis.

CASE STUDY

This study examines the New Port of Patras (SNP) as a case study. Patras has two ports: the Southern New Port (SNP) and the Northern Old Port (NOP). The SNP has been operational since July 2011 and features a reinforced concrete caisson platform extending 992 meters in a zigzag layout. It includes four dock stations with 15 berths (11 for mooring and 4 for side mooring). The port's breakwaters, also constructed with reinforced concrete caissons, span a total length of 1,236 meters. Additionally, the port's building infrastructure covers 6,974 m², housing facilities such as the passenger terminal, port administration offices, and fire station. The SNP serves as a key maritime transport hub between Patras and Italy (Bloutsos et al., 2023).

I-BIM technology allows for the development of a robust digital model of the port infrastructure, capturing structural details, material properties, and interdependencies among its components. The simulation encompasses the entire port facility, including the road network, buildings, and electromechanical installations. Using fragility curves (Figure 2, HAZUS, NIBS 2004), the seismic vulnerability of port structures is assessed, identifying weak points within the infrastructure. This approach enables precise risk assessment and the development of effective mitigation and restoration strategies to enhance port resilience. Additionally, I-BIM-based simulations facilitate the exploration of alternative solutions to optimize seismic performance while considering cost-effectiveness.

CONCLUSION

Historical evidence indicates that port facilities are vulnerable to both strong and moderate seismic events. In developed economies, the most significant impact of earthquakes is often not direct physical damage but rather the economic consequences of temporary disruptions or complete shutdowns of trade activities due to infrastructure failures. As crucial trade hubs, ports experience both the immediate effects of earthquakes and their long-term economic ramifications.

Interdependencies among critical port infrastructure elements play a pivotal role in assessing overall seismic risk and system functionality. Damage to key components can initiate cascading failures, exacerbating both economic and operational losses. The application of I-BIM in port infrastructures offers several advantages, including precise 3D modeling and seismic risk assessment. Additionally, risk maps generated through I-BIM provide spatial visualizations of damage distribution and projected functional losses. By leveraging I-BIM, ports can enhance their resilience and maintain operational continuity. Early vulnerability assessments, optimized restoration strategies, and proactive maintenance significantly reduce the economic and operational impacts of seismic events on global trade.

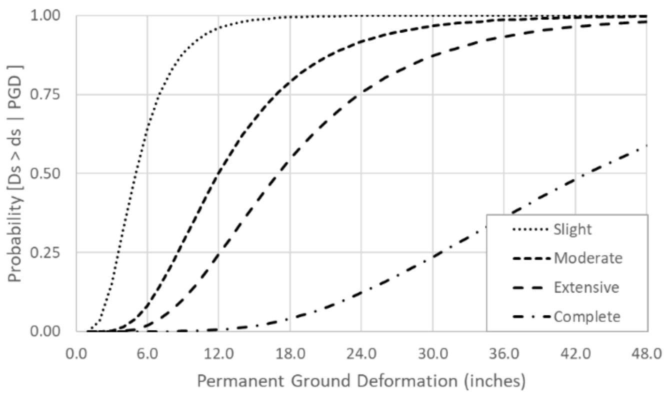

Figure 2. Fragility Curves for Port Waterfront Structures. (HAZUS, NIBS 2004)

REFERENCES

Shaw, R., & Goda, K. (2004). From disaster to sustainable civil society: the Kobe experience. *Disasters* 28(1), 16–40.
Robertson, I., Chock, G., & Morla, J. (2012). Structural analysis of selected failures caused by the 27 February 2010 Chile tsunami. *Earthq. Spectra* 28(1), 215–243.
Bloutsos, A., Aravantinou, A., Manariotis, I.D., & Yannopoulos, P. (2023). Seawater Quality Measurements at the Two Ports of Patras, Greece. *Environ. Sci. Proc.* 26(1), 6;
Werner, S.D., Rix, G.J., & DesRoches, R. (2008). Seismic risk management for seaports. Proc. 14th World Conference on Earthquake Engineering (14WCEE 2008), Beijing, China.
Conca, D., Bozzoni, F., & Lai, C. (2020). Interdependencies in seismic risk assessment of seaport systems: case study at largest commercial port in Italy. ASCE-ASME J Risk Uncertain Eng Syst A Civ Eng 6 (2): 04020006.
Fotopoulou, S., Karafagka, S., Karatzetzou, A., & Pitilakis, K. (2022). System-Wide Seismic Risk Assessment of Port Facilities; Application to the Port of Thessaloniki, Greece. *Sustainability* 14(3), 1424
National Institute of Building Sciences (NIBS) (2004). "Earthquake loss estimation methodology", HAZUS Technical manuals, Federal Emergency Management Agency, Washington, D.C.

Statistics of OWC Power Output in Real Seas

Almalki Y.R.[1,2,*] and Karmpadakis I.[1]

[1] Department of Civil & Environmental Engineering, Imperial College London, London, SW7 2AZ, UK
[2] Department of Civil Engineering, Al-Baha University, College of Engineering, Al-Baha 65799, Saudi Arabia

*corresponding author:
e-mail: y.almalki20@imperial.ac.uk

INTRODUCTION

The growing demand for renewable energy has driven interest in wave energy conversion, with oscillating water columns (OWCs) emerging as a promising technology (Heath, 2012). Recent studies highlight the potential of integrating OWCs into coastal infrastructure, offering both energy generation and coastal protection benefits (Almalki et. al. 2025). This study concerns the probabilistic nature of the hydrodynamics performance of an OWC-caisson under random waves. Key performance metrics and statistical models of power output are analysed to optimise design. Findings enhance understanding of energy conversion variability, aiding real-time adaptability and efficiency improvements for real-sea conditions.

PHYSICAL MODEL AND EXPERIMENT SETUP

The experiments were conducted in the wall-mounted flume at Imperial College London. The flume measures in a 60 m long, 0.3 m wide, and 0.7 m. The physical model, designed using Froude similarity (λ_L= 1: 20, λ_T = 1:$\sqrt{20}$), features a bottom horizontal plate and a rounded front lip. Key dimensions include a width of 0.3 m, breadth of 0.6 m, and chamber breadth of 0.4 m, with front and back drafts of 0.1 m and 0.35 m, respectively. A 27 mm circular orifice (0.5 % opening ratio) simulates the PTO mechanism, enabling pneumatic power measurement. A schematic representation of the experimental arrangement is shown in Figure 1.

Table 1. Details of the sea states parameters considered.

H_s [m]	0.015, 0.025, 0.035, 0.045, 0.055
T_p [s]	0.98, 1.23, 1.57

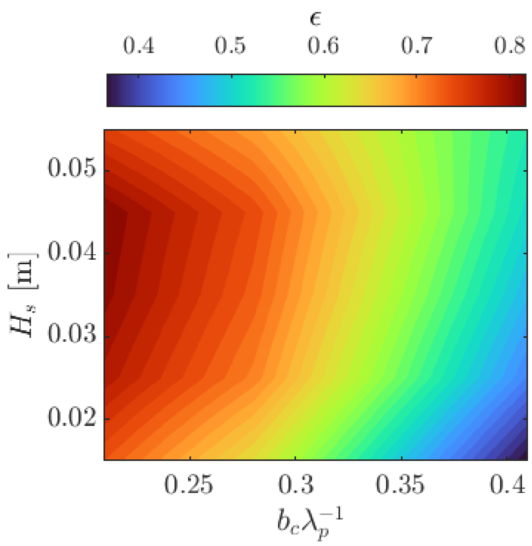

Figure 2 Device efficiency, ε, with respect to significant wave height, H_s, and relative chamber breath, $b_c\lambda_p$.

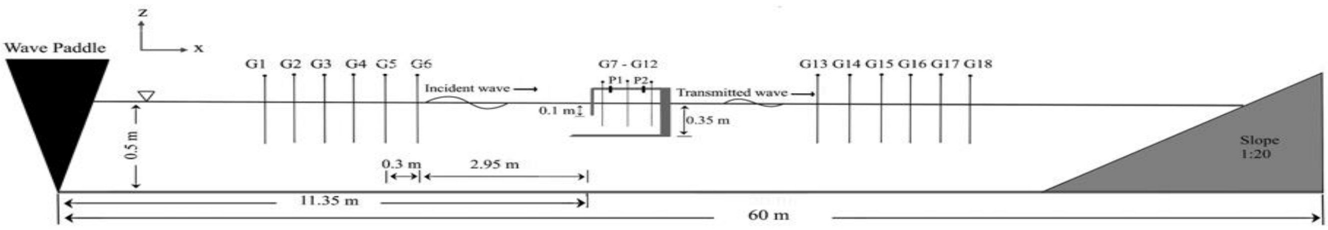

Figure 1 Schematic of the experimental setup arrangement.

The test matrix for this study includes irregular wave conditions, represented using the depth-limited TMA spectrum (TEXEL-MARSEN-ARSLOE) to model near-shore waves (Bouws, 1985). The incident wave conditions are presented in Table 1.

RESULT AND DISCUSSION

Figure 2 presents a contour plot illustrating the performance of a wave energy converter as a function of significant wave height, H_s, and relative chamber breadth, $b_c\lambda_p$.

Device efficiency, ε, generally increases with H_s, with the highest efficiencies observed at (H_s = 0.045 [m]) and the lowest value of $b_c\lambda_p$ .This suggests that optimal performance is achieved under relatively small geometric configurations and high wave conditions.

Individual wave energy generation events were statistically analysed, with the Gamma distribution shown to be best in modelling power peaks and tail behavior. Findings highlight spectral effects on OWC performance, aiding design optimisation for real-sea conditions.

ACKNOWLEDGEMENTS

The first author gratefully acknowledges the financial support provided by Kingdom of Saudi Arabia's support, which was vital to this research.

REFERENCES

Almalki, Y.R., Karmpadakis, I., & Swan, C. (2025). Extensive Experimental Investigation of Oscillating Water Column Devices Embedded in Pile-Supported Breakwaters. Available at SSRN 4692796.

Bouws, E., Günther, H., Rosenthal, W., & Vincent, C.L. (1985). Similarity of the wind wave spectrum in finite depth water: 1. Spectral form. *J. Geophys. Res. - Oceans* 90(C1), 975–986.

Heath, T.V. (2012). A review of oscillating water columns. Philos. Transact. A Math. Phys. Eng. Sci. 370(1959), 235–245.

Performance of Mixed Arrays of Heaving Wave Energy Converters in front of a Wall

Loukogeorgaki E.[1,*], Michailides C.[2] and Chatjigeorgiou I.K.[3]

[1] Department of Civil Engineering, Aristotle University of Thessaloniki, Thessaloniki, Greece
[2] Department of Civil Engineering, International Hellenic University, Serres, Greece
[3] School of Naval Architecture and Marine Engineering, National Technical University of Athens, Athens, Greece

*corresponding author:
e-mail: eloukog@civil.auth.gr

INTRODUCTION

Arrays of multiple Wave Energy Converters (WECs) can be deployed at near-shore locations in the seaward side of wall-type breakwaters facilitating costs' reduction, while exploiting both the incident and the reflected from the wall waves. Various researchers have investigated the enhanced power absorption ability of those arrangements considering though the deployment of homogeneous arrays (e.g. Loukogeorgaki et al., 2020). On the other hand, other studies have illustrated the performance improvement of isolated mixed arrays including WECs of different dimensions/ shapes (e.g. Göteman, 2017). Motivated by this and aiming at filling existing research gaps, in this paper we investigate numerically the performance of linear mixed arrays of cylindrical and oblate spheroidal heaving WECs placed in front of a bottom-mounted vertical wall. Emphasis is given on the effect of the array's distance from the wall on the WECs responses and the array's power absorption ability.

NUMERICAL MODELLING

A linear array of M semi-immersed heaving heterogeneous WECs is placed in the seaward side of a vertical, bottom-mounted wall of finite length l_w and of small thickness w at a marine area of constant water depth h (Figure 1). The mixed array consists of WECs that have either oblate spheroidal shape of semi-major axis a_1 and semi-minor axis b_1 or cylindrical cross-section of radius a_2 and draft b_2 (Figures 1b and 1c). Each WECj, j=1,…, M, is assumed to absorb power through a linear PTO mechanism modelled as a linear damping system of constant damping coefficient $bpto_j$, j=1,…, M. The WECs are distributed uniformly within the array with centre–to–centre spacing l_{bet} and are situated at a distance c from the wall. The action of regular unit-amplitude incident waves of frequency ω propagating at an angle β with respect to the global X axis (Figure 1a) is considered.

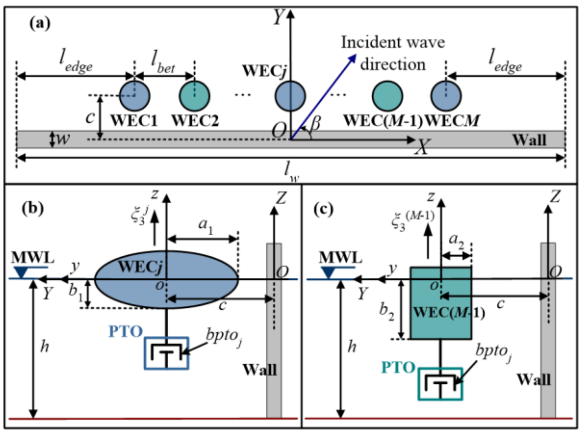

Figure 1. Geometry of the examined arrangement and definition of basic quantities: **(a)** X-Y plane; **(b)** Y-Z plane oblate spheroidal WEC; **(c)** Y-Z plane cylindrical WEC.

The hydrodynamic analysis of the above arrangement, including hydrodynamic interactions among the WECs and between the wall and the devices is conducted in the frequency domain and it is based on the boundary integral equation method (Lee, 1995). The 3D linear potential theory is employed, where, the wall is taken fixed at its position, while the WECs are assumed to undergo small amplitude oscillations only along their working direction, i.e., along their local vertical z axis (Figures 1b~1c). Hence, the WECs rigid-body modes except of heave are considered restrained.

Assuming inviscid and incompressible fluid with irrotational flow, the fluid motion is described in terms of the velocity potential, which satisfies the Laplace equation. The first-order boundary value problem is formed by subjecting the potentials to appropriate boundary conditions (Lee, 1995). Green's theorem is employed to formulate the boundary integral equations for the unknown diffraction and radiation potentials, and the boundary value problem is solved using a 3D high-order panel method (Lee, 1995). Hydrodynamic forcing quantities are calculated and the WECs heave motions' complex amplitudes, ξ_3^j, j=1,…, M, are obtained by solving the following linear system of equations, where M_{ji}, A_{ji}, B_{ji} and C_{ji} are respectively the mass, added mass, radiation damping and hydrostatic-gravitational stiffness coefficients, while B_{ji}^{PTO} are the PTO damping coefficients:

$$\sum_{j=1}^{M}\left[-\omega^2(M_{ji}+A_{ji})+i\omega(B_{ji}+B_{ji}^{\mathrm{PTO}})+C_{ji}\right]\xi_3^{\,j}=F_3^{\,i},\ i=1,...,M \qquad (1)$$

The mean power, $p(\omega)$, absorbed by the whole array at a specific ω is, finally, calculated using Eq. 2, where $p_j(\omega)$, j=1,…, M, is the power absorbed by the j^{th} WEC.

$$p(\omega)=\sum_{j=1}^{M}p_j(\omega)=\sum_{j=1}^{M}0.5bpto_j\omega^2\left|\xi_3^{\,j}\right| \qquad (2)$$

RESULTS AND DISCUSSION

The numerical model described above is applied for a mixed array of M=5 WECs. The array consists of three oblate spheroidal WECs corresponding to the two outer devices (WECj, j=1 & 5 in Figure 1a with M=5) and the middle one (WEC3 in Figure 1a with M=5), while the rest two WECs (WEC2 and WEC4 in Figure 1a with M=5) are cylindrical devices. Two mixed arrays (MXA1 and MXA2) are being examined. For MXA1, WEC2 and WEC4 have a_2=2.0 m and b_2/a_2=1.25, while cylindrical devices of a bit larger draft (b_2/a_2=1.5) are utilized in MXA2. For both arrays, the oblate spheroidal WECs have a_1=2.0 m and b_1/a_1=0.85. WECj, j=1, 3 & 5 and WECj, j=2 & 4 have the same PTO characteristics (i.e., in Eq. 1 B_{ji}^{PTO}=$bpto_1$, j=i=1, 3 & 5 and B_{ji}^{PTO}=$bpto_2$, j=i=2 & 4). The PTO damping coefficients are appropriately tuned to maximize energy absorption at the heave natural frequency of a single, isolated oblate spheroidal (ω_{n3}^{isoobl}) or cylindrical (ω_{n3}^{isocyl}) device. Hence, $bpto_1$ and $bpto_2$ are taken equal to the heave radiation damping of the corresponding single, isolated WEC at $\omega=\omega_{n3}^{isoobl}$ and $\omega=\omega_{n3}^{isocyl}$ respectively. For the examined oblate spheroidal geometry, ω_{n3}^{isoobl} is 2.4 rad/s leading to $bpto_1$=10,322.3 Ns/m. As for WECj, j=2 & 4, ω_{n3}^{isocyl} equals to 1.65 rad/s and 1.54 rad/s respectively for b_2/a_2=1.25 and 1.5 resulting to $bpto_2$=4010.4 Ns/m (MXA1) and $bpto_2$=3457.2 Ns/m (MXA2).

The WECs are placed in front of a wall of l_w/a_1=32 and w/a_1=0.5 with l_{bet}/a_1=4. Three different values of c/a_1 are investigated equal to 1.2, 1.5 and 2.0. The arrangement is deployed at an area of h=10 m and it is subjected to regular incident waves of β=270 deg (Figure 1a). Results are also compared with those of a homogeneous array consisting only of oblate spheroidal WECs (OBLA).

Figure 2 shows the variation of RAO_3 indicatively for WEC2 and WEC3 and for c/a_1=1.2 and 2.0. For both MXA1 and MXA2 and contrary to the OBLA, WEC2 (Figure 2a) due to its cylindrical shape depicts sharp peaks at 1.45 rad/s< ω < 1.7 rad/s as a result of resonance phenomena. Still, the c/a_1 increase leads to smaller peak values. The existence of the leeward boundary results also to RAO_3 local peaks at ω < 0.5 rad/s. Similar trend is observed for WEC3 (Figure 2b). However, RAO_3 of WEC3 for both MXA1 and MXA2 follows a quite intense variation at ω > 1.0 rad/s and exhibits local peaks and/or local minima close to zero similarly to heave exciting forces due to the existence of the wall. The interaction of WEC3 with the cylindrical WECs becomes pronounced for c/a_1=1.2, where resonance of WECj, j=2 & 4 introduces additional local maxima of the WEC3 response.

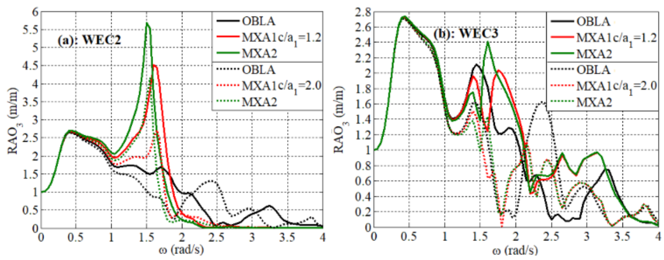

Figure 2. Effect of c/a_1 and array type on RAO_3.

Regarding $p(\omega)$ (Figure 3), for c/a_1=1.2 and for both MXA1 and MXA2, significant amount of power is absorbed at 1.0 rad/s < ω < 2.0 rad/s, where $p(\omega)$ obtains its maximum value approximately equal to 311 kW/m^2 (MXA1) and 349 kW/m^2 (MXA2). By increasing c/a_1 to 1.5, the frequency range where adequate power is absorbed becomes narrower (1.0 rad/s < ω < 1.8 rad/s), while the $p(\omega)$ peak value for MXA1 (~248 kW/m^2) is significantly reduced. The above trends become more pronounced for c/a_1=2.0, where the mixed arrays' absorption ability is highly reduced in the above frequency range. Still, $p(\omega)$ is increased at larger ω close to 2.4 rad/s, driven by the resonance of WECj, j=1, 3 & 5. Compared to the OBLA, mixed arrays show enhanced absorption ability when they are placed close to the wall (especially at c/a_1=1.2), since in that case the wall amplifies significantly RAO_3 resonance of the cylindrical WECs (Figure 2a). The opposite holds true for c/a_1=2.0, where also the wall does not impose any restrictions on the RAO_3 amplification of the oblate sphreoidal WECs due to resonance (Figure 2). Hence, the OBLA shows a better power absorption ability with major amount of power being absorbed at high frequencies (2.0 rad/s < ω < 2.7 rad/s). The latter conclusions are also illustrated in Figure 4, which includes the annual energy (E_{annual}) absorbed by the investigated arrays at three marine sites in Greece. For c/a_1=1.2, MXA1 and MXA2 lead to an average (among all sites) E_{annual} increase of 6.6% and 10.4% respectively compared to the OBLA. Still, the placement of MXA1 and MXA2 at c/a_1=2.0 results to an average E_{annual} decrease of 16.0% and 10.2% respectively. The improved energy absorption ability of all arrays at all sites when installed close to the wall is also clearly demonstrated.

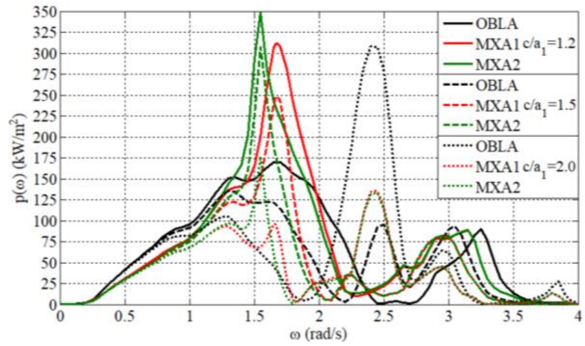

Figure 3. Effect of c/a_1 and array type on $p(\omega)$.

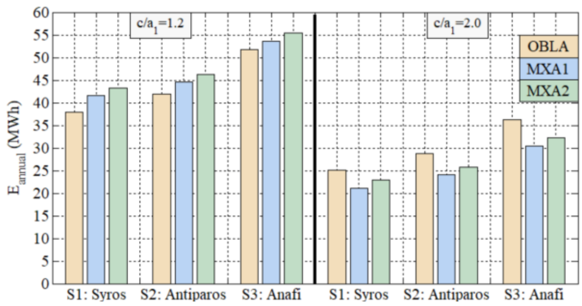

Figure 4. Effect of c/a_1 and array type on E_{annual} at three marine sites in Greece.

CONCLUSIONS

In this paper, we introduced mixed arrays of WECs in front of a vertical wall exploiting axisymmetric geometries that have excellent hydrodynamic efficiency (oblate spheroids) and excessive resonance features (cylinders). Compared to homogeneous arrays, mixed arrays can lead to improved power extraction, depending though on the array-wall distance. The mixed array's placement close to the wall introduces positive interactions between the WECs and among the wall and the WECs enhancing the array's hydrodynamic behaviour and, thus, its power absorption ability.

REFERENCES

Göteman, M. (2017). Wave energy parks with point-absorbers of different dimensions. *J Fluids Struct*. 74, 142–157.

Lee, C.H. (1995). WAMIT theory manual. Department of Ocean Engineering, MIT. Cambridge, Massachusetts, USA.

Loukogeorgaki, E., Boufidi, I. & Chatjigeorgiou, I.K. (2020). Performance of an array of oblate spheroidal heaving wave energy converters in front of a wall, *Water* 12(1), 18.

The Influence of Different Ramp Slopes on the Amount of Water Discharge in an OBREC: Preliminary Numerical Results in the Port of Ancona

Osouli S.[1,*], Postacchini M.[1], Sabbioni I.[2] and Brocchini M.[1]

[1] Department of Ingegneria Civile, Edile e Architettura, Università Politecnica delle Marche, Ancona, Italy
[2] Mentucci Aldo Costruzioni, Senigallia, Italy

*corresponding author:
e-mail: s.osouli@pm.univpm.it

INTRODUCTION

We investigate the effect of different ramp slopes on the functioning of Overtopping Breakwaters for the Energy Conversion (OBREC hereafter). Typically, an OBREC comprises various components, including ramps, a reservoir, a conveying system, and a turbine. Cavallaro et al. (2020) suggest that the OBREC performs optimally and offers high economic viability in regions with mild or less intense wave climates. The efficiency of ramps for these wave energy converters (WECs) is analyzed in this paper.

MATERIALS AND METHODS

Such devices have a reservoir to collect water which overtops through ramps. The FLOW-3D (Flow Science, 2023) CFD model was used to evaluate the wave-structure interactions. The wavemaker of this model was driven by waves generated by the FUNWAVE-TVD model (Shi et al., 2011). Table 1 shows, for a selected value of the joint probability density function, the main characteristics of the waves approaching from the NNE direction.

Table 1. Characteristics of sea waves coming from NNE direction.

		NNE
Density 0.005	H_s (m)	2.74
	T_m (s)	6.67
	T_p (s)	7.87
	$\alpha_{p,h1}$ [°]	35.00

To compare different slopes, a geometry like the real-scale breakwaters in the Port of Ancona was drawn using AutoCAD, and the corresponding STL files were utilized in FLOW-3D. The actual slope of the breakwater is 34°, and the water depth at the structure toe is ~6 m. For construction and practical purposes, the frontal ramp consists of a combination of two slopes: the first is 34°, extending 6 m from the seabed (water depth) across all models, and the second varies between 18° and 34° over the 2-m freeboard. The details are provided in Figure 1.

The numerical domain is 132 m long, 1 m wide and 10 m high. The cell size is 0.05 m in both x and z directions, while it is 1 m along the y direction, giving the total 528,000 cells. The volume of overtopped water was calculated beyond the ramp over a simulation time of 150 seconds. The setup and input wave energy are shown in Figure 2.

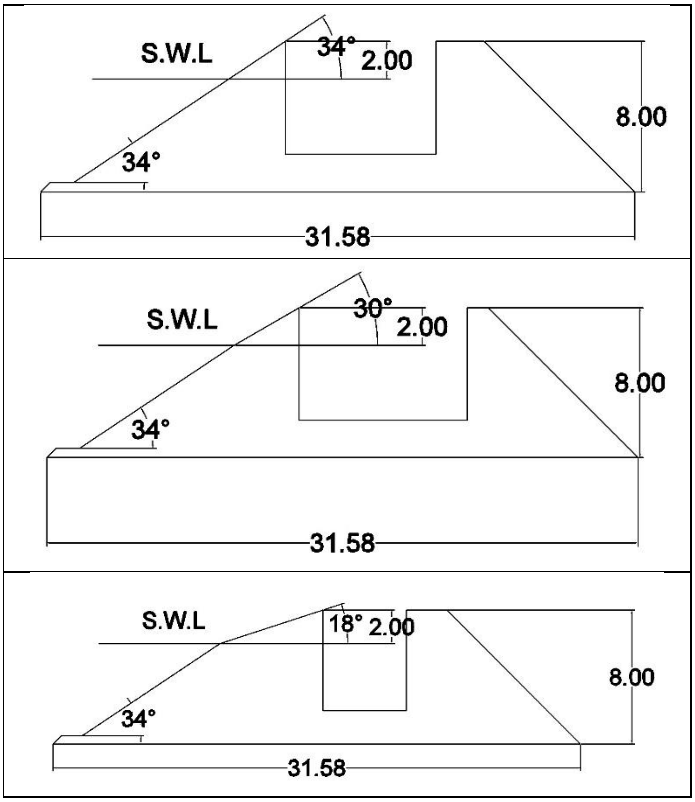

Figure 1. Samples for different ramp slopes upon the still water.

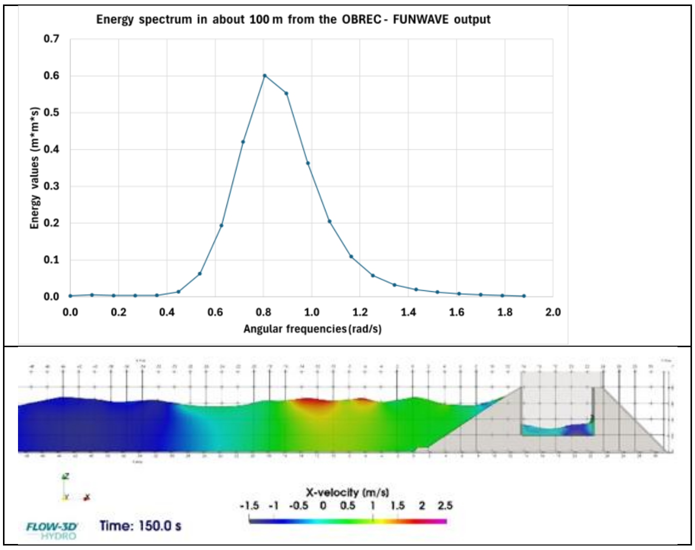

Figure 2. Numerical setup in FLOW-3D and wave energy spectrum as the wave maker boundary in FLOW-3D.

RESULTS

The comparison of overtopped volumes for different configurations, along with the free surface fluctuations recorded by a gauge located 30 m from the OBREC, are shown in Figure 3.

Based on the obtained results, the ramp slopes in freeboard significantly change the amount of water discharge: the 30° slope leads to the highest volume (10.57 m^3) and slopes of 26° and 34° provide volumes equal to 10.22 m^3. The gentle slopes of 18° and 22° lead to water discharges around 8.63 m^3 and 9.69 m^3, respectively.

Based on EurOtop (2018), the highest overtopping for short wind waves is achieved for slopes between 1:2 to 1:3 (i.e., 26° to 18°), while for longer waves, gentle slopes give a large overtopping due to surging waves (non-breaking waves). It should also be noted that, in the current study, only the freeboard slopes have been changed.

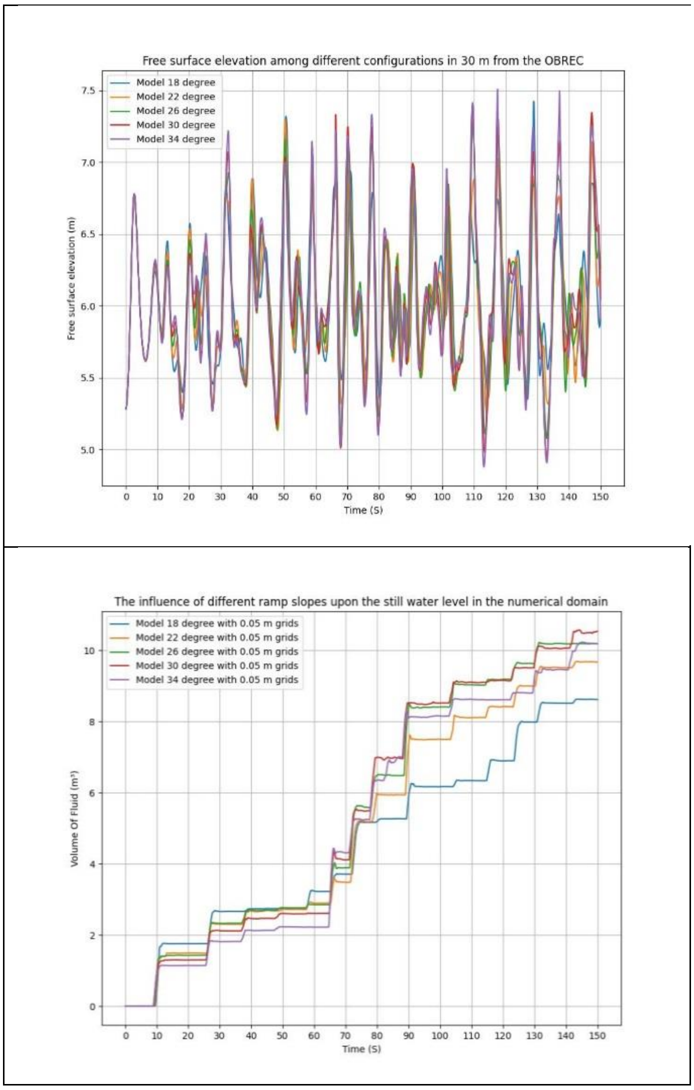

Figure 3. Effect of freeboard ramp slopes on water discharge and free surface elevation.

CONCLUSIONS

From the results of the overtopping tests, it is observed that freeboard slopes can influence the overtopped water discharge of about 20%, passing from the minimum to the maximum water volumes. Slopes of 26°, 30° and 34° show similar overtopped volumes. Detailed findings regarding the performance of the real-size ramp on the designed breakwater will be presented at the conference, particularly in relation to the OBREC installation at the Port of Ancona in Italy.

ACKNOWLEDGEMENTS

Financial support has been provided by European Union's (EU) Horizon Europe Framework Programme (HORIZON) via SEDIMARE (Grant Agreement No. 101072443), an MSCA Doctoral Network (HORIZON-MSCA-2021-DN-01).

REFERENCES

Cavallaro, L., Iuppa, C., Castiglione, F., Musumeci, R. E., & Foti, E. (2020). A simple model to assess the performance of an overtopping wave energy converter embedded in a port breakwater. *J. Mar. Sci. Eng.* 8(11), 1–20.

Flow Science, Inc. (2023). FLOW-3D, Version~2023R1. https://www.flow3d.com/

Shi, F., Harris, J.C., Kirby, J.T., & Grilli, S. (2011). FUNWAVE-TVD Fully Nonlinear Boussinesq Wave Model with TVD Solver Documentation and User's Manual (Version 3.0) Release Dec 2016 with TVD Solver - Documentation and User's Manual (Version 1.0).

EurOtop Manual on wave overtopping of sea defences and related structures An overtopping manual largely based on European research, but for worldwide application Second Edition 2018. www.overtopping-manual.com

Hydrodynamic Analysis and Performance Evaluation of Wave Energy Converter Arrays in Nearshore and Coastal Regions

Gerostathis Th.[1,*], Magkouris A.[2] and Belibassakis K.[2]

[1] Department of Naval Architecture, School of Engineering, University of Western Attica, Egaleo, 12243 Athens, Greece.
[2] School of Naval Architecture & Marine Engineering, National Technical University of Athens (NTUA), Zografos, 15780 Athens, Greece.

*corresponding author:
e-mail: tgero@uniwa.gr

INTRODUCTION

As the global demand for renewable energy grows, ocean wave energy is emerging as a viable option due to its high energy density and sustainability potential; Guo & Ringwood (2021). Wave Energy Converter (WEC) arrays offer a promising solution for harnessing this energy, particularly in nearshore-coastal regions; Babarit (2017). However, their deployment presents significant challenges, including wave transformation over variable seabed topographies, as well as complex hydrodynamic interactions among numerous devices. This work presents a modelling approach that integrates a three-dimensional Boundary Element Method (BEM) with a Coupled Mode Model (CMM) to predict the hydrodynamic performance of WEC parks in nearshore environments. By accurately simulating incident wave conditions and accounting for shoaling effects on wave propagation, the discussed approach aims to support optimization studies concerning WEC layouts and enhance energy extraction in coastal regions.

METHODOLOGY

The proposed methodology combines a 3D BEM with a Coupled Mode Model (CMM). First, the CMM is used to obtain the propagating wave field over an arbitrary seabed profile; Belibassakis et al. (2001). Next, the BEM model evaluates the diffraction of this field by the WEC array, as well as the hydrodynamic interactions among the devices located in close proximity; Babarit (2013). This approach captures the behavior of floating point-absorber WECs in intermediate to shallow water depths, where local seabed irregularities significantly affect wave propagation. The interaction effects between WECs are considered, as their hydrodynamic response can significantly influence the power absorbing capacity; Stratigaki et al. (2014). The model also accounts for variable depth, which impacts the energy distribution available for harnessing. A case study is conducted for a coastal area north of Ikaria Island in the Eastern Aegean Sea, which is characterized by high wave energy potential. Long-term wave data from this region are used to assess the feasibility of deploying WEC parks.

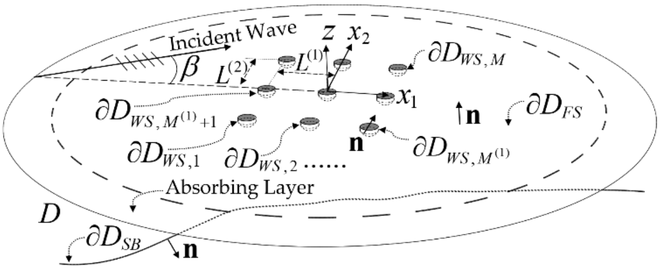

Figure 1. Sketch of a WEC park comprising nine (9) floating devices, illustrating the flow domain D and the parts of its boundary ∂D, along with basic parameters.

MODEL DESCRIPTION

A WEC array consisting of single degree–of–freedom heaving point absorbers is analyzed, comprising M identical devices, operating in a nearshore region with a varying seabed. The array is excited by harmonic incident waves. The heave response of each device is determined by modelling the surrounding wave field in the domain D (see Figure 1), incorporating both the effects of variable bathymetry and interactions among the devices. The flow field includes the propagating (incident and diffracted) field as well as M radiation fields, generated by the motion of the devices. Following standard hydrodynamic theory, each of these fields is described by a corresponding potential function. Assuming harmonic time-dependence of the form $\exp(-i\omega t)$, where ω is the angular frequency, the temporal evolution of each field is fully captured by using complex-valued potentials.

The incident field is derived by formulating and solving a coupled mode system, utilizing a local-mode representation for the potential function's (φ_I) vertical structure at each point of the domain. The latter representation comprises one propagating mode and an infinite series of evanescent modes, and is supplemented by an additional (sloping bottom) mode which accounts for the satisfaction of a no-entrance condition in areas where the bathymetric profile deviates from the horizontal plane; Athanassoulis & Belibassakis (1999).

The potential functions of the diffracted (φ_D) and radiated (φ_R) fields are expressed using boundary integral representations, involving the Green's function of the Laplace equation in 3D and discrete singularity strength distributions on ∂D, and are obtained as solutions to BVPs (governed by the Laplace equation) supplemented by appropriate BCs at the different surfaces that constitute the boundary. In particular, the BVPs for φ_D and φ_R involve the linearized Free Surface BC at ∂D_{FS} and no entrance conditions at ∂D_{SB} (see Figure 1). The BC applied to the wetted surfaces for the diffraction problem is defined so that the superposition of the φ_I and φ_D satisfies a no-entrance condition on these surfaces, while for the estimation of the m^{th} device radiation field a unitary excitation is applied, represented by the vertical component of the normal vector ($\mathbf{n}$) on the wetted surface of this device, treating the rest of the floaters as immobile and impermeable. The above BVPs are supplemented by an absorbing layer to treat conditions at infinity; see e.g., Turkel & Yefet (1998).

The vertical forces acting on each device include the Froude-Krylov (FK) forces (due to the incident field), the diffraction forces (due to the diffracted field) and the forces due to the M radiation fields. The FK and diffraction forces are evaluated by integration of each field's pressure multiplied by the vertical component of the normal vector on the corresponding wetted surface. The radiation forces (given that they depend on the unknown responses), are incorporated in the analysis via the added mass (**A**) and hydrodynamic damping (**B**) matrices, whose elements are defined by the component of the force, induced on the m^{th} WEC by the n^{th} (unitary) radiation field, that is in phase with the velocity and the acceleration, respectively, forming full $M \times M$ matrices that make the responses coupled and model the (constructive or destructive) interactions among the devices. Finally, the power extraction is modelled by a Power-Take-Off (PTO) System, that is imported in the equations of motion as additional (diagonal) damping ($\mathbf{B_{PTO}}$) and stiffness ($\mathbf{C_{PTO}}$) matrices. Based on the above, the response vector, (which describes the heaving motion of each device by a complex amplitude) is obtained for a single frequency and propagation angle by the linear system of the coupled equations of motion, which involve the inertia and added inertia of the WECs, the hydrodynamic and the PTO damping and the hydrostatic and PTO restoration matrices; Gerostathis et al. (2024).

RESULTS

Based on results from the above model, the power absorption of each WEC can be evaluated utilizing its response and the applied PTO damping. Additionally, by solving for an isolated device, the q-factor, (which is the ratio of the total power generated by a park of M WECs to M times the power of a single device), can be quantified for any given array configuration. For example, Figure 2 illustrates the q-factor for a park comprising 25 devices in a 5 × 5 arrangement, deployed north of the coast of Ikaria Island, in the Eastern Aegean Sea region. The results concern devices of radius a = 1.5 m, submerged volume equal to 9.89 m^3, while the PTO damping is set to $35.14\,\mathrm{kN/s}$ and the PTO stiffness is defined as 10% of the hydrostatic restoring coefficient. Details concerning the specific case study can be found in the work by Gerostathis et al. (2024). As shown in Figure 2, the interactions between the devices within the array are minimal at low frequencies, while at higher frequencies, the q-factor exhibits complex behaviour that is heavily dependent on the frequency as well as the propagation direction. The results can be also combined with wave climate data to predict the energy production of a WEC array at a geographic area of interest, providing valuable insights into its performance under real sea conditions. The presence of multiple WECs in an array modifies the local wave field, creating constructive or destructive interference patterns that influence the overall energy conversion efficiency. The spacing and arrangement of WECs play crucial roles in optimizing power capturing efficiency, as specific configurations enhance wave power absorption by leveraging hydrodynamic interactions. Additionally, nearshore seabed topography significantly alters wave characteristics, affecting WEC performance. Areas with steep depth gradients or shallow regions induce wave refraction and diffraction effects, which must be considered in park design.

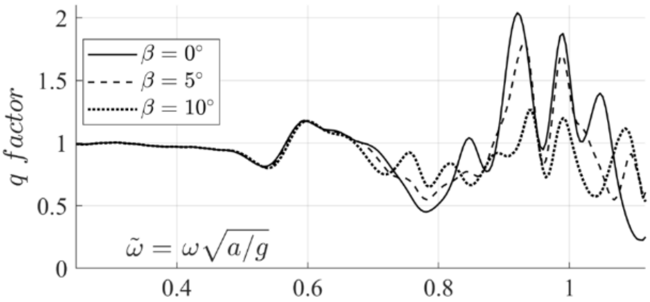

Figure 2. q-factor of 5 × 5 WEC arrangement for different wave propagation angles.

CONCLUSIONS

This study presents a numerical approach for assessing the performance of WEC parks in nearshore coastal environments. By integrating 3D BEM-based hydrodynamics with a coupled mode model, the methodology provides an accurate evaluation of the energy capturing potential. The findings highlight the importance of device positioning, seabed variations, and hydrodynamic interactions in optimizing WEC arrays. The proposed model serves as a valuable tool for designing efficient and sustainable wave energy projects, supporting the broader transition to renewable energy solutions in coastal regions.

REFERENCES

Athanassoulis, G.A., & Belibassakis, K.A. (1999). A consistent coupled-mode theory for the propagation of small-amplitude water waves over variable bathymetry regions. *J. Fluid Mech.* 389, 275–301.

Babarit, A. (2013). On the park effect in arrays of oscillating wave energy converters. *Renew. Energy* 58, 68–78.

Babarit, A. (2017). *Ocean Wave Energy Conversion: Resource, Technologies and Performance* (1st ed.). ISTE Press - Elsevier. ISBN: 978-1-78548-264-9.

Belibassakis, K.A., Athanassoulis, G.A., & Gerostathis, T.P. (2001). A coupled-mode model for the refraction–diffraction of linear waves over steep three-dimensional bathymetry. *Appl. Ocean Res.* 23(6), 319–336.

Gerostathis, T., Magkouris, A., & Belibassakis, K. (2024). A 3D BEM-Coupled Mode Model for the Performance Analysis of Wave Energy Converter Parks in Nearshore-Coastal Regions. *J. Mar. Sci.Eng.* 12(2).

Guo, B., & Ringwood, J.V. (2021). A review of wave energy technology from a research and commercial perspective. *IET Renew. Power Gener.* 15(14), 3065–3090.

Stratigaki, V., Troch, P., Stallard, T., Forehand, D., Kofoed, J.P., Folley, M., Benoit, M., Babarit, A., & Kirkegaard, J. (2014). Wave Basin Experiments with Large Wave Energy Converter Arrays to Study Interactions between the Converters and Effects on Other Users in the Sea and the Coastal Area. *Energies* 7(2), 701–734.

Turkel, E., & Yefet, A. (1998). Absorbing PML boundary layers for wave-like equations. *Appl. Numer. Math.* 27(4), 533–557.

Practical Guidance for Representative Wave Heights and Periods in the Surf Zone

Al Khalili U.[1,*], Christou M.[1] and Karmpadakis I.[1]

[1] Department of Civil and Environmental Engineering, Imperial College London, South Kensington Campus, London, SW7 2AZ, UK

*corresponding author:
e-mail: umniya.al-khalili18@imperial.ac.uk

INTRODUCTION

The design of coastal structures requires the definition of appropriate wave heights and periods that are representative of real seas. The selection of such parameters is dependent on the governing hydrodynamic processes on which the structure is designed for. The characteristics of the waves are often determined outside the surf zone based on hindcast data and subsequently transformed to the site location. However, the complexities of wave behaviour in coastal regions introduce significant challenges in capturing the full extent of these transformations. This work utilizes an extensive range of numerical simulations to develop a thorough understanding of the key physical mechanisms that govern this transformation. Furthermore, the findings of this work are utilized to develop new parametric guidance to be used in design for the evolution of representative wave heights and periods.

METHODOLOGY

Numerical simulations are conducted using the non-hydrostatic wave-flow model Simulating WAves till SHore (SWASH) (Zijlema et al., 2011). The present study considers the evolution of a broad range of unidirectional random sea-states from intermediate water to the shoreline. The numerical set-up is summarised by Figure 1. The bathymetry consists of an initially flat bed followed by a uniform variable bed slope. This work investigates 5 bed slope gradients from a steep 1:10 to a mild 1:80 slope. The properties of the numerical simulations are based on the work of Al Khalili et al. (2025).

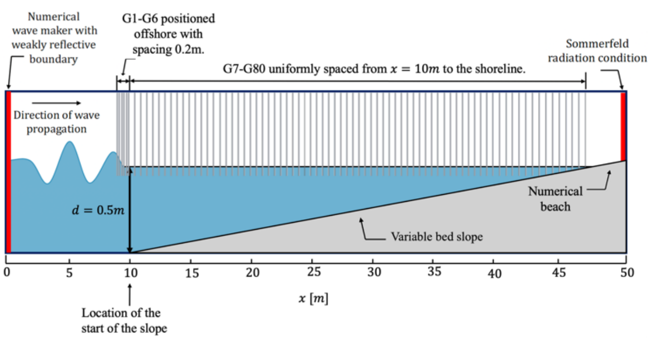

Figure 1. Schematic of the numerical set-up in SWASH.

The sea-states considered consist of four sets of varying peak period, T_p, as shown in Table 1. Within each set, the offshore significant wave height, $H_{s,0}$, is gradually increased to model near linear seas ($S_p = 0.01$) up to highly nonlinear seas ($S_p = 0.06$). The data is generated using a JONSWAP spectrum with a peak enhancement factor of $\gamma = 2.5$ to reflect realistic storm conditions in intermediate waters (Jonathan and Taylor, 1997). 20 random realisations (seeds) of each sea-state are simulated, each corresponding to approximately 3 hours in field scale. Hence, a total of approximately 150 million waves are recorded across 80 spatial locations along the length of the spatial domain.

Table 1. Test cases.

Sea-state	$T_p[s]$	$H_{s,0}[m]$	$S_p = \frac{2\pi H_{s,0}}{gT_p^2}[-]$	$k_pd[-]$
A1	1.2	0.023	0.01	1.53-0
A2		0.046	0.02	
A3		0.068	0.03	
A4		0.091	0.04	
A5		0.111	0.05	
A6		0.124	0.06	
B1	1.4	0.029	0.01	1.22-0
B2		0.057	0.02	
B3		0.086	0.03	
B4		0.115	0.04	
B5		0.139	0.05	
B6		0.156	0.06	
C1	1.6	0.034	0.01	1.02-0
C2		0.069	0.02	
C3		0.103	0.03	
C4		0.137	0.04	
C5		0.167	0.05	
D1	1.8	0.040	0.01	0.88-0
D2		0.080	0.02	
D3		0.119	0.03	
D4		0.159	0.04	

WAVE HEIGHT

Given the importance of the root-mean-squared wave height (H_{rms}) in design, several energy dissipation formulations have been proposed to capture this evolution in coastal regions. However, discrepancies between these formulations and the existing data are observed, with no model providing global accuracy across the cases investigated. This work will present practical insight into H_{rms} evolution in coastal waters.

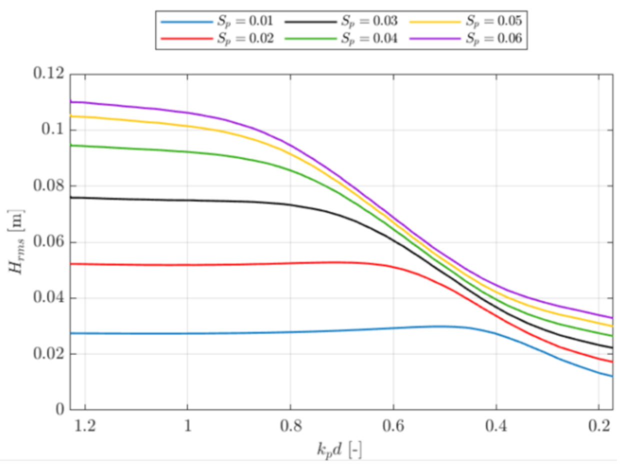

Figure 2. Evolution of H_{rms} with reduced k_pd over a bed slope of 1:30 and $T_p = 1.4s$.

Figure 2 shows the evolution of H_{rms} with reduced effective water depth (k_pd) for a range of sea-state steepnesses (S_p). In mild seas ($S_p \leq 0.02$), wave shoaling effects are prominent such that H_{rms} initially increases with reducing water depth. Conversely, steeper sea-states ($S_p \geq 0.03$) achieve breaking saturation even in intermediate water depth.

Hence, this earlier breaking saturation results in a reduction in H_{rms} further offshore. Moreover, the extent of H_{rms} reduction, which is related to the magnitude of energy dissipation, is more notable in steeper seas. Figure 3 addresses the role of the bed slope gradient on the evolution of H_{rms} normalised by the value in deep water, $H_{rms,deep}$. In mild seas (Figure 3a), a more prominent shoaling behaviour is observed in steeper bed slopes, resulting in a globally larger ratio of $H_{rms}/H_{rms,deep}$. Moreover, breaking saturation is observed to occur further inshore in such bathymetries. In shallower water, the results are shown to converge for slopes milder than 1:30. Conversely in steeper seas (Figure 3b), the occurrence of breaking saturation at the onshore location means no shoaling behaviour is observed. However, discrepancies in the breaking behaviour are observed across bathymetries. This is such that steep slopes are associated with a later location of breaking initiation resulting in a much narrow spatial domain across which breaking occurs.

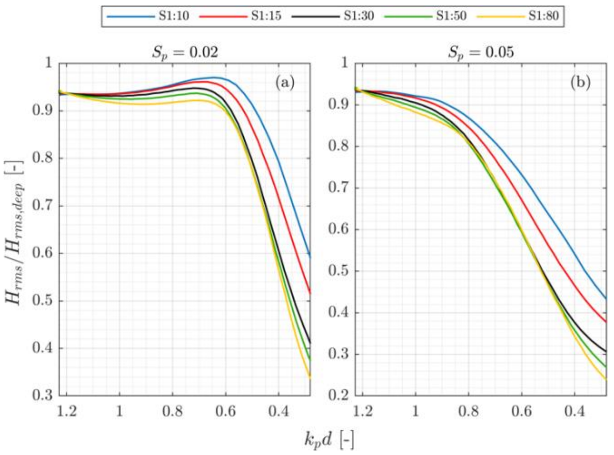

Figure 3. Evolution of $H_{rms}/H_{rms,deep}$, with reducing effective water depth, $k_p d$, for offshore steepness (a) $S_p = 0.02$ and (b) $S_p = 0.05$.

WAVE PERIOD

The parameter $T_{m-1,0}$ is commonly adopted to model sediment transport (Baldock et al., 2011) and wave overtopping (Altomare et al., 2016) due to its favourable weighting of low frequency energy components. The formulation of Hofland et al. (2017) is commonly adopted in design. However, discrepancies are observed with the current dataset. Instead, we propose a new formulation given by:

$$\frac{T_{m-1,0}}{T_{m-1,0,deep}} = 1 + a\exp(-b\tilde{d}) + \exp(-\tilde{d}) \qquad (1)$$

where $\tilde{d} = d/H_{m0,deep}\left(\frac{m}{100}\right)^{0.2}$, d is the local water depth, $H_{m0,deep}$ is the offshore spectral significant wave height and m is the bed slope gradient. This new formulation shows a strong correspondence with the existing data as shown in Figure 4a. More specifically, it is able to accurately capture the significant growth in infragravity energy observed in shallow water which result in an increase in $T_{m-1,0}$. This effect is shown to be magnified in milder bed slopes. Hence, the model parameters a and b are conditioned upon the bed slope gradient and are given by Figure 4b and 4c, respectively. The parameter a is shown to linearly increase with bed slope, m, whereas the parameter b exhibits an exponential decay.

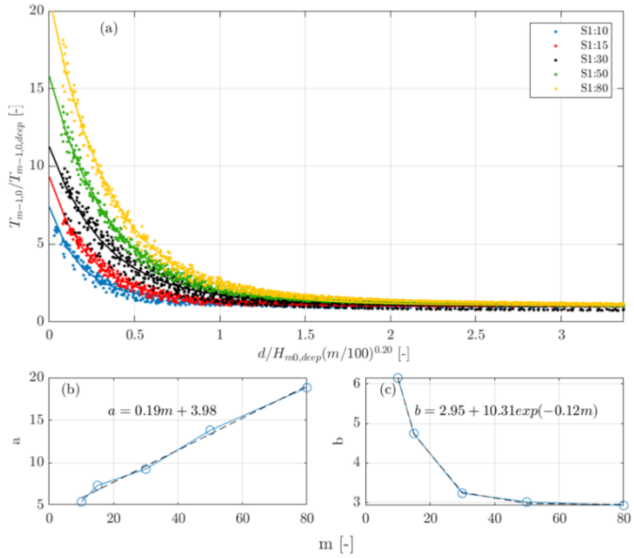

Figure 4. New $T_{m-1,0}$ formulation. (a) Data is shown in solid marker with the fitted distribution in a line. The colour corresponds to the bed slope. Variation in model parameter (b) a and (c) b, respectively, with bed slope, m.

CONCLUSION

The extensive numerical data set obtained in this investigation is employed to develop key understanding into physical effects that govern the evolution of parametric wave heights and periods in the coastal zone, with a highlighted interest into the influence of the bed slope gradient. These findings are utilised to provide parametric guidance for the evolution of H_{rms}. Moreover, a new model for $T_{m-1,0}$ is proposed which captures the growth of infragravity energy as a functions of bed slope effects.

REFERENCES

Al Khalili, U., Bellos, V., Christou, M., & Karmpadakis, I. (2025). Regular and random wave modelling over mild uniform bathymetry using SWASH. *Coastal Eng.* 199, 104745.

Altomare, C., Suzuki, T., Chen, X., Verwaest, T., & Kortenhaus, A. (2016). Wave overtopping of sea dikes with very shallow foreshores. *Coastal Eng.* 116, 236–257.

Baldock, T.E., Alsina, J.A., Caceres, I., Vicinanza, D., Contestabile, P., Power, H., & Sanchez-Arcilla, A. (2011). Large-scale experiments on beach profile evolution and surf and swash zone sediment transport induced by long waves, wave groups and random waves. *Coastal Eng.* 58,214–227.

Hofland, B., Chen, X., Altomare, C., Oosterlo, P. (2017). Prediction formula for the spectral wave period tm-1,0 on mildly sloping shallow foreshores. *Coastal Eng.* 123, 21–28.

Jonathan, P., & Taylor, P.H. (1997). On Irregular, Nonlinear Waves in a Spread Sea. *J. Offshore Mech. Arct. Eng.* 119, 37.

Zijlema, M., Stelling, G., Smit, P. (2011). Swash: An operational public domain code for simulating wave fields and rapidly varied flows in coastal waters. *Coastal Eng.* 58, 992–1012.

Experimental Measurements on a Physical Model for the Optimization of the Kato Pyrgos Fishing Shelter Layout in Cyprus

Tsoukala V.[1,*], Chondros M.[1], Ziros A.[1], Mplounas G.[1], Eleftheriadou E.[1], Sartampakos P.[2], Papadimitriou A.[1], Metallinos A.[1], Kalpias A.[3], Toumazis A.[4], Solomonidis C.[3] and Zervos S.[5]

[1] Laboratory of Harbour Works, School of Civil Engineering, NTUA, 9 Iroon Polytechniou Str., 15780, Zografou, Greece
[2] NIREAS Engineering, 8 Katsikogiani Str., 34132, Chalkis, Greece
[3] Rogan Associates S.A., 5 Chatzigianni Mexi Str., 11528, Athens, Greece
[4] Dion. Toumazis & Associates L.L.C., 4 Romanou Str., 1070, Nicosia, Cyprus
[5] Public Works Department, Ministry of Transport, Communications and Works, 165 Strovolou Str., 2049, Strovolos, Cyprus

*corresponding author:
e-mail: tsoukala@mail.ntua.gr

INTRODUCTION

The Kato Pyrgos fishing shelter, located along the northern coast of Cyprus, serves as a vital infrastructure for the local community and fishing industry. In recent years, the accumulation of sand and seagrass (Posidonia Oceanica) at the entrance and within the shelter basin has led to a reduction in navigable depth, creating significant challenges for vessel access. This sedimentation and organic debris buildup hinder the safe entry and exit of boats, necessitating an effective mitigation strategy. To address this issue, the Ministry of Transport, Communications, and Works of the Republic of Cyprus commissioned a comprehensive study through a competitive bidding process. The contract was awarded to the Rogan Associates S.A. – Dion. Toumazis & Associates L.L.C. JV, tasked with designing new coastal and port works to prevent sand and seagrass accumulation within the fishing shelter. As part of this study, the Laboratory of Harbour Works (LHW) of the School of Civil Engineering at the National Technical University of Athens was responsible for conducting physical modeling experiments to evaluate the performance of the proposed layout. The present work details the scope of the physical modeling study and the experimental setup.

OBJECTIVE OF PHYSICAL MODELLING

The primary objective of the physical model experiments is to assess the performance of the proposed fishing shelter layout (Figure 1) under realistic hydrodynamic conditions.

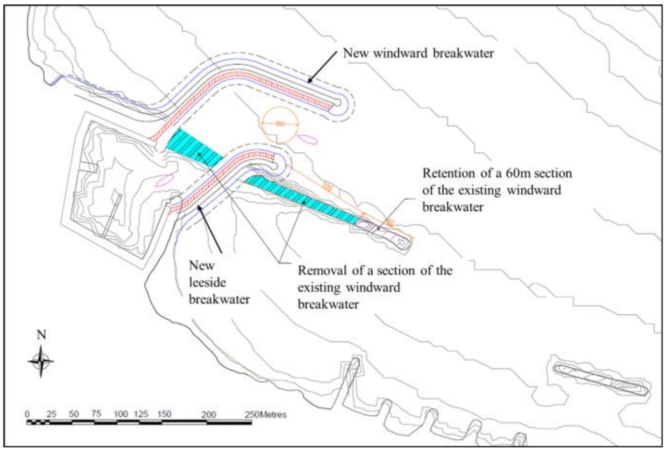

Figure 1. Proposed fishing shelter layout.

Specifically, the experiments aim to replicate the wave and coastal flow dynamics affecting the study area and provide empirical insights into the performance of the proposed design. The investigation focuses on three key parameters: (i) wave disturbance inside and outside the fishing shelter, (ii) wave-induced currents and (iii) transport and deposition of floating seagrass fragments. Based on these measurements, valuable conclusions are drawn regarding: (a) the efficiency and optimization of the proposed structures in mitigating sedimentation and seagrass accumulation; (b) the modification of wave action within and outside the fishing shelter; (c) the hydrodynamic response of the adjacent coastal zone and hence the sediment transport trends affecting the entrance; (d) the mechanisms governing seagrass accumulation and potential mitigation strategies; and (e) the water renewal and circulation patterns within the shelter basin. These findings contribute to the improvement of coastal infrastructure design by ensuring functionality, sustainability, and resilience.

EXPERIMENTAL SETUP

The physical model was designed to replicate approximately a 1.5 km × 0.6 km section of the study area, encompassing the headland west of the fishing shelter and the existing system of five groins and three detached breakwaters located east of the shelter (Figure 2).

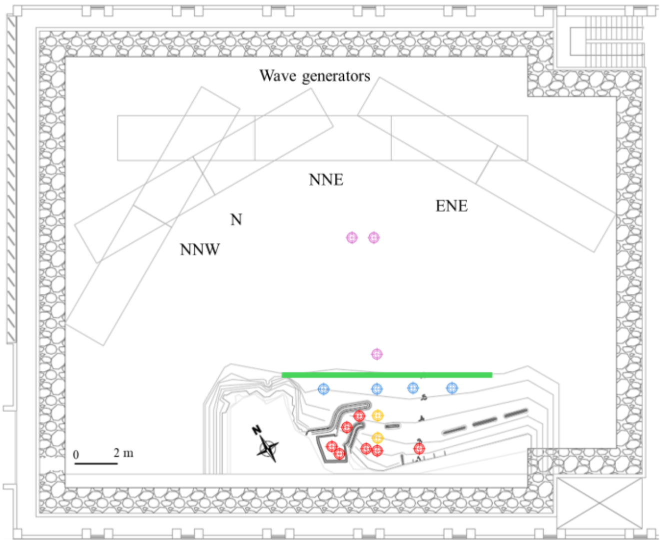

Figure 2. Layout of the physical model, showing the placement of wave generators and measurement instruments within the wave basin. Pink and light blue markers indicate the position of resistance-type wave gauges, red markers of acoustic wave gauges, and orange markers of the acoustic velocimeter. The green line indicates the area where Posidonia Oceanica leaf models are deployed.

A geometric scale of 1:80 was selected, ensuring compliance with Froude and Reynolds similarity laws (HYDRALAB III, 2007). Given the required model dimensions, experiments were conducted in the largest wave basin (DD2 Tank) of the LHW, measuring 35.2 m × 27.8 m × 1.0 m. The model was rotated counterclockwise by 30° relative to true North to maximize the effective use of the tank surface while ensuring adequate spacing from the wave generators. The modeled bathymetry included a minimum simulated depth of −6 m and a maximum elevation of +2 m. The water depth in the tank was approximately 39 cm over the flat bottom. The structural elements were constructed using graded gravel, carefully scaled to match the physical properties of natural rock materials used in the proposed works (Figure 3). The quay wall of the fishing shelter was represented by a vertical steel sheet. To minimize wave reflection and ensure accurate energy dissipation, peripheral riprap layers were placed along the tank boundaries. Floating Posidonia Oceanica leaf models were created using polyethylene strips (<1 cm in length, <1 mm in width) to mimic their transport and deposition behavior. To ensure uniform and spatially controlled seagrass deposition, a custom-built distribution system was developed using a modified plastic conduit mounted on tripods. After each test, Posidonia analogs were carefully removed using a fine-mesh retrieval net.

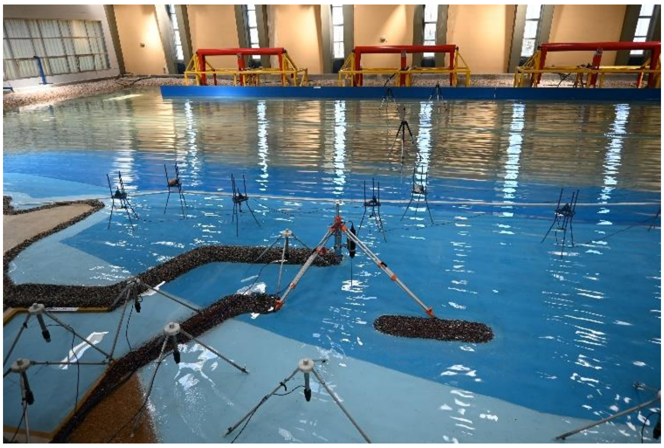

Figure 3. View of the wave basin, physical model, measurement instruments and wave generators.

SEA STATE CONDITIONS UNDER INVESTIGATION

The experiments simulate wave incidence from four dominant Mean Wave Directions (MWD) to which the fishing shelter is exposed, i.e., NNW, N, NNE and ENE. The simulated wave characteristics are summarized in Table 1.

Table 1. Wave scenarios under investigation.

Direction	MWD (degrees N)	H_s (cm)	T_p (s)
N	360	2.79	0.65
NNE	30	2.18	0.62
ENE	60	1.96	0.60
NNW	330	2.61	0.64

For all test cases, the water level is set at the Mean Sea Level. Wave generation was achieved using the largest three wave generators (8 m × 2 m each) of the LHW, which produced irregular long-crested waves of JONSWAP spectrum, with both oblique and normal wave incidence conditions.

MEASUREMENT INSTRUMENTS AND DATA ANALYSIS

A combination of hydrodynamic instruments was deployed to accurately capture wave characteristics, current velocities and directions, and Posidonia Oceanica transport patterns. Eight resistance-type wave gauges (HR Wallingford) were positioned in deep and intermediate waters, and seven acoustic wave gauges (General Acoustics) in shallower waters and within the shelter basin. Additionally, current velocity measurements were obtained using a high-resolution acoustic velocimeter (NORTEK Vectrino) with adjustable positioning (Figure 2). To track the motion of Posidonia analogs, two GoPro cameras were utilized for high-resolution trajectory analysis. For data processing, wave gauge recordings were analyzed using HR Wallingford's software, while acoustic wave gauge and current velocity data were processed using Python-based scripts developed by LHW. This rigorous experimental setup ensured the high fidelity of the physical model, allowing for a comprehensive assessment of the proposed interventions and their impact on the fishing shelter's hydrodynamics and sediment dynamics.

CONCLUSIONS

Physical modeling has proven to be an invaluable tool for assessing the performance and functionality of proposed coastal infrastructure. In this study, physical simulations provided critical insights that could not have been obtained through other methodologies with the same level of reliability. By replicating complex coastal processes occurring in the Kato Pyrgos coastal zone, the model facilitated a comprehensive evaluation of the proposed design. Beyond its technical merits, physical modeling offers significant advantages in optimizing port and coastal projects. These benefits extend across multiple dimensions:

- Economic advantages: Reduced construction and maintenance costs, along with the mitigation of potential damages, thereby enhancing the longevity of infrastructure.
- Environmental benefits: Minimized ecological impacts, improved ecosystem protection, and development of climate-resilient infrastructure.
- Social contributions: Enhanced safety and quality of life for coastal communities.
- Scientific value: Advancement of knowledge through the development of innovative methodologies and technologies.

The findings underscore the critical role of physical modeling in the holistic design and optimization of coastal and harbour engineering projects, ensuring sustainable and resilient infrastructure development.

REFERENCES

HYDRALAB III (2007), Guidelines for physical model testing of breakwaters: rubble mound breakwaters, Deliverable NA3.1, Version 1.3, August 2007.

A Practical Application of Assessing Wave Loads, Overtopping and Structural Stability on Crown Seawalls – The Case Study of Residential Developments on Al Marjan Island

Dimakopoulos A.S.[1,*], Vanino E. [2], Dasam K. [2], Vemuri S.[3], Nichannamettla V.[3], Buyukozer A. [3] and Iribarren E.[3]

[1] Department of Civil Engineering, University of Patras, Greece
[2] Jacobs, UK
[3] Jacobs, UAE

*corresponding author:
e-mail: a.dimakopoulos@upatras.gr

BACKGROUND

During the engineering design studies for the Al Danah Bay development project on Al Marjan Island (United Arab Emirates), a Computational Fluid Dynamics (CFD) model was used to predict wave overtopping and the loads acting on the seawall of the residential buildings located along the coastal front of the development. The CFD model was based on the OpenFOAM® computational toolkit and included 2D and 3D simulations of the wave propagation, shoaling and interaction with the coastal protection structures and residential developments. The model was used to calculate quasi-static and impulsive loads on the coastal protection seawalls as well as overtopping discharges and volumes.

METHODOLOGY

Initially a 2D numerical flume was set-up considering two scheme cross-sections and normal wave incidence to the shoreline to estimate wave loads and overtopping volume, which inherently yields conservative results. The permeability of the rubble mound breakwater supporting the seawall was introduced following recommendations from Dimakopoulos et al. (2023) and the Rock Manual (2007). Forces were monitored on the seawall and the residential building for wave conditions with return periods of 1 year (Serviceable Limit State) and 308 year (Ultimate Limit State). Wave overtopping evolution between the crown of the seawall and the residential building was monitored by using three overtopping monitors.

RESULTS AND CONCLUSIONS

Results indicated that wave overtopping was relatively low at the seawall (~1l/s/m) and the overtopping jet momentum was significantly attenuated by the time it reached the residential structure (<0.1l/s/m) reach at the residential structures. High impulsive wave pressures were recorded at the seawall, which resulted in relatively significant peak negative horizontal and vertical uplift loads (-352kN/m and 529kN/m, respectively). Further sensitivity studies on the 2D numerical flume were performed, looking to address uncertainties coming from mesh refinement, definition of permeability properties, and sequence of random waves. Sensitivity studies showed that these estimates were rather robust and not strongly dependent on modelling considerations. Current structural design guidance does not include the effect of dynamic structural response on stability checks, necessitating the application of wave loads as quasi-static forces, which resulted in a low safety coefficient of stability. To demonstrate that these loads were rather conservative, a 3D model was set-up which included oblique wave incidence (waves coming at 15 degree angle) and the curvature of the seawall at the cross-shore direction. To reduce the computational effort, comparative studies of bichromatic wave groups with the maximum wave were performed, which aimed at assessing wave load reduction due to oblique wave incidence and seawall curvature. These showed a reduction of impulsive uplift loads of approximately 50%, whilst drastically reducing peak negative horizontal loads by an order of magnitude. The seawall construction is now complete and the residential development is currently under construction.

Figure 1. The residential development at Al Marjan Island with the coastal protection structure (under construction).

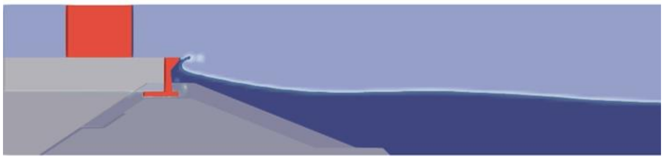

Figure 2. Impulsive wave load event in the 2D numerical flume.

Figure 3. Impulsive wave load event in the 3D numerical tank.

ACKNOWLEDGEMENTS

The first co-author’s contribution to the paper has been financed by the funding programme “MEDICUS” of the University of Patras

REFERENCES

Dimakopoulos, A.S., Pullen, T., & Allsop, N.W.H. (2023). Internal Pressures in Rubble Mound Breakwaters used in Coastal Protection - Recommendations for Assessing Wave

Pressures with CFD Models. Coasts, Marine Structures and Breakwaters 2023: Resilience and adaptability in a changing climate, Portsmouth, UK, January 2024, 1363–1378.
CIRIA, CUR. CETMEF, The rock manual. The use of rock in hydraulic engineering. 2nd Ed. CIRIA, London (2007).

Wave Action on Coastal Bridges: Engineering an Iconic 1,100-Meter Low-Lying Sea Bridge in KSA

Diplarakos N.[1,*], Fountoulis G.[1], Kolios D.[1] and Alexandris A.[1]

[1]Archirodon NV - Engineering Department. 80 I. Metaxa st, Koropi, Greece

*corresponding author:
e-mail: n.diplarakos@archirodon.net

INTRODUCTION

Wave loading on low-lying bridges is crucial to structural design, requiring close collaboration between marine analyst and structural designer. An iconic low-lying sea bridge, built in Saudi Arabia (2022–2023) as part of a luxury tourism development in the Red Sea coast, had to address such challenges. The bridge is part of a luxury tourism initiative featuring islands, resorts, and infrastructure, set within a pristine natural lagoon along the Red Sea coast of KSA. It connects the mainland to Shura Island, which is a centerpiece of the destination, hosting 11 of the 16 hotels planned in the first phase of the development. The bridge is positioned at the entrance to Shura Island, serving as a symbolic gateway to the luxurious destination. The 1.100 m-long sea bridge (see Figure 1) is conceived as an aesthetically unique structure of atypical cross section that integrates multiple elements, including a carriageway, planters, utility corridors, and a boardwalk, all arranged at varying levels.

Figure 1. Architect's vision of Shura bridge; a green pedestrian and vehicular structure harmoniously integrated into the pristine lagoon environment.

DESIGN FOR WAVE IMPACT

The Shura Bridge's aesthetic goals—blending with the natural landscape and keeping walkways near the sea for an enhanced visitor experience led to a low-lying design that seamlessly integrates with its surroundings.

Although the bridge lies within the sheltered lagoon, the impact of surge, sea level rise, and waves on its structural integrity, safety, and functionality were key design considerations. A thorough evaluation of sea states, hydrodynamic loads, and structural performance was essential to meet these challenges while maintaining the architects' vision of a bridge close to sea level.

Analysis using a comprehensive wave transformation model assessed design storm waves and surge. Numerical modeling showed that barrier islands along the western, southern, and eastern lagoon boundaries are impacted by Red Sea waves, while islands near the mainland and the Shura Bridge crossing are only affected by locally (within the lagoon) generated wind waves.

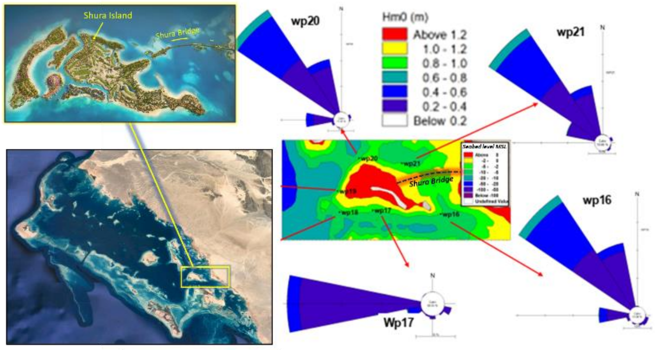

Figure 2. Location of Shura Island and bridge, within the Lagoon formed along the Red Sea coast; Sketch presents rose plots of H_{m0} calculated by the wave transformation model at various points around the island.

The design event is a 1 in 100-year return period event, considering projected sea level rise at the end of the 100yr design life of the structure. Design criteria require this event not to cause structural damage to the bridge or services contained within the bridge utility corridors, but also to limit overtopping discharges on the bridge deck to ensure that the bridge is still safe to cross.

The design still water level, (see Figure 3) forming the reference level of design waves, is computed as the sum of various components like astronomical tides, storm surge, seasonal changes and sea-level rise. For a design return period of 100 years, the extreme wave conditions near the Shura Bridge are characterized by a spectral significant wave height of H_{m0} = 1.6 m, at peak wave period T_p =4.2s and a mean wave direction MWD of 319 degN.

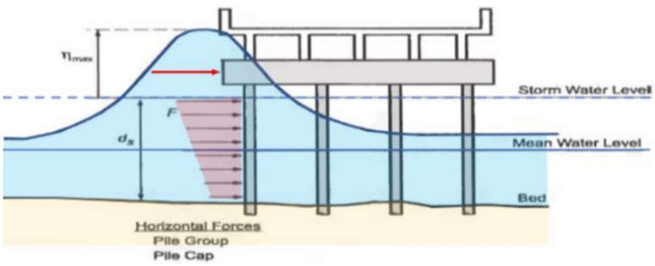

Figure 3. Hydrodynamic Load effects on bridge substructure elements (AASHTO, 2008).

For the bridge's structural design, hydrodynamic forces on piles and pier cross beams were calculated using the Morison equation (Morison, et al.,1950), while forces on the underdeck surface were estimated following Cuomo et al. (2007), a widely used empirical method based on physical model test results. An ANSYS model was also built to evaluate results of the empirical method and enhance understanding of the physics. The methodology by Cuomo et al. (2007) is directly applicable for simple deck geometries; however, for more complex cases, it requires assumptions about the distribution of wave loads beneath the deck. While numerical modeling of wave impact lacks the credibility of experimentally validated methods, it provides a better understanding of wave-structure interaction and enables evaluation of the load distribution predicted by the empirical method, which does not consider the underdeck girder geometry. For example, assuming simultaneous horizontal wave loading on all girders of the bridge is deemed a conservative approach for this case. Loads derived based on the empirical method and snapshots from the numerical analysis are shown in Figure 4.

An important factor in analyzing such structures is the air entrapment effect, where air can be trapped between girders, the deck, and the water surface. While this can result to the development of significant uplift forces, geometrical analysis and numerical modeling in this atypical case shows that formation of air entrapment between the girders is unlikely. Design waves approach at an angle to the bridge axis, with wavelengths shorter than the length of the span, allowing air to vent at the wave trough. Similarly, given the finite crest lengths of design storm waves (especially in shallow lagoonal waters) and their three-dimensional nature, the likelihood of multiple spans being struck simultaneously by a wave is also very low. As such, horizontal and uplift forces are not applied simultaneously across all spans of the 110-meter bridge module.

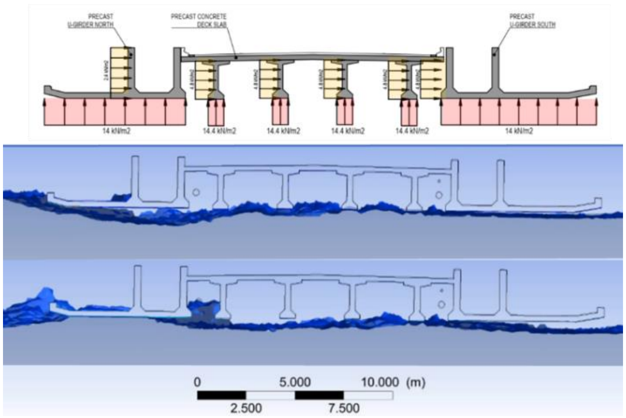

Figure 4. Hydrodynamic forces on the bridge underdeck calculated after Cuomo et al. (2007) for the 1 in 100 years event, and snapshots of wave motion underneath the bridge simulated with ANSYS.

STRUCTURAL DESIGN

Analysis of wave loads on the bridge structure demonstrated that the selection of a concrete deck structure with integral piers is the most suitable option; less bearings are required and at the integral piers, uplift forces on deck are directly tranfered to the piers. Bored piles selected for pier foundation can undertake reliablt the uplift forces.

Following a modularisation approach the 1.100 m long bridg has been split on 10 nos, 3 span modules 110 m long each presented in Figure 5. At both ends of the modules, where expansion joints are located, bearings are required. At these support locations uplift forces exceed the self-weight, necessitating introduction of anti-lift devices. One option considered was elastomeric bearings with anti-lift restrainers and anchors. However, procurement challenges and logistics suggested the need for a more versatile solution to avoid delays of product delivery and improve maintainability. As a result, separate anti-lift devices were designed and fabricated, allowing the use of standard elastomeric bearings. This approach simplifies bearing replacement and eliminates the need to replace the restrainer. Both options considered are presented in Figure 6.

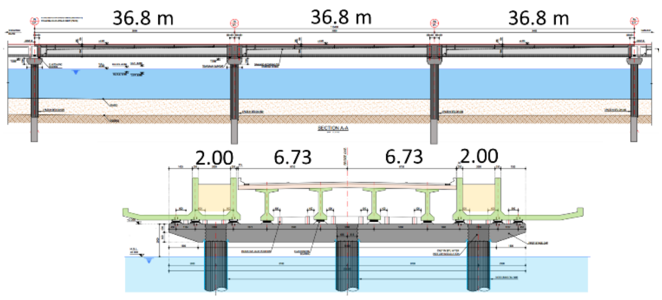

Figure 5. Typical 3-span module and cross section of the integral bridge.

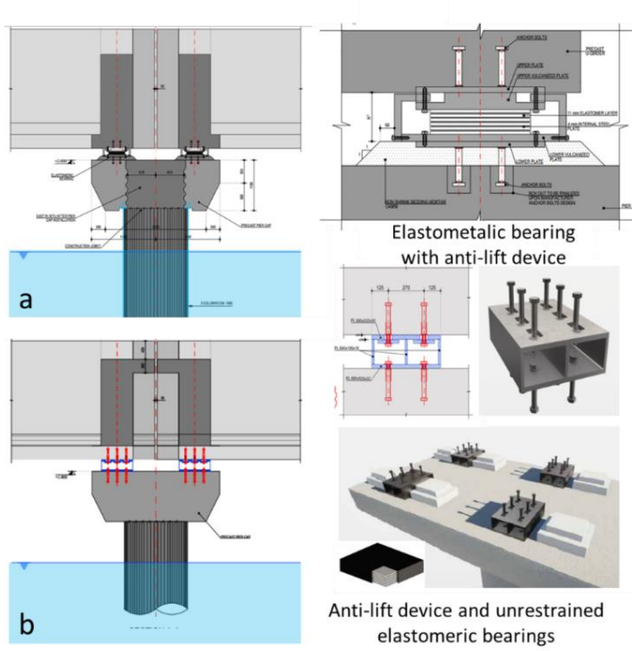

Figure 6. Elastomeric bearing with anti-lift device and unrestrained elastomeric bearings with restraining devices at expansion joint piers.

ACKNOWLEDGEMENTS

The contribution of Stergios Dimitrakis, formerly Technical Office Manager with Archirodon NV, who developed the numerical model by ANSYS (Figure 4) is greatly acknowledged. Structural design of the Bridge by Kalliergos O.T.M. S.A.

REFERENCES

AASHTO, 2008. Guide Specifications for Bridges Vulnerable to Coastal Storms, 1st Edition.

Cuomo G., Tirindelli M., & Allsop W. (2007). Wave-in-deck loads on exposed jetties, *Coastal Eng.* 54, 657–679.

Morison, J.R., O'Brien, M.P., Johnson, J.W., & Schaaf, S.A. (1950). The Force Exerted by Surface Waves on Piles. *J. Pet. Technol.* 2(5), 149–154.

Challenges in the Construction of a Submarine Pipeline: Experience from a Metal Cooling Pipeline in Rhodes-Soroni Area.

Roukounis C.N.[1,2,*], Sahinoglou I.[2]

[1] School of Rural, Surveying and Geoinformatics Engineering, National Technical University of Athens, 9 Heroon Polytechniou St., 15780 Zographou, Athens, Greece
[2] Sachinoglou Techniki IKE, 36 Agias Eleousis St., 15126 Amarousion, Athens, Greece

*corresponding author:
e-mail: babisrouk@gmail.com

INTRODUCTION

Submarine pipeline construction faces challenges such as environmental hazards, seabed instability, and corrosion. Recent studies (e.g. Guo et al. 2014; Dong et al. 2024) highlight the impact of marine and geotechnical conditions on pipeline integrity, as well as the effects of construction quality (Mehrafrooz et al. 2017). This publication concerns of the problems that arise during the construction of a submarine pipeline. An example of such a pipeline is provided for the metal cooling pipeline at the PPC installation in Rhodes - Soroni area.

CONSTRUCTION METHODOLOGY

The methodology for constructing a submarine pipeline is:

- Construction of the pipeline sections in the onshore area of the installation
- Transport of the sections to the coastal area
- Laying of the sections
- Transport of the sections to their location in sea
- Connection of the pipeline with the water inlet well inside the installation
- Installation of end-of-pipe indicators

CHALLENGES DURING THE CONSTRUCTION

The problems encountered during the construction and installation of the submarine pipeline are usually:

1. The construction of large sections of the pipeline by connecting small sections is not easy task in the onshore area since there must be a flat and large surface where the connection of the initial pieces of metal pipe, usually 12 m long, is made.

2. The transport of the 36 m pieces that are usually constructed is difficult to transport by crane and requires two excavators or two loaders or a combination of these to be transported to the their coastal location.

3. The laying of the pipeline sections must be done with care and they must be closed at both ends so that they float during transport.

4. In the onshore section and when they are laid in the relevant channel, they must not be filled with air because there is a possibility of sudden buoyancy of the pipeline, sudden entry of water into the pipeline that is transported into the connection shaft with the installation and possible drowning of the workers in the shaft.

5. The pipeline sections should be gradually filled with water so that they sink slowly because their sudden immersion results in damage to the ends of the pipeline and difficulty in connecting it to the remaining sections.

6. They should always be located within the channel so as not to prevent safe anchoring in the area where they are placed.

7. There should be a wave that does not exceed 40 cm height during the laying of the pipelines so that the pipeline is submerged without large movements of the boom of the floating crane.

8. There should be a buoy at the end of the pipe so that the position of the end is visible, which is always above the surface of the bottom.

9. The connection of the pieces on site should be done with care and the holes through which the screws pass should be oval in shape so that there is no inability to connect the successive pieces.

10. The concrete anchors that retain the pipeline on the bottom should be based on solid ground and not burden the pipeline.

ADDRESSING THE CHALLENGES

The above 10 main problems must be faced and solved by the pipeline manufacturer during its construction and placement on site. Usually these pipelines are constructed in areas that are not protected from wave action and for this reason there are delays due to weather conditions.

During the construction of a 2.0 diameter metal submarine pipeline in the Soroni area of Rhodes, all of the above problems were faced despite the fact that in remote areas of such projects there is no mechanical support for the equipment used for the construction of the project.

Figure 1. The transport of a section in situ for immersion

REFERENCES

Guo, B., Song, S., Ghalambor, A., & Lin T. (2014). Offshore Pipelines: Design, Installation, and Maintenance. 2nd Edition, Gulf Professional Publishing.

Mehrafrooz, B., Edalat, P., & Dyanati, M. (2017) Investigation on the Effects of Uncertainties in Construction Quality on the Bursting Capacity of Submarine Pipelines. *IJCOE* 2(3), 51–56

Dong, Y., Dengfeng, F., & Feng, X. (2024). Engineering Properties of Marine Soils and Offshore Foundations. *J. Mar. Sci. Eng.* 12(11), 2077.

Runway 10-28 of the International Airport of Thessaloniki «MAKEDONIA»: The Implementation of an Extensive Embankment in the Sea

Papaoikonomou M.[1,*], Efstathopoulou I.[1], and Samartzis Th.[2]

[1] Ministry of Infrastructure & Transport, 31 Giannitson Str., Thessaloniki, Greece
[2] AVAX-AKTOR, Greece

*corresponding author:
e-mail: papaoikmar@gmail.com

INTRODUCTION

The extension of runway 10-28 of the International Airport of Thessaloniki by 1000 m to the sea is a complex, state of the art, technical project, comprising the construction of an 5.500.000 m^3 embankment with its perimetric armouring, ground improvement techniques, measures of inducing / accelerating settlement.

The scope of this paper is firstly to introduce a detailed technical description of the embankment works, according to the approved technical study and tender documents, and then to analyze the specific issues caused by the fact that the infill material was transported by sea, subsequently building the embankment with equipment from the sea, managing such a volume of construction material, and finally comment on the critical design parameter for the operation of the project i.e. attainment of primary consolidation and stabilization of the settlement rate.

PROJECT PROFILE – TECHNICAL CHARACTERISTICS

The width of the runway is 60 m (including shoulders), while the width of the taxiway is 44 m (including shoulders). The distance between runway and taxiway centreline is 182,5 m.

The structure was implemented by:
Land and sea bottom excavation: total volume 1.540.000 m^3.
Sand-gravel embankment, 1063 m on the longest side, 906 m average length and width of 400÷450 m.
Total sand-gravel volume (taken into account material loss due to settlement): 5.500.000 m^3.
Perimetric armouring of the embankment constituted of a concrete wall seated on rockfill. Total length: 2262 m.
Ground improvement: installation of vertical plastic drains where sea depth exceeds 5.0 m (at a distance of 350 m from shore).
The measures to induce / accelerate settlement comprised implemention of deep vibroflotation, dynamic compaction and surcharging, using the building materials to erect a 5 m high temporary embankment in segments of 100-200 m. The criterion for surcharge removal was the stabilization of the settlement rate at less than 3 mm/month.

The structure extends to a sea depth of 14 m. The underground consists of sand to a depth of 15-30 m, at a distance up to 350 m from shore, changing to compressible clay with enclaves of sand at random depths, further than 350 m from shore.

The intent of ground improvement and means of accelerating settlemet was to induce the greatest part of the expected settlement during construction and diminish the long term differential settlement (secondary and creep deformation) to the internationally accepted (ICAO) standard of 4cm per 50m of runway/taxiway.

The materials utilized for construction were natural sand-gravel for the main embankment, sand as a drainage layer, rockfill and natural and precast concrete blocks for the perimetric armouring. The progress of the settlement and the general behavior of the construction was monitored via the installation of: Vibrating Wire Piezometers, either driven in place or in boreholes, Casagrande Piezometers, Settlement Plates on the sea bottom surface, Magnetic Extensiometers, Inclinometers, Surface Settlement Markers.

CONSTRUCTION MATERIAL MANAGEMENT

Transportation of sand-gravel by sea

The natural sand-gravel used in the main embankment came from the licensed natural quarry of Litohoro Pieria, 120 km away from the construction site. Because of the long distance, the sand-gravel was transported on site by sea, subsequently building the embankment from the sea, i.e. sand-gravel was transported on site by split barges, directly discharged and laid to a depth of -3.50 m, while the remaining quantity from -3.50 to the final layers was dragged ashore by dragline and transported to position by tracks.

Handling the incoming sand-gravel from the sea, as well as the deposition of sediment into the excavation trench, caused local selective accumulation of fine particles, which formed enclaves of fine particles (silt, sand, particle size <0,075 mm) on the bottom as well as in-between the body of the embankment. The accumulation of fine particles at the runway and taxiway bearing embankments prohibited the achievement of the required compaction degree.

To resolve the resultant situation :
- The sand-gravel handling positions were moved outside the perimeter of the project,
- The fine particle buildup before the sand-gravel handling positions was removed and fresh, sound material was brought in place. Volume of accumulated material removed and replaced: 220.000 m^3.
- The perimeter of the project was sealed, implementing the rockfill core and required surcharging of the armouring at full length, before settlement was stabilized in already surcharged segments and surcharge load could be moved onwards.
- To achieve the required degree of compaction, problematic areas were re-treated by a course of dynamic compaction, while surcharging also had remarkable results.

- Evaluation of the corrective measures was supported by drilling investigative boreholes when necessary.
- The performance of the embankment on seismic as well as operational loading was investigated and proved satisfactory, the extent of the enclaves of fine particles not compromising the safety of the structure.

Gross settlement

The gross settlement recorded by the settlement plates ranged from 0.60 m to 2.5 m, while the settlement derived from surface markers readings ranged from 5 cm to 67 cm. The overland section of the embankment exhibited 5 cm to 19 cm settlement, as derived from the installed surface markers.

The greatest part of total settlement, accounting to 70% to 85%, took place during construction, whereas the settlement induced by the surharging accounts for a small portion of total settlement progressing at a very slow pace.

Surcharging duration

The duration of the surcharge loading was estrimated by the geotechnical study at least 3 months per segment of application, 100-200 m long, and 39 months in total. The actual stay, though, proved dramatically longer: placement and actual overall stay of the surcharge lasted from September 2009 until 02.05.2028, i.e. 103.4 months or 8.5 years.

The surcharge was also applied at much longer segments, i.e. at the runway/taxiway embankment the surcharge length varied from 280 m to 1010 m, averaging 528 m per 3/month periods, while at the perimetric armouring the surcharge length varied from 130 m to 1220 m, averaging 680.5 m per 3month periods.

The surcharge lengths were increased to the extent possible, depending on the rate of the incoming sand-gravel from the quarry and the material equilibrium, so as no excess (redundant) quantity of sand-gravel was transported. To this intent, soil excavated from an adjacent construction site was utilised in a segment of the taxiway. Additionally, at the deeper segment of the runway, approximately 260 m long, the height of the surcharge was raised to 8 m, in order to expedite the rate of settlement.

On the other hand, excess rockfill 0,5-50 kg was brought on site to materialize the surcharge of the perimetric armouring at full length. The excess rockfill, amounting to 75.000 m^3, was utilised in the construction of the embankment.

By all the afore mentioned measures, the duration of surcharging:

a. Ranged between 7.7 and 14 months at the runway and taxiway embankments of the land and shallow sea sections, rising to 38 months at the deepest sea section, while the mean surcharge duration was 17.8 months.

b. Ranged between 7 and 12.5 months at the shallow sections of the perimetric armouring and between 36 and 60 months at the deepest sea section, while the mean surcharge duration was 30.9 months.

Monthly rate of settlement / Removal of surcharge

Stabilization of the rate of settlement at the required 3mm/month, in order to remove surcharge and proceed to pavement layers, proved in practice very challenging to achieve (Figure 1):

- Very slow progress: the rate stayed below 10 mm/month for up to 16 months before the upper limit of 3 mm/month was reached.
- Influence of ongoing works at adjacent areas: because of the height and magnitude of the embankments, ongoing works had an immediate effect on the surcharged areas comprising even negative figures (heave).

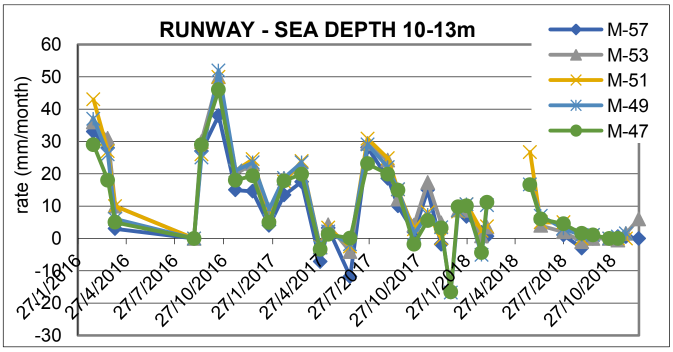

Figure 1. Fluctuation of monthly settlement rate.

To expedite soil consolidation at the deepest, most critical (because of the sea depth) segment of the runway, the surcharge load was increased by an additional 3m high sand-gravel load, in conjunction with modifying the design criterion for removing the surcharge to 8mm/month for 4 consecutive weekly measurements and provided that pore-water pressure stabilized for at least two months.

The monitoring of settlement continued during paving works using surface markers and finally asphalt layers were implemented only when:

- The treated area was not affected by surcharge removals at adjacent segments and exhibited stabilization of the settlement rate.
- The settlement rate indicated by all surface markers in the treated area was below the required standard of 3mm/month.
- The unbound aggregate layers of adjacent areas had been completed and properly compacted.

ACKNOWLEDGEMENTS

The authors would like to acknowledge the contribution of the personnel of the General Directorate of Transportation Infrastructure, the Technical Consultants and the Contractor, AVAX-AKTOR, to the realization of this project.

REFERENCES

Sotiropoulos and Associates S.A., Geotechnical Consultant to the contractor, Technical Reports.

Triton Consulting Engineers, Technical Consultant to the Ministry of Infrastructure & Transport, Technical Reports.

Audit Findings Evaluation of Coastal Engineering Studies

Gouloumis S.[1,*], Panopoulou E.[1], Kouros K.[1], Oikonomou V.[2] , Araviadis R.V.[3] and Michas S.[1]

[1] HYDROEX S.A., Evoias 3, GR 15125 Marousi, Athens, Greece
[2] Civil Engineer, Deputy Head of the Port Infrastructure Directorate and Head of the Studies and Planning Department, Greece
[3] Civil Engineer, employee of the P.I.D., Supervisor of the Technical Consultant Contract for review of coastal engineering studies. Greece

*corresponding author:
e-mail: spirosgls@gmail.com

INTRODUCTION

Based on the current legislation (Law 4607/2019 (A'65) article 33), the Directorate of Port Infrastructures, of SGMAP, of the Ministry of Maritime Affairs & Insular Policy is responsible for reviewing and approving all coastal engineering studies that have been conducted nationwide, as well as the examination of requests for exemption from the relevant obligation. To help with this duty and to effectively handle the high number of requests involved, as well as the significant technical and scientific needs of the inspection process, the agency has hired the company "Hydroexigiantiki S.A." as a technical consultant between September 2021 and December 2024.

About 250 applications, along with the studies and the accompanying documentation, have been reviewed during the review process and pertinent audit results have been developed. The 199 cases that were initially examined concerning the possible effects of projects on coasts that would potentially have a coastal impact and their treatment by the researchers, provide important information on the coastal problems over Greece and the proposed way of dealing with them.

DATA INVESTIGATION

The characteristics of the reviews have been examined and valuable conclusions made. The audit findings were initially grouped into those relating to the impact of port projects and those relating to purely coastal engineering problems.

Also, two more categories have been grouped: files submitted for the approval of coastal engineering studies or to be exempted of conducting a coastal engineering study (Exemptions). The 199 cases initially examined, can be categorized to 68 (34.2%) considering coastal engineering studies, while 131 (65.8%) requested to be exempted from conducting a coastal engineering study. 50 of the cases examined (25.1%) were requested to be resubmitted due to lack of data.

The total of 249 reports on coastal engineering studies and exemption requests reviewed, 166 (66.6%) were positively assessed, while 83 (33.3%) had lack of data, in approximately the same proportion of coastal engineering studies and exemption requests. While 27 applications (10.8%) pertain to coastal pipeline projects, a sizable portion of 53 applications (21.3%) are related to exemption dossiers for limited interventions considering projects supporting fish farming facilities. These studies have a 57.9% approval rate.

PROJECTS PROPOSED UNDER THE CONTEXT OF COASTAL ENGINEERING STUDIES

Classifying the coastal engineering studies in relation to the constructions projects they consider, 4 categories emerged: those proposing the construction of a coastal engineering/port project, studies aiming to the repair/development of an existing project, studies to address coastal erosion problems and finally studies whose sole purpose is the licensing of an existing installation.

KEY CONLUSIONS

The following conclusions have been drawn to date:

- The rate of inspection and exemption applications is particularly high, which is in line with the significant development activities in the construction of projects of any kind in the country in recent years
- It has been generally noted that in most cases, high-quality coastal engineering studies were provided, , including pertinent study and evaluation of the findings, as well as mathematical models and sufficient analyses.
- Although the obligation to carry out an audit does not apply to the technical part of the projects for which the coastal engineering studies are conducted, the audit procedure always requires that the proposed projects are examined in parallel, otherwise it is not possible to assess the results properly. In its replies, the Ministry, in addition to the decision to approve or reject the projects, sets out its (non-binding) views on the proposed projects, to inform and guide the project managers and supervisors.
- Some of the studies examined propose coastal sediment replacement projects of significant quantities, often intended to be repeated annually, not always feasible and lacking a thorough examination of the technical, economic and environmental implications.
- Regarding the requests for exemption from coastal engineering studies, the necessary conditions are not always met, or the required justification is not always provided. The Service has drawn up an information memorandum setting out the minimum supporting documents required for the exemption requests.

FUTURE INVESTIGATION

Data analysis is continuing (as well as the submission of studies and requests). The data are going to be visualized using Geographical Information Systems to easy the analysis of the recorded coastal engineering problems on the Greek coast and their treatment by the planners.

ACKNOWLEDGEMENTS
We would like to express our deep appreciation to the Ministry of Maritime Affairs & Insular Policy and the staff involved, regarding the high level of our collaboration in the audit procedures.

REFERENCES
"MINIMUM DELIVERABLES FOR PORT PROJECT STUDIES", Hellenic Government Gazette B 1047/2019.

Design and Implementation of a Customisable GNSS Based Wave Buoy

Vozza G.[1,*], Ligorio F.[1], Scala A.[1], Tomassetti E.[1], De Santis F.[2] and Cuomo G.[1]

[1] SPERI Società di Ingegneria e di Architettura SpA , Via Lungotevere delle Navi, 19, Rome, Italy
[2] EFFEDI Srl, Viale della Vittoria 104, 04019 Terracina, Latina, Italy

*corresponding author:
e-mail: gvozza@sperispa.com

Abstract
Accurate and reliable field data remain essential to enable deeper understanding of ocean dynamics. As part of the ongoing Sea Smart Eye Project, funded by Regione Puglia, we have developed a cost-effective, easily deployable wave monitoring systems to enable real time wave monitoring, and provide useful and robust metocean data to assimilate within our modelling system (Scala et al. 2024) leading to accurate modelling and forecasting of weather conditions, informing safe maritime operations and supporting the Blue Economy. Bearing this in mind, we designed a customisable wave buoy system based on state of the art GNSS technology. Our primary focus was on creating a low-cost solution that is lightweight yet robust, compact, and easy to produce and transport, making it ideal for rapid deployment and use in various marine environments. This buoy system provides high-resolution, real-time metocean data to aid in decision-making processes for the stakeholders of the Blue Economy. The harnessed field data are being integrated into our in-house numerical modelling system, based on the OpenTELEMAC suite, to further refine its accuracy in simulating metocean processes. This approach combines innovative hardware design with advanced numerical modelling, ensuring reliable and precise insights into local wave conditions. This paper describes the main characteristics of the buoy, gives some insights into its development and testing (both static and dynamic), and in situ performances.

GNSS BUOYS
Different technologies are available and GNSS based systems offer low-cost and easy to implement equipment thanks to satellite technology available nowadays. The first wave buoys developed were equipped with accelerometer sensors (Collins et al. 2024, Barber, 1946; Longuet-Higgins, 1946; Marks and Tuckerman, 1963; and Longuet-Higgins, 1963), later improved with Inertial Measurement Units (IMUs). The introduction of GNSS technology enabled the development of buoys equipped with GNSS (GNSS Buoys) which, as noted by Herbers et al. (2012), offer advantages, such as: no mechanical parts, determination of velocity in a fixed reference system, elimination of calibration, reduction in size and cost. The recent consumer market introduction of high-performance and affordable GNSS receivers could allow the creation of GNSS wave buoys that can be customised to specific user requirements.

THE PROTOTYPE
The main components of a wave buoy system typically include the sensor, the payload, and the platform (World Meteorological Organization, 2018).

A critical and most influential step in the development of a GNSS-based wave buoy is the selection and definition of the data collection sensor, as this has the greatest impact on the quality of the collected data. Consequently, this study primarily focuses on the analysis of the GNSS module used for data collection, hereafter GNSS SPERI for simplicity.

The GNSS SPERI consists of two key components, the GNSS receiver and the antenna. The GNSS receiver is a multiple bands and multi-constellation, operating with an acquisition rate ranging from 1 to 10 Hz and is paired with a multi-band antenna to ensure robust signal reception.

The prototype SPERI buoy platform is composed of two primary structural elements: the lower hemisphere, which houses the battery and remains almost fully submerged and the top structure, which accommodates the photovoltaic modules, the sensor, and a data management module. Figure 1 illustrates the architecture of the data collection system, comprising the sensor and payload.

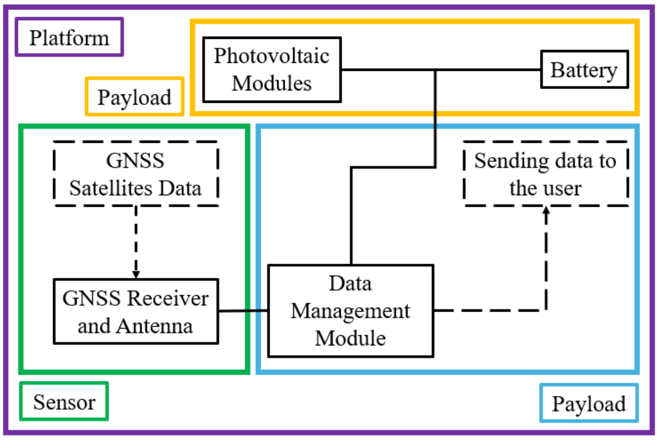

Figure 1. System architecture of the data collection system.

COMPARISON WITH A COMMERCIAL SYSTEM
The comparison in performance with an existing commercial product, the Spotter buoy (Sofar Ocean Technologies, Inc., San Francisco, CA, USA), was carried out by tests comprising data acquisition, data processing, and final data analysis.

Data acquisition of SPERI buoy and the Spotter buoy was conducted in a static test, a dynamic test under laboratory and dry conditions, and an operational test in real sea conditions. The primary purpose of the static test was to compare the positional precision of the GNSS SPERI against the Spotter buoy by means of simultaneous position acquisition from both devices in a 120 minutes static mode, under open-sky conditions. The accuracy and precision of the two buoys was compared in the dynamic test, where the ability in tracking and replicate a complex three-dimensional geometric structure with known dimensions (approximately 3 m^3) was tested. Also, the SPERI buoy was tested in open waters to measure real-sea states conditions, comparing the performance with the Spotter buoy. The primary goal of this test was to compare the data processing pipeline implemented in the SPERI, aimed at reducing GNSS positioning errors (based on Harigae et al., 2005, and Joodaki et al., 2013), and assess computational processing for the generation of wave parameters, including significant spectral wave height, H_{m0}, peak wave period, T_p, mean wave period, T_m, and mean wave direction, DIR.

Geographic coordinates and filtered 3D displacements were obtained from the Spotter buoy, while raw GNSS data were collected from the SPERI buoy. In the data analysis phase, the performance of the two buoys was compared in terms of accuracy and precision. The results indicate that the GNSS module integrated into the prototype buoy delivers performance comparable to the Spotter buoy. The Spotter buoy demonstrated an excellent three-dimensional displacement filtering. However, the customised prototype SPERI buoy, with its access to raw GNSS data in RINEX format, offers enhanced flexibility for GNSS data processing, enabling improved GNSS positioning. Figure 2 illustrates the tests campaign pipeline.

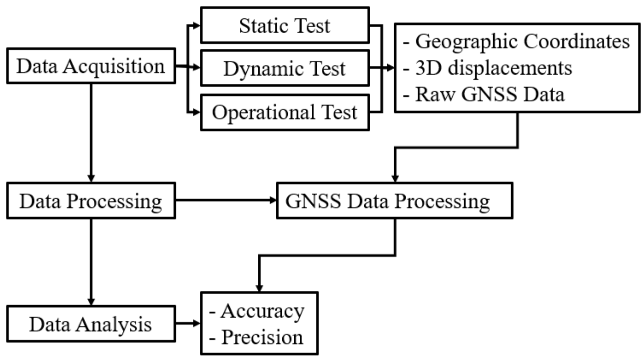

Figure 2. Tests campaign pipeline.

INITIAL CONCLUSIONS AND FURTHER WORK

This work is enabling the development and verification of a new low-costs easy to customise device based on GNSS technology, to support the consumer market for maritime and coastal engineering applications, understanding the main differences in performance with established wave buoy technologies, providing an important step for creating customised wave buoys and buoy clusters, and fostering interesting ideas for integrating custom and commercial buoys into complex survey systems. Custom buoys should be considered as a complementary technology to commercial buoys and those deployed in national wave monitoring systems, facilitating the integration of diverse data types to achieve a more comprehensible sea state measuring system.

ACKNOWLEDGEMENTS

This research is being carried out as part of the SeaSmartEye Project, funded by Regione Puglia within the “Aiuti ai programmi Integrati promossi da PICCOLE IMPRESE” - PIA (ART.27) framework. The authors wish to thank the colleagues and friends at SPERI SpA who have contributed to this work.

REFERENCES

Barber, N.F. (1946). Measurements of sea conditions by the motion of a floating buoy. Admiralty Research Laboratory, Note ARL/10, 3, 40.

Collins, C. O., Dickhudt, P., Thomson, J., de Paolo, T., Otero, M., Merrifield, S., Terrill, E., Schonau, M., Braasch, L., Paluszkiewicz, T., & Centurioni, L. (2024). Performance of moored GPS wave buoys. *Coastal Eng. J.* 66(1), 17–43.

Harigae, M., Yamaguchi, I., Kasai, T., Igawa, H., Nakanishi, H., Murayama, T., Iwanaka, Y., & Suko, H. (2005). Abreast of the waves: Open-sea sensor to measure height and direction. GPS World, 16(5).

Herbers, T.H.C., Jessen, P.F., Janssen, T.T., Colbert, D.B., & MacMahan, J.H. (2012). Observing ocean surface waves with GPS-tracked buoys. *J. Atmos. Ocean. Tech.* 29(7), 944–959.

Joodaki, G., Nahavandchi, H., & Cheng, K. (2013). Ocean wave measurement using GPS buoys. *J. Geod. Sci.* 3(3), 163–172.

Longuet-Higgins, M.S. (1946). Measurement of sea conditions by the motion of a floating buoy. Detection of predominant groups of swell, Admiralty Research Lab. Report, 103, N5.

Longuet-Higgins, M.S., Cartwright, D.E., & Smith, N.D. (1963). Observation of the directional spectrum of sea waves using the motions of a floating buoy, Ocean Wave Spectra, Prentice-Hall, New Jersey, 111–132.

Marks, W., & Tuckerman, R.G. (1963). A telemetering accelerometer wave buoy. Proc. International Conference on Ocean Wave Spectra (p. 281).

Scala, A., Le Goff, J., Ingelaere, C., De Cristofano, V., Lupoi, G., & Cuomo, G. (2024). Auto-calibration method for a Mediterranean regional wind wave model. Proc. Telemac User Conference, Chambéry, France.

World Meteorological Organization. (2018). Guide to wave analysis and forecasting. WMO-No. 702.

Integrated Modelling of Watershed-Coast System Morphodynamics in a Changing Climate: Considerations on the Use of Satellite Data

Samaras A.G.[1,*] and Nones, M.[2]

[1] Department of Civil Engineering, Democritus University of Thrace, University Campus - Kimmeria, 67100 Xanthi, Greece
[2] Department of Hydrology and Hydrodynamics, Institute of Geophysics, Polish Academy of Sciences, 01452, Warsaw, Poland

*corresponding author:
e-mail: achsamar@civil.duth.gr

INTRODUCTION

Watershed-Coast System (WACS), a term coined by Samaras & Koutitas (2014), refers to the entities consisting of watersheds of rivers/natural streams and the areas adjacent to their outlets, where sediment delivery from the upstream is critical for the balance of the coastal sediment budget, thus playing a key role in the evolution of coastal morphology. Samaras (2023) presented a working scheme for the integrated modelling of Watershed-Coast System morpho-dynamics in a changing climate and proposed a methodo-logical framework for adapting integrated modelling approaches for management and engineering purposes.

The present work investigates the role of satellite data within the aforementioned framework. The primary focus lies on their use for morphodynamics modelling in water-sheds and coasts, but it also extends to aspects of the general effort towards informed decision-making for resilient WACS in a changing climate.

THE METHODOLOGICAL FRAMEWORK

Figure 1 presents the methodological framework for the integrated modelling of WACS morphodynamics for man-agement and engineering (Samaras, 2023). Based on the four fundamental components: (A) climate change, (B) watershed dynamics, (C) coastal dynamics, and (D) integration of the Watershed-Coast System, it is essential to highlight the challenge posed by introducing the right part of this flowchart, that is: (a) the consideration of projected climate change-induced changes in management practices and engineering works in both fields (terrestrial, coastal) when defining future scenarios, and (b) the adaptability to methods for addressing ecological/socio-economic implications and stakeholders engagement.

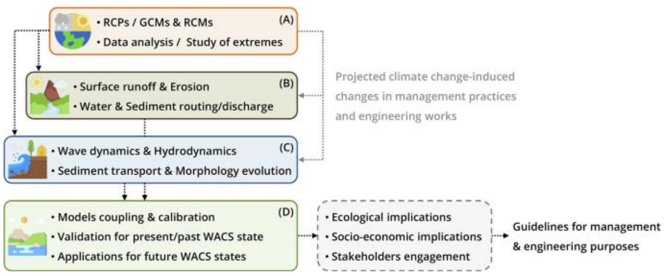

Figure 1. Methodological framework for the integrated modelling of WACS morphodynamics in a changing climate for management and engineering purposes (Samaras, 2023).

Samaras (2023) also theorized on the path towards informed decision-making for building resilient Watershed-Coast Systems in a changing climate through the integrated modelling of their morphodynamics. Systematizing this path to its essential aspects facilitates the effort of this work as well, which aims to first organise and group available methods and tools for each task, then analyse and evaluate them, and eventually propose a structured approach for the use of satellite data within this context. Figure 2 presents connections to the use of satellite information for the essential aspects presented by Samaras (2023).

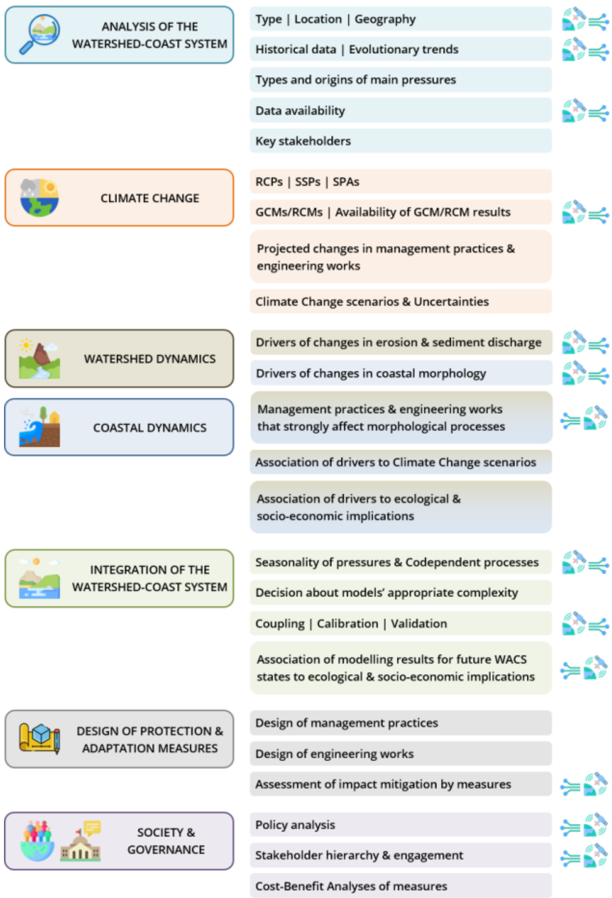

Figure 2. Essential aspects towards integrated modelling of WACS morphodynamics in a changing climate and informed decision-making for enhancing their resilience – Connections to the use of satellite data (outwards connections denote use for analysis/modelling, inwards connections denote use for assessment; adapted from Figure 7 of Samaras, 2023).

THE USE OF SATELLITE DATA TOWARDS RESILENT WATERSHED-COAST SYSTEMS

The study of climate dynamics is dependent on the use of satellite data for analysis of trends in associated variables and calibration/validation of climate models (Fu & Wu, 2024; Reiners et al., 2023), thus continuously improving our understanding of climate change (Tarpley et al., 2019). Regarding watershed dynamics, satellite data are used for the acquisition/analysis of weather data (Mendelsohn et al., 2007), relief and soil data (Chen et al., 2012; Li et al., 2024), land cover/use data (Gu & Zeng, 2024) and inland hydro-morphology (Biancamaria et al., 2016; Nones et al., 2024). Regarding coastal dynamics, satellite data are used for the acquisition/analysis of weather data (Pleskachevsky et al., 2016; Young & Ribal, 2019), various types of marine data (Ablain et al., 2017; Timmermans et al., 2020), as well as coastal morphology (Bergsma et al., 2021; Vitousek et al., 2023). It is noted that accurate information on the evolution of shoreline positions and/or bathymetry/topography in transitional areas is quintessential for the integrated model-ling of WACS, as those are the most robust data for the calibration and validation of morphodynamics models, with extension to the evaluation of the watershed-costal coupling approach used (see Samaras, 2023).

Beyond methods and tools that relate to the core of morphodynamics modelling, though, satellite data can also contribute to the assessment of the implications of modelling results, as well as to aspects of what is referred to as “Society & Governance” (see Figure 2 and Samaras, 2023). Satellite data can be used to: (a) quantify and analyse the socio-economic consequences of changes in WACS systems by tracking population exposure, economic losses, and impacts on livelihoods (Hassan & Rahmat, 2016); (b) support policy analysis and reshaping through environmental change monitoring, tracking compliance with regulations, and evaluating the impact of policy interventions (De Leeuw et al, 2010); and (c) enhance stakeholders engagement and communication by providing tangible information in order to raise awareness and facilitate participatory decision making (Agnoli et al., 2023; Zuniga-Teran et al., 2022). All in all, the multi-dimensional use of satellite data helps bridging the gaps between Science, Society and Governance, making resilience planning more democratic, transparent, inclusive, and evidence-based.

CONCLUSIONS

This works constitutes the first step towards a structured approach to the use of satellite data for the modelling of the morphodynamics in Watershed-Coast Systems, as well as for building their resilience through informed decision-making. Preliminary analysis identifies key aspects to this end, and aspires to eventually provide specific pathways through which natural scientists, engineers and policymakers could organize the study of such systems in a changing climate.

REFERENCES

Ablain, M., et al. (2017). Satellite Altimetry-Based Sea Level at Global and Regional Scales. *Surv. Geophys.* 38(1), 7–31.

Agnoli, L., et al. (2023). Perspectives on user engagement of satellite Earth observation for water quality management. *Technol. Forecast. Soc. Change* 189, 122357.

Bergsma, E.W., et al. (2021). Coastal morphology from space: A showcase of monitoring the topography-bathymetry continuum. *Remote Sens. Environ.* 261, 112469.

Biancamaria, S., Lettenmaier, D.P., & Pavelsky, T.M. (2016). The SWOT mission and its capabilities for land hydrology. In: Remote sensing and water resources. Cham: Springer International Publishing.

Chen, S., Liu, Y., & Wen, Z. (2012). Satellite retrieval of soil moisture: An overview. *Adv. Earth Sci.* 27(11), 1192.

De Leeuw, J., et al. (2010). The Function of Remote Sensing in Support of Environmental Policy. *Remote Sens.* 2(7), 1731–1750.

Fu, Y., & Wu, Q. (2024). Recent Emerging Shifts in Precipitation Intensity and Frequency in the Global Tropics Observed by Satellite Precipitation Data Sets. *Geophys. Res. Lett.* 51(15), e2023GL107916.

Gu, Z., & Zeng, M. (2024). The use of artificial intelligence and satellite remote sensing in land cover change detection: Review and perspectives. *Sustainability* 16(1), 274.

Hassan, M.I., & Rahmat, N.H. (2016). The Effect of Coastline Changes to Local Community’s Social-Economic. *Int. Arch. Photogramm. Remote Sens. Spatial Inf. Sci.* XLII-4/W1, 25–36.

Li, P., Zhang, Y., Liang, C., Wang, H., & Li, Z. (2024). High spatiotemporal resolution river networks mapping on catchment scale using satellite remote sensing imagery and DEM data. *Geophys. Res. Lett.* 51(6), e2023GL107956.

Mendelsohn, R., Kurukulasuriya, P., Basist, A., Kogan, F., & Williams, C. (2007). Climate analysis with satellite versus weather station data. *Clim. Change* 81(1), 71–83.

Nones, M., Guerrero, M., Schippa, L., & Cavalieri, I. (2024). Remote sensing assessment of anthropogenic and climate variation effects on river channel morphology and vegetation: Impact of dry periods on a European piedmont river. *Earth Surf. Process. Landf.* 49(5), 1632–1652.

Pleskachevsky, A.L., Rosenthal, W., & Lehrer, S. (2016). Meteo-marine parameters for highly variable environment in coastal regions from satellite radar images. *ISPRS J. Photogramm. Remote Sens.* 119, 464–484.

Reiners, P., Sobrino, J., & Kuenzer, C. (2023). Satellite-Derived Land Surface Temperature Dynamics in the Context of Global Change—A Review. *Remote Sens. 15*(7), 1857.

Samaras, A.G., & Koutitas, C.G., (2014). The impact of watershed management on coastal morphology: A case study using an integrated approach and numerical modeling. *Geomorphology* 211, 52–63.

Samaras, A.G. (2023). Towards integrated modelling of Watershed-Coast System morphodynamics in a changing climate: A critical review and the path forward. *Sci. Total Environ.* 882, 163625.

Tapley, B.D., et al. (2019). Contributions of GRACE to understanding climate change. *Nat. Clim. Change* 9(5), 358–369.

Timmermans, B.W., Gommenginger, G., Dodet, G., & Bidlot, J.R. (2020). Global Wave Height Trends and Variability from New Multimission Satellite Altimeter Products, Reanalyses, and Wave Buoys. *Geophys. Res. Lett.* 47(9), e2019GL086880.

Vitousek, S., Vos, K., Splinter, K.D., Erikson, L., & Barnard, P.L. (2023). A Model Integrating Satellite-Derived Shoreline Observations for Predicting Fine-Scale Shoreline Response to Waves and Sea-Level Rise Across Large Coastal Regions. *J. Geophys. Res. Earth Surf.* 128(7), e2022JF006936.

Young, I.R., & Ribal, A. (2019). Multiplatform evaluation of global trends in wind speed and wave height. *Science* 364(6440), 548–552.

Zuniga-Teran, A.A., et al. (2022). Stakeholder participation, indicators, assessment, and decision-making: applying adaptive management at the watershed scale. *Environ. Monit. Assess.* 194(3), 156.

Tracking Shoreline Changes in Northern Peloponnese, Western Greece: A Spatiotemporal Analysis Using Satellite Remote Sensing Observations

Panousis K.[1], Riedl J.M.[1,2], Georgoutsou K.F.[1], Dimakopoulos A.[1] and Pappas C.[1,*]

[1] Department of Civil Engineering, University of Patras, Greece
[2] University of Natural Resources and Life Sciences, Vienna, Austria

*corresponding author:
e-mail: cpappas@upatras.gr

INTRODUCTION

The length of the shoreline in Greece totals more than 13'000 km, with about half of it being in the mainland (~ 6'700 km). These coastal areas host sites of environmental and cultural importance (protected zones, cultural heritage, etc.) with critical infrastructures (ports, assets, etc.) and ecosystem services (e.g., recreational activities). Earth observations and satellite remote sensing techniques allow for detailed spatiotemporal mapping of the coastal zone, including accurate and robust tracking of shoreline position and its variability in time (from seasonal to interannual time scales) and space (with openly available satellite imagery of ~10 x 10 m resolution, e.g., Vitousek et al., 2023; Vos et al., 2023).

Here, taking advantage of publicly available satellite imagery and recently developed automated workflows for data processing and extraction of shoreline features (i.e., GEE; Gorelick et al., (2017) and CoastSat; Vos et al., 2020; Vos, Harley, et al., 2019; Vos, Splinter, et al., 2019), we track the spatiotemporal dynamics of selected shorelines in Northern Peloponnese, Western Greece including sites in waterfront of the city of Patras (~ 53 km long shoreline) and in its proximity (Figure 1). The overall objective is to demonstrate the applicability of such methodologies in monitoring coastal processes and in guiding sustainable and resilient coastal engineering applications.

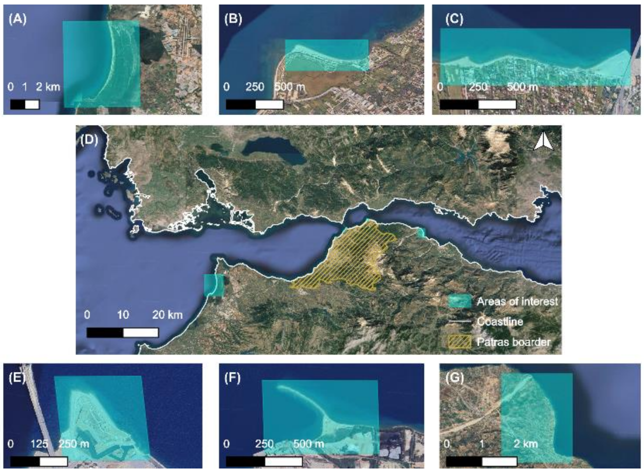

Figure 1. An overview of the study region in Northern Peloponnese and the selected shorelines for tracking their spatiotemporal changes at seasonal, annual and decadal time scales.

STUDY AREA

The study region consists of six coastal sites in the overall area of the Gulfs of Patras and Corinth in Northern Peloponnese, spanning from the West to the East as follows: (1) the embayed sandy beach of Kalogria, at the Kotychi and Strofylia National Park (Natura 2000 site; Mézard et al., 2008), (2) the waterfront of North Park of Patras 'Plage', (3) the shoreline of Rio, Patras, (4) the shoreline in the archaeological site of Rio Fortress, (5) the Cape Drepano with its unique geomorphology, and (6) the shoreline in the outlet of Foinikas river at the Gulf of Corinth (Figure 1).

METHODOLOGY

Shoreline dynamics for the period 1985 to 2024 were quantified with publicly available optical satellite imagery from the Landsat 5 (TM), Landsat 7 (EMT+) and Landsat 8 (OLI) (Tier 1) (data courtesy U.S. Geological Survey; Wulder et al., 2022) as well as the Sentinel-2 (MSI, Level-1C; Copernicus Sentinel data 2025/Sentinel Hub) satellite missions. Data pre- and post-processing, including data retrieval and shoreline extraction were performed using the CoastSat toolkit, a Python-based open-source software (Vos et al., 2020; Vos, Harley, et al., 2019; Vos, Splinter, et al., 2019). As detailed in Vos, Splinter, et al., (2019), CoastSat uses Google Earth Engine (GEE; Gorelick et al., 2017) functionalities to efficiently download analysis-ready time series of satellite imagery for selected locations that is then processed and classified using the modified Normalized Difference Water Index (mNDWI; Xu, 2006) separating pixels identified as 'water' from the ones that correspond to 'land', and used to delineate shoreline boundaries (Figure 2). The derived shoreline polygons were then further analysed to assess the spatiotemporal dynamics of the examined shorelines (Figure 3, 4).

RESULTS

Focusing on an example shoreline in the area of Patras (the waterfront of the North Park of Patras, 'Plage', see Figure 1), preliminary results demonstrate the applicability of the CoastSat algorithms to track the shoreline dynamics in the area of Western Greece. Based on the analysis of Sentinel-2 observations from 2017 to 2024, the shoreline was delineated throughout the available data archive, with approximately biweekly temporal resolution (excluding low quality imagery) and a spatial resolution of 10 x 10 m (Figure 3, 4). This analysis provided a detailed spatiotemporal quantification of shoreline dynamics in the selected location, including seasonal and interannual variability as well as spatial heterogeneity across the coastal zone (Figure 3, 4).

Automated workflows for harvesting publicly available satellite imagery, like the Python toolkit CoastSat (Vos et al., 2020; Vos, Harley, et al., 2019; Vos, Splinter, et al., 2019) deployed here, offer a robust and efficient way for looking at the coastal zone dynamics at seasonal annual and interannual time scales. Moreover, the continuously increasing Earth Observations, including finer spatial resolution and higher temporal frequency, paves the way for remotely sensed surveys of natural hazards in the coastal zone (e.g., mapping storm-induced shoreline erosion, and monitoring of coastal infrastructures). When combined with tailored field surveys (i.e., *in-situ* and aerial-based/UAV photogrammetry and lidar techniques) spatiotemporal scales, as well as knowledge gaps can be bridged, offering insides about various coastal processes towards sustainable and resilient coastal engineering applications.

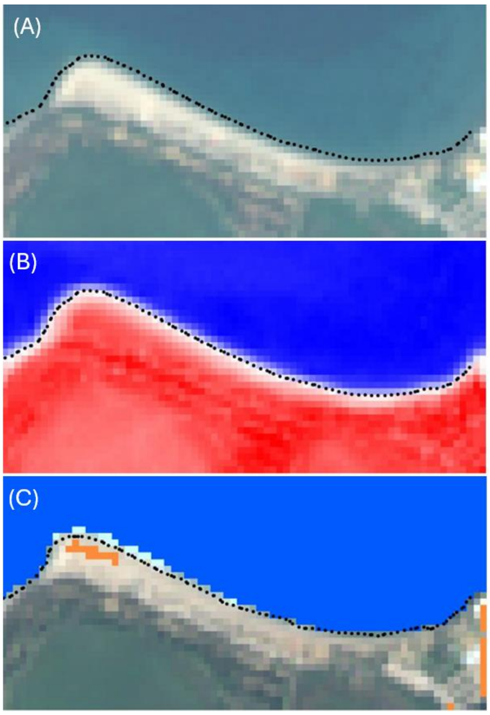

Figure 2. An overview of the CoastSat methodological workflow (Vos et al., 2020; Vos, Harley, et al., 2019; Vos, Splinter, et al., 2019) for the delineation of the shoreline at the North Park of Patras (‘Plage’, see Figure 1B), including (A) a true colour/RGB representation of the region of interest, (B) the modified Normalized Difference Water Index (mNDWI; Xu, 2006) and (C) the image classification in water (blue pixels), whitewater (pale cyan), and sand (orange). Dashed black line depicts the delineated shoreline.

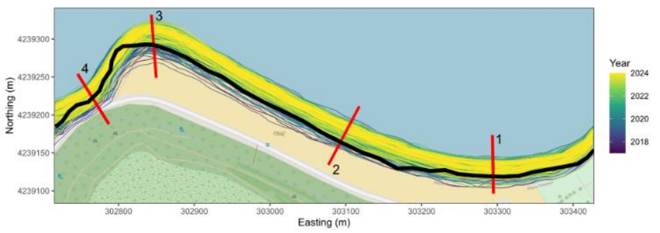

Figure 3. Shoreline dynamics in the North Park of Patras (‘Plage’; see also Figure 1B) based on the analysed Sentinel-2 observations for the period 2017 to 2024. Different coloured lines correspond to the delineated shoreline for specific dates (with a biweekly time interval), while the solid black line illustrates the reference shoreline (defined visually from a Sentinel-2 image on 28/03/2017). Four transects were selected perpendicularly to the shoreline and their locations are illustrated with solid red lines (see also Figure 4).

ACKNOWLEDGEMENTS

Landsat 5, 7, and 8 satellite imagery was made available from the U.S. Geological Survey. Sentinel-2 observations were provided by the European Space Agency. We thank the developers of CoastSat for making the python toolkit publicly available and providing user-friendly documentation and tutorials on the software as well as U.S. Geological Survey for the DSAS software and online resources.

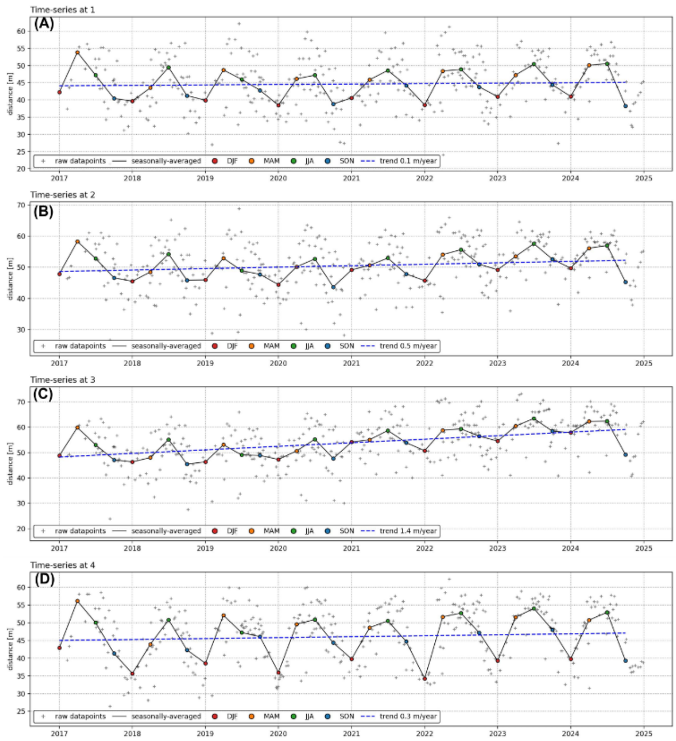

Figure 4. Time series of the shoreline dynamics across the four selected transects (see also Figure 3). Gray points correspond to the location of the derived shoreline (from 2017 to 2024 with a two-week time step), coloured points and solid black line the seasonal averages and dashed blue line the linear model fit.

REFERENCES

Gorelick, N., Hancher, M., Dixon, M. et al. (2017). Google Earth Engine: Planetary-scale geospatial analysis for everyone. *Remote Sens. Environ.* 202, 18–27.

Vitousek, S., Buscombe, D., Vos, K. et al. (2023). The future of coastal monitoring through satellite remote sensing. *Camb. Prism., Coast. Futures* 1, e10.

Vos, K., Harley, M.D., Splinter, K.D. et al. (2019). Sub-annual to multi-decadal shoreline variability from publicly available satellite imagery. *Coast. Eng.* 150, 160–174.

Vos, K., Harley, Splinter, K.D. et al. (2020). Beach Slopes from Satellite-Derived Shorelines. *Geophys. Res. Lett.*, 47(14), e2020GL088365.

Vos, K., Splinter, K.D., Mitchell, H.D. et al. (2019). CoastSat: A Google Earth Engine-enabled Python toolkit to extract shorelines from publicly available satellite imagery. *Environ. Model. Softw.* 122, 104528.

Vos, K., Splinter, K.D., Palomar-Vázquez, J. et al. (2023). Benchmarking satellite-derived shoreline mapping algorithms. *Commun. Earth Environ.* 4, 345.

Wulder, M.A., Roy, D.P., Radeloff, V.C. et al. (2022). Fifty years of Landsat science and impacts. *Remote Sens. Environ.* 280, 113195.

Satellite Derived Shoreline Detection Using PlanetScope data - A Probabilistic Method

Hewetson A.[1,*], Lawrence J.[1] and Karmpadakis I.[1]

[1] Imperial College London, South Kensington Campus, London, SW7 2AZ. UK

*corresponding author:
e-mail: alfred.hewetson19@imperial.ac.uk

SHORELINE MONITORING – THE WATERLINE METHOD

To understand coastal processes appropriate datasets are required to quantify the cause and effect between the hydroclimatic process and the resultant change in morphology. This typically involves expensive and time-intensive in-situ surveying to monitor the shoreline and geography of the coastal zone. However, remote sensing applications provide a more efficient alternative which is suitable for shoreline monitoring. The present study employs such remote sensing techniques to detect the shoreline within a large dataset of satellite images.

The waterline can be monitored through a process known as the waterline method (Dolan et al., 1978). This entails repeated imagery of a location, with respect to time, with the waterline being defined as the instantaneous interface between the land and sea. The change over time of the position of this line can be used to quantify the accretion or recession rates at this location. Satellites have been shown to be able to perform this form of surveying (Vitousek et al., 2023).

PLANETSCOPE SATELLITE DATA

PlanetScope images have a near daily return rate since beginning operation in 2017. PlanetScope now operates ~170 satellites in orbit providing images with worldwide coverage and a resolution of 3.7m. The waterline method can be enhanced by utilizing the daily return frequency of PlanetScope data, allowing a higher temporal resolution of the observed shorelines. An example image of a beach segment is shown in Figure 1.

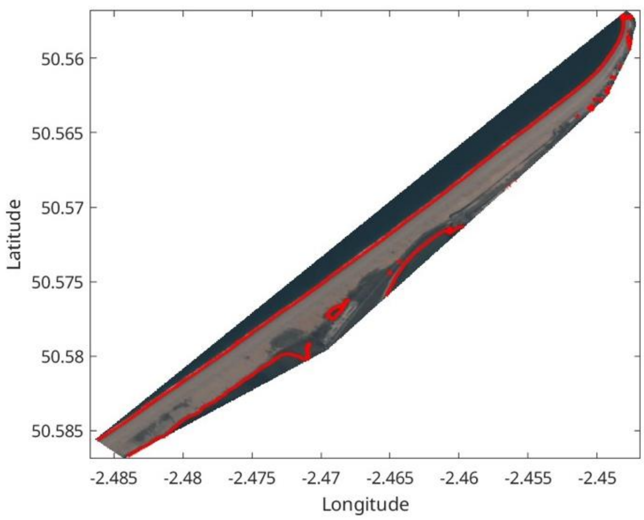

Figure 1. PlanetScope TCI (True Color Image) with the shoreline detected in red.

SHORELINE DETECTION

Past research has developed shoreline detection tools, such as CoastSat (Doherty et al., 2022; Vos et al., 2019). These discretize the land-sea interface by thresholding the image using a single index and defining a contour at that threshold. The most commonly applied index in such application is the normalized difference index, also known as NDWI (McFeeters, 1996). The latter is defined as:

$$NDWI = \frac{Green - IR}{Green + IR} \tag{1}$$

Equation 1 – Normalized difference water index is derived from Green, being the spectral response of the green band, and IR, the spectral response of the infrared band.

The present study provides an alternative approach. The shorleine is found using Top Of Atmosphere (TOA) PlanetScope images that are clipped to the location of interest. In using several multilayer perceptrons (MLP) acting together, each pixel's probability of being classed as land or sea is calculated. Characteristically, apart from the usual NDWI and NDVI index, we use the RGB and IR bands as well as 24 further band relationships for a total set of 28 indices to train the MLPs. The use of MLPs allows complex patterns of data to be understood due to the introduction of non-linear behavior within a neural network. The outputs of these MLPs for each pixel is a value between 1 and 0 indictive of the pixel belonging to either a land or a sea class. The final shoreline contour is then probabilistically defined without the use of a manual threshold.

$$NDVI = \frac{IR - Red}{IR + Red} \tag{2}$$

Equation 2 – the normalized difference vegetation index is derived from the red and infrared spectral response bands.

An example of this probabilistic index is shown in Figure 2, with the contour drawn at an equal probability of the shoreline being either land or sea. The root mean squared error (RMSE), the distance between the derived shoreline and a height contour relative to the instantaneous water-level, of this method, tested at Seaford UK, for cloud cover <90% is ~7m.

The advantage of this method is that it allows for spatial variability within satellite bands, for regions of clouds, shadows or geographical features, such as rocks, to still be correctly discretized. It also allows for further use case beyond just sandy beaches, due to the implementation of multiple indices allowing identification of different classes that could be interfacing with the sea.

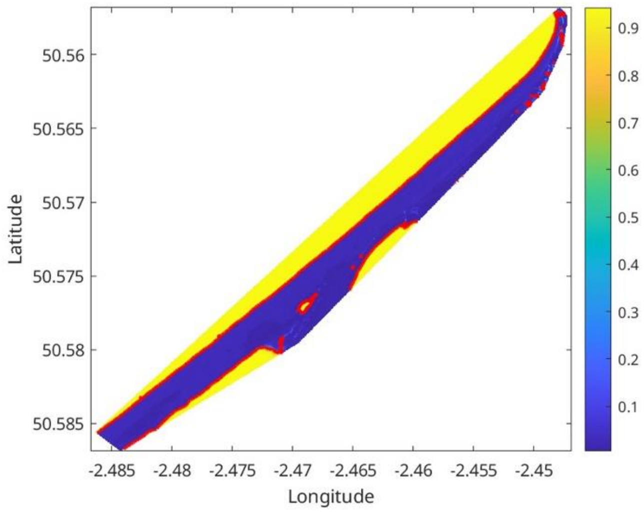

Figure 2. Probabilistic index of Figure 1 with the shoreline detected in red.

ACKNOWLEDGEMENTS

This research was funded by Radioactive Waste Management Ltd, trading as Nuclear Waste Services, via the Nuclear Waste Services Research Support Office (RWM167), project code RWM602.

REFERENCES

Doherty, Y., Harley, M.D., Vos, K., & Splinter, K.D. (2022). A Python toolkit to monitor sandy shoreline change using high-resolution PlanetScope cubesats. *Environ. Model. Softw.* 157, 105512.

Dolan, R., Hayden, B., & Heywood, J. (1978). A new photogrammetric method for determining shoreline erosion. *Coastal Eng.* 2, 21–39.

McFeeters, S. K. (1996). The use of the Normalized Difference Water Index (NDWI) in the delineation of open water features. *Int. J. Remote Sens*. 17(7), 1425–1432.

Vitousek, S., Buscombe, D., Vos, K., Barnard, P.L., Ritchie, A.C., & Warrick, J.A. (2023). The future of coastal monitoring through satellite remote sensing. Cambridge Prisms: Coastal Futures, 1, e10.

Vos, K., Splinter, K.D., Harley, M.D., Simmons, J.A., & Turner, I.L. (2019). CoastSat: A Google Earth Engine-enabled Python toolkit to extract shorelines from publicly available satellite imagery. *Environ. Model. Softw.* 122, 104528.

From Satellite to UAVs: The Role of Remote Sensing and Photogrammetry in Coastal Monitoring

Nikolakopoulos K.[1,*]

[1] GIS and Remote Sensing Laboratory, Department of Geology, University of Patras, 26504, Rio, Greece.

*corresponding author:
e-mail: knikolakop@upatras.gr

ABSTRACT

Monitoring the coastal environment is always a challenging task. A very detailed representation of the relief is necessary to understand and properly simulate many of coastal processes. Traditional in situ measurements with topographic equipment provide spatially sparse datasets on land and are not appropriate for mapping the spatial variability in wave and current fields, the shallow water bathymetry and the beach morphology. As an alternative solution to the in situ measurements remote sensing data and particularly high resolution satellite data and airphotos have been used in coastal monitoring in order to assess the morphological evolution of the coastline or to measure volume changes in the coastal area. As high-resolution digital surface models (DSMs) and orthophoto maps became a necessity in order to map with precision all the variations in coastal environments unmanned aerial vehicles (UAVs) photogrammetry offers an alternative solution to the acquisition of high accuracy spatial data along the coastline. This paper presents the feasibility of diverse remote sensing data for coastal monitoring and shallow water mapping. Different case studies from the Western Greece using satellite data (Landsat, Sentinel, Spot, Corona, IRS, Ikonos, worldview), airphotos, and UAVs data are presented.

MEDIUM RESOLUTION DATA

Since the launch of the first Landsat satellite back in 1972, several studies have used medium resolution (5–30m) satellite imagery such as Landsat, SPOT, Sentinel-2 for costal monitoring and coastline evolution. Landsat is the oldest observing satellite imagery program of the planet’s surface and is the only source of various types of historical data from almost 50 years ago Cracknell (2018). Millions of images have been acquired since then, which are now free to access. This historic archive of Landsat data, especially the older one, is very useful for researchers studying coastline evolution, as these images are unique with respect to observing the passing of time. A recent review study Apostolopoulos and Nikolakopoulos (2021), has focused on a statistical analysis of the most common methods, materials, software, and indices used in order to evaluate and quantify the shoreline evolution. As presented in Figure 1, Landsat data was used in almost 50% of the studies between 2000 and 2019. The launch of Sentinel-2 constellation gave a new impulse to the use of medium resolution satellite data in costal research. Both datasets provide the advantages of freely availability and continuity. Their suitability was examined in a recent study Apostolopoulos and Nikolakopoulos (2021). The results reveal that vectorized shorelines based on Landsat low-resolution images emerged significant deviation rates and thus are not suitable for shoreline monitoring studies. In contrast, the corresponding rates derived from the Sentinel-2 datasets gave better results proving that the spatial resolution analysis is related to the achievement of the best accuracy. Apostolopoulos and Nikolakopoulos (2020) followed a statistical analysis using the End Point Rate (EPR) and the Shoreline Change Envelope (SCE) rates derived from Digital Shoreline Analysis System (DSAS) software, and they have shown that medium resolution data such as Landsat are not suitable neither for shoreline forecasting not shoreline mapping. Moreover, their accuracy is very low as they presented a serious divergence that ranges between 6 and 11 m.

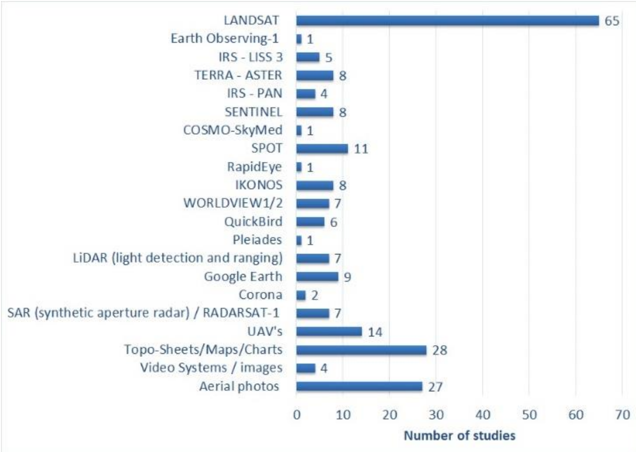

Figure 1. The most common data sources used in shoreline monitoring.

HIGH RESOLUTION DATA

High resolution satellite data and air photos or a combination of these were used to monitor the coastline’s changes or to measure volume changes in coastal areas Maglione et al. (2015), Mann and Westphal (2015).

High resolution data were used to reveal areas that are in a state of erosion along the coastline of the Prefecture of Achaia, elongated approximately 185 km, Apostololopoulos and Nikolakopoulos (2022). Analogue aerial photographs obtained from different missions (1960 and 1987) by the Hellenic Military Geographical Service (HMGS), orthomosaics for the years of 1945, 2008 and 2016 acquired through the National Greek Cadastre and Mapping Agency and three sets of declassified satellite imagery obtained by the recent declassified CORONA top-secret military archive, have providing images covering the study area for the years of 1965, 1968, and 1975 have been used. Eight sandy areas were revealed that are under erosion regime (Figure 2): the Araxos, Karnari, Kalamaki, Drepano, Loggos, Akoli, Diacopto, and Akrata while it is very likely all sites will show the same trend of change, similar to those computed using the available data from 1945 to 2016, in the next ten and twenty years.

High-resolution aerial photos at a scale of 1:30,000, orthomosaics, and satellite images were used and linear regression rates (LRR) were calculated to determine the changes in Kotychi Lagoon Apostolopoulos et al. (2023).

Seasonal sampling of water, sediment, and macrofaunal organisms in the lagoon was performed to monitor environmental and ecological parameters. The results showed that the lagoon's water surface shrank during the 1945–2016 period, showing different rates in four segments (Figure 3).

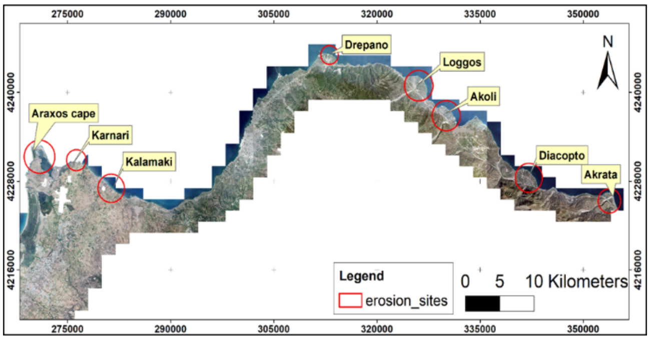

Figure 2. Areas in Achaia Prefecture which are under erosion regime (red cycles).

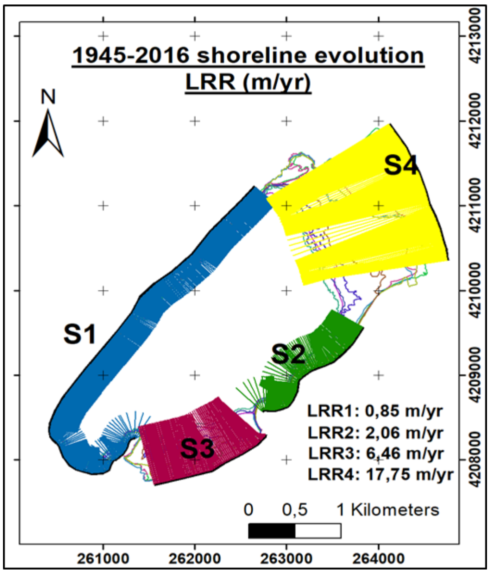

Figure 3. Kotychi Lagoon's LRR shoreline change rates for the 1945-2016 period separated into four different sections of change.

UAVs DATA

UAVs display exceptional capabilities in post-disaster mapping since they provide almost near real time data with high spatial resolution and low operational costs, they have a flexible survey planning, as well as they are able to collect data in hazardous environments. Moreover, it is noteworthy that it usually takes less than 45 minutes to one hour in the research area to receive the necessary information, while the generated processing products (i.e. orthophotos and Digital Surface Models) can be made available within 24 hours to the local authorities or stakeholders. A study focusing on the utilization of UAVs along with GNSS measurements to create high-resolution and high-precision maps of the damaged areas after the occurrence of weather extremes was published Kyriou et al. (2024). The coastline of Rion in Western Greece was selected as case study. Specifically, the specific area has been affected by recurrent storms causing severe damages to the coastline since 2017. Hence, repeated UAV campaigns following the same photogrammetric grid were carried out in 2016, 2017, 2018, 2021 and 2024. UAV data were processed using SfM (Structure-from-Motion) photogrammetry resulted in the generation of multitemporal orpthophotos and DSMs. These products were compared in GIS environment (Figure 4).

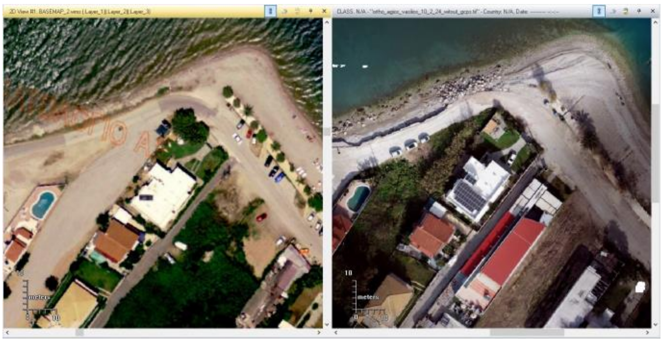

Figure 4. Damages on the road of Agios Vassilios at the east coastline of Rio in January 2024. The orthophoto of the Greek Cadastral (left), and the respective orthophoto of the UAV flight campaign of 2024 (right).

REFERENCES

Cracknell, A.P. (2018). The development of remote sensing in the last 40 years. *Int. J. Remote Sens.* 39, 8387–8427.

Apostolopoulos, D., & Nikolakopoulos, K. (2021). A review and meta-analysis of remote sensing data, GIS methods, materials and indices used for monitoring the coastline evolution over the last twenty years. *Eur. J. Remote Sens.* 54(1), 240–265.

Apostolopoulos, D., & Nikolakopoulos, K. 2020. Assessment and Quantification of the Accuracy of Low-and High-Resolution Remote Sensing Data for Shoreline Monitoring. *ISPRS Int. J. Geo-Inf.* 9(6), 391.

Apostolopoulos D.N. & Nikolakopoulos K.G. (2021). Statistical methods to estimate the accuracy of diachronic low-resolution satellite instruments for shoreline monitoring, *J. Appl. Remote Sens.* 16(1), 012007.

Maglione, P., Parente, C., & Vallario, A. (2015). High resolution satellite images to reconstruct recent evolution of Domitian coastline. *Am. J. Appl. Sci.* 12, 506–515.

Mann, T., & Westphal, H. (2014). Assessing Long-Term Changes in the Beach Width of Reef Islands Based on Temporally Fragmented Remote Sensing Data. *Remote Sens.* 6, 6961–6987.

Apostolopoulos D.N. & Nikolakopoulos K.G. (2022) Identifying sandy sites under erosion regime along the Prefecture of Achaia, using remote sensing techniques. *J. Appl. Remote Sens.* 17(2), 022206

Apostolopoulos, D.N.; Giannikopoulos, D.; Ramfos, A.; Faulwetter, S.; Panagiotaras, D.; Nikolakopoulos, K.G., & Avramidis, P. (2023). Monitoring the Kotychi Lagoon in Western Peloponnese, Greece, Using Remote Sensing Techniques and Environmental Assessment. *J. Mar. Sci. Eng.* 11, 411.

Kyriou A., Nikolakopoulos K., & Koukouvelas I. (2024) Mapping coastal erosion using UAVs, GNSS, and GIS: the case of Rio Greece", Proc. SPIE 13212, Tenth International Conference on Remote Sensing and Geoinformation of the Environment (RSCy2024), 1321202.

Long-term Geophysical and Hydrographic Surveillance of Pockmarks in Katakolo Port, Greece: A Key Factor for the Optimization of Port Operations and Safety

Kiousi D.[1], Sartampakos P.[2], Petropoulos C.[2], Mamitsa E.[2] and Tsoukala V.K.[1,*]

[1] Laboratory of Harbour Works, National Technical University of Athens, Iroon Polytechniou st., 15780 Athens, Greece
[2] NIREAS Engineering, 8 Katsikogianni D. Street, 34132 Chalkida Evia, Greece

*corresponding author
e-mail: tsoukala@mail.ntua.gr

INTRODUCTION

Seabed morphology comprises a fundamental factor in port stability (Oumeraci A., 1994), with geological anomalies, like pockmark formations, posing significant geotechnical risks (Judd A.G et al, 2007, Xu Z. et al., 2022). Formed by fluid escape, pockmarks can weaken foundation soils, accelerate erosion and induce sediment instability, threatening infrastructure such as breakwaters and quay walls (Kiousi D. et al., 2023, Prior B.D., 1999).

While bathymetric surveys identify surface features with great detail, sub-bottom profilers provide high-resolution imaging of subsurface structures, enabling a detailed assessment of pockmark evolution and associated geohazards (Rierra R. et al., 2022). Integrating sub-bottom profilers with hydrographic surveys enhances the understanding of sediment dynamics and supports informed engineering decisions for port construction and maintenance.

A previous hydrographic survey conducted in July 2022 at the Port of Katakolo (Kiousi D. et al., 2023) identified active pockmark formations through multibeam echosounder data, raising concerns about their impact on port stability. To further investigate these features and assess their evolution over time, a follow-up geophysical survey using a sub-bottom profiler was conducted on March 5th, 2025, in the same area. This study aims to provide a detailed subsurface analysis of the pockmarks, evaluate their temporal changes, and examine potential geotechnical implications of gas seepage activity. Understanding these processes is essential for the safety and operational continuity of the Port of Katakolo, a major maritime hub in Greece. By integrating sub-bottom profiling with hydrographic surveys, this research enhances knowledge of sediment dynamics and supports informed engineering decisions. The findings contribute to an early warning system for emerging geohazards, ensuring the long-term resilience of port infrastructure and mitigating risks that could threaten both operations and human life.

METHODOLOGY AND RESULTS

A high-resolution sub-bottom profiling (SBP) survey was conducted in the port of Katakolo to investigate the subsurface structure of the pockmark formations, following the multibeam bathymetric survey from July 2022. Data acquisition was performed using a sub-bottom profiler operating at 10 kHz, selected to balance penetration depth and resolution. A Differential Global Navigation Satellite System (DGNSS) antenna ensured accurate georeferencing.
The survey followed a configuration of five lines along the pier, with two of them extending to the edge of the breakwater. The vessel maintained a consistent speed and heading to minimize artifacts and ensure uniform data quality.

Data processing involved filtering, and noise reduction to enhance clarity and signal-to-noise ratio. Water column artifacts and external interferences were removed before interpretation. The processed SBP profiles were analysed individually and in correlation with bathymetric profiles from the 2022 survey, facilitating the identification of sedimentary layers, subsurface anomalies, and geological structures. This integration provided a detailed assessment of the subsurface conditions within the port, supporting sedimentological and geotechnical analyses.

Figure 1. (a) Preparation of the sub-bottom profiler, (b) Deployment of the sub-bottom profiler on the survey vessel.

The assessment for identifying pockmarks involved searching for circular or semicircular depressions in the sediment, which often indicate locations of gas or fluid release, reflective anomalies beneath the seabed surface, typically suggesting sediment disturbance due to gas escape, and the absence or weakening of reflections in specific areas associated with gaseous phases (gas blanking).

In Figure 2 the results of two survey lines are shown, with the upper part representing the seabed surface, with the strongest (black) reflections indicating denser or harder materials, while more diffuse or absent reflections may suggest low-density sediments or gaseous phases (e.g. gas within the sediments).

The monitoring revealed critical data regarding seabed stability and potential failures. Areas of diffuse reflection were observed, which are potentially linked to loose sedimentary material, alongside numerous vertical signal interruptions and discontinuities, indicating disturbances within the sediments. Low reflectivity regions may correspond to fine-grained sediments or organic material. The upward migration of gas has fractured the seabed, resulting in thinner, unconsolidated sediments and a significantly weakened, unstable substrate. This compromised seabed lacks the necessary support for the overlying infrastructure, leading to progressive structural deterioration. An on-site structural assessment corroborated these findings, revealing uneven construction, subsidence, and visible damage to the pier, including cracks and deformation. These observations highlight the ongoing impact of seabed instability on the integrity of the port. The extent of the damage is illustrated in Figure 3.

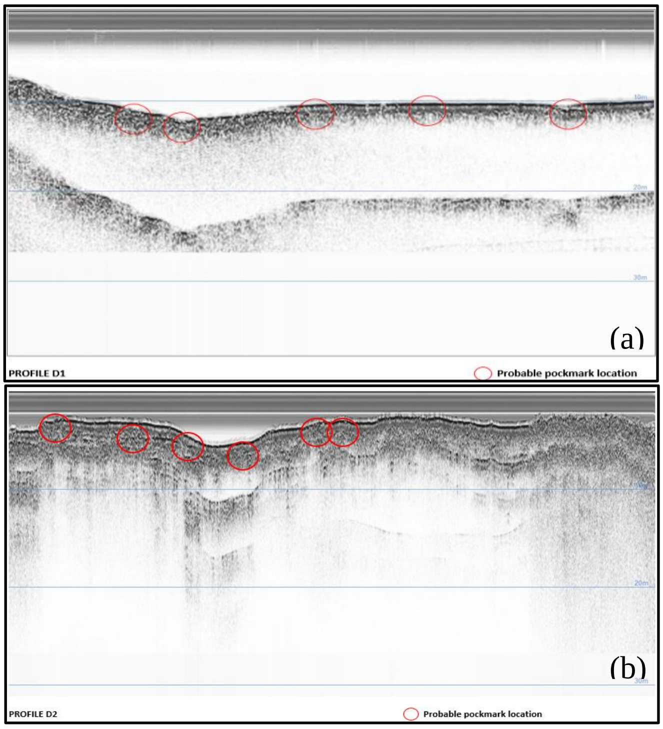

Figure 2. Sub-bottom profile data extracted from two survey lines (a,b) in the Port of Katakolo, showing possible gas or fluid release sites, with the red circles marking sediment disturbances and gas blanking.

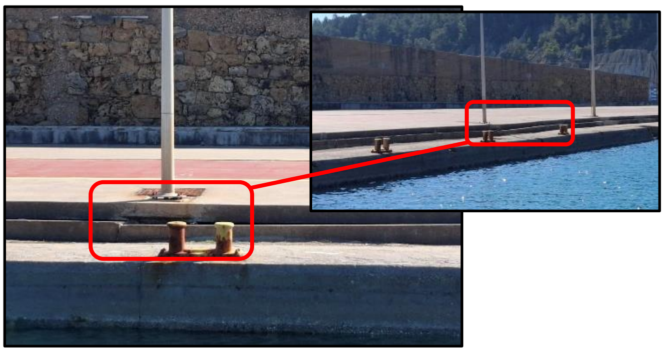

Figure 3. Close-up view of the pier showing visible cracks and structural damage beneath the light pole. The displacement of the concrete slabs indicates active subsidence.

CONCLUSIONS

The sub-bottom profiler survey in the port of Katakolo revealed significant geological and structural instability, with large gas chimneys beneath seabed craters that have fractured the subsurface layers, into thinner, unconsolidated sediments. This has resulted in a soft and unstable seabed, compromising the stability of the port infrastructure. Structural assessments confirmed the presence of visible subsidence, uneven construction, and cracks along the pier. The deformation and misalignment of structural elements indicate ongoing deterioration, posing a serious risk to the integrity and functionality of the port.

To effectively address these issues, further investigations are essential including direct structural testing to assess material integrity and load-bearing capacity. Given the dynamic nature of the subsurface conditions, annually geophysical and geotechnical surveys should be performed, mandating to track gas-related formations and their impact on the port's foundation. Regular assessments are critical to implementing timely mitigation measures, ensuring the long-term safety and operational viability of the port. This highlights the need for a robust port management strategy to adapt to evolving geological conditions.

REFERENCES

Judd, A.G., & Hovland, M. (2007). Seabed Fluid Flow: the impact on geology, Biology and the Marine Environment, vol.441 Cambridge University Press, New York.

Kiousi, D., Oikonomou, E., Sartampakou, A., & Sartampakos, P. (2023). The contribution of Hydrography to pockmark detection, and port construction and maintenance, with the use of modern sonar systems. 2nd International Conference on Design and Management of Port, Coastal and Offshore Works (DMPCO 2019) (2), Thessaloniki, Greece.

Kiousi, D., Sartampakos, P., & Tsoukala, V.K. (2025). Seabed Morphology Assessment and Pockmark Detection for Port Construction and Maintenance, Using a Multibeam Echo-sounder: A Case study in Katakolo Port, Western Peloponnese, Greece. Technical Annals, Technical Chamber of Greece.

Oumeraci, H. (1994). Review and analysis of vertical breakwater failures - lessons learned. *Coastal Eng.* 22, 3–29.

Prior B.D., Hooper R.J. (1999). Seafloor engineering geomorphology: recent achievements and future directions, *Geomorphology*, 31, 411–439.

Riera, R., Paumard, V., Gail, d.M., Saqab M.M., Lebrec, U., Lang, S.C., & Lane, A. (2022). Origin of Seafloor pockmarks overlying submarine landslides: Insights form semi-automated mapping of 3D seismic horizons (North West Shelf, Australia), *Mar. Pet. Geol.* 136, 105453.

Xu, Z., Li, Y., Yan, W., Lv, Y., Zhang, G., Lu, D., & Zhu, Z. (2022). Identifying Submarine Engineering Geologic Hazards in a Potential Gas Hydrate Target Area on the Southern Continental Margin of the South China Sea. *J. Mar. Sci. Eng.* 10, 12.

A Methodology to Correct Satellite Derived Chlorophyll-A Concentrations to Assess Coastal Waters' Eutrophication Status

Biliani I.[1] and Zacharias I.[1,*]

[1] Laboratory of Environmental Engineering, Department of Civil Engineering, University of Patras, Greece

*corresponding author:
e-mail: izachari@upatras.gr

INTRODUCTION

Eutrophication in coastal and inland waters, primarily driven by human activities such as agricultural runoff and industrial discharges (Alves et al., 2024), leads to nutrient enrichment that results in excessive algae growth and declining water quality.

Several indicators, particularly chlorophyll-a concentrations, are employed to assess trophic status through remote sensing techniques. The long-term dataset of satellite water bodies' chlorophyll-a concentrations can reveal variations in chlorophyll-a patterns, providing insights into the impacts of climate change (Sòria-Perpinyà et al., 2020) and serving as early warnings for harmful algal blooms (HABs) (Park et al., 2024), which threaten the ecological balance of the coastal environment.

Remote sensing-based chlorophyll-a assessments offer large-scale and long-term observations using satellite datasets such as Level 3 (L3) products. However, L3 datasets, since they are spatially and temporally averaged, often fail to capture the true variability of chlorophyll-a (Scott et al., 2019), particularly in shallow coastal waters.

This study aims to present an innovative methodology for enhancing chlorophyll-a data by utilizing MODIS Aqua data and advanced breakpoint detection to identify water bodies' trophic status and assess climate change trends.

MATERIALS AND METHODS

Case study

The Ambracian Gulf in the Epirus-Greece area was selected as a case study to validate the suggested technique because of its ecological significance and established eutrophication history. The Ambracian Gulf is renowned for its rich biodiversity and varied ecosystem (Kountoura et al., 2013). Its average depth is 35 m, and its size is around 405 km^2. The Gulf is connected to the Ionian Sea via the Aktio-Preveza strait and is a classic example of a semi-enclosed bay of the fjord type in the Mediterranean, with this narrow channel serving as the only point of connection with the open sea.

Data

217 Level-3 MODIS Aqua ready-to-use chlorophyll-a concentrations were acquired from the NASA Ocean Color Web Portal with a spatial resolution of 4km and monthly temporal coverage and spanned from 2003 to 2023. In addition, 7.502 MODIS Aqua Surface Reflectance georeferenced L2 images were acquired from NASA's Ocean Color Web portal. The dataset spanned between 2002 and 2023, with 1km spatial resolution and daily temporal coverage. Finally, chlorophyll-a concentrations for the L2 SR products were calculated using NASA's Ocean Color four-band chlorophyll-a algorithm (Biliani et al., 2024).

Methodology

Data quality was improved by filtering out erroneous pixels and implementing logical rules to detect abnormalities, such as abrupt fluctuations exceeding 25% over consecutive days and limiting results to a calibrated range of 50 mg/m^3. Non-equivalent data were tagged as missing rather than eliminated to preserve dataset integrity.

The Locally Estimated Scatterplot Smoothing (LOESS) algorithm (Cleveland, 1979) was applied to detect breakpoints in chlorophyll-a time series data, identifying significant ecological changes. Using forward and backward non-parametric regression with a minimum segment size of five days, the method ensured robustness by leveraging temporal dependencies. The LOESS methodology fills in missing values and refines chlorophyll-a estimates by smoothing noise and capturing local variations. A span size of 0.03, was chosen to optimise the balance between trend fidelity and noise reduction. The methodology corrects chlorophyll-a concentrations across long time series at individual station points, enhancing accuracy.

RESULTS

The study results that the conventional L3 chlorophyll-a product overstates seasonal peaks, which can surpass 60 mg/m^3, possible due to sensor limitations and imprecise processing assumptions. Although the chlorophyll-a concentrations derived from the L2 SR product gives more precise readings, peak concentrations of chlorophyll-a are still exaggerated. The suggested LOESS-based technique efficiently corrects these overestimations while keeping their natural variability. To more accurately reflect the phenological patterns of the Gulf, seasonal peaks are refined to a maximum of 5 mg/m^3. Furthermore, the linear trend analysis shows a positive chlorophyll-a trend from 2002 to 2023 in both the L2 SR and refined datasets, but the L3 dataset reveals a negative trend.

CONCLUSIONS

The proposed methodology provides a strong framework for monitoring water quality over long periods**.** The findings of this study show that the proposed methodology successfully eliminates chlorophyll-a inaccuracies when employing chlorophyll-a concentrations derived from the L2 surface reflectance products. Geolocation inaccuracies and temporal anomalies in L3 datasets can lead to significant variances. Through the adoption of statistical corrections and the use of a LOESS filter, on the proposed dataset improves the preservation of chlorophyll-a patterns and reduces noise from factors such as cloud cover. These enhancements have proven essential for monitoring ecological health and climate-induced changes in coastal environments.

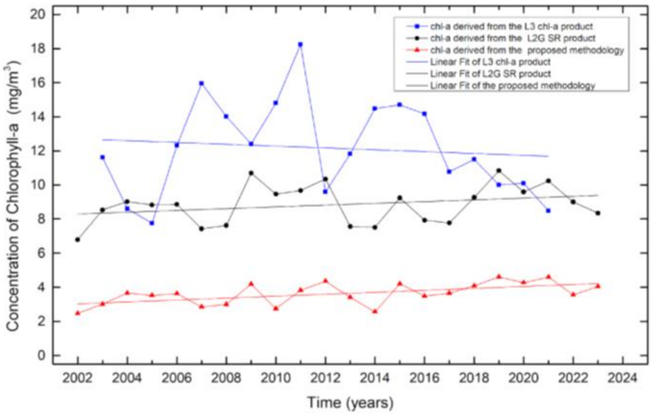

Figure 1. Monthly chlorophyll-a composites of the Ambracian Gulf derived from the ready to use L3 monthly chlorophyll-a products (in blue), from the L2G daily surface reflectance products before process (in black) and derived from the proposed methodology (in red). Graph visualization has been performed in Origin Lab (version 9).

REFERENCES

Alves, L., Nepomuceno, A., Cerda, M., Vogel, V., da Silveira Lobo, M.A., Barrozo, V., & Lamego, F. (2024). The eutrophication process in the lagoon systems of eastern Rio de janeiro investigated through the analysis of sedimentary phosphorus and historic of basin occupation. *Reg Stud Mar Sci.* 71, 103394.

Biliani, I., & Zacharias, I. (2024). Remote Sensing Applications : Society and Environment A methodology to assess the phenology patterns of a eutrophic water body , using remote sensing data and principal component analysis. *Remote Sens. Appl.: Soc. Environ.* 36, 101387.

Cleveland, W. S. (1979). Robust Locally Weighted Regression and Smoothing Scatterplots. *J. Am. Stat. Assoc.* 74(368), 829–836.

Kountoura, K., & Zacharias, I. (2013). Trophic state and oceanographic conditions of Amvrakikos Gulf: Evaluation and monitoring. *Desalin. Water Treat.* 51(13–15), 2934–2944.

Park, J., Khanal, S., Zhao, K., & Byun, K. (2024). Remote Sensing of Chlorophyll-a and Water Quality over Inland Lakes: How to Alleviate Geo-Location Error and Temporal Discrepancy in Model Training. *Remote Sens.* 16(15), 2761.

Scott, J.P., & Werdell, P.J. (2019). Comparing level-2 and level-3 satellite ocean color retrieval validation methodologies. *Opt. Express* 27(21), 30140.

Sòria-Perpinyà, X., Vicente, E., Urrego, P., Pereira-Sandoval, M., Ruíz-Verdú, A., Delegido, J., Soria, J.M., & Moreno, J. (2020). Remote sensing of cyanobacterial blooms in a hypertrophic lagoon (Albufera of València, Eastern Iberian Peninsula) using multitemporal Sentinel-2 images. *Sci. Total Environ.* 698, 134305.

Preliminary Results of the Implementation of the Coastal Vulnerability Index in Greece

Boumpoulis V.[1,*], Michalopoulou M.[1], Kazolias A.[2], Geraga M.[3], Depountis N.[1], and Papatheodorou G.[3]

[1] University of Patras, Department of Geology, Laboratory of Engineering Geology, Greece
[2] University of the Peloponnese, Department of Digital Systems, Sparti, Greece
[3] University of Patras, Department of Geology, Laboratory of Marine Geology and Physical Oceanography, Greece

*corresponding author:
e-mail: vasileios_boumpoulis@ac.upatras.gr

INTRODUCTION

A very important impact of global climate change and human interference is coastal erosion, a phenomenon that can contribute to the loss of land in marine environments (Boumpoulis et al., 2025). Coastal vulnerability can be defined as the susceptibility of a coastal area to be affected by either inundation or erosion processes, due to different climate related hazard such as storms-surges and sea level rise as well as from human activities (Anfuso et al., 2021; Benassai et al., 2014). Moreover, climate change can increase the intensity of climate related coastal hazards, especially coastal erosion and sea level rise, whose adverse impacts on coastal zones are expected to be significant even under the most optimistic emission scenario (IPCC, 2022). As a result, evaluating vulnerability to rising sea levels and coastal hazards becomes a vital aspect of coastal zone management and protection.

In this study, a method based on a specific vulnerability index—specifically, the Coastal Vulnerability Index (CVI) approach—was selected to assess vulnerability along the Hellenic coastlines. Accordingly, it was named as Hellenic Coastal Vulnerability Index (HCVI) due to its application in the entire country’s coastline.

In general terms, the CVI is a very productive, low-cost and effective tool for mapping and managing coastal risks. Despite this fact, there is no a specific framework in the literature addressing its use at a national scale. López Royo et al. (2016), estimated coastal vulnerability for the entire coastal zone of Spain using a modified CVI index, which was calculated for 4 different future climate models (RCPs) of sea level rise, based on IPCC future projections. Moreover, Furlan et al., (2021), developed a modified CVI index (MDim-CVI) for Italy, incorporating four different sub-indices: a) Coastal Forcing, b) Environmental, c) Social and d) Economic.

Aim of this reserach is the implementation of a Hellenic Coastal Vulnerability Index (HCVI) for the assessment of vulnerability along the coastlines and the creation of a national scale vulnerability map. This broader spatial perspective enables the identification of highly vulnerable hotspot provinces that require prioritized attention and more localized assessments to inform targeted decision-making.

METHODOLOGY

For the calculation of HCVI six variables were used: 1) Geological resilience, 2) Coastal Slope, 3) Historical shoreline change, 4) Significant wave height, 5) Sea level rise and 6) Tidal range.

The calculation of HCVI for the Hellenic shoreline was carried out using the equation proposed by Gornitz, (1991) according to which the result is equal to the square root of the product of the variables divided by the number of variables.

$$HCVI = \sqrt{\frac{a*b*c*d*e*f}{6}} \tag{1}$$

where *a*: Geological resilience, *b*: Significant wave height, *c*: Coastal slope, *d*: Historical shoreline change, *e*: Average tidal range, *f*: Sea level rise (SLR).

The data for the geological resilience variable used were extracted from the geotechnical map of Greece (EAGME, https://gaia.igme.gr/) and processed accordingly to be entered into the equation. Coastal slope was extracted from the Digital Elevation Model (DEM) (5X5 m) of Greece. The significant wave height, mean tide range and sea level rise used in the above equation were obtained from the Copernicus platform (Climate Copernicus) and processed accordingly.

Multi-spectral satellite images of Greece from 1984 to 2024 as derived from the satellite system of Landsat were used to extract the entire shoreline of Greece in various time periods for the calculation of the historical shoreline change. Moreover, the extracted shorelines were divided into segments of 100 meters, at the same locations where transects were created for calculating the historical shoreline change using the DSAS software (Digital Shoreline Analysis System version 6) (Himmelstoss et al., 2024).

RESULTS

Here are presented two geographic regions of Greece with the results of HCVI application which distinguished with high and very high vulnerability.

The first region is extended from the Gulf of Kavala to the Nestos National Park with the distribution of coastal vulnerability shown in Figure 1. HCVI values indicate very high vulnerability across nearly all areas, except for a small section in the western part of the Gulf of Kavala.

It can be said that the Gulf of Kyparissia is one of the most vulnerable regions in Greece. In particular, the Gulf is predominantly classified under the regime of high and very high vulnerability due to its low-lying topography, poor geological resilience, and high exposure to significant wave heights.

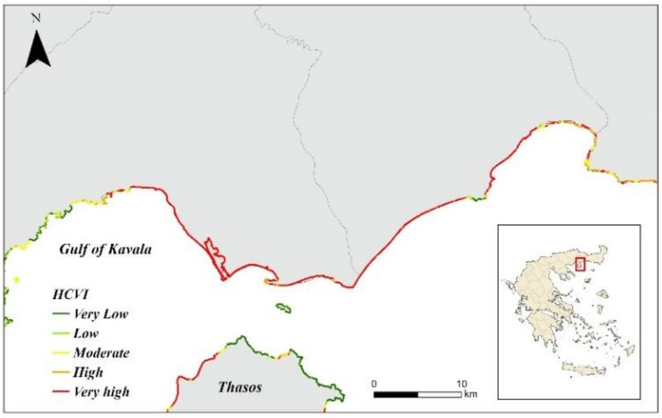

Figure 1. Spatial distribution of HCVI in the Gulf of Kyparissia

The second region is the Gulf of Kyparissia, with the distribution of coastal vulnerability shown in Figure 2.

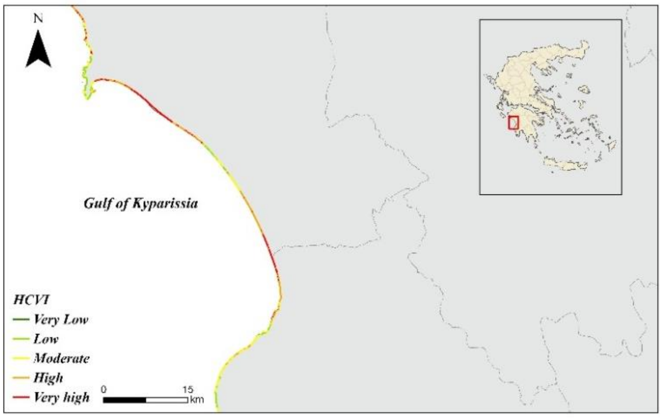

Figure 2. Spatial distribution of HCVI in the Gulf of Kyparissia

CONCLUSION

Among a variety of other indexes and methodologies, the Coastal Vulnerability Index (CVI) was chosen as a method for the calculation of coastal vulnerability in Greece. This Index was named Hellenic Coastal Vulnerability Index (HCVI) due to its application in the entire country's coastline.

Preliminary results indicate that 12% of the entire coastline is under the regime of high and very high vulnerability. However, the results need further evaluation and re-analysis. Furthermore, additional weighted variables are planned to be introduced into the HCVI equation, based on methodologies from existing literature. This could lead to adjustments of the index and improvements of the findings on the vulnerability of the Greek coast.

It is important to note that the coastal vulnerability assessment methodology used in this study was applied for the first time on a national scale in Greece. The importance of this application is great in that it can be used in national strategic decisions on the impacts of climate-related hazards on coastal zones.

ACKNOWLEDGEMENTS

The current research was funded by the Onasis Foundation in the framework of the project “Vulnerabilty of Greek coasts due to climate change” (“Initiative 1821-2021” - Protovoulia 21).

REFERENCES

Anfuso, G., Postacchini, M., Di Luccio, D., & Benassai, G. (2021). Coastal sensitivity/vulnerability characterization and adaptation strategies: A review. *J. Mar. Sci. Eng.* 9(1), 1–29.

Benassai, G., Di Paola, G., Aucelli, P., Passarella, M., & Mucerino, L. (2014). An inter-comparison of coastal vulnerability assessment methods. Engineering Geology for Society and Territory - Volume 4: Marine and Coastal Processes, 45–49.

Boumpoulis, V., Depountis, N., Dimas, A., & Papatheodorou, G. (2025). Presentation and analysis of the Geotechnical Coastal Vulnerability Index and validation of its application to coastal erosion problems. *Sci. Rep.* 15(1), 1424.

Furlan, E., Pozza, P.D., Michetti, M., Torresan, S., Critto, A., & Marcomini, A. (2021). Development of a Multi-Dimensional Coastal Vulnerability Index: Assessing vulnerability to inundation scenarios in the Italian coast. *Sci. Total Environ.* 772, 144650.

Gornitz, V. (1991). Global coastal hazards from future sea level rise. *Palaeogeogr. Palaeoclimatol. Palaeoecol.* 89(4), 379–398.

Himmelstoss, E.A., Henderson, R.E., Farris, A.S., Kratzmann, M.G., Bartlett, M.K., Ergul, A., McAndrews, J., Cibaj, R., Zichichi, J.L., & Thieler, E.R. (2024). Digital Shoreline Analysis System version 6.0: U.S. Geological Survey software release.

IPCC. (2022). Impacts of 1.5°C Global Warming on Natural and Human Systems. In *Global Warming of 1.5°C.*

López Royo, M., Ranasinghe R., & Jiménez J.A. (2016). A Rapid, Low-Cost Approach to Coastal Vulnerability Assessment at a National Level. *J. Coast. Res.* 32, 932–945.

Assessing Coastal Vulnerability in Southeast Cyprus: A Methodological Framework for Developing a Coastal Vulnerability Index

Tsakalos E.[1,2,*], Stagonas D.[1], Sarris A.[2], Kazantzaki M.[3], Polidorou M.[2], and Filippaki E.[3]

[1] Department of Civil and Environmental Engineering, University of Cyprus, Nicosia, Cyprus
[2] Digital Humanities GeoInformatics Lab, Sylvia Ioannou Digital Humanities Chair, Department of History and Archaeology, University of Cyprus, Nicosia, Cyprus.
[3] Institute of Nanoscience and Nanotechnology (INN), National Center for Scientific Research (NCSR) “Demokritos”, Athens, Greece

*corresponding author:
e-mail: tsakalos.evangelos@ucy.ac.cy

INTRODUCTION

Coastal erosion, driven by climate change and anthropogenic pressures, is an escalating global issue with far-reaching socio-economic and environmental consequences. Sea level rise remains a dominant factor influencing coastal retreat, with low-relief coastal zones being particularly vulnerable to shoreline recession and habitat loss. The eastern Mediterranean, a region with dynamic coastal processes, is experiencing accelerating sea level rise and increasing pressures from urbanization and tourism. In Southeast Cyprus, these factors contribute to substantial modifications in coastal morphology, making this area a critical case study for assessing long-term coastal change and vulnerability.

Understanding past coastal evolution is essential for developing reliable predictive models for future shoreline shifts (e.g. Filippaki et al., 2023). The reconstruction of palaeoshorelines, combined with sedimentary and geospatial analyses, provides crucial insights into the natural processes that have shaped the coastline over millennia. While previous studies have attempted to predict coastal evolution based on historical sea level changes, many of these approaches have relied predominantly on qualitative assessments (e.g. Paravolidakis et al., 2018; Liu and Jezek, 2004) or simplified parametric and analytical models (e.g., Bruun, 1988; Dean, 1991). More recent morphodynamic models such as SBEACH and XBeach (e.g. Alexandrakis et al., 2013; Monioudi et al., 2016) have also been used; however, their validity in representing complex coastal processes remains debated. These limitations highlight the need for a more data-driven and interdisciplinary methodology, incorporating both palaeoenvironmental assessments and geochronological techniques to enhance model reliability.

This study introduces a research approach that combines field-based observations, absolute dating of coastal sedimentary formations, and geospatial analysis to develop a Coastal Vulnerability Index (CVI) tailored to Southeast Cyprus. By addressing the limitations of previous models, this framework provides a robust tool for long-term coastal risk assessment and management.

METHODOLOGICAL FRAMEWORK

This study adopts a systematic methodology encompassing diverse scientific approaches to assess the long-term evolution of the coastline and its vulnerability to future sea level changes. It establishes a chronological framework of sea transgression, reconstructing past shoreline positions and sedimentation regimes in the selected coastal area - an approach that has not been previously pursued in this region.

To achieve this, Optically Stimulated Luminescence (OSL) dating is applied to sediments from aeolianite outcrops and beachrock formations to determine their absolute ages and reconstruct past shoreline positions. Beachrock formations serve as indicators of palaeoshoreline locations, strongly linked to past eustatic sea level changes and coastal development patterns. Aeolianite deposits, provide insights into the rate of wind-driven sediment supply and the evolution of coastal dune systems over time.

Figure 1. Location map of the study area in Southeast Cyprus. Right: Field photos from the site showing (top) beachrock sampling for Optically Stimulated Luminescence (OSL) dating, and (bottom) elevation measurement using GNSS equipment.

The integration of these datasets enables the development of a high-resolution temporal framework for environmental changes affecting the coastline. Furthermore, sedimentological analyses (grain size distributions) and the assessment of microtextural surface features of quartz grains (e.g. Tsakalos et al., 2015) using Scanning Electron Microscopy (SEM) provide information on depositional environments, transport histories, and post-depositional processes, allowing for a more detailed understanding of sedimentary dynamics in the study area.

Building upon this palaeoenvironmental foundation, a Coastal Vulnerability Index (CVI) is formulated as a geospatial tool to assess current and future coastal vulnerability. The index integrates seven key parameters (Table 1): geomorphology, coastal slope, rate of shoreline change, relative sea level change, wave height, tidal range, and wind direction.

Table 1. Ranges for vulnerability ranking of the seven variables used, shown together with their thresholds.

Variable	Categories				
	Very Low (1)	Low (2)	Moderate (3)	High (4)	Very High (5)
Geomorphology	Rocky cliffs	Med. cliffs	Low cliffs, plains	Cobble beaches	Sand beaches, deltas
Coastal slope (%)	>1.2	1.2 to 0.9	0.9 to 0.6	0.6 to 0.3	<0.3
Erosion/accretion (m/yr)	> (+2.0)	(+1.0) to (+2.0)	(-1.0) to (+1.0)	(-2.0) to (-1.0)	< (-2.0)
RSL change (mm/yr), incl. tectonic regime	<1.8	1.81 to 2.5	2.51 to 3.0	3.01 to 3.4	>3.4
Wave height (m)	<0.55	0.55 to 0.85	0.86 to 1.05	1.06 to 1.25	>1.25
Tide range (m)	>6.0	4.0 to 6.0	2.0 to 4.0	1.0 to 2.0	<1.0
Wind angle (°)	0 to 20 (sheltered)	21 to 45	46 to 70	71 to 85	86 to 90 (exposed)

These variables are analysed, weighted, and incorporated into a GIS-based model, facilitating the spatial representation of coastal vulnerability along the coastline. To project future coastal vulnerability, the CVI is applied under three distinct sea level rise scenarios: current conditions, and projections for 0.5 m, 1.0 m, and 1.5 m of sea level rise. This enables the development of a series of high-resolution digital maps, illustrating shoreline displacement trends and vulnerability zones over time.

CONCLUSION

This study presents an integrated methodological framework for assessing coastal vulnerability, combining palaeoenvironmental reconstructions, geospatial analysis, and predictive tools. The development of a Coastal Vulnerability Index, tailored to the Southeast Cyprus coastal zone, offers a scientifically sound approach to evaluating short - and long - term shoreline dynamics.

By linking coastal evolution with future projections, this research provides a comprehensive assessment of coastal susceptibility to sea level rise and erosion. The application of this framework under different climate scenarios supports evidence-based decision-making for coastal adaptation strategies. As climate change continues to reshape global coastlines, the need for robust, data-driven approaches to predicting and mitigating coastal hazards is more urgent than ever. This research contributes to that effort, offering methodologies that can be replicated and adapted in other vulnerable coastal environments worldwide.

ACKNOWLEDGEMENTS

This study has received funding from the European Union's Horizon2020 Research and Innovation Programme under the Marie Skłodowska-Curie Grant Agreement No 101034403.

REFERENCES

Alexandrakis, G., Ghionis, G., et al., (2013). Coastal erosion and protection in Europe: a comprehensive overview Greece, In: Pranzini E., Williams A. (eds), Earthscan Ltd, London, 355–377.

Bruun, P., (1988). The Bruun Rule of erosion by sea level rise, *J. Coastal Res.* 4, 622–648.

Dean, R.G. (1991). Equilibrium beach profiles: characteristics and applications, *J. Coast. Res*.7, 53-84

Filippaki, E., Tsakalos, E., Kazantzaki, M., & Bassiakos, Y., (2023). Forecasting Impacts on Vulnerable Shorelines: Vulnerability Assessment along the Coastal Zone of Messolonghi Area - Western Greece. *Climate* 11, 24.

Liu, H., & Jezek, K.C., (2004). Automated extraction of coastline from satellite imagery by integrating Canny edge detection and locally adaptive thresholding methods. *Int. J. Remote Sens.* 25(5), 937–958.

Monioudi, I.N., Karditsa, A., Chatzipavlis, A., Alexandrakis, G., Andreadis, O.P., Velegrakis, A.F., Poulos, S.E., Ghionis, G., Petrakis, S., Sifnioti, D., et al., (2016). Assessment of vulnerability of the eastern Cretan beaches (Greece) to sea level rise. *Reg. Environ. Chang.* 16, 1951–1962.

Paravolidakis, V., Ragia, L., Moirogiorgou, K., & Zervakis, M.E. (2018). Automatic coastline extraction using edge detection and optimization procedures. *Geosciences* 8 (11), 407.

Tsakalos, E. (2015). Geochronology and exoscopy of quartz grains in environmental determination of coastal aeolianites. *J Archaeol. Sci. Rep*. 7, 679–686.

Empirical Formulations of Wave Setup on Reef Lined Coasts

Pouliasis G.[1,*] and Higuera P.[1,2]

[1] Moody's RMS, London, United Kingdom
[2] Department of Civil and Environmental Engineering, The University of Auckland, New Zealand
*corresponding author:
e-mail: georgios.pouliasis@moodys.com

INTRODUCTION

Coral reefs are valuable ecosystems that, among other benefits, are known to provide coastal protection from flooding and erosion (Ferrario et al., 2014). Wave setup, the superelevation of mean water level due to wave breaking, is a crucial component of wave runup and a key driver of coastal flooding on reef-lined coasts (Buckley et al., 2015). Thus, accurately predicting wave setup on reefs is essential for assessing coastal hazards and designing coastal infrastructure.

On sloping beaches, wave setup is commonly expressed as a function of the Iribarren number $\xi_0 = \frac{\beta_b}{\sqrt{H_0/L_0)}}$ where β_b is the beach slope, H_0 and L_0 are the offshore wave height and wavelength (Dalinghaus et. al. 2023). In the case of fringing reefs, Gerritsen (1980) expressed wave setup as a function of the offshore wave steepness and a submergence parameter based on experimental observations. Later, Gourlay (1996) also derived an empirical wave setup relationship based on laboratory experiments on idealized 2D reef profiles. However, the proposed formulation included some intrinsic parameters, such as the profile factor, which may be difficult to estimate in practice. More recently, Buckley et. al. (2022) showed through numerical simulations that wave setup is influenced by the reef submergence, the fore reef slope Iribarren number and, to a lesser extent, bed roughness. In practice, wave setup over reefs is most often estimated using numerical models. Examples of works where numerical models have been validated against experimental measurements to capture the wave transformation over a reef include Zijlema (2012), Buckley et. al. (2014) and more recently Zhang et. al. (2019). However, the superior performance of numerical models, particularly phase-resolving wave models, comes at a high computational cost, which makes them unsuitable for use in regional scale studies.

The present study aims to bridge the gap between accuracy and computational efficiency by providing a set of accurate and practical to use formulas to predict wave setup on coasts protected by fringing reefs. We derive three parametrisations based on a large dataset of numerically simulated waves and verify their performance against additional numerical and experimental data.

METHODOLOGY

The numerical data was provided by the BEWARE (Bayesian Estimator for Wave Attack in Reef Environments, Pearson et. al., 2017) dataset, which comprises of 174,372 XBeach simulations, each representing a combination of reef geometry and hydrodynamic forcing conditions. The geometric parameters varied include the fore reef slope β_f, reef flat width L_r, beach slope β_b, and bed roughness c_f, while the hydrodynamic forcing parameters include reef water depth h_r, offshore significant wave height H_0 and peak period T_p (see Figure 1). For each combination, four 30-minute simulations were run with random realizations of the surface elevation at the offshore boundary using a standard JONSWAP spectrum. The dataset provides the wave setup at different locations across the reef. In this study, the empirical formulas are trained to predict wave setup at the toe of the beach, denoted with $\bar{n}$, as this is the most relevant location for coastal flooding.

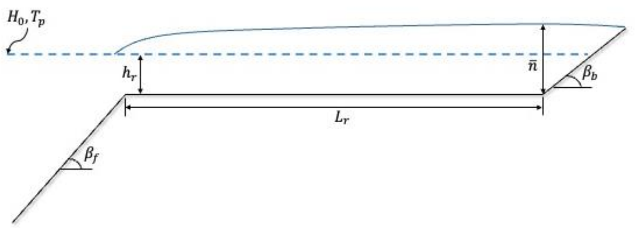

Figure 1: Schematisation of reef geometric and hydrodynamic parameters (re-created from Pearson et. al., 2017).

To parametrise wave setup, two normalisations of wave setup were explored, one by the width of the reef flat L_r (Form A) and by the offshore significant wave height H_0 (Form B). Form A, relates dimensionless wave setup $\bar{n}/L_r$ to reef submergence h_r/H_0, relative wave height H_0/L_r, relative period $T_p\sqrt{\frac{g}{L_r}}$, fore reef slope β_f, beach slope β_b, and bed roughness c_f. However, detailed geometric information about the reef may not always be available, especially in regional studies. Therefore, Form B follows a more conventional approach and connects the dimensionless wave setup $\bar{n}/H_0$ to the Iribarren number and the reef submergence parameter. For practical purposes the slope used to derive the Iribarren number is taken as the average slope between the mean water level and the 100 m depth contour. This is a simplification that aims to combine β_f, L_r, β_b into a single parameter. Hence, this is termed the equivalent Iribarren number and denoted as ξ_{eq}. The dataset was randomly split between a training set with 70% of the observations and a testing set containing the remaining 30% of the observations. The fitting was performed using ordinary least squares regression.

RESULTS

Form A is provided in Equation (1). After experimentation it was found that including the reef submergence term in a hyperbolic tangent function improved the performance of the formulation significantly. However, bed roughness may be difficult and uncertain to estimate for practical applications.
Moreover, analysis of the covariates revealed that the beach slope is above the significance level of 1%. By omitting

these two covariates, a reduced version of Form A is obtained in Equation (2). Form B is provided in Equation (3).

$$\frac{\bar{n}}{L_r} = 0.024\left(1 - \tanh\frac{h_r}{H_0}\right)^{0.83}\left(\frac{H_0}{L_r}\right)^{0.495}\left(T_p\sqrt{\frac{g}{L_r}}\right)^{0.859}\beta_f^{0.251}\beta_b^{-0.01}c_f^{0.026} \tag{1}$$

$$\frac{\bar{n}}{L_r} = 0.0227\left(1 - \tanh\frac{h_r}{H_0}\right)^{0.833}\left(\frac{H_0}{L_r}\right)^{0.497}\left(T_p\sqrt{\frac{g}{L_r}}\right)^{0.857}\beta_f^{0.253} \tag{2}$$

$$\frac{\bar{n}}{H_0} = 0.291\xi_{eq}^{0.452}\left(1 - \tanh\frac{h_r}{H_0}\right)^{0.80} \tag{3}$$

The best performance on the testing set was achieved by Equation (2), followed by (1) and (3) (Table 1). To offer further validation, the formulas were tested against physical modelling data obtained by Demirbilek et. al. (2007), denoted as ERDC, and SWASH simulations carried out on 5 transects along the eastern coast of Florida. Equation (2) matched the observations well (Figure 2). Equation (3) resulted in a larger scatter, particularly for the SWASH simulations (Figure 3). However, given the simplifications of the formula, the result is still considered acceptable.

Table 1. Goodness of Fit for Equations (1), (2) and (3) calculated on the test set.

Equation	RMSE	Adj-R^2
(1)	0.125	0.954
(2)	0.121	0.958
(3)	0.221	0.851

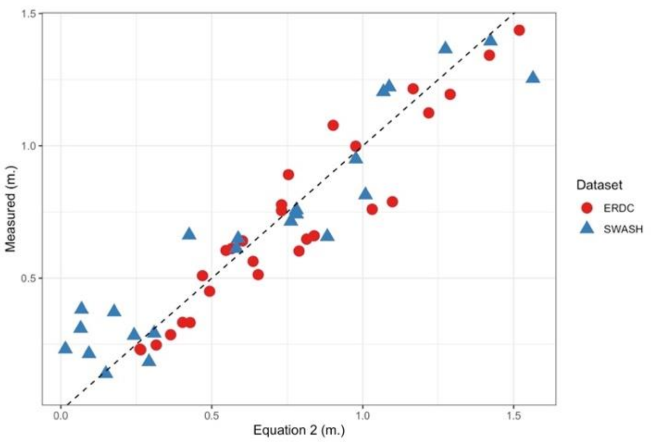

Figure 2: Comparison between wave setup for SWASH and ERDC datasets and the prediction using Equation (2).

CONCLUSIONS

In the present study we derived three empirical formulations to predict wave setup on reef lined coasts based on a large numerical dataset. The best agreement with test data was achieved by normalising setup with the width of the reef flat. To account for limited availability of detailed geometric reef characteristics, a second, simplified, form was provided, which also performed satisfactorily. These formulations offer efficient alternatives to numerical models and can be integrated into early warning systems for reef-lined coasts, providing rapid estimates of wave setup during storms and enabling large-scale flood risk assessments. Future research should compare against field measurements.

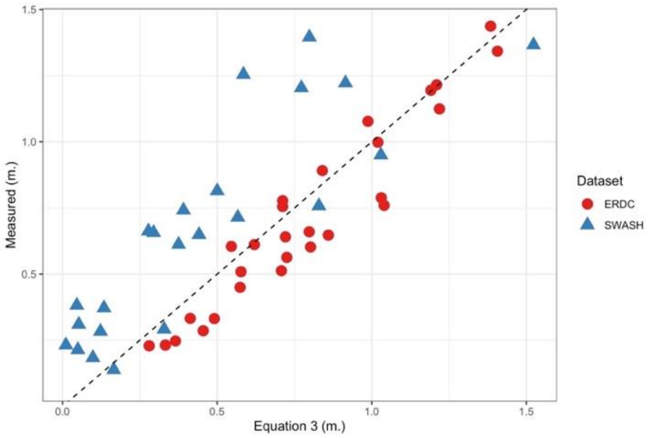

Figure 3: Comparison between wave setup for SWASH and ERDC datasets and the prediction using Equation (3).

REFERENCES

Buckley, M., Lowe, R., & Hansen, J. (2014). Evaluation of nearshore wave models in steep reef environments. *Ocean Dyn.* 64, 847–862.

Buckley, M.L., Lowe, R.J., Hansen, J.E., & Van Dongeren, A.R. (2015). Dynamics of wave setup over a steeply sloping fringing reef. *J. Phys. Oceanogr.* 45(12).

Buckley, M. L., Lowe, R. J., Hansen, J. E., van Dongeren, A. R., Pomeroy, A., Storlazzi, C.D., et al. (2022). Wave-driven hydrodynamic processes over fringing reefs with varying slopes, depths, and roughness: Implications for coastal protection. *J. Geophys. Res. Oceans* 127, e2022JC018857.

Dalinghaus, C., Coco, G., & Higuera, P. (2022). A predictive equation for wave setup using genetic programming. *Nat. Hazards Earth Syst. Sci.* 23(6), 2157–2169.

Demirbilek, Z., Nwogu, O.G., & Ward, D.L. (2007). Laboratory study of wind effect on runup over fringing reefs, Report 1: data report.

Ferrario, F., Beck, M.W., Storlazzi, C.D., Micheli, F., Shepard, C.C., & Airoldi, L. (2014). The effectiveness of coral reefs for coastal hazard risk reduction and adaptation. *Nat. Commun.* 5(1), 3794.

Gerritsen, F. (1980). Wave attenuation and wave set-up on a coastal reef. Proc. *Coastal Eng. Proc.* 444–461.

Gourlay, M.R. (1996). Wave set-up on coral reefs. 2. Set-up on reefs with various profiles. *Coastal Eng.* 28(1-4), 17–55.

Pearson, S.G., Storlazzi, C.D., van Dongeren, A.R., Tissier, M.F.S., & Reniers, A.J.H.M. (2017). A Bayesian based system to assess wave-driven flooding hazards on coral reef-lined coasts. *J. Geophys. Res. Oceans* 122(12), 99–117.

Zhang, S.J., Zhu, L.S., & Zou, K. (2019). A comparative study of numerical models for wave propagation and setup on steep coral reefs. *China Ocean Eng*. 33(4), 424–435.

Zijlema, M. (2012). Modelling wave transformation across a fringing reef using SWASH. *Coastal Eng. Proc.* 1(33), 26.

Early Warning System for Coastal Hazards in Thermaikos Gulf (Aegean Sea)

Makris C.[1,*], Androulidakis Y.[2], Kolovoyiannis V.[2], Kombiadou K.[3], Baltikas V.[4], Kartsios S.[5], Pytharoulis I.[5], Mallios Z.[4] and Krestenitis Y.[4]

[1] Department of Civil Engineering, School of Engineering, Democritus University of Thrace, Xanthi, 67100, Greece
[2] Department of Marine Sciences, University of the Aegean, Mytilene, Lesvos Island, 81100, Greece
[3] Centre for Marine and Environmental Research (CIMA), University of Algarve, Faro, 8005-139, Portugal
[4] Department of Civil Engineering, Faculty of Engineering, Aristotle University of Thessaloniki, Thessaloniki, 54124, Greece
[5] Department of Meteorology and Climatology, School of Geology, Aristotle University of Thessaloniki, Thessaloniki, 54124, Greece

*corresponding author:
e-mail: cmakris@civil.duth.gr

SCOPE OF STUDY

Thermaikos Gulf (TG) in the northwestern Aegean Sea (east-central Mediterranean) is a data-scarce area in terms of *in situ* monitoring. At the same time, it is a hotspot for significant anthropogenic pressures and natural hazards (Androulidakis et al., 2024a). This situation necessitates reliable metocean forecasts. To this end, the Wave4Us (https://wave4us.web.auth.gr/) Operational Forecast Platform (OFP; Krestenitis et al., 2015; Androulidakis et al., 2025) provides high-resolution model predictions for weather conditions, ocean circulation, Sea Level Elevation (SLE), wave characteristics, and river discharges (Figure 1). Based on these, it simulates coastal hazards like pollutant transport (oil spills and nutrients), Marine Heat Waves (MHW; Androulidakis et al., 2024b) and coastal flooding. This study presents the potential of the OFP's outputs and evaluates its predictive skill using satellite and field data, confirming its accuracy. The results highlight Wave4Us as a reliable tool for environmental impact assessment that can serve as the basis of an Early Warning System (EWS) for emergency response in the region.

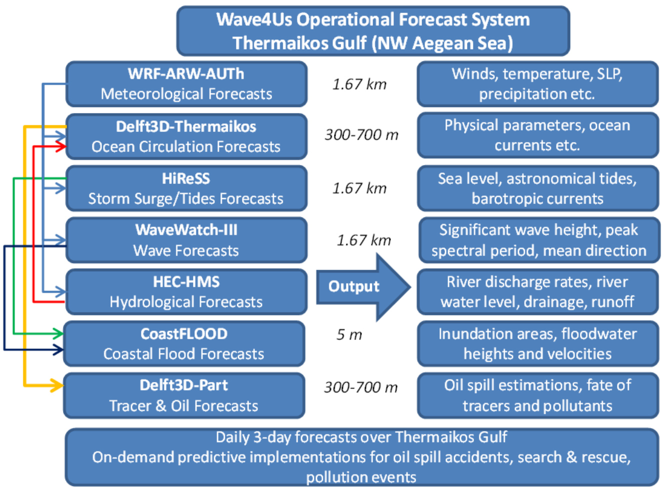

Figure 1. Wave4Us OFP work scheme and data flow (modules, interactions, coupling schematics, model resolution, and featured output).

METHODOLOGY

Study Area

TG is a naturally protected semi-enclosed coastal area influenced by anthropogenic stressors and meteorological and ocean dynamics. Major freshwater inputs from rivers and drainage channels shape the local hydrodynamics and hydrology, impacting seawater quality, ecosystem health, and circulation (Androulidakis et al., 2023). Intense urbanization, agriculture, maritime traffic, tourism, and industrial activities are sources of marine pollution, while extreme weather events (e.g., low-pressure systems, storm surge, high waves and flooding) also affect TG's vulnerability. Despite improvements in wastewater treatment, TG has yet to achieve a "good environmental state" (Androulidakis et al., 2024a). Limited field monitoring classifies it as a data-poor region. Given the projected climate change impacts, an integrated suite of high-resolution environmental forecasting is crucial for stakeholders, aiding decision-making in coastal management, hazard mitigation, and digital transformation initiatives (Makris et al., 2022).

Numerical Models

Wave4Us incorporates the following simulation models in an integrated way (1- and 2-way coupling; Figure 1): WRF-ARW-AUTh for meteorological forecasts (Krestenitis, et al., 2015a); Delft3D-Thermaikos and Delft3D-Part for coastal circulation, pollution transport and hydrodynamic connectivity (Androulidakis et al., 2023); HiReSS and WaveWatch-III for storm tides and wave dynamics (Krestenitis et al., 2015b), HEC-HMS for hydrological pluvial and fluvial flows (Androulidakis et al., 2023), and CoastFLOOD for littoral inundation (Makris et al., 2023).

RESULTS

The upgraded version of the Wave4Us system provides the following outputs regarding important coastal hazards. The OFP successfully simulated an oil spill of approximately 5,000 m² detected in the northern part of Thessaloniki Bay (northern TG) on 4/11/2017, due to a hydrocarbon leakage at the mooring point of the permanent refinery supply pipeline outside the Thessaloniki Port (Figure 2).

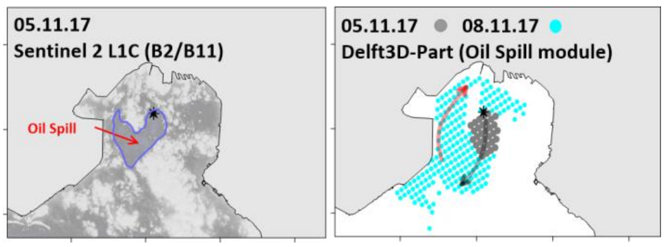

Figure 2. Oil spill spreading from Sentinel-2 L1C (observation) on 5/11 and from Delft3D-Part model (forecast) on 5/11 (gray) and 8/11 (blue) in the northern TG.

Figure 3 presents the forecast of the brackish water spread during Storm Numa (18-20/11//2017), which imposed large river discharges into the TG. During this event, primary production was enhanced in areas where the brackish waters expanded (Chlorophyll-a (Chl-a) increases). The observed and predicted variability of Sea Surface Temperature (SST) shows strong agreement throughout the 2017 annual cycle, particularly during the summer months when MHWs (Hobday et al., 2016) typically occur (Figure 4). Five MHWs were identified in the simulations, exhibiting characteristics similar to those observed in the events. During the atmospheric cyclone Foivos in January 2019, a significant rise in SLE and intense wave-induced set-up were recorded, both successfully simulated by the individual OFP models (HiReSS and WaveWatch-III, respectively). The extent of coastal flooding due to the total water level from storm tides and waves in TG's coastal zone was ultimately assessed using the CoastFLOOD model (Figure 5).

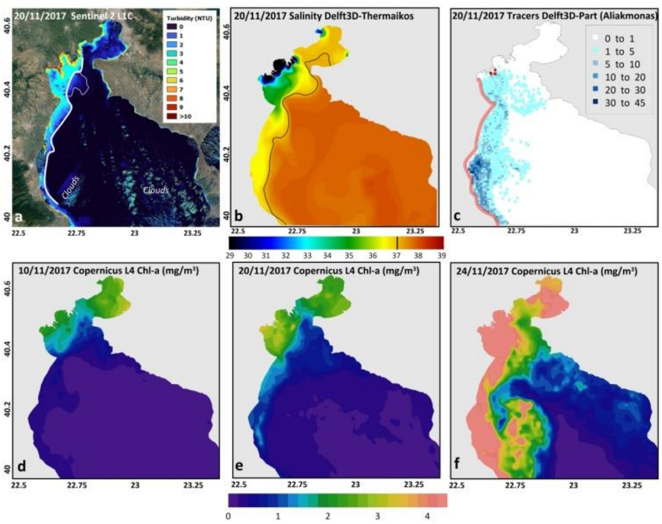

Figure 3. (a) Turbidity (Sentinel 2 1LC), (b) forecast salinity (Delft3D-Thermaikos) and (c) passive tracer spread (Delft3D-Part) on 20/11/2017. (d, e, f) Chl-a concentrations from satellite data (Copernicus CMS).

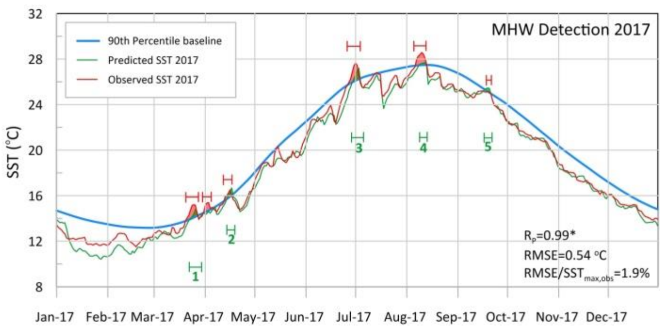

Figure 4. Satellite observations (Copernicus) and forecasts (Delft3D-Thermaikos) of SST and detection of MHWs for 2017 in the study area.

CONCLUSIONS

Wave4Us OFP provides specialized forecasts addressing key coastal hazards. It improves accuracy in extreme freshwater outflow predictions, which transport pollutants during storms, and enhances oil spill simulations, aiding first-level responder efforts. It contributes to better detecting pollutant dispersion risks, forecasting eutrophication, and predicting MHWs. A robust coastal flooding model can also offer quick early warnings of inundation hazards due to extreme weather events. These high-resolution forecasts can support coastal management, ecosystem resilience, and marine renewable energy planning.

Figure 5. Forecast of flooded coastal areas and floodwater levels by CoastFLOOD model on 24-25/01/2019 (left). Zoom into the Macedonia Airport area (right).

ACKNOWLEDGEMENTS

The research is partially supported by the Interreg Euro-MED0200814 project LocAll4Flood co-funded by the EU.

REFERENCES

Androulidakis, Y. et al. (2023). Hydrography of Northern Thermaikos Gulf based on an integrated observational-modeling approach. *Cont. Shelf. Res*. 269, 105141.

Androulidakis, Y. et al. (2024a). Oceanographic research in Thermaikos Gulf: a review over five decades. *J. Mar. Sci. Eng*. 12(5), 795.

Androulidakis, Y, Kolovoyiannis, V., Makris, D., & Krestenitis, Y. (2024b). Evidence of 2024 Summer as the Warmest During the Last Four Decades in the Aegean, Ionian, and Cretan Seas. *J. Mar. Sci. Eng*. 12(11), 2020.

Androulidakis, Y. et al. (2025). Operational platform for metocean forecasts in Thermaikos Gulf (Aegean Greece). *J. Oper. Oceanogr*. (under review).

Hobday, A.J. et al. (2016). A hierarchical approach to defining marine heatwaves. *Progr. Oceanogr*. 141, 227–238.

Krestenitis, Y. et al. (2015a). Operational Oceanographic Platform In Thermaikos Gulf (Greece): Forecasting And Emergency Alert System For Public Use. Proc. 36[th] IAHR World Congress, Hague, The Netherlands.

Krestenitis, Y. et al. (2015b). Operational Forecast System of Storm Tides in the Aegean Sea (Greece). Proc. 2015 ASLO Aquatic Sciences Meeting, Granada, Spain.

Makris, C. et al. (2022). Towards an Operational Forecast Model for Coastal Inundation due to Storm Surges: Application during Ianos Medicane. Proc. SafeThessaloniki 2022, Thessaloniki, Greece.

Makris, C., Mallios, Z., Androulidakis, Y., & Krestenitis, Y. (2023). CoastFLOOD: A High-Resolution Model for the Simulation of Coastal Inundation Due to Storm Surges. *Hydrology* 10(5), 103.

Deployment of a Compound Coastal Flooding Early Warning System

Papadimitriou A.[1,*], Metallinos A.[1], Chondros M.[1], Sartampakos P.[2], Kanelleas P.[1] and Tsoukala V.[1]

[1] Laboratory of Harbour Works, NTUA, 9 Iroon Polytechniou Str., 15780 Zografou, Greece
[2] Nireas Engineering, Katsikogianni 8, 34132 Chalkis, Greece

*corresponding author:
e-mail: andrewtnt@mail.ntua.gr

INTRODUCTION

Coastal flooding is one of the most threatening and detrimental natural disasters affecting coastal areas (Chondros et al., 2021), mainly caused by Sea Level Rise (SLR) due to astronomical tide and storm surge, along with the concurrent wave action. The risk increases further in coastal areas with the presence of river or stream outflows, potentially leading under extreme conditions to the inundation of even larger domains, a phenomenon defined as a compound flood event. The simultaneous occurrence of extreme river discharge and storm surge can cause extreme damage far exceeding the ones those events would cause separately with many real-life examples worldwide, showing their destructive capabilities and importance. Despite of this, the a priori assessment of coastal flooding vulnerability focusing on dominant physical drivers, to identify potential flood-prone areas is not commonly adopted in the literature. Furthermore, while many studies have focused on analyzing the long-term impact of compound flood events, to this day, few research efforts have tackled the near-real time prediction of such events, to assist with community preparedness and facilitate the proper adaptation measures.

The scope of this research is to present a wholistic methodological framework to first assess the coastal flooding vulnerability and afterwards develop and implement an Early Warning System, called EWS_CoCoFlood hereafter, which derives data from open metocean databases and combines numerical modelling and machine learning. The goal of EWS_CoCoFlood is to enhance the resilience of coastal communities while simultaneously providing reliable warnings about the imminent threat of compound flooding.

STUDY AREA AND AVAILABLE DATA

The study site is located in the city of Pyrgos, Ilis in southwestern Greece and encompasses the surrounding coast in each side of the Alfeios River mouth (extending at a total of ~ 9km). Several low-lying areas and residencies with close proximity to the coastline can be identified along the coastline north, while the sea bottom slope is relatively mild. Upstream Alfeios river, a hydroelectric dam is situated which however can be overtopped and can act as a spillway. A detailed topo-bathymetric survey was conducted by Nireas Engineering & Municipality of Pyrgos to provide valuable insights about the bottom contours and upper beach face elevations and was combined with a detailed DEM with a resolution of 5 m, provided by the Hellenic Cadastre.

Offshore sea-state wave characteristics and sea level data from hindcast simulations and projections incorporating climate change impacts were obtained from the Copernicus Clmate Data Store (CDS, https://cds.climate.copernicus.eu/) effectively obtaining three analysis periods, the historical (1976-2005), the medium term (2041-2070) and long term future (2071-2100). Parameters such as population and land use were provided by the registry of the municipality of Pyrgos and earth observation databases (CORINE).

COASTAL FLOODING VULNERABILITY INDEX

Coastal flooding inundation is dependent on a multitude of physical drivers (often acting in tandem) whereas the risk and associated impacts have strong implications to the economy and the community safety. Therefore, estimating beforehand flood-prone areas is a rather complex task. In this spirit during this research the team of LHW attempts to create a Coastal Flooding Vulnerability Index (CFVI) in the spirit of the Coastal Vulnerability Index (Tsaimou et al., 2023). The selected parameters (shown in Table 1) that were be considered for the estimation of the CVFI were based on data collection from field measurement campaigns, renowned metocean databases, wave propagation simulations utilizing a Parabolic Mild Slope wave model (Maris PMS) developed by Scientia Maris (2022) and coastal profile modelling utilizing the CSHORE model (Kobayashi, 2009). Evaluation of the parameters was undertaken using spatial segments of 50 m along the shoreline.

Table 1. Parameters selected for the CFVI calculation.

Parameter	Source
Land use	CORINE
Residents / m^2	Municipality of Pyrgos
Active profile height (m)	Topo-bathymetric survey
Significant wave height (m)	CDS and Maris PMS
Sea level rise (mm)	CDS
Rate of shoreline change (m/day)	CDS, PMS & CSHORE
Marine bed slope (%)	Topo-bathymetric survey
Land slope (%)	Topo-bathymetric survey
River proximity (m)	GIS
Number of compound events	CDS

The ranking of the individual indices was based on boundaries utilized in previous studies (Tsaimou et al., 2023) where applicable, whereas for parameters without available ranking in the literature the boundaries were defined based on the expertise and discretion of the LHW team. The CVFI is then calculated by the following relationship:

$$CFVI = \sqrt{\frac{p_1 \times p_2 \times p_3 \times p_4 \times p_5 \times p_6 \times p_7 \times p_8 \times p_9}{9}} \quad (1)$$

where p denotes the parameters shown in Table 1. To obtain the CVI ranking 5 classes were defined ranging from 1 (very low vulnerability) to 5 (very high vulnerability) determined utilizing the historical dataset values and segregating in classes based on quantiles. Figure 1 showcases the values of CVFI along the study area for the historical period, indicating that the most vulnerable areas are situated at residential areas north the river mouth, which have been subjected to several flood events over the past decades.

Figure 1. CVFI for the historical dataset.

EWS_CoCoFLOOD WEB APPLICATION

To deploy the operational EWS_CoCoFlood several numerical simulations of wave propagation, overtopping and flooding inundation were performed. To briefly summarize, for each of the historical and future periods, several wave propagation simulations with Maris PMS were conducted to obtain nearshore wave characteristics along the 10 m depth contour. Thereafter, CSHORE was employed to estimate wave overtopping discharges along cross-sections of an average of 100 m distance apart, which were used to feed the HEC-RAS (USACE 2020) numerical model to estimate the flood depths in the hinterland. The scenarios that were set as boundary conditions in the simulations were selected by employing a weighted K-Means algorithm. For more details on the methodological framework the interested reader is referred to the publication of Papadimitriou et al., 2024.

The simulation results were then as output to train an Artificial Intelligence (AI) algorithm that will be capable of predicting the flood depths of the study using only a handful of parameters. Effectively, the user has to specify wave characteristics (H_s, T_p, MWD), water level elevation WL and the river discharge Q and in a few seconds the flood depths are illustrated in a web-application as shown in Figure 2.

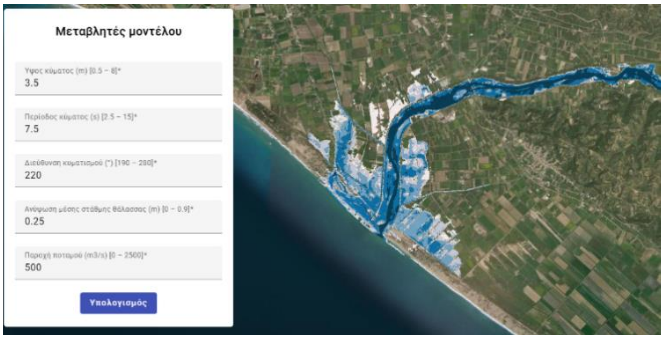

Figure 2. EWS_CoCoFlood web-application

It should be noted that after evaluating several options for the AI-based algorithm, a multilayer Feed-Forward Artificial Neural Network was selected as the optimal architecture, comprised of two hidden layers with 12 units (neurons), capable of predicting the water depths due to imminent compound flood events. Finally, a training /validation split of 80%/20% was implemented during the training procedure of the ANN.

CONCLUSIONS AND FUTURE RESEARCH

In this research, a methodological framework to assess coastal flooding vulnerability, with the development of a complex index is firstly presented. The index, developed and applied in the coastal area of Pyrgos, Greece, combines physical and social parameters with the goal to provide a comprehensive yet simple approach to estimate flood-prone areas. Thereafter, having identified the areas more vulnerable to coastal flooding, the development of an Early Warning System for the accurate and timely prediction of the imminent compound flooding in the same area is presented. The developed EWS_CoCoFlood, represents a novel tool, leveraging advanced numerical simulations of waves and hydrodynamics, alongside open databases and Artificial Neural Networks. The tool, bundled in a user-friendly web-application, is poised to serve as a valuable tool in enhancing the resilience of coastal areas, against the impending threat of compound riverine and coastal flooding. The ongoing and subsequent phases of the research are centered on the integration of rainfall-induced flooding dynamics and incorporation of storm-induced erosion, to further expand the applicability and longevity of EWS_CoCoFlood.

ACKNOWLEDGEMENTS

This research is carried out in the context of the project "Adaptation to Climate Change Through the Development of an Early Warning System for Compound Coastal Flooding: Implementation in the Alfios River Estuary in the Coastal Zone of Municipality of Pyrgos, Greece - EWS_CoCoFlood" under the call for proposals "Physical Environment & Innovative Actions 2022 - Priority Axis 3 Research and Application". The project is financed by the Green Fund (3523 - 699/2022)."

REFERENCES

Chondros M., Metallinos, A., Papadimitriou A., Memos, C., & Tsoukala V.K. (2021). A Coastal Flood Early-Warning System Based on Offshore Sea State Forecasts and Artificial Neural Networks, *J. Mar. Sci. Eng.* 9, 1272.

Kobayashi, N. (2009). Documentation of cross-shore numerical model CSHORE; Research Report No. CACR-09-06, University of Delaware, Newark, DE, USA.

Scientia Maris (2022). Maris PMS Guide. Athens, Greece

USACE (2020): HEC-RAS Hydraulic Reference Manual, U.S.Army Corps of Engineers, Hydrologic Engineering Center, Version 6.0.

Tsaimou C., Papadimitriou A., Chalastani V., Sartampakos P., Chondros M., & Tsoukala V.K. (2023). Impact of Spatial Segmentation on the Assessment of Coastal Vulnerability-Insights and Practical Recommendations. *J. Mar. Sci. Eng.* 11, 1675.

An Index Based Approach for Multi-risk Assessment of Future Climate Change Related Hazards

Boumpoulis V.[1,2,*], Masina M.[3,2], Ferrario D.[2,3], Maraschini M.[3,2], Nguyen D. [2,3], Dal Barco MK. [2,3], Fonseca H. [2,3], Rufo O. [2,3], Torresan S.[3,2] and Critto A. [2,3]

[1] Department of Geology, University of Patras, Patras, Greece
[2] Department of Environmental Sciences, Informatics and Statistics, Ca' Foscari University of Venice, Venice, Italy
[3] Euro-Mediterranean Center on Climate Change Foundation, Venice, Italy

*corresponding author:
e-mail: vasileios_boumpoulis@ac.upatras.gr

INTRODUCTION

Climate-related hazards and their adverse impacts on human and natural systems are anticipated to intensify in the future as a result of climate change. In response, several methods have been developed in recent decades for risk assessment. Among these index-based approaches are highlighted as some of the simplest and most efficient methods for calculating risk.

Despite the plethora of risk assessment studies referencing traditional single risk approaches (Kappes et al., 2012) the interaction between these individual hazards often overlaps, necessitating a risk management strategy that addresses both multi hazards and their combined effects (Šakić Trogrlić et al., 2024) as neglecting them potentially can lead to underestimation or overestimation of risks (Stalhandske et al., 2024). Therefore, the main aim of this study is the development of a relative multi risk assessment methodology, using an index-based approach to investigate the future evolution of climate related hazards for multiple critical functions in the Veneto Region.

METHODOLOGY

The multi risk assessment approach follows the IPCC definition of risk, expressed as a function of hazard (H), exposure (E) and vulnerability (V). The proposed procedure includes the following steps: 1) the selection of appropriate indicators for evaluating hazard, exposure and vulnerability, 2) relative single risk assessment and 3) relative multi-risk assessment.

For hazard characterization in the Veneto Region, the climate-related hazards of heatwaves, drought, flooding from intense rainfall, soil erosion and coastal flooding were considered. The data used in the analysis are expressed as thirty years anomaly values, which represent the variations in future conditions compared to the historical reference period 1976–2005. The anomaly values were examined for two future time horizons (2021–2050 and 2071–2100) in three different Representative Concentration Pathway scenarios (RCP2.6, RCP4.5 and RCP8.5).

For exposure and vulnerability analysis five distinct capital typologies were selected based on existing methodologies in climate risk assessments (Bonato et al., 2021; Mysiak et al., 2018; Sambo et al., 2023). Hazard, vulnerability and exposure indicators values were normalized between 0 and 1 to calculate the relative risk index, providing a practical framework for risk assessment. The calculated relative risk values were then classified into three classes (low, medium, high) through an equal interval classification. In the final step of the methodology for the relative multi-risk assessment, the single relative risk values were reclassified on a scale from 0 (absence of high relative risk) to 1 (presence of high relative risk), with the aim of identifying areas where multiple high relative risks overlap.

RESULTS

The main result of this analysis indicates the percentage of the regional territory affected by multiple receptor-hazard combinations with high relative risk for each time horizon and emission scenario. The maximum number of receptor-hazard combinations at high relative risk is two for the 2021-2050 timeframe under the RCP4.5 scenario and for 2071-2100 timeframe under the RCP2.6, while for 2021-2050 timeframe under the RCP2.6 and 8.5 the maximum number is three. The situation worsens for the 2071–2100 timeframe under RCP4.5 and RCP8.5 scenarios, with the number of receptor-hazard combinations at high relative risk increasing to four and seven, respectively.

CONCLUSION

The proposed relative multi risk assessment approach is a quick, low cost and effective tool for initial detection of the most vulnerable areas, which can support the local authorities in identifying suitable management and mitigation strategies against future climate change related hazards.

REFERENCES

Bonato, M., Sambo, B., Sperotto, A., Lambert, J.H., Linkov, I., Critto, A., Torresan, S., & Marcomini, A. (2021). Prioritization of Resilience Initiatives for Climate-Related Disasters in the Metropolitan City of Venice. *Risk Anal.* 42(5), 931–952.

Kappes, M.S., Keiler, M., von Elverfeldt, K., & Glade, T. (2012). Challenges of analyzing multi-hazard risk: A review. *Nat. Hazards* 64(2), 1925–1958.

Mysiak, J., Torresan, S., Bosello, F., Mistry, M., Amadio, M., Marzi, S., Furlan, E., & Sperotto, A. (2018). Climate risk index for Italy. *Philos. Transact. A Math. Phys. Eng. Sci.* 376(2121), 20170305.

Šakić Trogrlić, R., Thompson, H.E., Menteşe, E.Y., Hussain, E., Gill, J.C., Taylor, F.E., Mwangi, E., Öner, E., Bukachi, V. G., & Malamud B.D. (2024). Multi-Hazard Interrelationships and Risk Scenarios in Urban Areas: A Case of Nairobi and Istanbul. *Earths Future* 12(9), 1–24.

Sambo, B., Bonato, M., Sperotto, A., Torresan, S., Furlan, E., Lambert, J.H., Linkov, I., & Critto, A. (2023). Framework for multirisk climate scenarios across system receptors with application to the Metropolitan City of Venice. *Risk Anal.* 43(11), 2241–2261.

Stalhandske, Z., Steinmann, C.B., Meiler, S., Sauer, I.J., Vogt, T., Bresch, D.N., & Kropf, C.M. (2024). Global multi-hazard risk assessment in a changing climate. *Sci. Rep.* 14(1), 1–14.

Assessing the Coastal Flooding Risk from Present till 2100 at the Ancient City of Delos, Greece

Mallouri D.[1,*], Petrakis S.[1], Fadin L.[2], Moretti J. C.[3], Vandarakis D.[1], Moraitis V.[1], Drakopoulou P.[1], and Kapsimalis V.[1]

[1] Hellenic Centre for Marine Research, Greece
[2] École française d'Athènes, Greece
[3] Institute for Research on Ancient Architecture, France

*corresponding author:
e-mail: d.malliouri@hcmr.gr

ABSTRACT

The research objective in the present paper is twofold; first, the combination of state-of-art climatic information, nonstationary extreme value wave analysis and numerical modeling for the derivation and simulation of characteristic coastal flooding scenarios, and at a subsequent step, the assessment of a climate-related risk of coastal flooding incorporating site-specific aspects. The proposed methodology is implemented at the archaeological site of Delos, Greece–an island of exceptional archaeological significance but highly vulnerable to coastal inundation due to its low elevation and proximity to the sea. Through the adopted approach, the coastal flooding risk of the coasts of Delos is estimated at high spatial resolution (e.g., of 1m) throughout the 21st century, and the ancient structures being most exposed to coastal flooding are determined. The findings provide valuable insights into the natural hazard of coastal inundation at Delos, offering essential tools and information to protect the archaeological site from the adverse effects of this hazard in the future. Therefore, the adopted approach could be a key element for coastal zone planning and management, as it assesses spatially the coastal flooding risk, which is vital information for stakeholders to protect coastal regions and archaeological sites against coastal flooding.

INTRODUCTION

Global warming-induced sea level rise is among the most significant impacts of climate change, posing a substantial threat to coastal lowlands by causing future flooding with serious effects on social, economic, cultural, and touristic infrastructures. This coastal flooding risk is related to climate change, not only due to the rising sea level that threatens to inundate coastal areas but also because of the increased frequency and intensity of destructive wave storms and storm surges that are capable of degrading coastal defenses.

Most approaches assess the coastal flooding risk on a regional scale (Su et al., 2024). Despite its significance, due to the increased computational cost, these studies usually do not result in flooding results of high spatial resolution. The proposed approach aims to produce detailed flooding maps for each examined scenario. This is accomplished through global and regional climatic scenarios, coastal modelling, and by considering both coinciding and non-coinciding scenarios of the most essential drivers of coastal flooding, such as mean sea level rise, extreme storm surge, tide, extreme wave runup, and assesses their nonstationary variability (Galiatsatou et al. 2019; Malliouri et al. 2023).
Subsequently, the present paper first composes a climate-related risk of coastal flooding based on the likelihood and consequence of a design flooding event and secondly incorporates site-specific aspects into the qualitatively assessment of the climate-related flooding risk. The adopted methodology is close to the general notion of risk assessment, presenting also some innovative points that make it more suitable for coastal archaeological sites.

The case study is Delos Island, located in the middle of the Cyclades in the Aegean Sea. This is an island of exceptional archaeological significance but highly vulnerable to coastal inundation due to its low elevation and proximity to the sea (Figure 1). Delos Island has been inscribed on the UNESCO World Heritage List since 1990 (https://whc.unesco.org/en/list/530/).

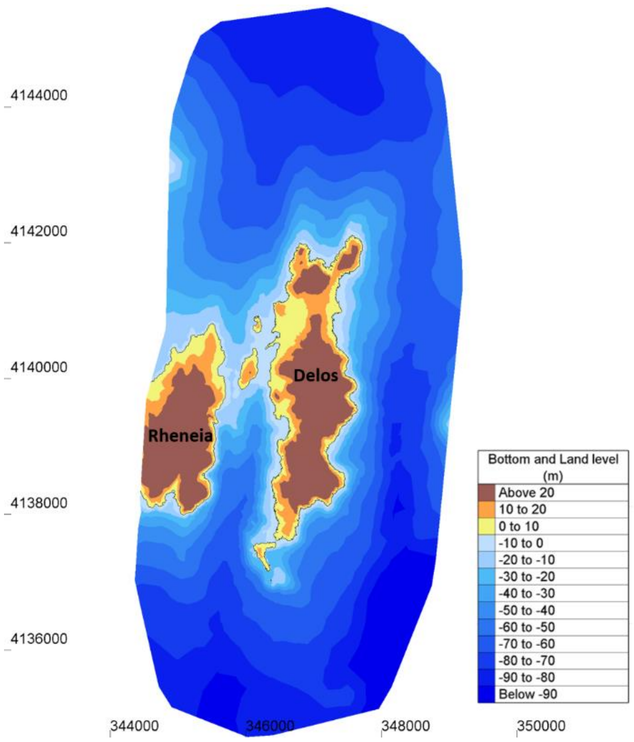

Figure 1. Bathymetry and topography of Delos Island in Greece. (Projected in ETRS89/UTM zone 35N: EPSG:25835).

METHODOLOGY

In the present analysis, 18 wave scenarios were simulated corresponding to 3 mean wave directions (MWD), 3-time snapshots and 2 future shared socioeconomic pathway (SSP) scenarios, namely a pessimistic one SSP8.5 and an optimistic one SSP4.5. The time snapshots are the present, near future, and distant future, corresponding to the years 2025, 2050 and 2100. Each flooding scenario corresponds to a one-time snapshot and one SSP scenario and gathers the results of three wave scenarios of different MWD that are associated with the specific time snapshot and SSP scenario.

Moreover, the flooding scenarios consist of four sub scenarios: the first for flooding conditions due to mean sea level MSL, the second due to the coincidence of MSL and extreme sea level ESL (MSL+ESL), including mean sea level rise, tide and storm surge, the third due to MSL and significant wave runup (MSL + Ex. Runup), and the fourth due to coincidence of all examined flooding drivers, which is the most extreme sub scenario (MSL + ESL + Ex. Runup).
Two opensource models were implemented: the SWAN model (Holthuijsen et al., 1993), developed at Delft University of Technology, which is a third-generation wave model that computes random, short-crested wind-generated waves in offshore and coastal regions, and the phase resolving SWASH model, which is more appropriate in surf and swash zone, i.e. in swallow waters and onshore. A risk assessing approach is implemented at a subsequent step, based on a matrix approach (Kovačević et al., 2019).

RESULTS

The results of the six flooding scenarios are derived by applying the proposed approach. The modern and ancient structures near the shoreline of the medium at present and high coastal flooding risk in the future are mainly the ancient city of Delos, the South-West Seafront, the commercial buildings, and the Asklepieion (see Figure 2). The part of the ancient city of Delos prone to coastal flooding includes the Ancient Harbor, the Modern mole, the Agora of Theophrastus, Bases and Monuments North of the Agora of Theophrastus, the Sanctuary of Artemis, a part of the Sanctuary of Apollo, and the Agora of the Hermaists or Competaliasts. Regarding the obtained coastal flooding risk through the proposed risk assessing approach incorporating archaeological aspects, three segments of the western shoreline of Delos are characterized by a medium present risk but by a high risk in 2100.

CONCLUSIONS

The paper deals with the coastal flooding risk assessment at present and in the near and distant future at Delos Island in Greece. This is accomplished through global and regional climatic scenarios, the implementation of nonstationary multivariate extreme value analysis to wave storms' parameters, and numerical modeling. From the proposed methodology, it is derived that apart from the mean sea level rise and extreme sea level, extreme wave runup should be considered in assessing the potential consequences and extent of coastal flooding. In addition, this is necessary in micro-tidal and micro-storm surge seas, as in the present case study, where the dominant driver of coastal flooding is wave storms and the associated runup.

Referring to the site-specific concluding remarks, three segments of the western shoreline of Delos are characterized by a medium present risk but by a high risk in 2100. Specifically, these segments are adjacent to the ancient city of Delos, the South-West Seafront, the commercial buildings and the Asklepieion. The part of the ancient city of Delos exposed to coastal flooding includes the Ancient Harbor, the Modern mole, the Agora of Theophrastus, Bases and Monuments North of the Agora of Theophrastus, the Sanctuary of Artemis, a part of the Sanctuary of Apollo, and the Agora of the Hermaists or Competaliasts.

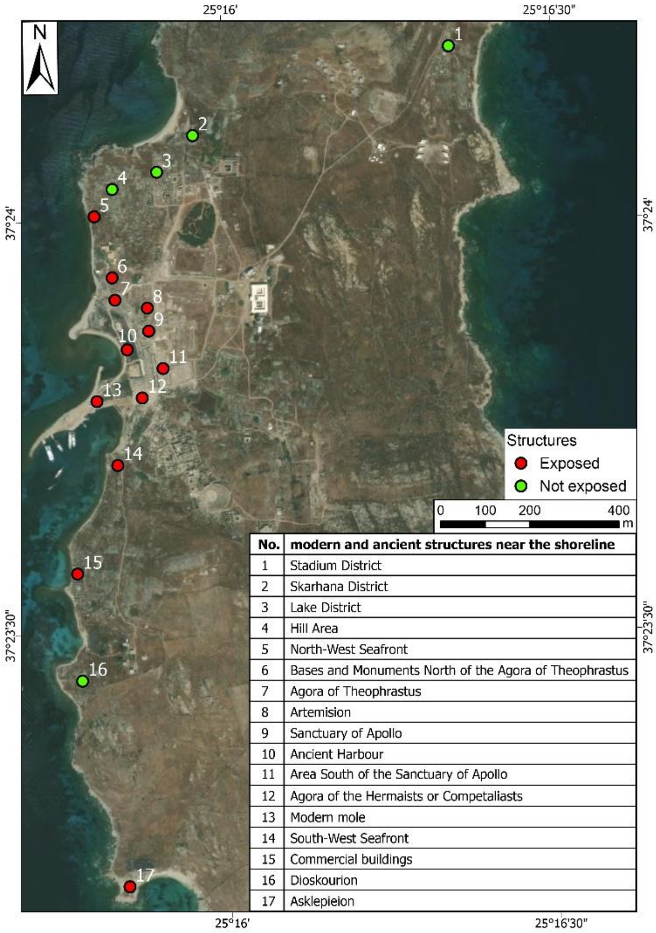

Figure 2. The modern and ancient structures near the shoreline of Delos, exposed to coastal flooding (red color) and not exposed to coastal flooding (green color).

ACKNOWLEDGEMENTS

D. Malliouri acknowledges support of this work by the Research Project "ESSENCE": Risk Assessment in Coastal Areas, at Hellenic Centre for Marine Research (HCMR), funded by a private international fund.

REFERENCES

Galiatsatou, P., Makris, C., Prinos, P., & Kokkinos, D. (2019). Nonstationary joint probability analysis of extreme marine variables to assess design water levels at the shoreline in a changing climate. *Nat. Hazards* 98, 1051–1089.
Holthuijsen, L.H., Booij, N., & Ris, R.C. (1993). A Spectral Wave Model for the Coastal Zone, in: Ocean Wave Measurement and Analysis. ASCE, 630–641.
Kovačević, N., Stojiljković, A., & Kovač, M. (2019). Application of the matrix approach in risk assessment. *Oper. Res. Eng. Sci.: Theory Appl.* 2, 55–64.
Malliouri, D.I., Moraitis, V., Petrakis, S., Vandarakis, D., Hatiris, G.A., & Kapsimalis, V. (2023). A Non-Stationary and Directional Probabilistic Analysis of Coastal Storms in the Greek Seas. *Water* 15.
Su, J., Murawski, J., Nielsen, J.W., & Madsen, K.S. (2024). Coinciding storm surge and wave setup: A regional assessment of sea level rise impact. *Ocean Eng.* 305, 117885.